

Transport Properties Measurements of Next-Generation Refrigerants and Mixture

By

Dipayan Mondal

A dissertation submitted in partial fulfillment of the
requirements for the degree of

Doctor of Philosophy (Ph.D.)

in

Mechanical Engineering



Department of Science and Advanced Technology

Graduate School of Science and Engineering

Saga University

Japan

September 2021

Approval

Department of Science and Advanced Technology
Graduate School of Science and Engineering
Saga University
1, Honjo-machi, Saga 840-8502, Japan

This is to certify that the dissertation submitted by

Dipayan Mondal

titled “**Transport Properties Measurements of Next-Generation Refrigerants and Mixture**” has been approved by the dissertation committee for the partial fulfillment of the requirements for the degree of *Doctor of Philosophy (Ph.D.) in Mechanical Engineering* from the Department of Science and Advanced Technology, Graduate School of Science and Engineering, Saga University, Japan in September 2021.

Dissertation Committee:

1. 宮良 明男
Dr. Akio MIYARA
Professor, Department of Mechanical Engineering
Saga University, Japan
**Chairman
(Supervisor)**
2. 光 秋 雄一
Dr. Yuichi MITSUTAKE
Professor, Institute of Ocean Energy
Saga University, Japan
Member
3. 仮屋 王史
Dr. Keishi KARIYA
Associate Professor, Department of Mechanical Engineering
Saga University, Japan
Member
4. 石田 賢治
Dr. Kenji ISHIDA
Lecturer, Department of Mechanical Engineering
Saga University, Japan
Member

Acknowledgments

At first, it is my immense pleasure to express the praise and gratitude to the Merciful Almighty God, who provides me blessings, wisdom, peace of mind, strength, and good health and makes me capable of completing this research work.

I would like to express my sincere gratitude to Professor Dr. Akio Miyara to accept me as a Ph.D. student without any hesitation in his laboratory. It is my proud privilege and a great pleasure to work under his supervision. I am grateful to him for his expert guidance, encouragement, suggestions, and extraordinary kindness throughout my research work. Without his support, help, and trust, it would not be possible for me to achieve this milestone. I appreciate all his contributions of time from his very busy schedule, support, and ideas as an excellent supervisor as well as a good motivator. In addition, I would also like to sincerely acknowledge the MEXT (Ministry of Education, Culture, Sports, Science, and Technology) to grant me a scholarship for this study.

I would like to express my appreciation to Assoc. Prof. Dr. Keishi Kariya for his insightful recommendations, inspirations, and support through my research. I would like to thank the other members of my dissertation committee, Professor Dr. Yuichi Mitsutake, and Dr. Kenji Ishida for their time, insightful comments, thoughts, and suggestions to improve this work.

I would like to thankfully acknowledge the ‘New Energy and Industrial Technology Development Organization (NEDO)’ and ‘Thermal Management Materials and Technology Research Association (TherMAT)’, Japan for providing the financial support during this work. The authors also thank the Chemours Company located in the USA, and the National Institute of Advanced Industrial Science and Technology (AIST), AGC Inc., Daikin Industries, Ltd., Japan for providing the samples.

I would like to thank the “Khulna University of Engineering & Technology” of Bangladesh for granting me study leave for my doctoral study. Special thanks to Dr. Mohammad Ariful Islam, Professor of Khulna University of Engineering & Technology, Bangladesh to introduce me to my supervisor and for his valuable guidance and suggestions in my research.

I also addressed my thanks to all my lab members for their supports (especially, Alam, Hasan, Yamaguchi, Hori, Miyoshi, Amakusa, Morotomi, and Tuhin san). I would like to express my gratitude to all my international and Japanese friends for making my Japanese life more comfortable and enjoyable. Finally, I deeply grateful to my beloved parents and wife for their patience, moral support, and endless love in this journey of my doctoral degree.

This dissertation is dedicated to my beloved parents, wife, and lovely daughter whose love, encouragement, and prayer have enabled me to attain such achievement and integrity.
Thanks to all for their support throughout my life that has led me to this point.

Abstract

Concerns about the global warming potential (GWP) of conventional refrigerants have prompted researchers to seek out low-GWP alternatives having other suitable properties in terms of environmental context. With the awareness of the environmental issues, the reduction of greenhouse gas emissions in accordance with the Kyoto Protocol is more familiarized to meet the new outcomes of next-generation refrigerants. Refrigerants belong to the hydrofluoroolefins (HFOs), hydrochloro-fluoroolefins (HCFOs) and hydrofluoroether (HFEs) families are promising candidates for designing high-temperature heat pumps and organic Rankine cycles owing to their favorable properties especially for low-GWP. The viscosity and thermal conductivity are the important transport properties of working fluids that are used as the key tools to design and implement the optimum energy systems, efficient processes, selection of the refrigerant for the practical appliances, and simulations. Therefore, the motivations of this research are to measure the viscosity and thermal conductivity of next-generation potential low GWP refrigerants. In this research work, the viscosities and thermal conductivities of R1336mzz(E), 3,3,4,4,5,5-HFCPE, R1132(E), and a mixture of R1123+R32 were measured over a wide range of temperature and pressure by using the tandem capillary tubes method and transient hot-wire method, respectively.

In the tandem capillary tubes method, the pressure drop of a laminar flow was determined to measure the viscosity of test fluids. This is an improved technique of the Hagen-Poiseuille theory-based capillary tube method by considering pipe end and kinetic energy correction coefficients. In this method, the measuring cell known as viscometer was constructed using almost the same diameter but different lengths of two capillary tubes that are horizontally installed in series connection to minimize the end effects of capillary tubes. For R1336mzz(E), the viscosity measurements were performed over the pressures from 0.5 to 4.0 MPa and temperatures from 314 to 394 K for the liquid phase, 353 to 453 K for the vapor phase, and 413 to 453 K for the supercritical region, respectively. The measured liquid, vapor, and supercritical viscosity data were reported at a range of 79.6 to 251.3 $\mu\text{Pa s}$, 10.8 to 16.2 $\mu\text{Pa s}$, and 18.1 to 53.6 $\mu\text{Pa s}$ corresponding to the above pressure and temperature. The expanded uncertainties for this measurement are calculated at 2.26 % for liquid, 2.30 % for vapor, and 2.32 % for supercritical phase using $k=2$ and the 95 % confidence level. For

3,3,4,4,5,5-HFCPE, the kinematic viscosities were measured by using this method at the range of temperatures from 332 to 494 K over the pressure up to 4.0 MPa in the liquid phase, while in the vapor phase from 413 to 514 K at pressures up to 2.0 MPa. The measured liquid and vapor kinematic viscosities were reported at a range of 0.0009 to 0.0041 cm² s⁻¹, and 0.0014 to 0.0065 cm² s⁻¹ for the above pressure and temperature. The expanded uncertainties of the measurements for both liquid and vapor phases were 2.24 % and 2.94 % with k=2 and a 95% confidence level, respectively. For R1132(E), the viscosity measurements were performed over the pressure up to 4.0 MPa at a temperature range from 302 to 335 K for liquid and 323 to 345 K for vapor phases, respectively. Corresponding to the above pressure and temperature, the measured liquid and vapor viscosities of R1132(E) were reported at a range of 63.8 to 114.5 μPa s, and 12.5 to 15.2 μPa s, respectively. For the binary mixture of R1123+R32, the viscosities of the mixture refrigerant were measured by this method over the pressure up to 4.5 MPa and a temperature range from 251 to 313 K for the liquid phase and from 323 K to 383 K in the vapor phase, respectively. Mass fractions of measured R1123/R32 refrigerant mixture were 0.428/0.572 in the liquid phase and 0.425/0.575 in the vapor phase. The measured liquid, and vapor viscosity data were reported at a range of 84.2 to 200.4 μPa s, and 14.6 to 19.1 μPa s, respectively. The expanded uncertainties of viscosity measurements for R1123+R32 were estimated at 2.21 % and 2.60 % of the liquid and vapor phases, respectively. Therefore, the measured viscosity data for each refrigerant are compared and correlated with the predicted or calculated data from the existing correlations and models, REFPROP, and/or other research data. Moreover, the simplified correlations in terms of saturation temperature for the above-mentioned refrigerants are developed to predict the saturated viscosities for liquid and vapor phases, respectively.

On the other hand, the well-known transient hot-wire method was used to measure the thermal conductivity of fluids. Two thin (diameter 15 μm) platinum wires in parallel connection had been used in this hot wire apparatus as short and long wire, which is worked as both electrical heat source and resistance thermometer to measure the temperature rise during experiments. In addition, the two wires compensating system was considered to eliminate the axial heat conduction. The temperature ranges were considered for the measurements from around room temperature to the high temperature for pure working fluids in this study. For R1336mzz(E), the thermal conductivity data were reported in the temperature from 313 to 393 K over the pressure until 4.0 MPa for liquid state and

temperature from 313 to 453 K at pressure up to 2.5 MPa for vapor state. Also, the thermal conductivity in a supercritical region was recorded from temperature range 413 to 453 K and pressures at 3.0 to 4.0 MPa. Corresponding to the above pressure and temperature, the measured liquid, vapor, and supercritical thermal conductivities were reported as 52.0 to 70.2 mW m⁻¹ K⁻¹, 12.6 to 21.6 mW m⁻¹ K⁻¹, and 21.5 to 45.5 mW m⁻¹ K⁻¹, respectively. The expanded uncertainties for the thermal conductivity measurements of R1336mzz(E) were reported as 3.06 %, 3.16 %, and 3.23 % at the liquid, vapor, and supercritical regions, respectively. For 3,3,4,4,5,5-HFCPE, the measurements of the thermal conductivity were performed over temperatures from 333 to 473 K and pressure up to 4.0 MPa. This measured liquid and vapor thermal conductivity data were found in the range of 51.0 to 85.1 mW m⁻¹ K⁻¹ and 15.7 to 23.0 mW m⁻¹ K⁻¹, respectively. The combined standard uncertainties were calculated as 1.54 % and 1.76 % for liquid and vapor phases, respectively, where the expanded uncertainties were found as 3.08 % and 3.52 % with k=2 and a confidence level of 95 % for the liquid and vapor thermal conductivity measurements. Therefore, the measured thermal conductivities of the above-mentioned refrigerants are compared and correlated with the predicted or calculated data from the existing correlations and models, REFPROP, and/or other research data. Moreover, the simplified correlations in terms of saturation temperature for each refrigerant are developed to predict the saturated thermal conductivities for liquid and vapor phases by extrapolating the experimental data until the saturation conditions, respectively.

Table of Contents

Acknowledgments	i
Abstract	iii
Table of contents	vi
List of figures	ix
List of tables	xiii
Nomenclature	xv
1 Introduction	1
1.1 Overview	1
1.2 Fundamental concepts of refrigerants used as working fluids	2
1.2.1 Desirable properties of ideal refrigerants	2
1.2.2 Factors considering the selection of refrigerants as working fluids	3
1.2.3 Various refrigerants used as working fluids	4
1.3 Environmental impact of refrigerants	11
1.4 International agreement on environmental issues	13
1.5 Refrigerant reclamation and disposal	17
1.6 Measures to mitigate the effects of ODP and GWP	17
1.7 Research potentiality	18
1.8 Research objectives	18
1.9 Dissertation outline	19
References	20
2 Literature Review	23
2.1 Progression of refrigerants	23
2.2 History of conventional research related to this research	26
2.3 Various methods to measure transport properties of fluids	28
2.3.1 Methods for viscosity measurements of fluids	28
2.3.2 Methods for thermal conductivity measurements of fluids	32
2.4 Progression of capillary viscometer and transient hot-wires method	34
2.4.1 Progression history of capillary viscometer	34

2.4.2	Progression history of transient hot-wires method	38
	References	41
3	Theory and Experimental Apparatus	49
3.1	Theory and Experimental Apparatus for Viscosity Measurement	49
3.1.1	Theory of the tandem capillary tubes (TCT) method	49
3.1.2	Experimental apparatus for viscosity measurement	54
3.1.3	Apparatus reliability test for viscosity measurement	56
3.1.4	Uncertainty calculation for viscosity measurement	58
3.2	Theory and Experimental Apparatus for Thermal Conductivity Measurement	61
3.2.1	Theory of the transient hot-wires (THW) method	61
3.2.2	Experimental apparatus for thermal conductivity measurement	65
3.2.3	Bridge circuit to measure the transient temperature rise	66
3.2.4	Apparatus reliability and validity test for thermal conductivity measurement	67
3.2.5	Polarization technique and typical data measurements	68
3.2.6	Uncertainty calculation for thermal conductivity measurement	70
3.3	Theory for deviations in terms of AAD, MAD, and Bais	71
	References	72
4	Experimental Measurement and Results	75
4.1	Test Fluids	75
4.2	Experimental Viscosity Measurement	77
4.2.1	Viscosity measurement of R1336mzz(E)	77
4.2.1.1	Overview of R1336mzz(E)	77
4.2.1.2	Measured viscosities of R1336mzz(E)	79
4.2.1.3	Data deviations of R1336mzz(E)	87
4.2.1.4	Correlations for the saturated viscosity of R1336mzz(E)	89
4.2.1.5	Conclusion	91
4.2.2	Kinematic viscosity measurement of 3,3,4,4,5,5-HFCPE	92
4.2.2.1	Overview of 3,3,4,4,5,5-HFCPE	92
4.2.2.2	Measured kinematic viscosities of 3,3,4,4,5,5-HFCPE	94
4.2.2.3	Correlations at saturation conditions for kinematic	101

viscosity of 3,3,4,4,5,5-HFCPE	
4.2.2.4 Conclusion	103
4.2.3 Viscosity measurement of R1132(E)	104
4.2.3.1 Overview of R1132(E)	104
4.2.3.2 Measured viscosities of R1132(E)	106
4.2.3.3 Data deviations of R1132(E)	111
4.2.3.4 Conclusion	113
4.2.4 Viscosity measurement of the binary mixture of R1123+R32	114
4.2.4.1 Overview of a binary mixture of R1123+R32	114
4.2.4.2 Measured viscosities of a binary mixture of R1123+R32 and correlation	117
4.2.4.3 Data deviations of R1123+R32	128
4.2.4.4 Correlations at saturation conditions for R1123+R32	129
4.2.4.5 Conclusion	132
4.3 Experimental Thermal Conductivity Measurement	133
4.3.1 Thermal conductivity measurement of R1336mzz(E)	133
4.3.1.1 Overview of R1336mzz(E)	133
4.3.1.2 Measured thermal conductivities of R1336mzz(E)	135
4.3.1.3 Comparison with related research and data deviations of R1336mzz(E)	144
4.3.1.4 Correlations at saturation state for R1336mzz(E)	147
4.3.1.5 Conclusion	150
4.3.2 Thermal conductivity measurement of 3,3,4,4,5,5-HFCPE	151
4.3.2.1 Overview of 3,3,4,4,5,5-HFCPE	151
4.3.2.2 Measured thermal conductivities of 3,3,4,4,5,5-HFCPE	152
4.3.2.3 Correlations at saturation condition	160
4.3.2.4 Conclusion	162
References	162
5 Conclusions and Recommendations	171
5.1 Conclusions	171
5.2 Future Recommendations	173
Appendix	A1

List of Figures

1.2.1	Factors considering in an integrated approach to select the refrigerant as working fluids	3
1.2.2	Various refrigerants that are used as working fluid	4
1.2.3	A typical example showing the behavior of minimum-boiling or positive azeotrope mixture of chloroform and methanol	8
1.2.4	A typical example showing the behavior of maximum-boiling or negative azeotrope mixture of water and formic acid	9
1.2.5	A typical example showing the behavior of the zeotropic mixture	10
1.3.1	Diagram showing chlorine effect on the ozone layer	11
1.3.2	Sketch for impact of global warming potential	12
2.1.1	The progression of refrigerants	24
2.3.1	Schematic view of the main test section of a typical capillary viscometer	29
2.3.2	Schematic view of the main test section of a typical rotational viscometer	29
2.3.3	Schematic view of the main test section of a typical vibrational viscometer	30
2.3.4	Schematic view of the main test section of a typical moving piston or oscillating viscometer	30
2.3.5	Schematic view of the main test section of a falling ball or sphere viscometer	31
2.4.1	A conventional capillary viscometer	35
2.4.2	Capillary viscometers: (a) Ostwald viscometer; (b) pressure capillary viscometer	36
2.4.3	Ubbelohde suspended level viscometer	37
2.4.4	Rankine capillary viscometer	37
2.4.5	Tandem capillary tubes viscometer	38
2.5.1	Several instruments of transient hot-wire technique for fluids	41
3.1.1	The original viewpoint of experimental apparatus to measure the viscosity of refrigerants (a) electric heating system (b) oil bath heating or nybrine cooling system	50
3.1.2	The original viewpoint of (a) layout of the apparatus, and (b) the measuring cell	51
3.1.3	Experimental apparatus for tandem type capillary tubes viscometer	55
3.1.4	Variation of viscosities of R134a with density	58
3.1.5	Deviations between experimentally measured viscosity and REFPROP	58

3.2.1	The original viewpoint of the measuring cell as well as the pressure vessel of the apparatus	61
3.2.2	The original view of experimental apparatus to measure thermal conductivity of refrigerants (a) electric heating system (b) oil bath heating or nybrine cooling system	62
3.2.3	Schematic illustration of the thermal conductivity measuring apparatus	65
3.2.4	A schematic diagram of the measuring bridge circuit	66
3.2.5	Comparative study of thermal conductivity for R134a with the calculated values by REFPROP as well as reference values	67
3.2.6	Variation of unbalanced voltage with logarithmic time	69
4.1.1	Pressure vs. temperature curve of test fluids used to investigate the measurements	76
4.2.1.1	Molecular structures of R1336mzz(E)	78
4.2.1.2	Distribution of the measurements for the viscosity of R1336mzz(E)	80
4.2.1.3	Variation of the liquid viscosity of R1336mzz(E) with density	82
4.2.1.4	Variation of the vapor viscosity of R1336mzz(E) with density	83
4.2.1.5	(a) Variation of the viscosity of supercritical R1336mzz(E) with density, and (b) P-T diagram with defined sub-regions of supercritical phase: liquid-like, pseudocritical, and vapor-like.	84
4.2.1.6	Variation of liquid viscosities of R1336mzz(E) with temperature and pressure	85
4.2.1.7	Variation of vapor and supercritical viscosities of R1336mzz(E) with temperature and pressure	86
4.2.1.8	Comparison of viscosity data of liquid R1336mzz(E) with other green refrigerants: R1336mzz(Z), R1233zd(E), and R1234ze(Z)	87
4.2.1.9	Comparison of the experimental viscosity data in the liquid phase with predicted values by the ECS model	88
4.2.1.10	Comparison of the experimental viscosity data in the vapor and supercritical regions with predicted values by the ECS model	88
4.2.1.11	Extrapolated data for liquid viscosity at the saturated conditions	90
4.2.1.12	Saturated viscosity vs. temperature	90
4.2.2.1	Molecular structure of 3,3,4,4,5,5-HFCPE	92
4.2.2.2	Experimentally measurement points of 3,3,4,4,5,5-HFCPE	94
4.2.2.3	Variation of liquid kinematic viscosities of 3,3,4,4,5,5-HFCPE with temperature	98
4.2.2.4	Variation of vapor kinematic viscosities of 3,3,4,4,5,5-HFCPE with temperature	99
4.2.2.5	3D Presentation of the kinematic viscosities of 3,3,4,4,5,5-HFCPE with temperature and pressure	100

4.2.2.6	Comparison of liquid kinematic viscosities of 3,3,4,4,5,5-HFCPE for pressure at 4.0 MPa and 1.0 MPa	100
4.2.2.7	Extrapolated liquid kinematic viscosities at saturation conditions	102
4.2.2.8	Variation of saturated kinematic viscosities with the saturation temperature	102
4.2.3.1	Molecular structure of R1132(E)	104
4.2.3.2	Temperature and pressure ranges for the experimental points of R1132(E)	106
4.2.3.3	Variation of the viscosity of liquid R1132(E) with density	109
4.2.3.4	Variation of the viscosity of vapor R1132(E) with density	109
4.2.3.5	Variation of the liquid viscosities of R1132(E) with temperature and pressure	110
4.2.3.6	Variation of the vapor viscosities of R1132(E) with temperature and pressure	111
4.2.3.7	Comparative study of viscosity data deviations for liquid R1132(E)	112
4.2.3.8	Comparative study of viscosity data deviations for vapor R1132(E)	112
4.2.4.1	Molecular structure of (a) R1123 and (b) R32	115
4.2.4.2	Temperature and pressure ranges for the binary mixture of R1123+R32	118
4.2.4.3	Variation of interaction coefficient as a function of temperature at the liquid phase	120
4.2.4.4	Variation of viscosity data of liquid R1123+R32 mixture as a function of density	124
4.2.4.5	Variation of viscosity data of vapor R1123+R32 mixture as a function of density	125
4.2.4.6	Variation of the liquid viscosities of R1123+R32 with temperature and pressure	126
4.2.4.7	Variation of the vapor viscosities of R1123+R32 with temperature and pressure	127
4.2.4.8	Deviations of experimental viscosity from calculated values for the liquid R1123+R32	128
4.2.4.9	Deviations of experimental viscosity from calculated values for the vapor R1123+R32	129
4.2.4.10	Extrapolated value of liquid phase viscosity at saturation conditions	130
4.2.4.11	Saturated viscosity vs. temperature	131
4.3.1.1	Molecular geometry of R1336mzz(E) and R1336mzz(Z)	134
4.2.1.2	Measurement points of R1336mzz(E)	136
4.3.1.3	Experimental thermal conductivity of R1336mzz(E) with density in a liquid region	141
4.3.1.4	Experimental thermal conductivity of R1336mzz(E) with density in a vapor region	142

4.3.1.5	Experimental thermal conductivity of R1336mzz(E) with density in a supercritical region	142
4.3.1.6	Experimental thermal conductivity of R1336mzz(E) with temperature	143
4.3.1.7	3D presentation of thermal conductivities of R1336mzz(E) with temperature and pressure	144
4.3.1.8	Comparative liquid thermal conductivity of R1336mzz(E) and R1336mzz(Z) (Alam et al., 2017) concerning the temperature and pressure, respectively	145
4.3.1.9	Comparative vapor thermal conductivity of R1336mzz(E) and R1336mzz(Z) (Alam et al., 2017) concerning the temperature and pressure, respectively	145
4.3.1.10	Comparative study of thermal conductivity data deviations for liquid R1336mzz(E)	146
4.3.1.11	Comparative study of thermal conductivity data deviations for vapor and supercritical R1336mzz(E)	147
4.3.1.12	Extrapolated data of R1336mzz(E) at saturated state in a liquid region	148
4.3.1.13	Saturated thermal conductivity data concerning saturated temperature	149
4.3.2.1	Molecular structure of 3,3,4,4,5,5-HFCPE	151
4.3.2.2	Experimental points for 3,3,4,4,5,5-HFCPE showing temperature and pressure	153
4.3.2.3	Variation of measured liquid thermal conductivities of 3,3,4,4,5,5-HFCPE with temperature	157
4.3.2.4	Variation of measured vapor thermal conductivities of 3,3,4,4,5,5-HFCPE with temperature	157
4.3.2.5	3D Presentation of the thermal conductivities of 3,3,4,4,5,5-HFCPE with temperature and pressure	159
4.3.2.6	Comparison of thermal conductivities of 3,3,4,4,5,5-HFCPE for pressures at 4.0 MPa and 1.0 MPa	159
4.3.2.7	Extrapolated liquid thermal conductivities at saturation conditions	160
4.3.2.8	Variation of saturated thermal conductivities in terms of saturation temperature	161

List of Tables

1.4.1	The key summary of the history of the Montreal Protocol	14
1.4.2	The key summary of the history of the Kyoto Protocol	15
1.6.1	List of test fluids	18
3.1.1	Capillary tubes dimensions	51
3.1.2	Measured viscosities of R134a	57
3.1.3	Summary of uncertainties for viscosity measurements	60
3.2.1	Length of platinum thin wires	63
3.2.2	Thermal conductivity ($\text{mW m}^{-1} \text{K}^{-1}$) of R134a compared to REFPROP and reference data	68
3.2.3	Summary of uncertainties for thermal conductivity measurements	71
4.1.1	Sample information	76
4.2.1.1	Fundamental information of R1336mzz(E)	78
4.2.1.2	Experimental data for the liquid viscosity, η ($\mu\text{Pa s}$) of R1336mzz(E)	80
4.2.1.3	Experimental data for the vapor viscosity, η ($\mu\text{Pa s}$) of R1336mzz(E)	81
4.2.1.4	Experimental data for the supercritical viscosity, η ($\mu\text{Pa s}$) of R1336mzz(E)	81
4.2.1.5	Statistical analyses of the viscosity deviations in terms of AAD, MAD, and Bais	89
4.2.1.6	Saturated viscosity, η_{sat} ($\mu\text{Pa s}$) of R1336mzz(E)	91
4.2.2.1	Fundamental properties of 3,3,4,4,5,5-HFCPE	93
4.2.2.2	Experimental liquid kinematic viscosities, ν_{exp} ($\text{cm}^2 \text{s}^{-1}$) of 3,3,4,4,5,5-HFCPE	95
4.2.2.3	Experimental vapor kinematic viscosities, ν_{exp} ($\text{cm}^2 \text{s}^{-1}$) of 3,3,4,4,5,5-HFCPE	97
4.2.2.4	Saturated kinematic viscosity, ν_{sat} ($\text{cm}^2 \text{s}^{-1}$) of 3,3,4,4,5,5-HFCPE	103
4.2.3.1	Basic information of R1132(E)	105
4.2.3.2	Experimental viscosity, η ($\mu\text{Pa s}$) of R1132(E) at the liquid phase	107
4.2.3.3	Experimental viscosity, η ($\mu\text{Pa s}$) of R1132(E) at vapor phase	107
4.2.3.4	Study comparison of the viscosity deviations in terms of AAD, MAD, and Bais	113
4.2.4.1	Fundamental properties of R1123 and R32	116

4.2.4.2	Experimental viscosity, η_{exp} ($\mu\text{Pa s}$) of R1123+R32 mixture at liquid phase	118
4.2.4.3	Experimental viscosity, η_{exp} ($\mu\text{Pa s}$) of R1123+R32 mixture at vapor phase	122
4.2.4.4	Comparison of the experimental viscosity of R1123+R32 with the calculated data	129
4.2.4.5	Saturated viscosities, η_{sat} ($\mu\text{Pa s}$) of R1123+R32	131
4.3.1.1	Basic properties of HFO refrigerants R1336mzz(E) and R1336mzz(Z)	134
4.3.1.2	Experimental liquid thermal conductivity, λ ($\text{mW m}^{-1} \text{K}^{-1}$) of R1336mzz(E)	137
4.3.1.3	Experimental vapor thermal conductivity, λ ($\text{mW m}^{-1} \text{K}^{-1}$) of R1336mzz(E)	138
4.3.1.4	Experimental supercritical thermal conductivity of HFO refrigerant R1336mzz(E)	140
4.3.1.5	Thermal conductivity data deviations in terms of AAD, MAD, and Bais	147
4.3.1.6	Saturated thermal conductivity, λ_{sat} ($\text{mW m}^{-1} \text{K}^{-1}$) of R1336mzz(E)	149
4.3.2.1	Fundamental properties of 3,3,4,4,5,5-HFCPE	152
4.3.2.2	Experimental thermal conductivities, λ ($\text{mW m}^{-1} \text{K}^{-1}$) of liquid 3,3,4,4,5,5-HFCPE	154
4.3.2.3	Experimental thermal conductivities, λ ($\text{mW m}^{-1} \text{K}^{-1}$) of vapor 3,3,4,4,5,5-HFCPE	156
4.3.2.4	Saturated thermal conductivities, λ_{sat} ($\text{mW m}^{-1} \text{K}^{-1}$) of 3,3,4,4,5,5-HFCPE	161
5.1	Experimental conditions to measure viscosities of test fluids	172
5.2	Experimental conditions to measure thermal conductivities of test fluids	172
5.3	Summary of uncertainties for viscosity measurements	172
5.4	Summary of uncertainties for thermal conductivity measurements	173

Nomenclature

English Symbols

a	correction coefficients of kinetic energy
b	correction coefficients of pipe end
C	constant value
d	diameter of the capillary tube (m)
E	unbalanced voltage (V)
l	length of the wire (m)
L	length of capillary tube (m)
M	molar mass (kg mol^{-1})
m	mass flow rate (kg s^{-1})
m_i	mass fraction of each component ($i=1$ and 2)
P	pressure (MPa)
ΔP	pressure difference (MPa)
Q	heat transfer rate per unit length ($\text{mW m}^{-1} \text{s}^{-1}$)
q	flow rate ($\text{m}^3 \text{s}^{-1}$)
r	radius of capillary tube (m)
r_o	distance from the wire (m)
R	universal gas constant ($\text{J mol}^{-1} \text{K}^{-1}$)
S	slope
T	temperature (K)
ΔT	temperature rise (K)
t	time (s)
u	standard uncertainty
u_c	combined uncertainty
u_e	expanded uncertainty
x, y	quantity used in uncertainty analysis
Z	interaction coefficient used in Eqs. (4.2.4.1) and (4.2.4.2)

Greek Symbols

α'	heat transfer coefficient ($\text{kW m}^{-2} \text{K}^{-1}$)
α	thermal diffusivity ($\text{m}^2 \text{s}^{-1}$)
γ	Euler's constant
η	viscosity ($\mu \text{Pa s}$)
λ	thermal conductivity ($\text{mW m}^{-1} \text{K}^{-1}$)
ν	kinematic viscosity ($\text{cm}^2 \text{s}^{-1}$)
ρ	density of fluid (kg m^{-3})
φ	diameter of platinum wire (μm)

Subscripts

<i>cal</i>	calculated
<i>exp</i>	experimental
<i>i</i>	input
<i>l</i>	long capillary tube
<i>L</i>	long platinum wire
<i>mix</i>	mixture
<i>REFP</i>	REFPROP
<i>ref</i>	reference
<i>S</i>	short platinum wire
<i>s</i>	short capillary tube
<i>sat</i>	saturated
<i>sat, L</i>	saturated at liquid
<i>sat, V</i>	saturated at vapor
1, 2	pure components 1 and 2

Chapter 1

Introduction

1.1 Overview

The ozone layer depletion and global warming are caused by human activities that release pollutants into the atmosphere. Increased amounts of ozone-depleting substances (ODS) such as chlorofluorocarbons (CFCs), hydro-chlorofluorocarbons (HCFCs), hydrofluorocarbons (HFCs), and their mixtures have been discovered to be the source of ozone depletion. When refrigerants with high global warming potential (GWP) are used, however, global warming continues by introducing too many greenhouse gases into the atmosphere. Heat-trapping emissions (carbon dioxide, CFCs, methane, and other greenhouse gases) add to the cooling conditions in the environment that lead to ozone depletion and global warming. Due to several environmental issues such as ozone depletion, global warming, and their relationship to the various refrigerants used, finding a suitable refrigerant has become one of the most pressing issues in recent years. As a result of this problem, we decided to replace traditional working fluids with new, lower-GWP alternatives. In terms of environmental concern, alternative working fluids can have low toxicity, low flammability, and zero or near-zero ozone depletion potential (ODP), as well as a low or ultralow GWP (UNEP, 2018, 2014). Some working fluids from the Hydrochlorofluoroolefins (HCFOs), Hydrofluoroolefins (HFOs), and Hydrofluoroether (HFEs) families have recently been considered as promising candidates for designing high-temperature heat pumps and ORCs due to their favorable properties, especially for low global warming potential. The thermodynamic and transport properties of these potential working fluids are significant tools to design energy systems, equipment, and simulation. Nonetheless, very few experimental data are available in the open literature of these working fluids. The objectives of this study are to measure the transport properties like viscosity and thermal conductivity of low-GWP working fluids R1336mzz(E), 3,3,4,4,5,5-HFCPE, R1132(E), and mixture (R1123+R32) over a wide temperature and pressure range.

1.2 Fundamental concepts of refrigerants used as working fluids

Refrigerants are those working fluids capable of transferring heat between heat sources and heat sinks in the refrigeration cycle, air conditioning, and heat pump systems, transitioning from a liquid to a gas and back again. Owing to their toxicity, flammability, and exposure to ozone depletion and climate change, refrigerants are highly controlled.

1.2.1 Desirable properties of ideal refrigerants

The refrigerants should have promising properties for operating as working fluids in organic Rankine cycles and heat pumps. The following are the basic properties for the probable good refrigerants:

- ❖ The refrigerants should be capable to transfer heat efficiently. To minimize friction loss, the viscosity should be low, and the thermal conductivity should be high to decrease the heat transfer region in the evaporator and condenser.
- ❖ They must have high latent heat and low specific heat.
- ❖ It is needed for refrigerants to have chemical stability.
- ❖ The refrigerants should have a low boiling point and low freezing point.
- ❖ The refrigerants should have no toxicity and fire risk.
- ❖ They should be noncorrosive as well as nonexplosive.
- ❖ They must have high critical temperature and pressure to reduce power consumption.
- ❖ It is essential to have a low specific volume to minimize the size of the compressor.
- ❖ They should have a high coefficient of performance (COP) in the working temperature range to lower the system's operating costs.
- ❖ They should be readily available and cheap.
- ❖ It is important to be environmentally friendly.
- ❖ They should have satisfactory oil solubility and miscibility.
- ❖ They should have easy leak detection ability.

In summary, refrigerant specifications can be split into two categories. In the first category, in the case of leakage, the refrigerants must be risk-free, non-toxic, and non-flammable. In the second category, at a fair cost, the thermodynamic and transport properties of the refrigerants must be ideal for the device and the working conditions as well as operating conditions.

1.2.2 Factors considering the selection of refrigerants as working fluids

Due to the environmental issues, the factors considering the selection of refrigerants as working fluids for organic Rankine cycles and heat pumps are to be summarized as the key outlines as below.

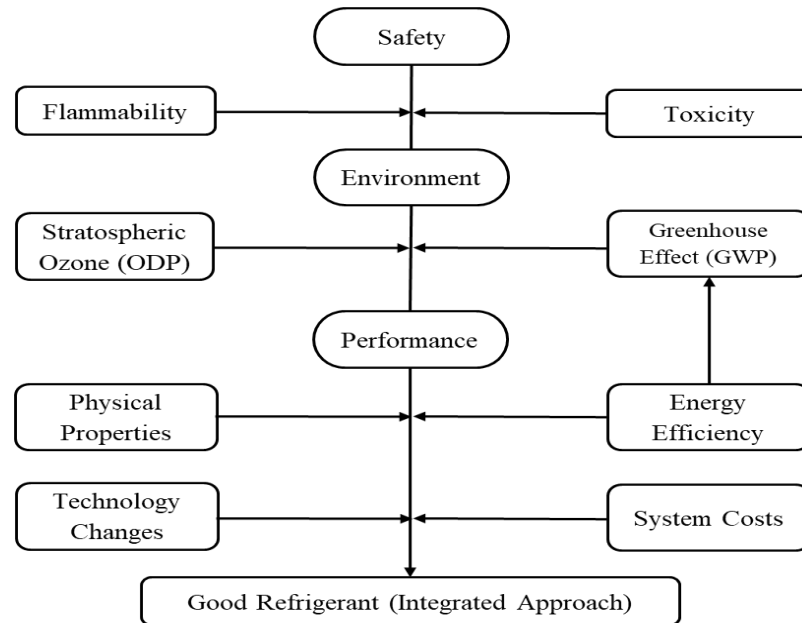


Fig. 1.2.1 Factors considering in an integrated approach to select the refrigerant as working fluids (EDGE, 2017)

Safety: The basic consideration is to identify the safety category that would be evaluated for the selection of refrigerants. The refrigerant safety classification has consisted of two sub-groups as below,

- (i) **Toxicity:** *Class A* refers to refrigerants with no evidence of toxicity at concentrations less than or equivalent to 400 parts per million (ppm), whereas *Class B* refers to refrigerants with evidence of toxicity at concentrations below 400 ppm. In other words, refrigerants classified as *Class A* are less harmful than those classified as *Class B*.
- (ii) **Flammability:** *Class 3* denotes highly flammable refrigerants with a lower flammability limit of less than or equal to 0.10 kg/m^3 at 21°C and 101 kPa , or/and a heat of combustion greater than or equal to 19 kJ/kg . *Class 2* denotes flammable refrigerants with a lower flammability limit of more than 0.10 kg/m^3 at 21°C and 101 kPa or/and a heat of combustion of less than 19 kJ/kg . Again, *Class 2L* denotes lower flammable refrigerants that have lower flammability than *Class 2* refrigerants,

whereas *Class 1* denotes non-flammable refrigerants that do not exhibit flame propagation when tested in air at 21°C and 101 kPa.

Environmental Impact: The environmental effects of refrigerants are largely determined by the ODP and GWP values that will be discussed in section 1.3. The goal will have an ODP value of zero or nearly zero, as well as a lower GWP value.

Performance: Performance indicates the ability to do something for an expected goal.

- (i) **Physical Properties:** Low condensing pressure, high evaporator pressure, and low freezing point are only a few of the desirable physical properties of refrigerants.
- (ii) **Energy Efficiency:** More energy-efficient refrigerants have a higher heat-transfer coefficient, which necessitates a smaller area and lower pressure drop.
- (iii) **Technology Changes:** To further reduce the refrigerant's environmental effects, new blends are being launched to the market. New technology and applications that use new and next-generation refrigerants are now being implemented.
- (iv) **System Costs:** When compared to older technologies, some of the newest types of systems are considerably more expensive.

All of these factors must be taken into account by the construction industry in order to choose a "good" refrigerant in an integrated approach.

1.2.3 Various refrigerants used as working fluids

The working fluids are used as refrigerants in refrigeration, air conditioning, and heat pumping systems. For practical applications, precise experimental and prediction data of the thermo-physical properties of pure and mixture working fluids are needed. The description of various working fluids used as refrigerants is in Fig. 1.2.2.

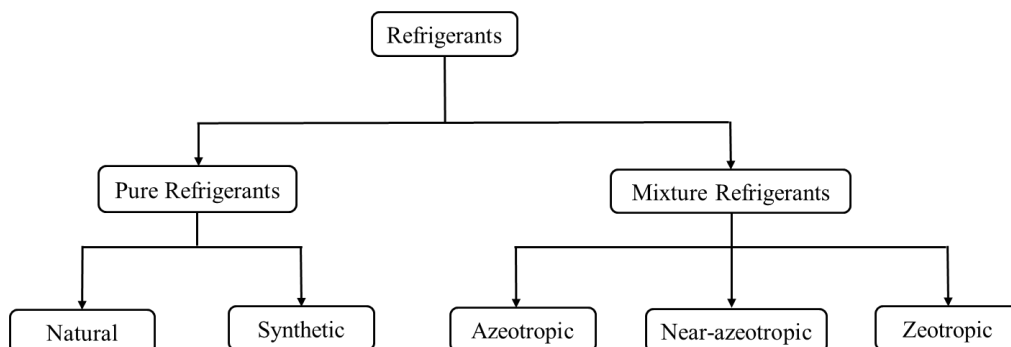


Fig. 1.2.2 Various refrigerants that are used as working fluid

(A) Pure refrigerants: Refrigerants in the organic Rankine cycles and heat pumps are made up of two kinds of pure refrigerants used as working fluids. They are natural and synthetic refrigerants.

(a) Natural refrigerants: As refrigerants, a variety of natural fluids are used. These fluids must possess characteristics that make them suitable for use in the structures. In refrigeration and air-conditioning systems, the working fluids must absorb heat without freezing at low temperatures and reject heat at higher temperatures and pressures (Riffat et al., 1997). Natural refrigerants are often less harmful to the environment than other types of refrigerants. They are treated as suitable substitutions to the CFCs for a long-time horizon. They have very low GWP and zero or near zero ODP. Natural refrigerants, on the other hand, are flammable or poisonous. Consequently, the use of these refrigerants necessitates the installation of special protection devices. As a result, they were gradually phased out in favor of commercial refrigerants. Natural refrigerants include ammonia (NH_3), carbon dioxide (CO_2), hydrocarbons (HCs), water, and air (Abas et al., 2018; Benhadid-Dib and Benzaoui, 2012; Emani and Mandal, 2018; Riffat et al., 1997).

- (i) **Ammonia (R717):** Ammonia (NH_3) is a well-known and widely used refrigerant in refrigeration systems due to its excellent properties, good performance, and low cost. It has an ODP value of 0 and a GWP of 0. The cost of ammonia is much smaller than the cost of other working fluids in many countries. It has a lower density than air and has excellent water mixing properties, making it useful in water purification systems. Nonetheless, ammonia is a poisonous, toxic, flammable, and material-compatible working solvent. It can also be mixed in water, corroding copper, and copper alloys in current facilities. As a result, it necessitates additional safety measures, as well as an indirect system in many implementations.
- (ii) **Carbon Dioxide (R744):** As a natural refrigerant, carbon dioxide (CO_2) is designated as R744. It has numerous properties such as non-toxicity, non-flammability, and odorless. It is treated as a working fluid with zero ODP and the lowest effective GWP. Because of its low liquid density, it takes up less space and the system charge are also lower. However, in comparison to other natural and synthetic refrigerants, it has a low performance and high operating pressure. Because of the high pressure, the system is vulnerable to leakage, and performance will suffer as a result.
- (iii) **Hydrocarbons (HCs):** In both domestic and industrial uses, hydrocarbons have been

used in low-capacity air conditioners and room ventilation, as well as low-charge devices. While hydrocarbons are outstanding working fluids with excellent thermodynamic, thermophysical, and material stability properties, they are extremely flammable as compared to other fluids. They are mostly used in applications with low working fluid charges because of their flammability. The research projects are being conducted to examine the behavior and components of low-charge vapor compression systems with reasonably large capacities. The most widely used hydrocarbons are propane (R290), propylene (R1270), and propane-butane blends (R600), and isobutane (R600a).

- (iv) **Water (R718):** Water is an environmentally safe refrigerant that is widely used. It's a non-toxic, low-cost operating fluid that's readily available. As water can be used only for high-temperature applications, the refrigeration capacity drops dramatically for low-density water vapor.
- (v) **Air (R729):** In comparison to other working fluids, the air is the cheapest and safest refrigerant. It is safe for the climate, humans, and food, and it is completely healthy, non-toxic as well as harmless. However, It is seldom used as a refrigerant due to its low boiling point and heat capacity. It's also widely used in aircraft air conditioning nowadays.

(b) Synthetic refrigerants: Synthetic fluids are used as refrigerants in commercial refrigeration, cold storage, and air conditioning systems. The widely used synthetic refrigerants are chlorofluorocarbons (CFCs), hydrochlorofluorocarbons (HCFCs), hydrofluorocarbons (HFCs), hydrofluoroolefins (HFOs), and hydrofluoroethers (HFEs). These refrigerants are man-made and are not found in nature. CFCs and HCFCs stimulated economic development and human comforts at the risk of ozone depletion and climate change since their discovery. HFCs are exposed to UV in the troposphere as well as decomposed into acid and radioactive compounds, which eventually rain down (Abas et al., 2018; Benhadid-Dib and Benzaoui, 2012; Tsai, 2005).

- (i) **Chlorofluorocarbons (CFCs):** Chlorofluorocarbons are those synthetic refrigerants that are composed of chlorine, fluorine, and carbon. CFCs are volatile methane and ethane compounds. The Montreal Protocol on Substances was approved to protect the ozone layer by banning the substances occurring in ozone depletion. As a result of their major exposure to ozone layer degradation, CFC refrigerants have been prohibited. R11, R12, R13, R112, R112a, R113, R113a, R114, R114a, R115, and so

on are examples of CFCs refrigerant.

- (ii) **Hydrochlorofluorocarbons (HCFCs):** The elements hydrogen, chloride, fluorine, and carbon make up hydrochlorofluorocarbon refrigerants. As a result, HCFCs contribute to the depletion of the earth's ozone layer in the same way that CFCs do. Furthermore, since they contain less chlorine than CFCs, they have a lower ozone depletion potential than CFCs. The Montreal Protocol imposed a ban due to their susceptibility to ozone depletion. R21, R22, R31, R121, R121a, R122, R122a, R123, R123a, R124, R124a, R141, and so on are examples of HCFCs refrigerant.
- (iii) **Hydrofluorocarbons (HFCs):** Hydrofluorocarbons are a type of synthetic refrigerant that are saturated compounds composed of hydrogen, fluorine, and carbon. They don't contain chlorine and don't harm the ozone layer. They have a zero ODP. As a consequence, CFCs and HCFCs may be replaced by HFCs. On the other hand, HFC refrigerants contribute to the greenhouse effect due to their high GWP value. HFCs refrigerants include R32, R23, R41, R125, R134, R134a, R143, R143a, R152, R152a.
- (iv) **Hydrofluoroolefins (HFOs):** Hydrofluoroolefins are members of the HFC family, but they are made from unsaturated hydrocarbons like propylene. They have zero ODP value and a much lower GWP value than their HFCs equivalents. The maximum refrigerating capacity of HFOs is equivalent to that of R134a, while the maximum refrigerating capacity of HCs is lower than R134a. HFOs have excellent thermal stability and compatibility with a wide range of materials. HFOs' unsaturated carbon bonds warped readily in the atmosphere, but they remained relatively stable in refrigeration systems. As a result, they will provide us with systems that are stable, long-lasting, and cost-effective. R1234yf, R1233zd(E), R1336mzz(Z), R1336mzz(E), R1132(E), R1234ze(Z), R1224yd(Z), and so on are examples of HFOs refrigerants.
- (v) **Hydrofluoroethers (HFEs):** Hydrofluoroethers are a kind of organic solvents. They are typically colorless, odorless, tasteless, low toxicity, low viscosity, and liquid at room temperature. Owing to zero ODP and a reasonably low GWP, they are treated as alternatives to the CFCs, HFCs, HCFCs, and PFCs (perfluorocarbons) (Tsai, 2005). HFE refrigerants have certain physical and thermochemical properties in common with other refrigerants, such as high volatility, low or non-flammability, low surface tension. R7500, R7200, R7100, R7000, R356mmz, and so on are common possible HFE refrigerants.

(B) Mixture Refrigerants: Mixture refrigerants are made up of blending two or more pure working fluids. If pure working fluids are not suitable as well as fail to behave satisfactorily in a domestic refrigeration system, a mixture of pure fluids may be used to achieve the desired properties. Azeotropic mixtures, near azeotropic mixtures, and zeotropic mixtures are examples of refrigerant mixtures (Didion and Bivens, 1990).

(a) Azeotropic mixture: An azeotropic mixture consisting of two or more pure liquids is a constant boiling point mixture that has the same composition in liquid and vapor conditions. Owing to its constant boiling point and no changes in the composition of this mixture on boiling, the mixture component can not be altered by the simple fractional distillation process. This mixture is formed by a non-ideal solution. Azeotrope mixture refrigerants include R502, R500, R503, and R410A (Azeotrope; Didion and Bivens, 1990). Azeotrope mixtures can be divided into two types: minimum-boiling or positive azeotrope and maximum-boiling or negative azeotrope.

- (i) **Minimum-boiling or positive azeotrope:** In a minimum-boiling or positive azeotrope, the mixture boils at the lowest temperature of any other percentage of its components, resulting in the highest vapor pressure. The mixture distills at this stage at a fixed temperature with no difference in composition. Fig. 1.2.3 shows the behavior of a typical minimum-boiling or positive azeotrope mixture of chloroform and methanol.

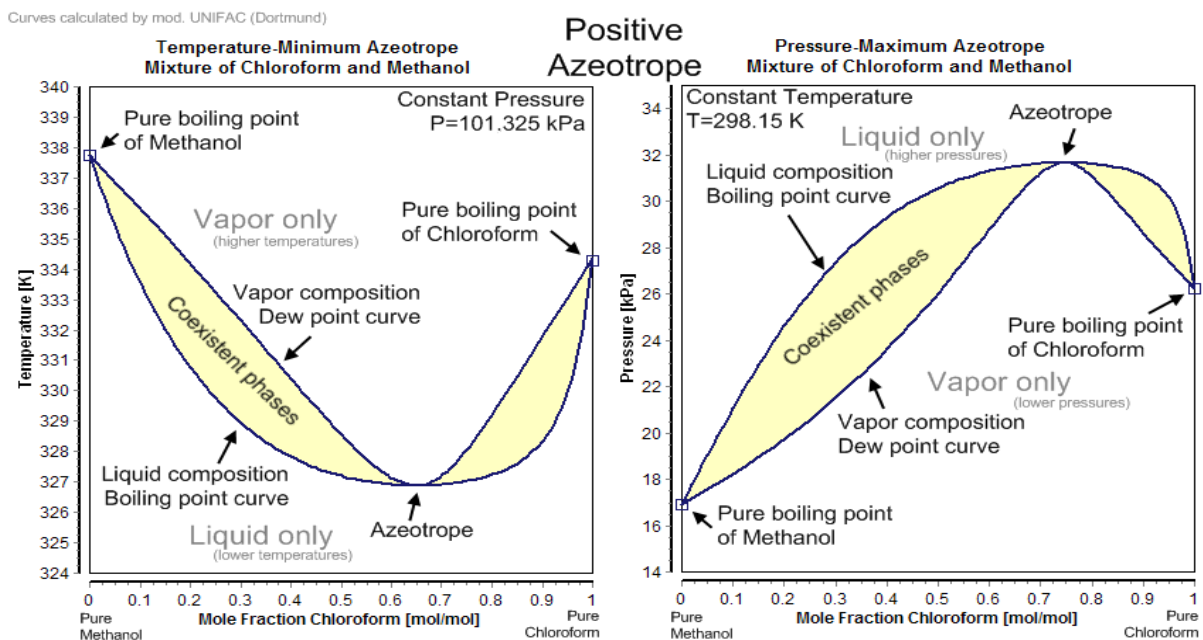


Fig. 1.2.3 A typical example showing the behavior of minimum-boiling or positive azeotrope mixture of chloroform and methanol (<https://en.wikipedia.org/wiki/Azeotrope>)

- (ii) **Maximum-boiling or negative azeotrope:** While in the maximum-boiling or negative azeotrope, the mixture boils at the highest temperature of any other percentage of its components, resulting in the lowest vapor pressure of the mixture. Fig. 1.2.4 shows the behavior of a typical maximum-boiling or negative azeotrope mixture of water and formic acid.

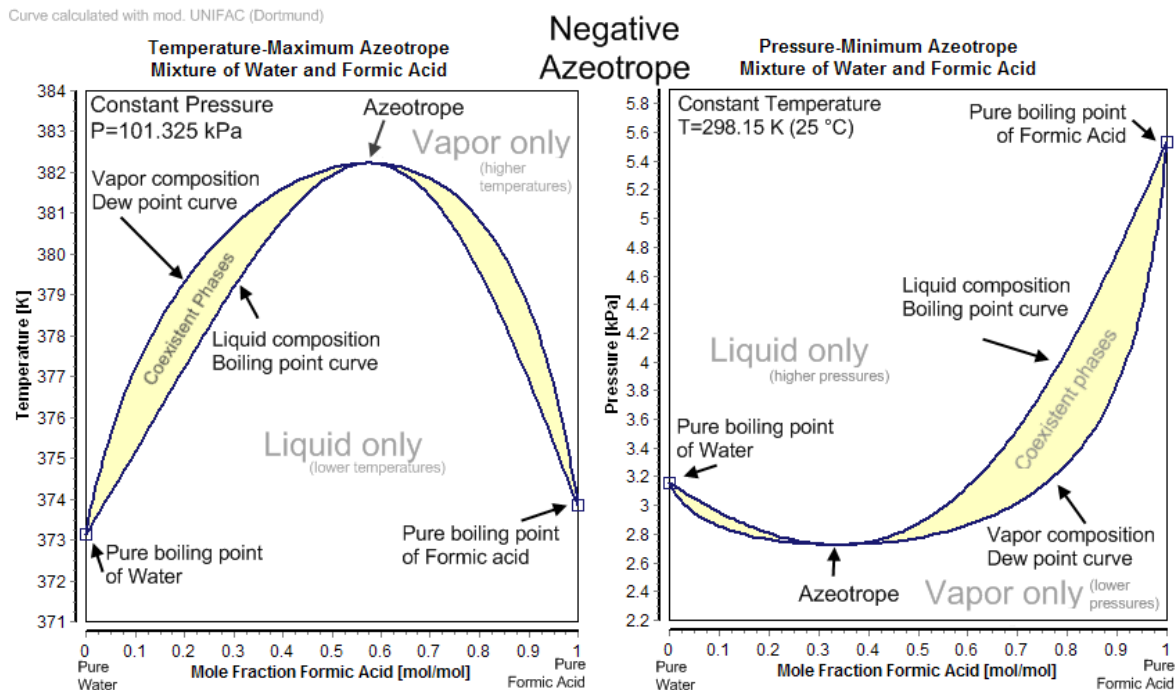


Fig. 1.2.4 A typical example showing the behavior of maximum-boiling or negative azeotrope mixture of water and formic acid (<https://en.wikipedia.org/wiki/Azeotrope>)

(b) Near-azeotropic mixture: A near azeotropic is the mixture with a small temperature difference during phase change and a small variation of the composition in liquid and vapor phases at equilibrium. The azeotropic refrigerant mixtures exhibit near-azeotropic behavior when the temperature or pressure is changed from the azeotrope stage. Examples of the near-azeotropic mixture are the addition of a small amount of propane to R502, R410A. R401 is a mixture of R32 and R125 and it is also known as AZ20. For standard condenser pressures and temperatures, the bubble and dew points for this concentration vary by less than 0.1°C (Sweeney and Chato, 1996). Although it appears that this variation could be reduced even further by increasing the concentration of R125. R410A was developed as an alternative to R22, and changing its composition reduces its suitability for that role while also increasing its flammability and toxicity. Near-azeotropic mixtures usually work well with existing equipment (Sundaresan, 1992; Sweeney and Chato, 1996).

(c) **Zeotropic mixture:** Zeotropic or non-azeotropic mixtures are made up of two or more pure liquids that do not boil at the constant temperature as a pure liquid and have different compositions of liquid and vapor phases. This behavior creates a temperature glide during phase change at that point the concentrations of the vapor and the liquid are changing frequently. The most popular kind of refrigerant blend is a zeotropic mixture. Fig. 1.2.5 shows the behavior of a zeotropic mixture where no meeting point of bubble and dew point lines. When the mixture is being cooled, the liquid starts to form the dew point temperature and progresses until it reaches the bubble point temperature. The temperature glide is defined as the difference between the dew and bubble point at constant pressure. The large temperature glides have a more significant effect compared to small ones. The refrigerant temperature reduces gradually due to temperature glides in the evaporator. On the other hand, the temperature rises steadily in the evaporator. Zeotropic mixtures include R401A, R406A, R407A, R408A, R409A, and the mixture of R1123 with R32, etc (Rajapaksha, 2007, 2005; Zeotrope).

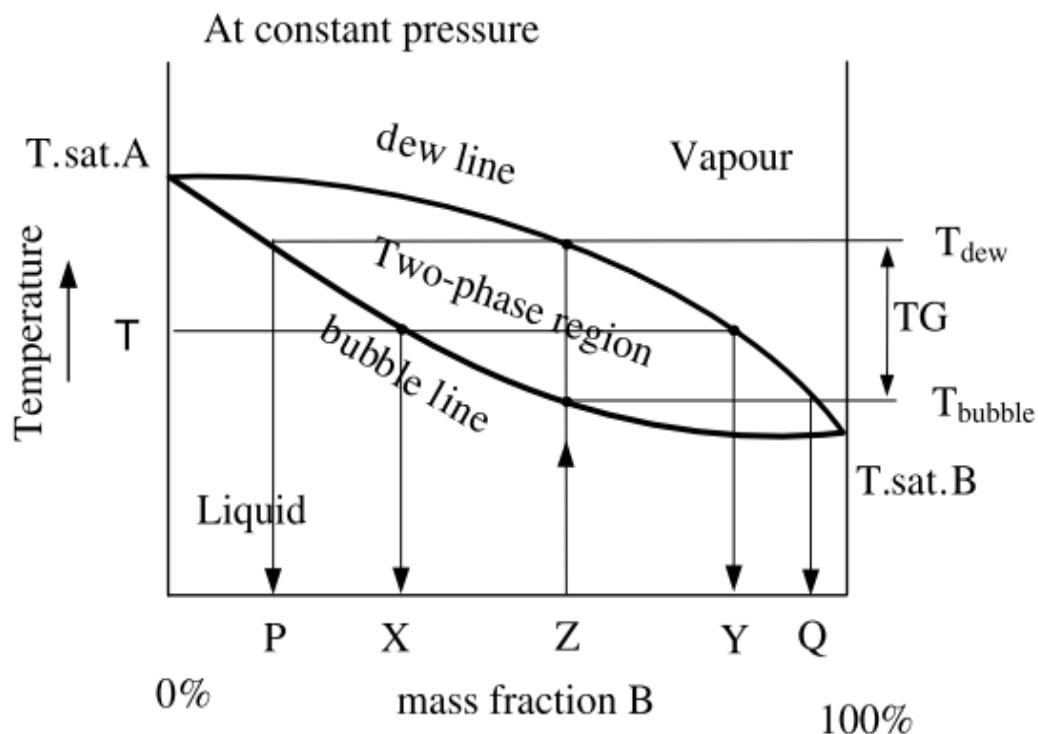
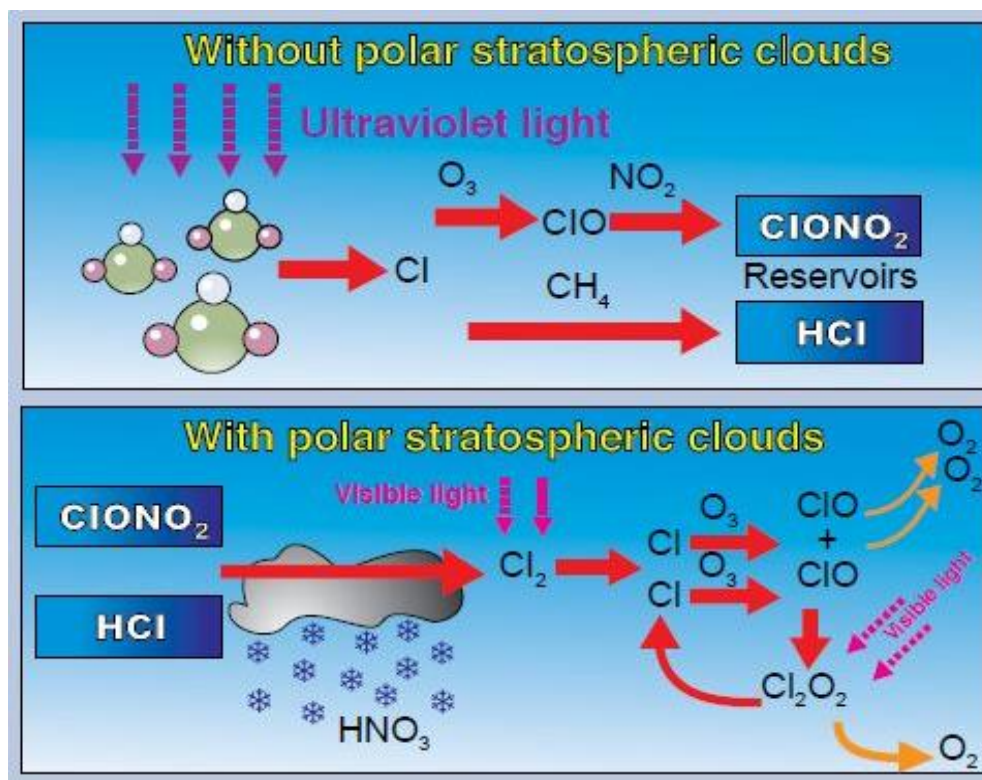
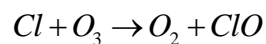


Fig. 1.2.5 A typical example showing the behavior of the zeotropic mixture (Rajapaksha, 2007, 2005)

1.3 Environmental impact of refrigerants

The working fluids being toxic or explosive are dangerous to people's health as well as a threat to the environment because of their ozone depletion potential (ODP) and global warming potential (GWP). Working fluids can be ranked according to their impact on the stratospheric ozone layer (ODP) or as greenhouse gases (GWP) (UNEP, 2018, 2014). The impact of working fluids on the ozone layer and the greenhouse effect is based on three main indications. They are as follows (a) Ozone Depletion Potential (ODP) (b) Global Warming Potential (GWP) (c) Total Equivalent Warming Impact.

(a) *Impact of Ozone Depletion Potential (ODP)*: The ODP is an index to characterize the working fluids to the depletion of the ozone layer. The working fluids containing chlorine or bromine attaining ODP and contribute to breaking down the ozone layer (Solomon et al., 1994). The value of this index is compared to a reference fluid either R11 or R12 that has ODP one. The reaction of chlorine with the ozone layer is as follows and Fig 1.3.1:



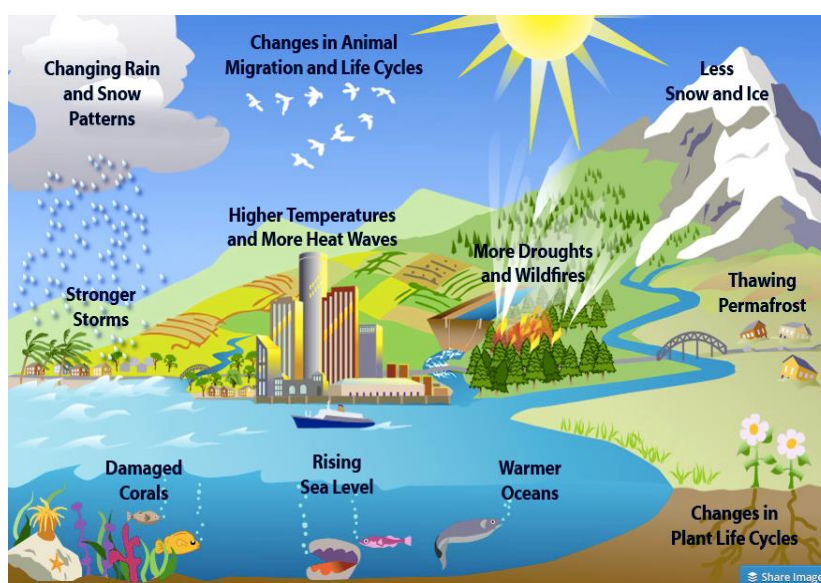
Source: <http://www.theozonehole.com/ozonedestruction.htm>

Fig.1.3.1 Diagram showing chlorine effect on the ozone layer

The chlorine atom reacts with ozone to form chlorine monoxide (ClO) and O_2 . The molecule ClO is unstable. It breaks down and forms Cl_2O_2 , which is easily photolyzed and liberating atomic chlorine again. Therefore, it reacts with the ozone particles repeatedly until a more stable compound is formed. Due to the catalytical cycle, one atom of Cl can destroy thousands of ozone molecules before it is passivated through reaction with N_2O , methane or other substances. In Fig 1.3.1, the upper panel shows no polar stratospheric clouds, and the lower panel shows polar stratospheric clouds. Since ozone depletion has become the dominant environmental issue. Chlorofluorocarbons (CFCs), Hydrochlorofluorocarbons (HCFCs), and other ozone-depleting substances that are used for refrigeration and air-conditioning system deplete the ozone layer. Nowadays, all over the world try to find alternative ones after the phaseout of CFCs and HCFCs.

(b) Impact of Global Warming Potential (GWP):

Some of the working fluids have a significant contribution to warm the Earth by absorbing energy and slowing the rate of energy escapes to space. They act as greenhouse gases behave like a blanket insulating the Earth. The global warming potential (GWP) is used to compare the global warming impacts of different fluids on Earth. The value of this index is compared to a reference fluid CO_2 that has GWP one. The time usually used for calculating GWPs is 100 years.



https://medium.com/@swami_rara/essay-on-global-warming-c7d7771db248

Fig. 1.3.2 Sketch for impact for global warming potential

Nowadays global warming potential is one of the most challenging issues in society and becomes a universal concern. Two types of global warming contributions are considered for refrigeration and air conditioning systems. They are the direct global warming potential due to the refrigerants emission and the indirect global warming potential due to the emission of CO₂ consuming energy required to operate the systems. The equivalent effect of these two contributions is called the total equivalent warming impact. The impact of GWP was presented in the following Fig. 1.3.2. The impact of global warming is being concerned across the world. Each year Antarctica has loosed around 134 billion tons of ice since 2002. In addition, rising sea level, the heat content of the oceans has increased, increased humidity, changing rain and snow patterns, changing animal migration and life cycles, changing plant cycles, intense storms and thawing permafrost, etc. are contributions to global warming (Benhadid-Dib and Benzaoui, 2012; NRDC).

1.4 International agreement on environmental issues

The Montreal Protocol, signed in 1987, is an international agreement to limit the emission of ozone-depleting substances like chlorofluorocarbons (CFCs) and hydro-chlorofluorocarbons (HCFCs), which are widely used in refrigeration. A considerable amount of ozone-depleting material pollution has reduced as a result of national legislation and individual scientific actions. They addressed new controls to phase out CFCs by the end of 1995 and HCFCs by 2030 at the fourth Montreal Protocol meeting in 1992. The Kyoto Protocol, which extends the 1992 United Nations Framework Convention on Climate Change, was approved in Kyoto, Japan in 1997. They decided to take scientific steps to minimize greenhouse gas emissions. The European Union, the United States, and Japan have set carbon reduction goals of less than 8%, 7%, and 6%, respectively. However, the Montreal and Kyoto Protocols mandated that former refrigerants that deplete the ozone layer be replaced in the manufacturing and commercial sectors in order to regulate the environment. As a result, finding possible replacement refrigerants with zero ODP and ultra-low GWP is a difficult task. This is a serious concern for the whole world and mankind. In Tables 1.4.1 and 1.4.2, the successive phases of the Montreal and Kyoto Protocols (EDGE, 2017; EESI) are mentioned.

Table 1.4.1 The key summary for the history of the Montreal Protocol (EDGE, 2017)

Year	Information
1974	➤ Scientists discovered a connection between ozone layer depletion and CFC emissions in the atmosphere.
1977	➤ The United Nations Environment Programme launched the world plan of action on ozone depletion.
1985	➤ The Vienna Convention for ozone layer protection was approved.
1985	➤ The first ozone hole was discovered over the Antarctic.
1987	➤ Representatives from 46 countries signed the Montreal Protocol in Montreal, Canada.
1989	➤ The Protocol of Montreal came into effect. If their intake of Ozone Depleting Substances (ODS) is poor, developing countries are granted a grace period to comply.
1992	➤ The Copenhagen Amendment officially established the Multilateral Fund and introduced hydrochlorofluorocarbons (HCFCs), hydrobromofluorocarbons (HBFCs), and hydrobromocarbons (methyl bromide) to the phase-out schedules.
1994-96	➤ CFCs and halons were banned in developing countries, with exceptions for essential applications, after a phase-out over the previous years.
1999	➤ For Article 5 parties (developing countries), the implementation cycle started on July 1, 1999, when the first monitoring measure of CFC output and use, based on the average of 1995–97 levels, was implemented.
1999	➤ The Beijing Amendment applied bromochloromethane to the list of substances to phase out.
2002	➤ Bromochloromethane was being phased out completely in both developed and developing countries.
2005	➤ CFCs and halons intake and usage were reduced by 50%, carbon tetrachloride (CTC) was reduced by 85%, trichloroethane (TCA) was reduced by 30%, and methyl bromide was reduced by 20% in developing countries.
2007	➤ CFCs demand and production in developed countries were to be reduced by 85%.
2009	➤ The Vienna Convention and the Montreal Protocol must be ratified universally.
2010	➤ For developing nations, CFCs, halons, and CTC were being phased out completely.
2013	➤ Consumption and processing of HCFCs in developing countries should be frozen at their current levels.
2016	➤ The Kigali Agreement to Update the Montreal Protocol was signed in Kigali, Rwanda.
2024	➤ Freeze of HFC in developing countries to be 20% of 2021 levels by 2045.
2030	➤ HCFCs will be phased out completely in both developed and developing countries.

Table 1.4.2 The key summary for the history of the Kyoto Protocol (EESI)

Year	Information
1750	➤ The atmosphere contained 280 parts per million (ppm) of heat-trapping CO ₂ until the industrial revolution.
1989	➤ According to a Swedish scientist, CO ₂ generated by the burning of coal and oil could warm the planet.
1955	➤ CO ₂ levels in the atmosphere had risen to 315 ppm, according to a US scientist.
1988	➤ Global warming "is really occurring today," a Nasa scientist told the US Congress.
1992	➤ A global climate agreement established voluntary targets for reducing CO ₂ and other greenhouse gas emissions.
1992	➤ In Rio de Janeiro, Brazil, at the UN Conference on Environment and Development, also known as the Earth Summit, the UN Framework Convention on Climate Change (UNFCCC) was adopted and opened for signatures. The UNFCCC's 154 signatories promised to keep "greenhouse gas emissions in the environment at a level that avoids harmful interaction with the climate system."
1994	➤ After 50 ratifications, the UNFCCC Treaty became effective.
1995	➤ At the first Conference of the Parties (COP 1) in Berlin, Germany, an UN-organized research panel stated about signs of man-made pollution that are impacting the environment.
1996	➤ Geneva, Switzerland hosted the 2 nd Conference of the Parties (COP 2). Parties were urged to speed up talks on a legally binding protocol during the Geneva Ministerial.
1997	➤ Kyoto, Japan hosted the COP 3, and the Kyoto Protocol was accepted and approved by more than 150 signatory's climate treaty members.
1998	➤ Buenos Aires, Argentina hosted the COP 4, and the Buenos Aires Plan of Action was approved by the parties to establish processes for implementing the Kyoto Protocol and also agreed to review the convention's financial mechanism.
1999	➤ Bonn, Germany hosted the COP 5, and the parties kept negotiating in order to insist on the implementation of guidance.
2000	➤ Part I of COP 6 took place in the Hague, Netherlands. After a stumbling block, the parties decided to meet again. Part II of COP 6 was held in Bonn, Germany. On the so-called Bonn Agreements, a consensus was reached.
2001	➤ Marrakesh, Morocco hosted COP 7, and the Kyoto Protocol's comprehensive rules for implementation were approved.
2002	➤ COP 8 took place in Delhi, India. The Delhi Ministerial Declaration, which included a call for developed countries to move technologies to developing countries, was ratified by the parties.
2003	➤ COP 9 took place in Milan, Italy. New pollution monitoring standards based on IPCC guidance were introduced and adopted.

2004	➤	Buenos Aires, Argentina hosted the COP 10. The adaptation solutions were first discussed by the parties, and then “numerous decisions and conclusions” were debated and ratified by the parties.
2005	➤	Montreal, Canada hosted COP 11 and the first conference meeting of the parties on the environment to the Kyoto Protocol (CMP 1). CMP1 was added to the annual meeting of the COP.
2006	➤	Nairobi, Kenya hosted COP 12/CMP 2. The Special Climate Change Fund's financial processes were reviewed, and further decisions were taken regarding it.
2007	➤	Bali hosted COP 13/CMP 3. After the Kyoto Protocol expired in 2012, the parties settled on a Bali Action Plan to discuss GHG reduction measures. Developing countries were not required to meet binding GHG goals under the Bali Action Plan.
2008	➤	Poznan, Poland hosted the COP 14 and the CMP 4. Negotiations on a financial scheme to assist developing nations in dealing with climate change have started.
2009	➤	The UN Framework Convention on Climate Change (UNFCCC) held COP 15 and CMP 5 in Bonn, Germany, to launch discussions on draft talks that will serve as the foundation for a Copenhagen deal.
2010	➤	The Copenhagen Accord, declared in December 2009, was signed by the US and more than 130 other countries.
2011	➤	In Durban, South Africa, COP 17 was held. The Durban Platform for Enhanced Action, which is a forum for developing a new international carbon reduction protocol, was agreed upon by the parties.
2012	➤	In Doha, Qatar, the COP 18 was held. Parties decided to expand the Kyoto Protocol beyond its current expiration date, establishing a new commitment process.
2013	➤	Warsaw, Poland hosted COP 19 and CMP 9. Parties were scheduled to build a greenhouse gas reduction roadmap in Paris for 2015.
2014	➤	Peru hosted the COP 20 and the CMP 10. Delegates to the conference met to discuss and hope of reaching a global warming deal.
2016	➤	COP 22, CMP 12 and the first session of the Conference of the parties serving as the Meeting of the Parties to the Paris Agreement (CMA 1) were held in Morocco.
2017	➤	In Germany, COP 23, CMP 13, and CMA 1-2 were carried. Japan presented the technical proposals for implementing the Paris Agreement's guidance.

1.5 Refrigerant reclamation and disposal

Refrigerants are found throughout the industrialized world, in homes, offices, and factories, in devices such as refrigerators, air conditioners, central air conditioning systems (HVAC), freezers, and dehumidifiers. When these units are serviced, there is a risk that refrigerant gas will be vented into the atmosphere either accidentally or intentionally, hence the creation of technician training and certification programs in order to ensure that the material is conserved and managed safely. Mistreatment of these gases has been shown to deplete the ozone layer and is suspected to contribute to global warming (Report, 1999).

Refrigerant reclamation is the act of processing used refrigerant gas which has previously been used in some type of refrigeration loop such that it meets specifications for new refrigerant gas. In the United States, the Clean Air Act of 1990 requires that used refrigerant be processed by a certified reclaimer, which must be licensed by the United States Environmental Protection Agency (EPA), and the material must be recovered and delivered to the reclaimer by EPA-certified technicians (Code, 1995).

1.6 Measures to mitigate the effects of ODP and GWP

It is important to figure out how to reduce the environmental effects of refrigerants' ODP and GWP. There are having some essential steps to minimize the environmental impact of refrigeration, heat pump and air conditioning systems. A few of the steps are listed as:

- ❖ To minimize the direct emissions of refrigerant into the atmosphere.
- ❖ To limit the indirect emissions of refrigerant generated by the use of electricity to power the devices.
- ❖ To mitigate ozone loss and global warming by reducing leakages in structures.
- ❖ To reduce in system charge can lead to further emission reductions.
- ❖ It is needed to use the refrigerants having zero ODP and ultra-low GWP.
- ❖ To advance the system maintenance and testing procedures so that further emissions can be reduced.
- ❖ To minimize the impurities from refrigerants and improve the operating efficiency. Furthermore, wherever possible, it should be attempted to improve refrigerant recycling and reuse.

1.7 Research potentiality

Due to the high ozone depletion (ODP) and global warming potential (GWP), the Montreal and Kyoto Protocols prohibit the use of conventional chlorofluorocarbons (CFCs) and hydrochlorofluorocarbons (HCFCs) as working fluids. The new refrigerants with low GWP are the primary focus throughout the world to overcome the destructive impact of global warming. Therefore, it is very important to find new alternatives with low GWP and zero or nearly zero ODP instead of conventional working fluids. Recently, hydrofluoroolefins (HFOs), hydrochlorofluoroolefins (HCFOs), and Hydrofluoroether (HFEs) are the most promising alternatives to low-GWP fluids. Nevertheless, the measured values of transport properties especially viscosity and thermal conductivity are essential for the design of efficient chemicals, equipment, and simulation for ORCs and heat pumps as well as the HVAC&R system. The accurate experimental data of these properties are required to measure for the selection of potential working fluid. Therefore, in this present study, the viscosity measurements are performed using the method tandem capillary tubes and thermal conductivity by transient hot-wires method of a few next-generation working fluids that are listed below in Table 1.6.1.

Table 1.6.1 List of test fluids

No	Name	Type of working fluid
1	R1336mzz(E)	HFO pure
2	3,3,4,4,5,5-HFCPE	Pure
3	R1132(E)	HFO pure
4	R1123 + R32	Zeotropic mixture

1.8 Research objectives

This research aims to increase the knowledge about the transport properties of next-generation refrigerants, and the environmental impacts of refrigerants used as working fluids. Transport properties are important particularly for refrigerants in modern technology of refrigeration, air conditioning, and heat pumps systems. The experimental viscosity and thermal conductivity of new potential refrigerants will be measured for a wide temperature and pressure range.

The objectives of this work are summarized as below:

1. To ensure the validity as well as reliability of the experimental apparatus used to measure the viscosities and thermal conductivities of refrigerants.
2. To perform the viscosity measurement of next-generation refrigerants and refrigerant mixture (e.g., R1336mzz(E), 3,3,4,4,5,5-HFCPE, R1132(E), and R123+R32) by the method tandem capillary tubes.
3. To perform the thermal conductivity measurement of these refrigerants and mixture by the transient hot-wires technique.
4. To develop the simplified correlations for estimating the saturated liquid and vapor viscosities and thermal conductivities by the extrapolating approach from the experimental data to vapor-liquid saturation conditions.
5. To estimate the uncertainties for the viscosity and thermal conductivity measurements using the law of propagation by the GUM method.

1.9 Dissertation outline

This dissertation is written as well as organized in several sections, each of which is referred to as a chapter as follows:

The current chapter, Chapter 1, provides an introduction highlighting the overview of this research, as well as the fundamental concepts of working fluids used as refrigerants, environmental impacts of working fluids, international measures on environmental issues, measures to mitigate the effects of ODP, and GWP, the potentiality and purposes of this work.

Chapter 2 describes the literature review of the present study. In the literature review, the history of refrigerants propagation, history of conventional research related to this research, various techniques to measure transport properties of refrigerants, and finally, the progression of capillary viscometer and transient hot wires technique were presented.

Chapter 3 shows the experimental apparatus and theory for the capillary viscometer and transient hot wires technique to measure the viscosities and thermal conductivities of next-generation refrigerants and refrigerants mixture. In this chapter, the apparatus is validated first and then the apparatus would be capable of measuring. Also, the uncertainties of the viscosities and thermal conductivities measurements are estimated in this chapter.

Chapter 4 demonstrates the experimental measurement and results of this study. In this chapter, the viscosity and thermal conductivity data of next-generation refrigerants and refrigerants mixture are plotted and correlated with the other researcher and developed the simplified correlations to predict the viscosities and thermal conductivities at saturation conditions.

Chapter 5 summarizes the findings as conclusions of this analysis and makes proposals for future studies in this field.

References

- Abas, N., Kalair, A.R., Khan, N., Haider, A., Saleem, Z., Saleem, M.S., 2018. Natural and synthetic refrigerants, global warming: A review. *Renew. Sustain. Energy Rev.* 90, 557–569. <https://doi.org/10.1016/j.rser.2018.03.099>
- Azeotrope. <https://en.wikipedia.org/wiki/Azeotrope>.
- Benhadid-Dib, S., Benzaoui, A., 2012. Refrigerants and their environmental impact substitution of hydro chlorofluorocarbon HCFC and HFC hydro fluorocarbon. Search for an adequate refrigerant. *Energy Procedia* 18, 807–816. <https://doi.org/10.1016/j.egypro.2012.05.096>
- Code, U.S., 1995. Section 608 of the Clean Air Act of 1990, <https://www.law.cornell.edu/uscode/text/42/7671g>.
- Didion, D.A., Bivens, D.B., 1990. Role of refrigerant mixtures as alternatives to CFCs. *Int. J. Refrig.* 13, 163–175. [https://doi.org/10.1016/0140-7007\(90\)90071-4](https://doi.org/10.1016/0140-7007(90)90071-4)
- EDGE, 2017. Refrigerants and Materials Selection to Reduce Climate Impact: EDGE Guidance Document for the Building Sector based on the Montreal Protocol. Version 1, Publ. April 3, 2017. https://www.edgebuildings.com/wp-content/uploads/2017/04/170403-RefrigerantSelection_EDGE_MontrealProtocol.pdf.
- EESI. Timeline of Major UN Climate Negotiations, A Brief Overview of COP Decisions, Environment and Energy Study Institute (EESI), <http://www.eesi.org/policy/international>.
- Emani, M.S., Mandal, B.K., 2018. The Use of Natural Refrigerants in Refrigeration and Air

- Conditioning Systems: A Review. IOP Conf. Ser. Mater. Sci. Eng. 377. <https://doi.org/10.1088/1757-899X/377/1/012064>
- NRDC. Global Warming. https://www.nrdc.org/stories/global-warming-101?gclid=EAIaIQobChMIzY-Dkee22AIVB7jACh09xQlZEAAAYASAAEgI27PD_BwE#causes.
- Rajapaksha, L., 2007. Influence of special attributes of zeotropic refrigerant mixtures on design and operation of vapour compression refrigeration and heat pump systems. Energy Convers. Manag. 48, 539–545. <https://doi.org/10.1016/j.enconman.2006.06.001>
- Rajapaksha, L., 2005. Zeotropic Refrigerant Mixtures in Vapour Compression Refrigeration Systems - Issues and Implications. Eng. J. Inst. Eng. Sri Lanka 38, 52–59. <https://doi.org/10.4038/engineer.v38i4.7228>
- Report, 1999. Emissions of Greenhouse Gases Report by the US Department of Energy, Report#:EIA/DOE-0573(98), <https://web.archive.org/web/20000818233746/http://www.eia.doe.gov:80/oiaf/1605/ggript/>.
- Riffat, S.B., Afonso, C.F., Oliveira, A.C., Reay, D.A., 1997. Natural refrigerants for refrigeration and air-conditioning systems. Appl. Therm. Eng. 17, 33–42. [https://doi.org/10.1016/1359-4311\(96\)00030-0](https://doi.org/10.1016/1359-4311(96)00030-0)
- Solomon, S., Wuebbles, D., Isaksen, I., Kiehl, J., Lal, M., Simon, P., Sze, N.D., 1994. Ozone depletion potentials, global warming potentials, and future chlorine/bromine loading 13.1-13.36, <https://csl.noaa.gov/assessments/ozone>.
- Sundaresan, S.G., 1992. Near Azeotrope Refrigerants to Replace R502 in Commercial Refrigeration NEAR AZEOTROPE REFRIGERANTS TO REPLACE R502 IN COMMERCIAL REFRIGERATION, in: International Refrigeration and Air Conditioning Conference. Paper 136. <http://docs.lib.purdue.edu/iracc/136>.
- Sweeney, K.A., Chato, J.C., 1996. The Behavior of a Near-Azeotropic Refrigerant Mixture of R-321R-125 in an Enhanced Tube. ACRCTR-94 ,Prepared as part of ACRC Project 37 Effect of Geometric Variables and R-22 Alternatives on Refrigerant-Side Evaporation and Condensation.

<https://www.ideals.illinois.edu/bitstream/handle/2142/11157/tr094.pdf?sequence=2>.

Tsai, W.T., 2005. Environmental risk assessment of hydrofluoroethers (HFEs). *J. Hazard. Mater.* 119, 69–78. <https://doi.org/10.1016/j.jhazmat.2004.12.018>

UNEP, 2018. Montreal Protocol on Substances that Deplete the Ozone Layer, 2018 Assessment Report of the Refrigeration, Air Conditioning and Heat Pumps Technical Options Committee, Assessment.

UNEP, 2014. Montreal Protocol on Substances that Deplete the Ozone Layer, 2014 Report of the Refrigeration, Air Conditioning and Heat Pumps Technical Options Committee.

Zeotrope. https://en.wikipedia.org/wiki/Zeotropic_mixture.

Chapter 2

Literature Review

A literature review is a comprehensive survey and/or study of scientific sources on a particular subject. It provides an overview of current knowledge, allowing one to understand the relevant theories, ideas and methods, and gaps in the existing research. In this chapter, the history of refrigerants propagation, the history of conventional research related to this research, various techniques to measure transport properties of refrigerants, and the progression of capillary viscometer and transient hot wires technique are presented. This review will be discussed below in several sections.

2.1 Progression of refrigerants

The knowledge of the refrigerants progression is necessary to identify new potential refrigerants in near future. Calm (2012, 2008, 2006) and collaborators (Calm and Hourahan, 2011) have reported the historical development as well as introduced the successive generations of refrigerants, as shown in Fig. 2.1.1. There are four generations of refrigerants progression discussed here. In 1830-1930s, the most commonly used refrigerants for 100 years stage were solvents and other volatile fluids, and they are treated as first-generation refrigerants. However, the motto of the first-generation refrigerant was “whatever worked”. The physical characteristics of first-generation refrigerants were only worked capability as refrigerant and availability. They were mostly flammable, poisonous, and extremely reactive. The earliest refrigerants of this category were ammonia and carbon dioxide that were widely used. Hydrocarbons were launched later in small systems but achieved less acceptance despite their safer properties than the other more toxic and caustic choices. Propane combined with ammonia, carbon dioxide, and water was used as an odorless refrigerant for a long time. In 1931-1990s, the second generation was recognized by a move to fluorochemicals for safety and durability. The second-generation refrigerants’ aimed to improve “safety and durability”. The second-generation refrigerants were stable, non-flammable, and non-toxic.

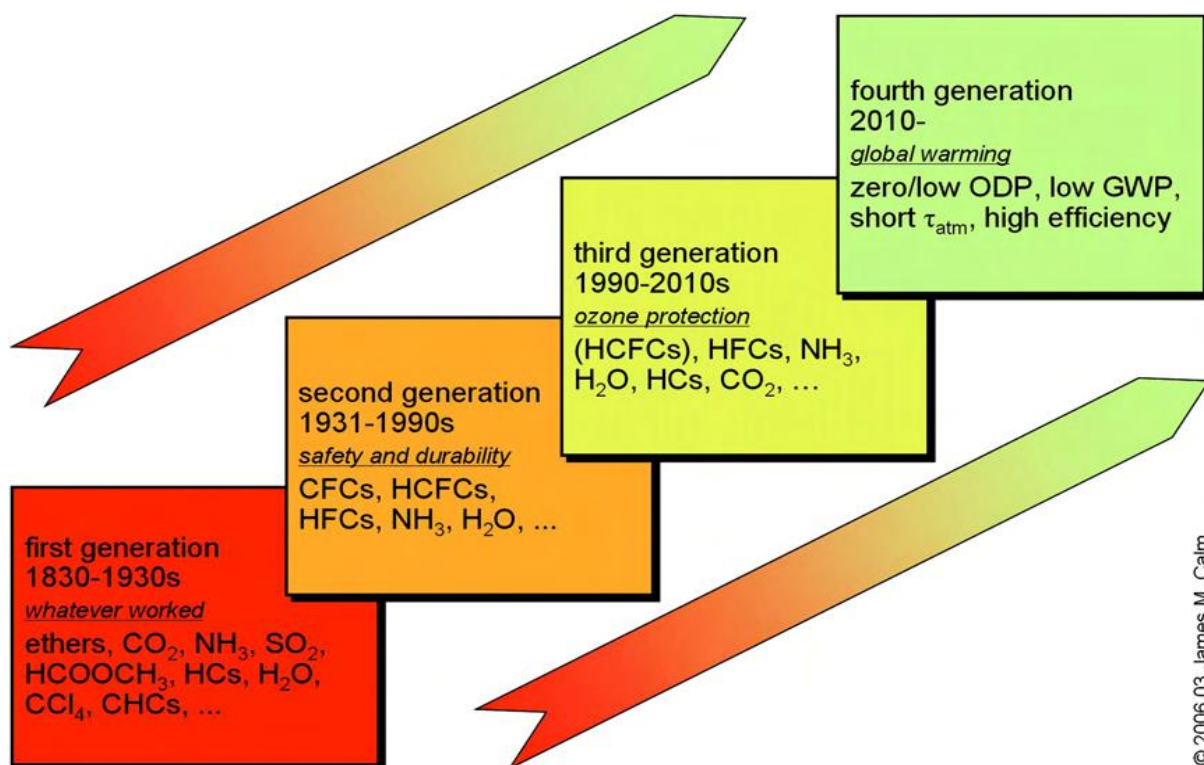


Fig. 2.1.1 The progression of refrigerants (Calm, 2008, 2006)

The property table was stated by Midgley (1937) to find the desired ideal boiling point of chemicals. He eliminated the inadequate volatile, toxic, unstable compounds first and then the inert gases because of boiling points. Finally, only eight compounds were left to satisfy the desired properties. They are carbon, nitrogen, oxygen, sulfur, hydrogen, fluorine, chlorine, and bromine. The commercial production of R12 started in 1931 followed by R11 in 1932. Firstly, Chlorofluorocarbons (CFCs) and then hydrochlorofluorocarbons (HCFCs) dominated the second generation of refrigerants. In 1990-2010s, linkage of released CFCs including CFC refrigerants to depletion of protective ozone catalyzed the third generation with a focus on stratospheric ozone protection. The aim of the 3rd generation refrigerants was “ozone protection”. According to the Montreal Protocol (1987), the use of ozone-depleting substances (ODSs) was being controlled in the practical area. The Vienna Convention and Montreal Protocol implied forces on the industries to the uncontrolled use of ozone-depleting substances and made a replacement with low ODP, but then still unregulated issue regarding global climate changes. Hydrofluorocarbons were considered as the long-term refrigerants in this generation. At that time the interest was also in “natural refrigerants”, especially carbon dioxide, ammonia, hydrocarbons, and water. In late 1989, the first alternative refrigerant was

introduced to the market by manufacturers. Then the manufacturers launched the replacements for the majority of the ozone-depleting working fluids. After the Kyoto Protocol (1997), most of the researchers as well as others focused on the 4th generation refrigerant. In 2010-after, the fourth-generation refrigerants aim to mitigate “global warming”. The fourth generation is still in determination but is likely to include refrigerants with zero or very low ODP, low GWP, short atmospheric lifetime, and high efficiency. The fourth-generation refrigerants include candidates with the least initially, low-GWP HFCs, unsaturated hydrofluorochemicals (e.g., HFOs, HCFOs), ammonia, carbon dioxide, hydrocarbons, water, and so on (Calm and Hourahan, 2011). The fourth assessment report of IPCC imitates that the warming of the earth by greenhouse gases is abandoned. Increases in the world average air and water levels, rapid melting of snow and ice, and increasing global average sea level are all indicators of climate change (IPCC, 2007). The Kyoto Protocol is a climate-change agreement focused on CO₂ equivalents derived from greenhouse gas emissions. The European Parliament banned the use of fluorochemical refrigerants with GWPs of more than 150 in air conditioners. Similar guidelines are also announced in other developed countries like United States, Canada, Australia, and Japan.

Next-generation Refrigerants: The next step is to conduct a global scientific and policy hunt for low-GWP next-generation refrigerants. The potential next-generation refrigerants (Calm, 2008; Pham and Sachs, 2010) include the HFOs and HFO/HFC blends as well as “natural refrigerants” such as ammonia, carbon dioxide, hydrocarbons, air, and water. All involve significant trade-offs among GWP, energy efficiency, safety, and cost. Environmental policies must take into account the indirect impact of increased CO₂ pollution from less effective refrigerants, as well as the refrigerant's actual global warming potential (GWP).

2.2 History of conventional research related to this research

The thermodynamic properties and transport properties are the key tools to design and implement the energy systems, efficient processes and to select the refrigerants used as working fluid in ORCs and heat pumps. The measurement of thermodynamic properties requires few steps to calculate the value, and the measurement uncertainty is very small, so there are many reports with high accuracy. On the other hand, the measurements of transport properties like viscosity and thermal conductivity, which are the main focus of this research, have a higher measurement uncertainty than the former and are more difficult to achieve.

There are several methods for measuring viscosities that have been proposed so far, such as the capillary tube method, rotational method, vibrational method, and rolling ball or sphere method. However, Diller et al. (1993) measured the viscosities of R123, R134a, and R141b from a temperature range of 120 K to 320 K and pressure at 30 MPa with a torsional crystal viscometer to obtain an estimated value of 2% uncertainty. Oliveira and Wakeham (1993) also measured the viscosities of R32 and R125 using the vibrating wire method and set the measurement uncertainty to 0.5 to 1%. Assael et al. (1994) measured the viscosities of R32 and R134a in the temperature 270 to 340 K over the pressure up to 20 MPa with a vibrating fine wire viscometer and obtained a measured value with an uncertainty of 0.5%. Gulik et al. (1995) measured the viscosity of R152a by the vibrating wire method, and the measurement uncertainty was 2 %. Geller et al. (1996) measured the viscosity of R32 and R32+lubricant mixtures using a capillary tube viscometer, and the measurement uncertainty was 1.2% and 1.8%, respectively. Laesecke et al. (1999) use a gravity tube viscometer with a straight vertical capillary to determine the viscosity with estimating the uncertainty of 3.3% for ammonia and 2% for R32 and R134a. Zhelezny et al. (2009) reported an experimental investigation and modeling to measure the dynamic viscosity for refrigerant + oil solutions using the rolling ball method. Cousins and Laesecke (2012) used the capillary method to measure the viscosities of R1234yf and R1234ze(E) under liquid phase conditions. Meng et al. (2013) measured the viscosities of R1234yf and R1234ze(E) by the vibration thin wire method and set the expanded uncertainty of the experimental device to 2.0%. Dang et al. (2015a) measured the liquid viscosity of the mixed refrigerant of R32 and R1234yf and the mixed refrigerant of R125 and R1234yf with a piston viscometer and set the expanded uncertainty for all measurements less than 2.0%. Furthermore, the author Dang et al. (2015b) also measured the vapor viscosity of the mixed refrigerant of R32 and R1234yf and the mixed refrigerant of R125 and R1234yf using the rolling ball method, and the expanded

uncertainty of the experimental device was 1.5%. Alam et al. (2018b) measured the viscosity of R1336mzz(Z) both for the liquid and vapor phase using a tandem capillary tube method and estimated the measurement uncertainty less than 3.04 and 3.21%, respectively. Miyara et al. (2018) measured the viscosity of R1233zd(E) both for the liquid and vapor phase using the tandem capillary tube method and set the measurement uncertainty less than 3.0 and 3.1%, respectively. Alam et al. (2019a, 2019b) reported the kinematic viscosity of HFE-356 and viscosity of R1224yd(Z), respectively, both for liquid and vapor phases using the same technique. Mondal et al. (2020) measured the viscosity of the binary mixture of R1123+R32 by the method of tandem capillary tubes with the uncertainty of the measurement of less than 2.9 and 3.0% both for liquid and vapor phases, respectively.

On the other hand, regarding thermal conductivity measurement, there are various measurement methods such as the transient hot-wire method, the laser flash method, and the steady-state method of coaxial cylinders, but most of the data are reported by the transient-hot wire method. Makita et al. (1981) measured the thermal conductivity for four gaseous fluorocarbon refrigerants such as R12, R13, R22, and R23 by a vertical coaxial cylinder apparatus, and obtained a measured value with an uncertainty of 2%. Assael et al. (1992) measured the thermal conductivity of the liquids of R11 and R12 using the transient hot-wire method at temperatures up to 250 to 340 K and pressures up to 30 MPa and obtained measurements with 0.5% uncertainty. There are also reported some measured values for refrigerants that are candidates for next-generation refrigerants. Assael and Karagiannidis (1993) measured the thermal conductivity of the liquids of R22, R123, and R134a in temperatures up to 250-340 K and pressures up to 30 MPa and obtained measurements with 0.5% uncertainty. Assael et al. (1994) reported the liquid viscosity measurements of R134a and R32 using a vibrating wire method over the temperature from 270 to 340 K at pressures up to 20 MPa, where the uncertainty estimation was 0.5%. Yata et al. (1996) measured the thermal conductivity of some Freon-based refrigerants, including R32, R125, R143a, and so on, in liquids from a temperature of 254 K to 345 K and a pressure of 30 MPa by the transient hot-wire method, with an uncertainty of 1%. Gross and Song (1996) measured the thermal conductivity of R32 and R125 by the transient hot-wire method in liquids and gases and obtained measurements with an uncertainty of 2% or less. Besides, Neindre et al. (2001) measured the thermal conductivity of R32 in gases and liquids over a wide temperature and pressure range by the transient hot-wire method, where the measurement uncertainty was 1.5%. Also, many researchers have reported the results of refrigerant thermal conductivity measurement using the transient hot-wire method. Baginsky and Shipitsyna (2009) reported

the liquid state thermal conductivity and thermal diffusivity for R134a in their research work. Verba et al. (2017) measured the vapor of R410A using the coaxial tube steady-state method and obtained measurements with an uncertainty of 1.5% to 2.5%. Perkins and Huber (2011) measured the thermal conductivity of R1234ze(E) and R1234yf by the transient hot-wire method, with expanded uncertainty of 1 % or less for liquids and 3% for gases both for the 95 % confidence level. Again, Perkins et al. (2017) also obtained thermal conductivity data for liquid, vapor, and supercritical R1233zd(E) with a relative expanded uncertainty ranging at a 95% confidence level from 1% to 4% depending on the temperature and pressure with larger uncertainties in the critical region. Alam et al. (2017) measured the thermal conductivity of R1336mzz(Z) saturated liquid and vapor (temperature range 314 to 496K) and obtained measured values of uncertainty 2.07% and 2.26% or less, respectively. Furthermore, the author Alam et al. (2019b, 2019a, 2018a) measured the liquid and vapor thermal conductivities of R1224yd(Z), HFE-356mmz, and R1233zd(E) using the transient hot-wire technique in a wide temperature and pressure. Hapenciuc et al. (2019) reported a steady-state hot wire technique for thermal conductivities measurements for several fluids. Mylona et al. (2019) measured the thermal conductivity for refrigerant mixtures containing R1234yf and R1234ze(E) by the transient hot-wire technique in a wide range of temperature and pressure. Perkins and Huber (2020) measured the thermal conductivity of R1336mzz(Z) by the transient hot-wire technique and correlated it with the extended corresponding state model. Mondal et al. (2021) measured the thermal conductivity of R1336mzz(E) by the transient hot-wire method and developed the saturation correlation for the measurement.

2.3 Various methods to measure transport properties of fluids

2.3.1 Methods for viscosity measurements of fluids

Viscometers measure the viscosity as well as the flow properties of fluids. Viscosity occurs from the internal friction of a fluid and is known as a liquid's resistance to flow or shear stress. There are several methods for measuring the viscosity of fluid samples. A few of them are discussed briefly below (Mckenna and Lyng, 2013; Shire, 2015; Viscometer; T. Viscometer; Viswanath et al., 2007; Webster, 2005):

- (i) **Capillary viscometers:** Capillary viscometers (Kestin et al., 1973; Mckenna and Lyng, 2013; T. Viscometer), based on the Hagen-Poiseuille theorem, are the widely used method for measuring the viscosity of the fluids by forcing a liquid through the capillary tube. One of the simplest but popular techniques for measuring the viscosity

of fluids, which requires advanced knowledge of the sample's density and volume. The fluid is transferred into a capillary tube of well-defined dimensions and a narrow diameter. The time taken for the sample to travel through the capillary correlates to its viscosity.

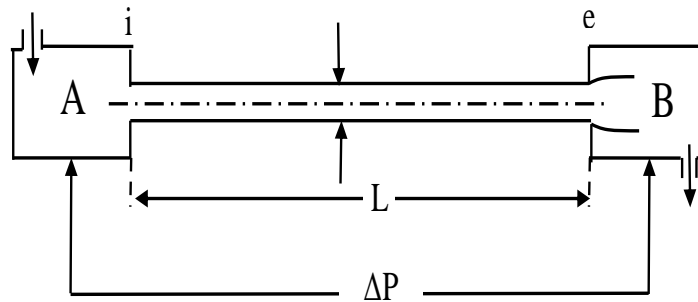


Fig. 2.3.1 Schematic view of the main test section of a typical capillary viscometer

- (ii) **Rotational viscometers:** Rotational viscometers (Mckenna and Lyng, 2013; T. Viscometer) apply comparatively low amounts of torque to a sample of the liquid to promote mechanical deformation. The torque used to rotate the sample fluid in a horizontal plane is determined and is proportional to the sample's viscosity. Analysts would be able to make a map for a complete flow curve of the material's flow dynamics in response to differing degrees of shear force and calculate more advanced material parameters using a rotational rheometer.

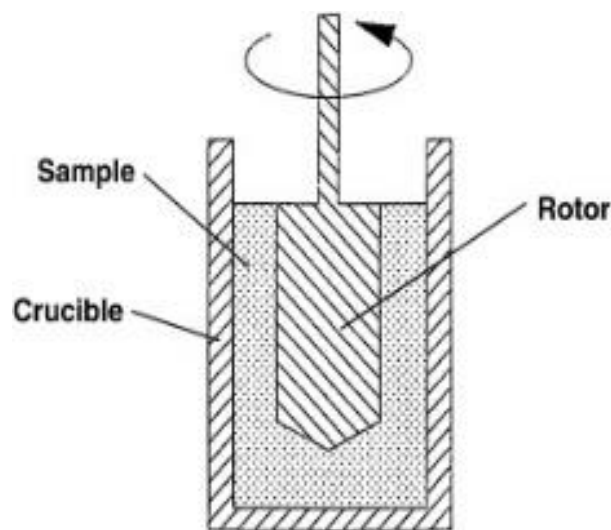


Fig. 2.3.2 Schematic view of the main test section of a typical rotational viscometer

- (iii) **Vibrational viscometers:** The viscosity of the sample fluid can also be determined in vibrational viscometers (Akpek et al., 2014; T. Viscometer) by adding oscillating vibrations to the sample and measuring the fluid's damping impact. Power input, oscillation decay time, and variations in the resonated frequency can all be used to determine the sample's viscosity.

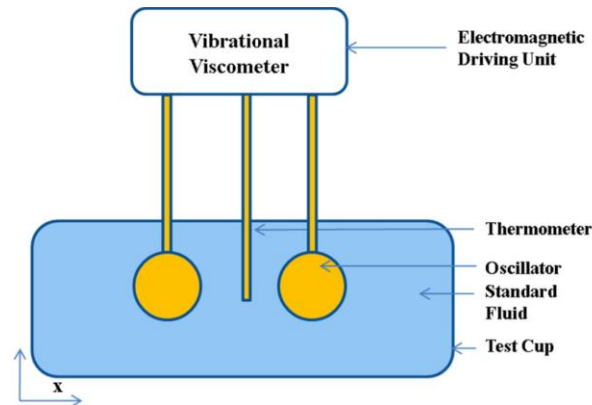


Fig. 2.3.3 Schematic view of the main test section of a typical vibrational viscometer

- (iv) **Moving or oscillating piston viscometers:** The measurements are taken in moving or oscillating piston viscometers (Viscometer; T. Viscometer) by first introducing a sample into the thermally operated measuring chamber where the piston moves. With a regulated magnetic field, electronics force the piston into oscillatory motion inside the measuring chamber. Shear stress is applied on the liquid sample owing to the piston movement, and finally, the viscosity is measured by calculating the piston movement time according to Newton's law of viscosity.

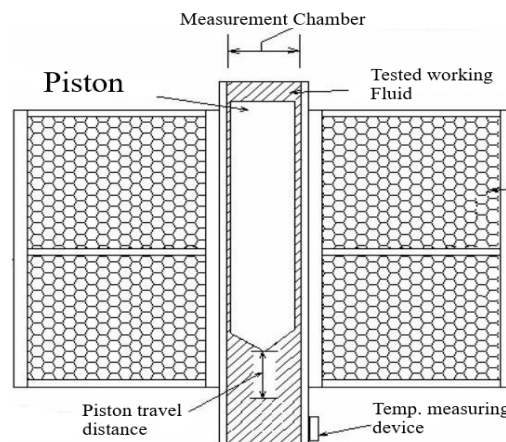


Fig. 2.3.4 Schematic view of the main test section of a typical moving piston or oscillating viscometer

- (v) **Falling sphere or ball viscometers:** The falling-sphere or ball viscometers (Dang et al., 2015b; Viscometer), which uses a vertical glass tube to keep the fluid stationary, is based on Stokes' theorem. A known size and density sphere or ball is permitted to move down into the working fluid through the vertical glass tube. The viscosity is equivalent to the time it takes for an internal falling sphere or ball to fall over a given distance.

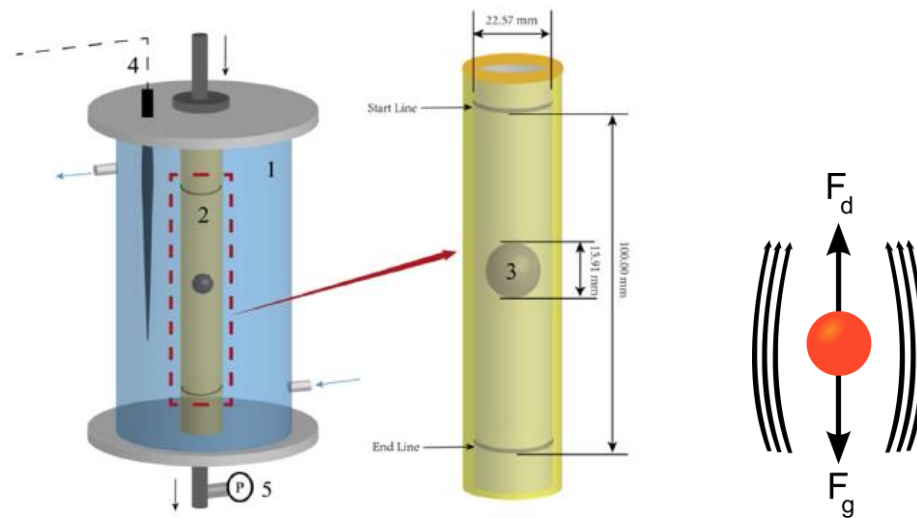


Fig. 2.3.5 Schematic view of the main test section of a falling ball or sphere viscometer (Dang et al., 2015b)

- (vi) **Microfluidic Rheometers:** Microfluidic rheometers (Shire, 2015; T. Viscometer) are novel tools for measuring fluid dynamic viscosity by pushing a liquid sample into a microfluidic channel in a laminar flow. Pressure drops are used to assess viscosity in microfluidic rheometers. Dynamic viscosities are calculated by assessing the differential flow rates, the viscosity of the reference substance as well as the location of the interface between the two fluids inside the microfluidic channel.
- (vii) **Non-Contact Rheology:** It tests the same properties as a rotational rheometer, but it's designed for more complex and delicate systems like gels, weak pastes, and viscoelastic materials that can crack under very low shear. Non-contact rheology, unlike conventional rotational rheometers, allows for a detailed measurement of a sample's rheological properties at rest without applying mechanical stress.

2.3.2 Methods for thermal conductivity measurements of fluids

Thermal conductivity measurements of sample fluids are a complicated task due to eliminating the effects of convection caused by the temperature gradient of the fluid during measurement. However, it is essential to finish the measurement before convection occurs for eliminating the influence of convection. There are several methods for measuring the thermal conductivity of samples. A few of them are discussed below (Jaeger and Sass, 1964; Jagueneau et al., 2019; Mathis, 2000; Measurement; Webster, 2005; Zhao et al., 2016):

- (i) **Steady-state methods:** The steady-state techniques utilized for the measurement of the thermal conductivity both of fluids and solids. In general, steady-state methods are used where the temperature of the sample being analyzed does not change with time. A sample of unknown conductivity, which would be tested, is placed between two reference samples of known conductivity. The setup for this method is usually made vertically and the sample fluids lie always in between the two reference samples. To prevent any convection inside the sample, heat is applied from the top and directed downward. Once the sample has reached steady-state (zero heat gradient or constant heat over the entire sample), measurements are taken.
- (ii) **Transient methods:** In the transient techniques, the measurements have been performed during the process of heating up. The measurements are handled easily and faster, and to overcome the drawbacks associated with the steady-state methods. Needle probes are commonly used for transient processes. This section converges the four widely used transient techniques, such as transient hot-wires (THW) method, transient plane source (TPS) method, transient line source (TLS) method, and laser flash method.
 - (a) ***Transient hot-wires (THW) method:*** The transient hot-wires (THW) method is a widely used and accurate procedure for determining the thermal conductivity of liquids and gases over a broad temperature and pressure range. This method is based on the transient temperature rise of a thin vertical metal wire with infinite length when a step voltage is applied to it. As the wire is submerged in the liquid, it can be used as an electrical heating element as well as a resistance thermometer. Owing to have very short time intervals of measuring, there is no effect of convection during the thermal conductivity measurement with high accuracy. In this method, two identical thin hot wires

varied only by lengths are used in the measurement cell to eliminate effects due to axial heat conduction.

- (b) ***Transient plane source (TPS) method:*** Transient plane source method is another transient heat reflectance technique that enables to measure the thermal transport properties by utilizing a plane sensor and a special mathematical model representing heat conductivity. This method usually uses two sample halves, with the sensor sandwiched between them. The samples should normally be homogeneous, but the heterogeneous sample is to be tested possibly by the proper selection of the sensor size to optimize sample penetration.
- (c) ***Transient line source (TLS) method:*** The infinite line source with constant power per unit length is the physical model behind this approach. When doing an experiment, the temperature of a point at a fixed distance is measured and the temperature is tracked over time. A transient line source approach is widely used to measure the thermal conductivity of samples for designing the geothermal heat pump (GHP) system on a mass scale.
- (d) ***Laser flash method:*** The laser flash method is used to measure the thermal conductivity of solids applied to liquids of low thermal conductivity (Tada et al., 1978) as well as the thermal diffusivity of a thin disc in the thickness direction. This method is based upon the measurement of the temperature rise at the rear face of the thin-disc specimen produced by a short energy pulse on the front face. The sample liquid was inserted in between a small thin metal disk and a sample holder. The temperature of the metal disk immediately increases as the laser beam is absorbed in the front side, and heat then flows downwards into the sample liquid as a one-dimensional heat transfer. Without using some reference materials or calculating the thickness of the sample liquid layer, the thermal conductivity of a liquid can be determined from the temperature drop of the disk.

2.4 Progression of capillary viscometer and transient hot-wires method

2.4.1 Progression history of capillary viscometer

Capillary viscometers are the most popular types of viscometers that are used to measure the viscosity of working fluids. They are simple to use, feasible in terms of sample amount, simple to control the temperature, and reasonably cost-effective. A viscometer is used to determine the volumetric flow rate of liquid passing through a capillary, which is normally done by noting the time it takes for a known amount of liquid to travel through two graduation marks. The liquid will flow through the capillary tube either by the presence of gravity (Gravity Type Viscometer) or the force induced by exterior sources. The liquid is pushed into the capillary at a fixed rate in the instruments that use an external force, and the pressure drop through the capillary is calculated. Capillary viscometers can calculate viscosity directly from the flow rate, pressure, and the instruments' different dimensions. Firstly, to achieve “constants” for the viscometer, most capillary viscometers should be calibrated with one or more liquids of known viscosity. A capillary viscometer must have a liquid reservoir, a capillary tube with known dimensions, a way to measure and monitor the applied pressure, a way to measure the flow rate, and a thermostat to keep the temperature constant. There are a variety of capillary viscometers using a combination of the above components (Mckenna and Lyng, 2013; Viswanath et al., 2007).

For over a century, the transpiration viscometer has been used as a primary or secondary device, in which a gas or liquid is required to pass through a thin capillary. It is important to use a working equation that is based on an adequate flow model of the process to ensure accuracy that is commensurate with the attention lavished on the instrument's construction.

If an insufficient hypothesis is used as a foundation, the former may be falsified almost as well as the latter. A review of the literature on the topic shows that many researchers used deficient algorithms to minimize their data and thereby used approximations, which also introduced systemic uncertainties that surpassed the measurement's margin of error. As a result, it seems that a hypothesis that integrates recent developments in our interpretation of the Navier-Stokes equations' suitable solutions is already superior. To test the viscosity of fluids, start with a steady-state viscometer, which can be used with a single capillary or two capillaries in tandem. The results are then extended to include the Rankine viscometer under the basis that its function can be considered quasi-steady. The numerical solution of the Navier-Stokes equations with a suitably chosen flow model is the foundation of the change of

the various working equations. The simplest approach of transpiration viscometer is to use the fully developed laminar flow from a computational standpoint (Kestin et al., 1973).

In most capillary viscometers (Kestin et al., 1973; Viswanath et al., 2007), the pressure difference, ΔP is calculated between two reservoirs. The capillary is chosen to be long enough to allow the flow to develop a parabolic velocity profile at the exit. The fluid at the exit, e, enters into tank B in the terms of a jet, as shown schematically in the sketch. Due to the low Mach number of the flow, the pressure at exit e must be equal to that in reservoir B, with the jet energy dissipated practically at constant pressure as seen in Fig. 2.4.1.

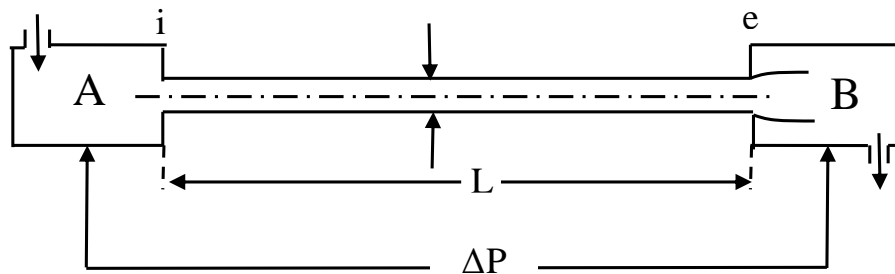


Fig. 2.4.1 A conventional capillary viscometer

In the Ostwald viscometer (Mckenna and Lyng, 2013; Viswanath et al., 2007), the widely used gravity type viscometer of the U-tube type arrangement is designed and implemented. It consists of two reservoirs and a capillary tube as shown in Fig. 2.4.2 (a). It is also known as the Ostwald viscometer. Several modifications were made to the original design of the Ostwald viscometer that is known as the modified Ostwald viscometer. In the meanwhile, the pressure from either compressed gas or a piston induced a constant flow through the tube in the high-pressure capillary viscometer, as shown in Fig. 2.4.2 (b). For the basic measurement, the time t required for a given volume V of the sample fluid to flow through a length L of capillary tubing. There are taken place relative motion to each other between the axial portion of the sample and the portion in contact with the tube walls. The driving force for the fluid flow is to be found from the gravity (as measured from the hydrostatic head difference between two liquid reservoirs) for the U-tube glass type viscometers but pressurized by gas or a piston for the high-pressure capillary viscometers.

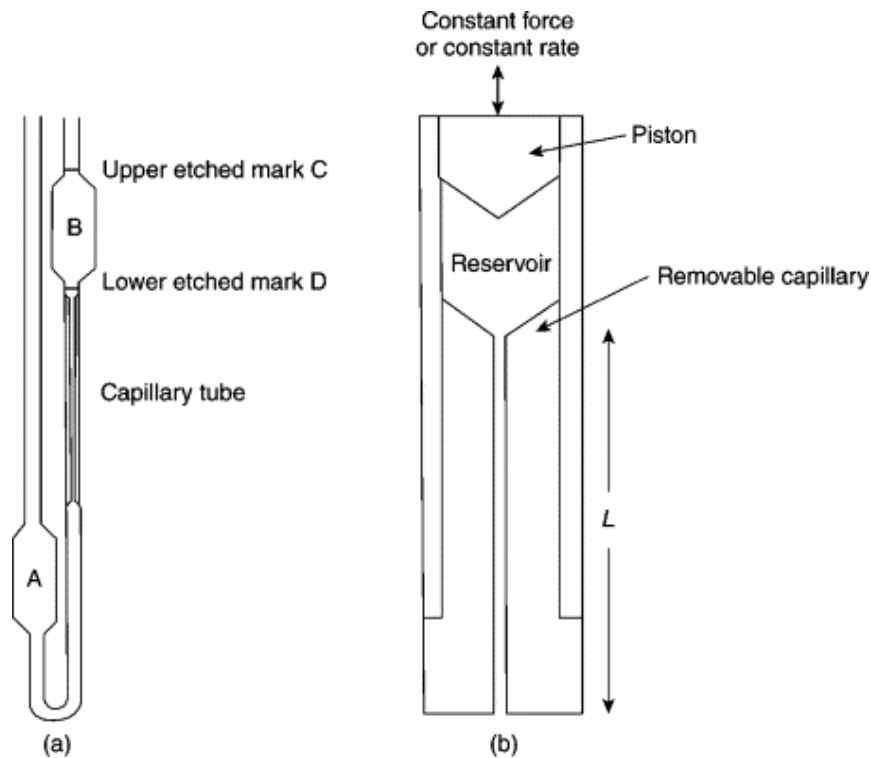


Fig. 2.4.2 Capillary viscometers: (a) Ostwald viscometer; (b) pressure capillary viscometer (Mckenna and Lyng, 2013)

In suspended level viscometers (Viswanath et al., 2007), the test liquid is suspended in the capillary until it becomes filled. Suspended level viscometers have the advantage of providing a consistent driving head of liquid regardless of the amount of sample charged through the viscometer. As a consequence, the viscometer constant is no longer affected by temperature. The impact of surface tension is significantly minimized by having the lower meniscus diameter roughly equal to the average diameter of the upper meniscus. The Ubbelohde suspended level viscometer, shown schematically in Fig. 2.4.3, can be used to determine the kinematic viscosity of transparent Newtonian liquids. The U-tube must be filled at the bottom and clear of air bubbles and particulates. Fill the viscometer via tube (L) with the required amount of sample liquid for the viscometer being used. Fill bulb (A) with liquid and make sure that the liquid level in the bulb (B) is below the ventilation tubes exit (M). Immerse the viscometer in a water or oil bath stabilized at the temperature specified in the individual monograph, and control the temperature. Enable the sample temperature to reach equilibrium by keeping the viscometer vertical for a while. Close tube (M) and raise the liquid level in the tube (N) to around 8mm above the mark (E). Close tube (N) and open tube (O) to keep the liquid at this stage (M). Using an effective accurate timing unit, open tube (N) and calculate the time it takes for the liquid level to drop from mark (E) to mark (F).

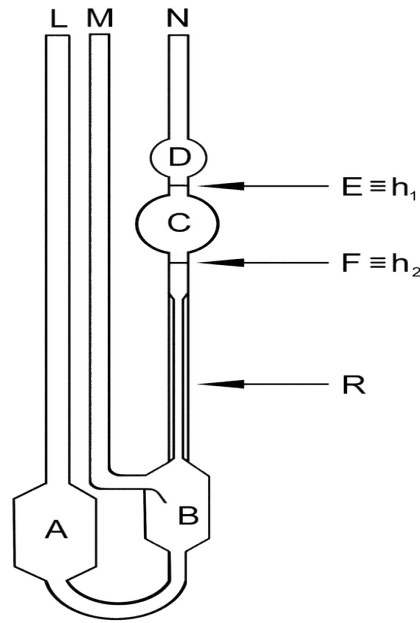


Fig. 2.4.3 Ubbelohde suspended level viscometer

The Rankine viscometer (Kestin et al., 1973) measures viscosity by forcing a certain amount of fluid through the capillary tube from reservoir 1 to reservoir 2. As a result, the head (ΔP), which drives the flow becomes unpredictable, and the flow is nonsteady. The Rankine viscometer is commonly used only in the asymptotic limit of a function. The following Fig. 2.4.4 depicts a Rankine capillary viscometer.

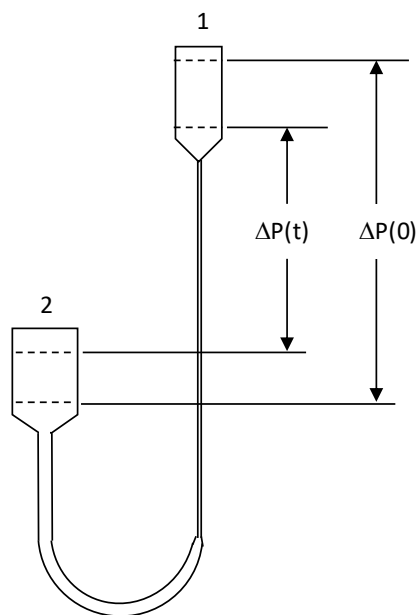


Fig. 2.4.4 Rankine capillary viscometer

Above all capillary viscometers are capable of measuring the viscosity of working fluids. Despite this, measuring accuracy is needed. Therefore, the tandem capillary tube method (Alam et al., 2018b; Miyara et al., 2018; Mondal et al., 2020) was introduced in this research to accurately measure the viscosity of refrigerants as working fluids. The method of tandem capillary tubes is developed based on Hagen-Poiseuille's equation. The newly developed method of tandem capillary tubes shown in Fig. 2.4.5 is considered with corrections due to kinetic energy and end effect. As a result, accurate measurements with high precision can be obtained using this approach.

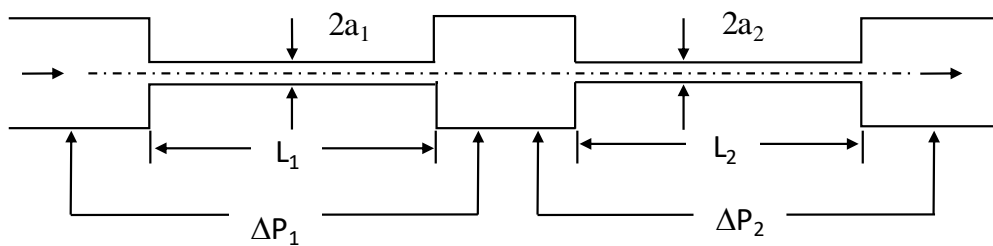


Fig. 2.4.5 Tandem capillary tubes viscometer

2.4.2 Progression history of transient hot-wires method

The first “transient” hot-wire instrument was proposed by Stålhane and Pyk in 1931. However, the authors Stålhane and Pyk (1931) are credited as the pioneers of the transient hot-wire method to measure the thermal conductivity of solids and powders (and some liquids). In their instrument, the Constantan hot wire is wrapped around a tube with a thermometer inside. The whole rod was normally submerged in the powder, which was held at a steady temperature. From their further investigation, they found the relationship between the time and temperature rise for a fine straight wire subjected to a step-change in the heat contribution to the wire. After that, the authors Eucken and Englert (1938) improved the design of Stålhane and Pyk and designed an absolute transient hot-wire instrument for low temperatures. They used a cross-like configuration, with the 0.1 mm platinum wire in the center, two wires on each side serving as possible leads, and the other two serving as support wires. The resistance of the wire was used to determine the temperature. Van der Held and Van Drunen (1949) and Van der Held et al. (1953) utilized a manganese wire of 0.3 mm diameter, and a 0.1 mm diameter copper/constantan thermocouple both placed in a thin

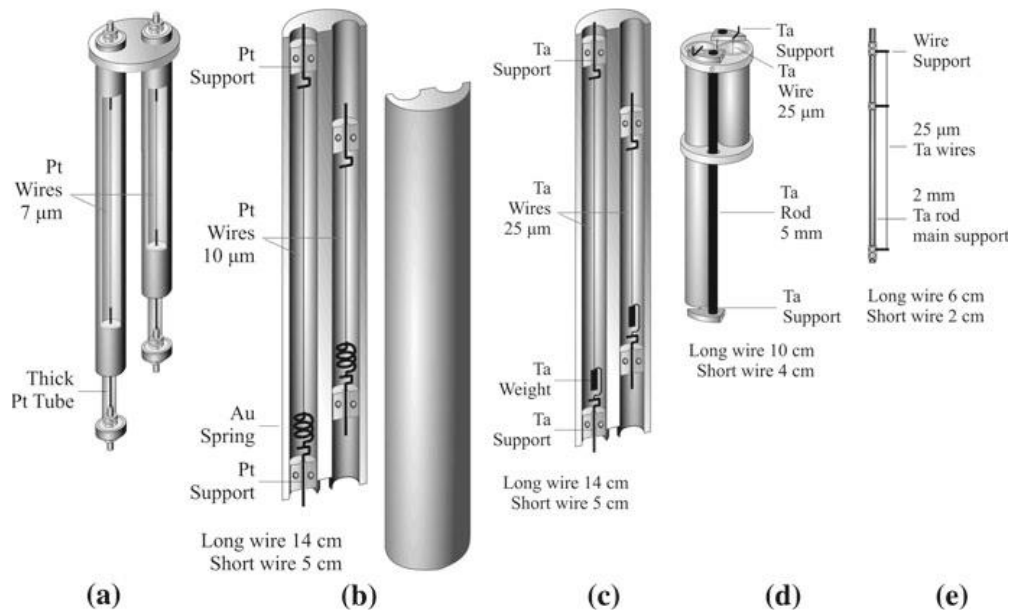
capillary with both ends attached into the glass vessel wall. In this way, the sample liquid is placed in between the glass vessel and the capillary. Gillam et al. (1955) employed the ideas of Stålhanne and Pyk, and Eucken and Englert, to construct a simple apparatus of lower uncertainty, 0.3 % for liquids and solids. They also used a platinum wire (0.1 mm diameter) with potential leads. The temperature was gained from the resistance of the wire, and the resistance adjustment was recorded using an integrated Kelvin bridge. Turnbull (1962), measured the thermal conductivity of molten salts in the liquid and solid states, and organic silicates. They used a 0.1 mm diameter platinum wire immersed in the sample in a borosilicate glass cell, which was heated by direct current connected in a three-lead Wheatstone bridge. The temperature rise of the wire was found from the reading of the bridge galvanometer deflection. Horrocks and McLaughlin (1963) used a four-terminal transient hot-wire instrument to measure the thermal conductivity of liquids, with an absolute uncertainty of 0.25 %. They used a platinum wire with a diameter of 60 μm and a length of 15 cm that had been annealed for an hour. A platinum spring at the top kept the wire from sagging, and platinum potential leads were mounted about 1 cm from the ends. They investigated the corrections due to the finite wire diameter, boundary medium, and finite wire length, as well as the effects of convection and radiation. It's also worth noting that they used a time scale for calculations of around 10s, which was constrained by the timing electronics available. In other contexts, Harman's work from 1971, written by Wakeham et al. (1991), is quoted as one of the first implementations of the technique, with equipment that used an automated Wheatstone bridge to calculate the resistance difference between the two hot wires. Although both of the above research works are of great importance to advance the modern transient hot-wire instrument, the authors (Assael and Antoniadis, 2009) believe that the technique origins can be traced back to the first heated-wire experiments in 1780, as they briefly presented at the 30th International Thermal Conductivity Conference. This viewpoint will direct the presentation in this work, which will begin with an introduction of the principle of the technique.

The transient hot-wire technique is a well-known, absolute method for determining the thermal conductivity of liquids, gases, solids, melts, and nanofluids. This technique has two distinguishing characteristics (e.g., the broad range of uses and very low uncertainty) that make the technique unique. Indeed, when used correctly, it can accomplish uncertainties of less than 1% for liquids, gases, and solids, and less than 2% for nanofluids and melts. Except for the very low-pressure gas region and the critical region, it has been shown that it can be

applied effectively to a wide range of temperatures and pressures. The thermal conductivity of a medium is measured using this method by monitoring the rate at which the temperature of a thin metallic wire rises over time. It has been subjected to a step-change of voltage. As a result, a line source of basically uniform heat flux per unit length is generated in the medium, which is constant in time. It has the effect of generating a temperature field that grows over time in the medium. The thermal conductivity is calculated using the temperature of the wire as a function of time. It's worth noting that the wire serves as both a line source of constant heat flux per unit length and a temperature resistance thermometer, assuming the content is pure, which is typically platinum or tantalum. Furthermore, two wires that are similar except for their length are used to prevent end effects. As a result, if arrangements are made to quantify the difference of resistance between the two wires as a function of time, the calculation refers to the resistance shift of a finite part of an infinite wire (as the very identical end effects are subtracted), from which the temperature increase can be calculated. Today's instruments use highly precise automated electronic bridges that allow for over 1000 measurements of the transient temperature increase from less than 1 ms to 1 s (or 10 s in the case of solids) and are combined with finite element methods to achieve a very low uncertainty.

Regardless of the successful application of the transient hot-wire method for measuring the thermal conductivity of liquids, gases, solids, melts, and nanofluids, over wider temperature and pressure ranges, there are also certain situations in which the technique cannot be used properly. In the case of the critical region, this method cannot be worked properly as it needs a temperature rise of a few kelvins. The fluid physical properties change at near-critical conditions are too significant, with either the temperature or even height of the measurement cell. In the case of the low pressure dilutes gas region, the measurements seem to deviate from expectations systematically. It has been shown that although viscosity measurements at very low pressure and up to high temperatures agree very well with calculated results employing the best available potentials, this does not happen for thermal conductivity. Although viscosity measurements (Wakeham, 2009) at very low pressures and up to high temperatures agree well with measured findings using the best available potentials, this is not the case for thermal conductivity. It has also been shown (Wakeham, 2009) that this minor variation seems to increase with the molecule polarity and/or complexity. Even though the deviations are minor for engineering purposes, their nature is of great scientific significance. Again, in the case of thin films, this procedure cannot be used correctly for low-uncertainty

measurements because the sensor's thickness is comparable to the sample's thickness, resulting in heat losses.



Source: Assael and Antoniadis, 2009

Fig. 2.5.1 Several instruments of transient hot-wire technique for fluids (Assael et al., 2010; Assael and Antoniadis, 2009)

References

- Akpek, A., Youn, C., Maeda, A., Fujisawa, N., Kagawa, T., 2014. Effect of Thermal Convection on Viscosity Measurement in Vibrational Viscometer. *J. Flow Control. Meas. Vis.* 02, 12–17. <https://doi.org/10.4236/jfcmv.2014.21003>
- Alam, M.J., Islam, M.A., Kariya, K., Miyara, A., 2018a. Measurement of thermal conductivity and correlations at saturated state of refrigerant trans-1-chloro-3,3,3-trifluoropropene (R-1233zd(E)). *Int. J. Refrig.* 90, 174–180. <https://doi.org/10.1016/j.ijrefrig.2018.02.004>
- Alam, M.J., Islam, M.A., Kariya, K., Miyara, A., 2017. Measurement of thermal conductivity of cis-1,1,1,4,4,4-hexafluoro-2-butene (R-1336mzz(Z)) by the transient hot-wire method. *Int. J. Refrig.* 84, 220–227. <https://doi.org/10.1016/j.ijrefrig.2017.08.014>
- Alam, M.J., Kariya, K., Yamaguchi, K., Hori, Y., Miyara, A., 2019a. Measurement of

- thermal conductivity and kinematic viscosity of 1,1,1,3,3,3-hexafluoro-2-methoxypropane (HFE-356mmz). *Int. J. Refrig.* 103, 1–8. <https://doi.org/10.1016/j.ijrefrig.2019.03.024>
- Alam, M.J., Miyara, A., Kariya, K., Kontomaris, K.K., 2018b. Measurement of Viscosity of cis-1,1,1,4,4,4-Hexafluoro-2-butene (R-1336mzz(Z)) by Tandem Capillary Tubes Method. *J. Chem. Eng. Data* 63, 1706–1712. <https://doi.org/10.1021/acs.jced.8b00036>
- Alam, M.J., Yamaguchi, K., Hori, Y., Kariya, K., Miyara, A., 2019b. Measurement of thermal conductivity and viscosity of cis-1-chloro-2,3,3,3-tetrafluoropropene (R-1224yd(Z)). *Int. J. Refrig.* 104, 221–228. <https://doi.org/10.1016/j.ijrefrig.2019.05.033>
- Assael, M.J., Antoniadis, K.D., 2009. No Title, in: *Proceedings of 30th International Thermal Conductivity Conference* (Pittsburgh, PA).
- Assael, M.J., Antoniadis, K.D., Wakeham, W.A., 2010. Historical evolution of the transient hot-wire technique. *Int. J. Thermophys.* 31, 1051–1072. <https://doi.org/10.1007/s10765-010-0814-9>
- Assael, M.J., Dymond, J.H., Polimatidou, S.K., 1994. Measurements of the viscosity of R134a and R32 in the temperature range 270–340 K at pressures up to 20 MPa. *Int. J. Thermophys.* 15, 591–601. <https://doi.org/10.1007/BF01563789>
- Assael, M.J., Karagiannidis, E., 1993. Measurements of the Thermal Conductivity of R22, R123, and R134a in the Temperature Range 250–340 K at Pressures up to 30 MPa. *Int. J. Thermophys.* 14, 183–197.
- Assael, M.J., Karagiannidis, E., Wakeham, W.A., 1992. Measurements of the Thermal Conductivity of R11 and R12 in the Temperature Range 250–340 K at Pressures Up to 30 MPa. *Am. Soc. Mech. Eng.* 13, 735–751.
- Baginsky, A.V., Shipitsyna, A.S., 2009. Thermal conductivity and thermal diffusivity of the R134a refrigerant in the liquid state. *Thermophys. Aeromechanics* 16, 267–273. <https://doi.org/10.1134/S0869864309020115>
- Calm, J.M., 2012. Refrigerant transitions ... again, in: *ASHRAE/NIST Refrigerants Conference: Moving Towards Sustainability*. National Institute of Standards and

- Technology (NIST), Gaithersburg, MD, USA, and ASHRAE. Atlanta, GA, USA.
- Calm, J.M., 2008. The next generation of refrigerants - Historical review, considerations, and outlook. *Int. J. Refrig.* 31, 1123–1133. <https://doi.org/10.1016/j.ijrefrig.2008.01.013>
- Calm, J.M., 2006. Environmental and Performance Studies of R-123 as a Chiller Refrigerant — Resulting Recommendations for Environmental Protection, in: 11th International Refrigeration and Air Conditioning Conference at Purdue, Paper R147, Purdue University, West Lafayette, IN, USA.
- Calm, J.M., Hourahan, G.C., 2011. Physical, safety, and environmental data for refrigerants, in: 23rd International Congress of Refrigeration (ICR 2011, Prague, Czech Republic), International Institute of Refrigeration (IIR/IIF), Paris, France.
- Cousins, D.S., Laesecke, A., 2012. of Dimethyl Ether and Two Next-Generation Alternative Refrigerants. *J. Res. Natl. Inst. Stand. Technol.* 117, 231–256.
- Dang, Y., Kamiaka, T., Dang, C., Hihara, E., 2015a. Liquid viscosity of low-GWP refrigerant mixtures (R32 + R1234yf) and (R125 + R1234yf). *J. Chem. Thermodyn.* 89, 183–188. <https://doi.org/10.1016/j.jct.2015.05.009>
- Dang, Y., Kim, H.S., Dang, C., Hihara, E., 2015b. Measurement of vapor viscosity of R1234yf and its binary mixtures with R32, R125. *Int. J. Refrig.* 58, 131–136. <https://doi.org/10.1016/j.ijrefrig.2015.06.010>
- Diller, D.E., Aragon, A.S., Laesecke, A., 1993. Measurements of the viscosities of saturated and compressed liquid 1,1,1,2-tetrafluoroethane (R134a), 2,2-dichloro-1,1,1-trifluoroethane (R123) and 1,1-dichloro-1-fluoroethane (R141b). *Fluid Phase Equilib.* 88, 251–262. [https://doi.org/10.1016/0378-3812\(93\)87116-I](https://doi.org/10.1016/0378-3812(93)87116-I)
- Eucken, A., Englert, H., 1938. *Gesamte Gerichtl. Kalte-Industrie* 45, 109.
- Geller, V.Z., Francisco, S., Thermodynamics, E., 1996. Viscosities of HFC-32 and HFC-32] Lubricant Mixtures I 17, 75–83.
- Gillam, D.G., Rombén, L., Nissen, H.-E., Lamm, O., 1955. Accurate Determination of Thermal Conductivities. *Acta Chem. Scand.* 9, 641–656. <https://doi.org/10.3891/acta.chem.scand.09-0641>

- Gross, U., Song, Y.W., 1996. Thermal conductivities of new refrigerants R125 and R32 measured by the transient hot-wire method. *Int. J. Thermophys.* 17, 607–619. <https://doi.org/10.1007/BF01441507>
- Gulik, P.S. van der, 1995. Viscosity of saturated R152a measured with a vibrating wire viscometer. *Int. J. Thermophys.* 16, 867–876. <https://doi.org/10.1007/BF02093469>
- Hapenciuc, C.L., Negut, I., Borca-Tasciuc, T., Mihailescu, I.N., 2019. A steady-state hot-wire method for thermal conductivity measurements of fluids. *Int. J. Heat Mass Transf.* 134, 993–1002. <https://doi.org/10.1016/j.ijheatmasstransfer.2019.01.098>
- Horrocks, J.K., McLaughlin, E., 1963. Non-steady-state measurements of the thermal conductivities of liquid polyphenyls. *Proc. R. Soc. London. Ser. A. Math. Phys. Sci.* 273, 259–274. <https://doi.org/10.1098/rspa.1963.0087>
- IPCC, 2007. *Climate Change 2007: The Physical Science Basis. Contribution of Working Group I to the Fourth Assessment Report of the Intergovernmental Panel on Climate Change*, Cambridge University Press, Cambridge, United Kingdom and New York, NY, USA.
- Jaeger, J.C., Sass, J.H., 1964. A line source method for measuring the thermal conductivity and diffusivity of cylindrical specimens of rock and other poor conductors. *Br. J. Appl. Phys.* 15, 1187–1194. <https://doi.org/10.1088/0508-3443/15/10/307>
- Jagueneau, A., Jannot, Y., Degiovanni, A., Ding, T., 2019. A steady-state method for the estimation of the thermal conductivity of a wire. *Int. J. Heat Technol.* 37, 351–356. <https://doi.org/10.18280/ijht.370142>
- Kestin, J., Sokolov, M., Wakeham, W., 1973. Theory of capillary viscometers. *Appl. Sci. Res.* 27, 241–264. <https://doi.org/10.1007/BF00382489>
- Kyoto-Protocol, 1997. *Kyoto Protocol to the United Nations Framework Convention on Climate Change*, United Nations (UN), New York, NY, USA.
- Laesecke, A., Lüddecke, T.O.D., Hafer, R.F., Morris, D.J., 1999. Viscosity measurements of ammonia, R32, and R134a. Vapor buoyancy and radial acceleration in capillary viscometers. *Int. J. Thermophys.* 20, 401–434.

<https://doi.org/10.1023/A:1022644718603>

Makita, T., Tanaka, Y., Morimoto, Y., Noguchi, M., Kubota, H., 1981. Thermal conductivity of gaseous fluorocarbon refrigerants R 12, R 13, R 22, and R 23, under pressure. *Int. J. Thermophys.* 2, 249–268. <https://doi.org/10.1007/BF00504188>

Mathis, N., 2000. Transient thermal conductivity measurements: Comparison of destructive and nondestructive techniques. *High Temp. - High Press.* 32, 321–327. <https://doi.org/10.1068/htwu289>

Mckenna, B.M., Lyng, J.G., 2013. Principles of food viscosity analysis, Instrumental Assessment of Food Sensory Quality. Woodhead Publishing Limited. <https://doi.org/10.1533/9780857098856.1.129>

Measurement, T.C. https://en.wikipedia.org/wiki/Thermal_conductivity_measurement.

Meng, X., Qiu, G., Wu, J., Abdulagatov, I.M., 2013. Viscosity measurements for 2,3,3,3-tetrafluoroprop-1-ene (R1234yf) and trans-1,3,3,3-tetrafluoropropene (R1234ze(E)). *J. Chem. Thermodyn.* 63, 24–30. <https://doi.org/10.1016/j.jct.2013.03.013>

Midgley, J.T., 1937. From the Periodic Table to Production. *Ind. Eng. Chem.* 29, 239–244.

Miyara, A., Alam, M.J., Kariya, K., 2018. Measurement of viscosity of trans-1-chloro-3,3,3-trifluoropropene (R-1233zd(E)) by tandem capillary tubes method. *Int. J. Refrig.* 92, 86–93. <https://doi.org/10.1016/j.ijrefrig.2018.05.021>

Mondal, D., Hori, Y., Kariya, K., Miyara, A., Alam, M.J., 2020. Measurement of Viscosity of a Binary Mixture of R1123+R32 Refrigerant by Tandem Capillary Tube Method. *Int. J. Thermophys.* 41, 83 (1–20). <https://doi.org/10.1007/s10765-020-02653-4>

Mondal, D., Kariya, K., Tuhin, A.R., Miyoshi, K., Miyara, A., 2021. Thermal Conductivity Measurement and correlation at saturation condition of HFO refrigerant trans-1,1,1,4,4,4-hexafluoro-2-butene (R1336mzz(E)). *Int. J. Refrig.* 129, 109–117. <https://doi.org/10.1016/j.ijrefrig.2021.05.005>

Montreal-Protocol, 1987. Montreal Protocol on Substances that Deplete the Ozone Layer Montreal, United Nations (UN), New Work, NY, USA.

- Mylona, S.K., Hughes, T.J., Saeed, A.A., Rowland, D., Park, J., Tsuji, T., Tanaka, Y., Seiki, Y., May, E.F., 2019. Thermal conductivity data for refrigerant mixtures containing R1234yf and R1234ze(E). *J. Chem. Thermodyn.* 133, 135–142. <https://doi.org/10.1016/j.jct.2019.01.028>
- Neindre, B. Le, Garrabos, Y., Sabirzianov, A., Goumerov, F., 2001. Measurements of the thermal conductivity of chlorodifluoromethane (HCFC-22) in the temperature range from 300 K to 515 K and at pressures up to 55 MPa. *J. Chem. Eng. Data* 46, 193–201. <https://doi.org/10.1021/je0002078>
- Oliveira, C.M.B.P., Wakeham, W.A., 1993. The viscosity of R32 and R125 at saturation. *Int. J. Thermophys.* 14, 1131–1143. <https://doi.org/10.1007/BF02431279>
- Perkins, R.A., Huber, M.L., 2020. Measurement and Correlation of the Thermal Conductivity of cis-1,1,1,4,4,4-hexafluoro-2-butene. *Int. J. Thermophys.* 41, 4868–4874. <https://doi.org/10.1007/s10765-020-02681-0>
- Perkins, R.A., Huber, M.L., 2011. Measurement and Correlation of the Thermal Conductivity of 2,3,3,3-Tetrafluoroprop-1-ene (R1234yf) and trans-1,3,3, 3-Tetrafluoropropene (R1234ze(E)). *J. Chem. Eng. Data* 56, 4868–4874. <https://doi.org/dx.doi.org/10.1021/je200811n>
- Perkins, R.A., Huber, M.L., Assael, M.J., 2017. Measurement and Correlation of the Thermal Conductivity of trans-1-Chloro-3,3,3-trifluoropropene (R1233zd(E)). *J. Chem. Eng. Data* 62, 2659–2665. <https://doi.org/10.1021/acs.jced.7b00106>
- Pham, H., Sachs, H., 2010. Next Generation Refrigerants : Standards and Climate Policy Implications of Engineering Constraints. ACEEE Summer Study Energy Effic. Build. 282–294.
- Shire, S.J., 2015. The molecular basis of high viscosity of monoclonal antibodies (mAbs) at high concentration. *Monoclon. Antibodies* 163–192. <https://doi.org/10.1016/b978-0-08-100296-4.00009-9>
- Stålthane, B., Pyk, S., 1931. First transient hot wire 61, 389.
- Tada, Y., Harada, M., Tanigaki, M., Eguchi, W., 1978. Laser flash method for measuring

- thermal conductivity of liquids - Application to low thermal conductivity liquids. *Rev. Sci. Instrum.* 49, 1305–1314. <https://doi.org/10.1063/1.1135573>
- Turnbull, A.G., 1962. Thermal Conductivity of Organic Silicates. *Therm. Anal. Mater.* 7, 79–81. <https://doi.org/10.1021/je60012a024>
- Van der Held, E.F.M., Hardebol, J., Kalshoven, J., 1953. *Physica* 19, 208.
- Van der Held, E.F.M., Van Drunen, F.G., 1949. A method of measuring the thermal conductivity of liquids. *Physica* 15, 865–881. [https://doi.org/10.1016/0031-8914\(49\)90129-9](https://doi.org/10.1016/0031-8914(49)90129-9)
- Verba, O.I., Raschektaeva, E.P., Stankus, S. V., 2017. Thermal conductivity of R-410A mixture in the vapor phase. *Thermophys. Aeromechanics* 24, 135–139. <https://doi.org/10.1134/S0869864317010140>
- Viscometer. <https://en.wikipedia.org/wiki/Viscometer>.
- Viscometer, T. Types of Viscometers, <https://www.formulaction.com/en/about-us/news/blog/5-ways-measure-viscosity>.
- Viswanath, D.S., Ghosh, T.K., Prasad, D.H.L., Dutt, N.V.K., Rani, K.Y., 2007. *Viscosity of Liquids: Theory, Estimation, Experiment, and Data*, Springer Editions, Dordrecht, Netherlands.
- Wakeham, W.A., 2009. No Title, in: *Proceedings of 30th International Thermal Conductivity Conference* (Pittsburgh, PA).
- Wakeham, W.A., Nagashima, A., Sengers, J.V., 1991. *Experimental Thermodynamics. Vol. III, Measurement of the Transport Properties of Fluids* (Blackwell Scientific Publications, London).
- Webster, J.G., 2005. The measurement, instrumentation and sensors handbook [Book Review], *IEEE Electrical Insulation Magazine*. <https://doi.org/10.1109/mei.2000.855618>
- Yata, J., Hori, M., Hagiwara, T., Minamiyama, T., 1996. Thermal conductivity of propane and butane in the liquid phase. *Fluid Phase Equilib.* 125, 267–274. [https://doi.org/10.1016/s0378-3812\(96\)03091-9](https://doi.org/10.1016/s0378-3812(96)03091-9)

- Zhao, D., Qian, X., Gu, X., Jajja, S.A., Yang, R., 2016. Measurement techniques for thermal conductivity and interfacial thermal conductance of bulk and thin film materials. *J. Electron. Packag. Trans. ASME* 138. <https://doi.org/10.1115/1.4034605>
- Zhelezny, V.P., Sechenyh, V. V., Semenyuk, Y. V., Grebenkov, A.J., Beliayeva, O. V., 2009. An experimental investigation and modelling of the viscosity refrigerant/oil solutions. *Int. J. Refrig.* 32, 1389–1395. <https://doi.org/10.1016/j.ijrefrig.2009.02.013>

Chapter 3

Theory and Experimental Apparatus

This chapter describes the theory of experimental method, apparatus set up, and validation of the experimental apparatus both of viscosity and thermal conductivity measurements. The chapter also describes the procedure to measure uncertainties of measurements. The new experimental apparatus for measuring both the viscosity and thermal conductivity were developed separately in MIYARA & KARIYA Laboratory, Thermal Energy Engineering Lab, Department of Mechanical Engineering at the Saga University, Japan. There are two different types of apparatus prepared in this laboratory for measuring the viscosity and thermal conductivity of refrigerants. The only difference is in the heating system of the measuring cell in the apparatus; one uses electricity, while the other uses oil for heating or nybrine to keep the system cold.

3.1 Theory and Experimental Apparatus for Viscosity Measurement

The viscosity measurement was conducted by the method of tandem capillary tubes over a wide range of temperature and pressure. The liquid, vapor, and supercritical viscosities (sometimes kinematic viscosities) were measured for the environmentally friendly refrigerants used as working fluids (e.g., R1336mzz(E), 3,3,4,4,5,5-HFCPE, R1132(E), and a mixture of R1123+R32). In this method, the measuring cell known as viscometer was constructed using almost the same diameter but different lengths of two capillary tubes that are horizontally installed in series connection to minimize the end effects of capillary tubes. In the following parts, the working principle of this procedure, a summary of the experimental apparatus, a reliability test as well as validation of the apparatus, and the measurement uncertainties are discussed.

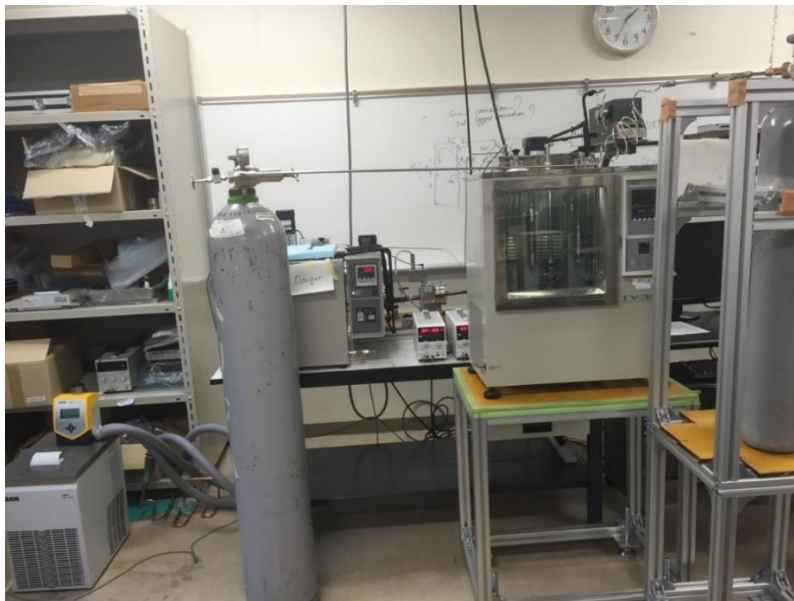
3.1.1 Theory of the tandem capillary tubes (TCT) method

The capillary tube method, which is based on the Hagen-Poiseuille principle, is a technique for determining the viscosity of fluids by forcing a liquid through the capillary tubes. The unknown

viscosity of the refrigerant used as working fluid has been measured using the tandem capillary tubes technique in the present study. In our laboratory, we have developed two types of tandem capillary apparatus: (a) an electric heating system, and (b) an oil bath heating or nybrine cooling system. Figs. 3.1.1 and 3.1.2 show the original view of the apparatus, where Table 3.1.1 indicates the dimensions of the capillary tubes.



(a)

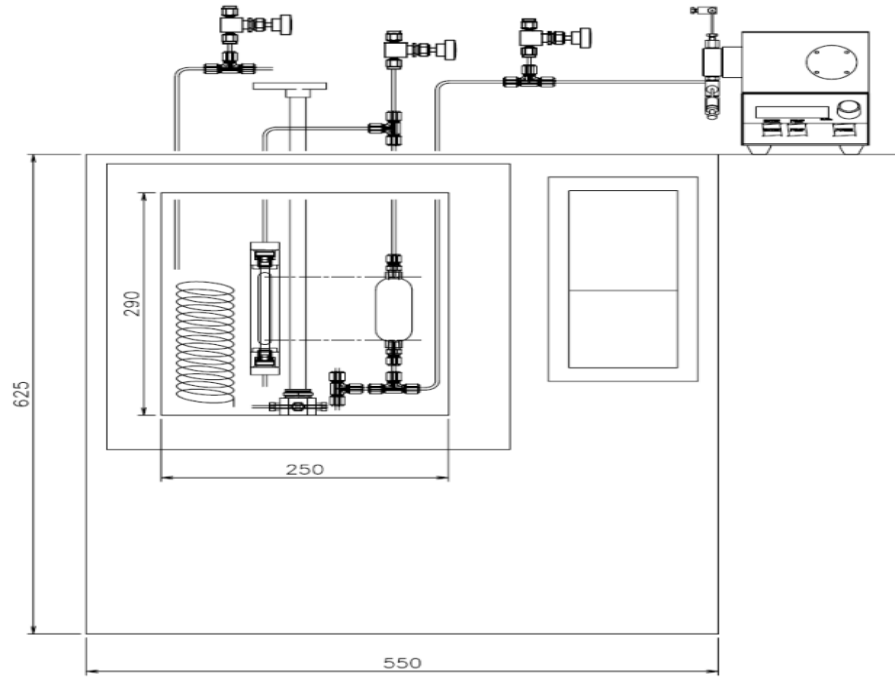


(b)

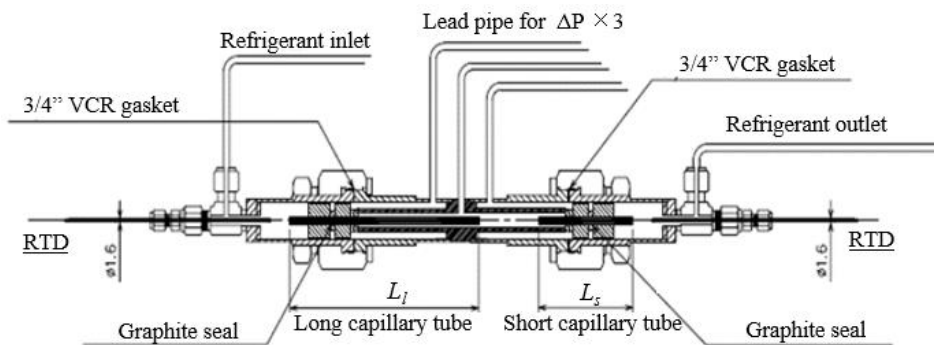
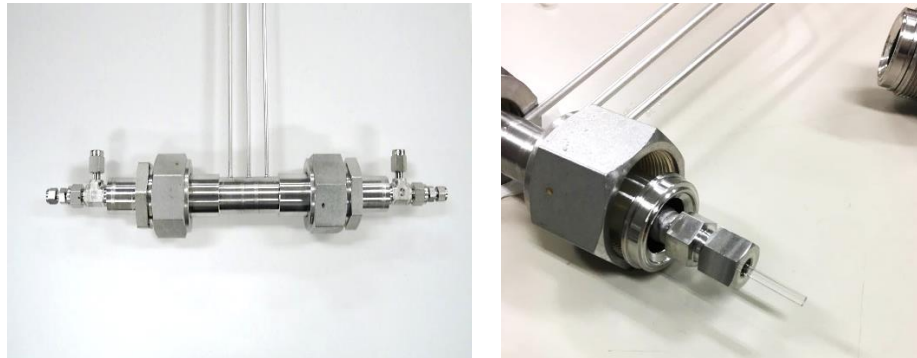
Fig. 3.1.1 The original viewpoint of experimental apparatus to measure the viscosity of refrigerants (a) electric heating system (b) oil bath heating or nybrine cooling system

Table 3.1.1 Capillary tubes dimensions

Type	Capillary	Length (mm)	Inner diameter (mm)
Electric (<i>heating</i>)	Long	99.85	0.1269
	Short	50.16	0.1268
Oil/nybrine(<i>heating or cooling</i>)	Long	99.98	0.1278
	Short	49.92	0.1279



(a)



(b)

Fig. 3.1.2 The original viewpoint of (a) layout of the apparatus, and (b) the measuring cell

In this instrument, two capillary tubes are used as a long and short tube in series connection to eliminate the end effects of capillary tubes and to measure the viscosity from pressure drop of fluid in laminar flow. This is an improved technique of the well-established Hagen-Poiseuille theory-based capillary tube method. As a consequence of using the Hagen-Poiseuille theory, the relationship between fluid viscosity η and pressure drop ΔP through a horizontal tube of radius r and length L at q flow rate can be seen as follows.

$$\eta = \frac{\pi r^4 \Delta P}{8qL} \quad (3.1.1)$$

To realize a stable laminar flow, a capillary tube with a small diameter is used. However, the pressure drop of the capillary tube can not be measured directly. Therefore, pressure is measured at a chamber connected to the capillary tube and the viscosity is calculated from the following equation (Viswanath et al., 2007).

$$\eta = \frac{\pi r^4 \Delta P}{8q(L + b)} - \frac{a\rho q}{8\pi(L + b)} \quad (3.1.2)$$

where a and b are the kinetic energy and pipe end correction coefficients, respectively. ρ is the test fluid density.

Fig. 3.1.3 (b) shows the principle of the tandem capillary method. Long and short capillary tubes are connected in series and pressure is measured at the chamber connected to the tubes. As illustrated in this figure, the actual pressure change includes inlet/outlet pressure drop regions and fully developed laminar flow regions. The inlet/outlet pressure drops in the long and short tubes are equal. By superimposing the pressure distributions of long and short tubes, the pressure gradient of the fully developed laminar flow region can be estimated by

$$\frac{\Delta P}{L} = \frac{\Delta P_l - \Delta P_s}{L_l - L_s} \quad (3.1.3)$$

From the equations (3.1.1) and (3.1.3), the following equation is obtained and the viscosity can be calculated.

$$\eta = \frac{\pi r^4 (\Delta P_l - \Delta P_s)}{8q(L_l - L_s)} \quad (3.1.4)$$

In the above equations, the radius raised to the fourth power introducing any change in the radius of the capillary tube simulates significant effects on experimental data of test fluids. To minimize pressure drop at both the inlet and outlet flow of the tubes, capillary tubes are used as long and short tubes in series connection. Therefore, the viscosity measurements using tandem capillary tubes are more precise than a single capillary tube method. The difference in the diameter of the two capillary tubes also affects the measurement even if the difference is very small. From equation (3.1.2), the kinetic energy and end effects of tubes can be considered for the tandem capillary tubes method as long and short tubes as follows:

$$\eta_l = \frac{\pi r_l^4 \Delta P_l}{8q(L_l + b r_l)} - \frac{a \rho q}{8\pi(L_l + b r_l)} \quad (3.1.5)$$

$$\eta_s = \frac{\pi r_s^4 \Delta P_s}{8q(L_s + b r_s)} - \frac{a \rho q}{8\pi(L_s + b r_s)} \quad (3.1.6)$$

where subscripts l and s represent the long and short tubes used in the apparatus, respectively. For a test fluid $\eta = \eta_l = \eta_s$. Therefore, it can be derived as follows from equations (3.1.5) and (3.1.6).

$$\pi(r_l^4 \Delta P_l - r_s^4 \Delta P_s) = 8q\eta[(L_l - L_s) + b(r_l - r_s)] \quad (3.1.7)$$

where, $(L_l - L_s) \gg b(r_l - r_s)$, So it is possible to be concluded as

$$\eta = \frac{\pi(r_l^4 \Delta P_l - r_s^4 \Delta P_s)}{8q(L_l - L_s)} \quad (3.1.8)$$

In terms of capillary tube diameter, $d = 2r$, the final form of viscosity measuring equation can be found as

$$\eta = \frac{\pi(d_l^4 \Delta P_l - d_s^4 \Delta P_s)}{128q(L_l - L_s)} \quad (3.1.9)$$

where, η ($\mu\text{Pa s}$) is the experimental viscosity, ΔP (MPa) is the pressure drop of each capillary tube having the diameter of d (m) and length of L (m), and q ($\text{m}^3 \text{s}^{-1}$) of the flow rate. Also, subscript l represents the long, whereas, s represents the short Pyrex capillary tubes.

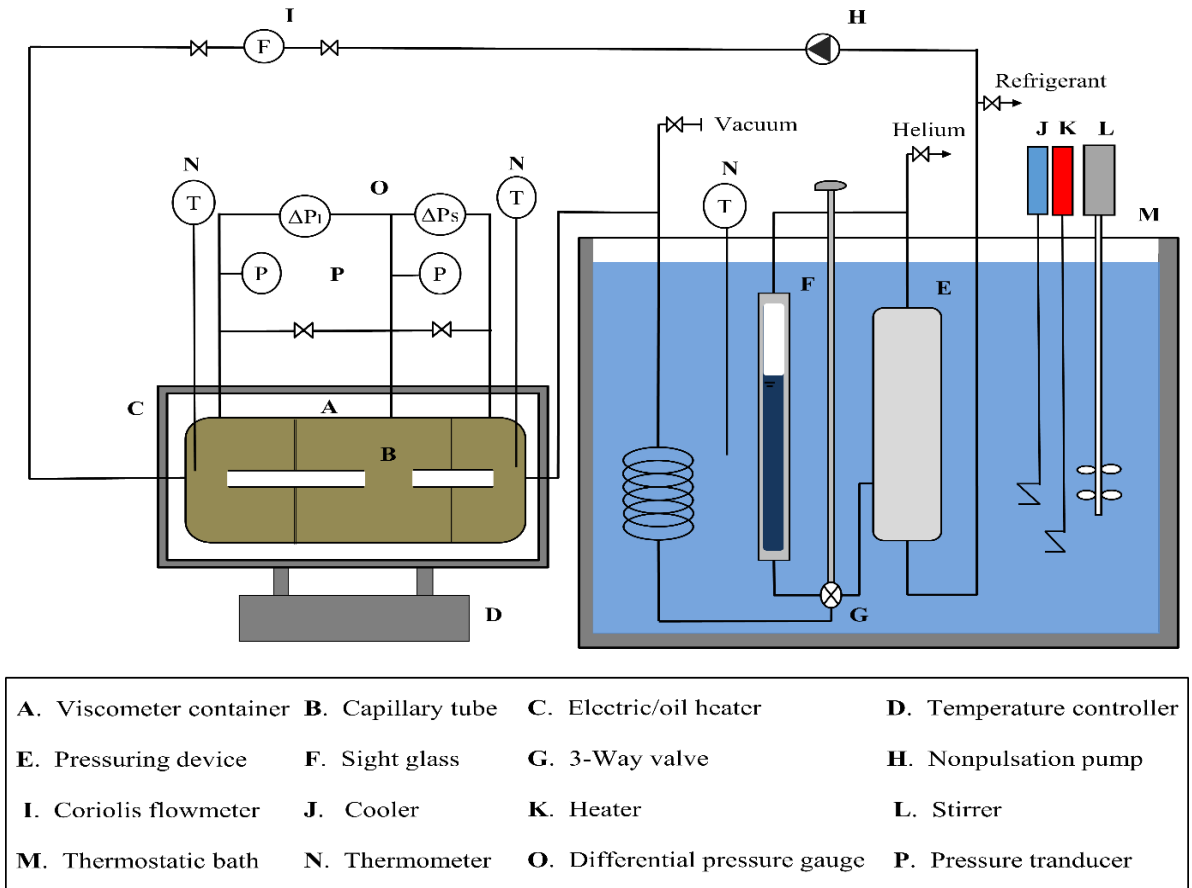
Again, in terms of kinematic viscosity $\nu = \frac{\eta}{\rho}$; whereas the fluid density $\rho = \frac{m}{V}$ (kg m^{-3}) is defined as its mass per unit volume. Again, the volume flow rate $q = \frac{m}{\rho}$ ($\text{m}^3 \text{s}^{-1}$) is defined as the mass flow rate per fluid entrance density, then the above equation can be written as below

$$\nu = \frac{\pi \left(d_l^4 \Delta P_l - d_s^4 \Delta P_s \right)}{128 m (L_l - L_s)} \quad (3.1.10)$$

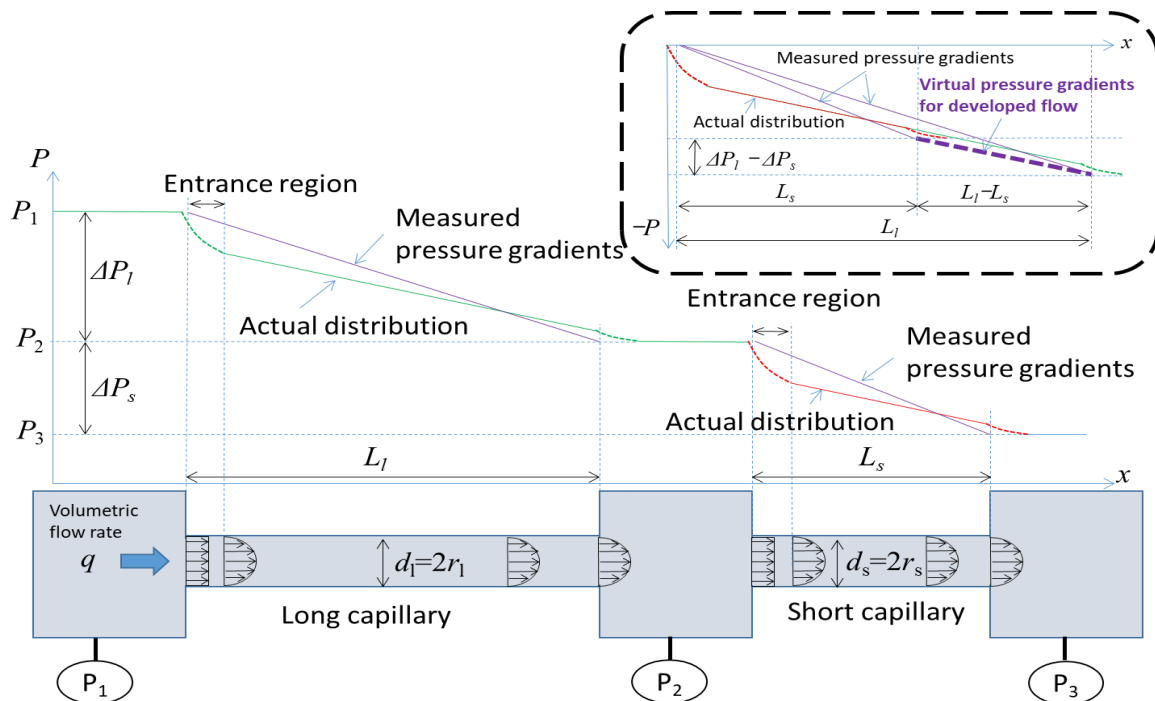
where ν ($\text{cm}^2 \text{s}^{-1}$) is the kinematic viscosity and m is the mass flow rate of the fluid.

3.1.2 Experimental apparatus for viscosity measurement

The tandem capillary tube technique is an improved technique of the well-established Hagen-Poiseuille theory-based capillary tube method. An experimental apparatus was constructed based on this method in our laboratory and the detailed experimental procedures are reported and explained in our group works elsewhere (Alam et al., 2018b; Miyara et al., 2018; Mondal et al., 2020). Using this apparatus, the viscosity measurements of the several pure refrigerants (Alam et al., 2019, 2018b; Miyara et al., 2018) and mixture refrigerants (Mondal et al., 2020, 2019) were conducted previously, and the validation of this method was reported by Miyara et al. (2019). Fig. 3.1.3 illustrates the apparatus for the tandem type capillary tubes viscometer. The test refrigerant was filled in the measurement cell known as viscometer container (A). As the apparatus was made up by using two capillary Pyrex tubes (B) of varying lengths, with the measurement cell held within an electric/oil heater (C) to achieve the desired measurement temperature, whereas attached a digital temperature controller (D) to adjust the heater temperature. The inner diameter of the capillary tubes was measured from the length and mass of mercury-filled in the capillary tube by reading microscope and gravimetric method, respectively. The heater (C) was used as an electric heater in high-temperature side measurement or as an oil heater in low-temperature side measurement. The refrigerant was pumped with a non-pulsation pump (H) through the capillary tubes at a moderate flow rate, and a Coriolis mass flowmeter (I) was used to determine the flow rate.



(a) Flow loop of the viscometer to measure the viscosity



(b) Pressure distribution of tandem capillary tubes

Fig. 3.1.3 Experimental apparatus for tandem type capillary tubes viscometer

To ensure the level of liquid in the measurement cell, a sight glass (F) was connected with the pressuring device (E) that was put in a thermostatic bath (M) at the same height as the measurement cell. The helium cylinder induced the helium gas to the system through pressuring device to adjust the required pressure for the measurement. The differential pressure gauge (O) was to measure the pressure drop of each capillary tubes. Furthermore, the system pressure and system temperature were obtained by using the pressure transducer (P) and platinum pt100 resistance thermometer (N), respectively. Finally, the viscosity of test fluids was obtained from the equation based on the Hagen-Poiseuille theory as above as Eq. (3.1.9) and for kinematic viscosity as Eq. (3.1.10).

3.1.3 Apparatus reliability test for viscosity measurement

In order to ensure the validity as well as reliability of the apparatus the experimentally measured data were tested and compared with the reference fluid data. For this analysis, R134a had been used as a reference fluid and to get the viscosity data until 4.16 MPa pressure over the temperature ranges from 303.60 to 355.96 K at the liquid and 343.49 to 374.53 K at the vapor phases, respectively. The measurement details and the validation of the tandem capillary method were reported elsewhere in Alam et al. (2018) and Miyara et al. (2019). Table 3.1.2 and Fig. 3.1.4 show the measured viscosity data of R134a were found in strong agreement with the predicted data by REFPROP, which used Huber et al. (2003)'s correlation for viscosity estimation. The maximum deviation for the measured data from the calculated data was -2.10% , whereas the minimum deviation was -0.06% . Furthermore, Fig. 3.1.5 shows the measured data of R134a were agreed in the deviations of $\pm 1.5\%$. The measurement uncertainty for R134a viscosity was calculated using the law of uncertainty propagation (Bell, 2001; JCGM 100, 2008; Taylor and Kuyatt, 1994). The estimated expanded uncertainty for the viscosity measurement of R134a was found as 2.2% . These findings indicate that the measurement method, as well as the apparatus, are both reliable.

Table 3.1.2 Measured viscosities of R134a

T (K)	P (MPa)	η_{exp} ($\mu\text{P s}$)	η_{cal}^* ($\mu\text{Pa s}$)	$\Delta\eta^{**}$
(a) Liquid phase				
303.60	3.683	191.16	192.59	-0.74
303.60	3.765	193.24	192.86	0.19
303.60	3.817	195.22	193.04	1.13
303.60	3.345	194.02	191.39	1.37
303.60	3.311	193.18	191.27	1.00
303.60	3.355	193.65	191.42	1.16
312.82	4.048	173.03	173.44	-0.24
312.76	4.069	173.14	173.64	-0.29
312.75	4.064	172.28	173.65	-0.79
312.77	3.061	168.06	170.00	-1.14
312.78	3.061	168.17	169.98	-1.07
312.78	3.042	168.42	169.90	-0.87
313.50	1.796	165.57	163.72	1.13
313.01	1.763	165.39	164.65	0.45
312.96	1.701	164.99	164.51	0.29
312.83	1.706	165.57	164.82	0.46
332.81	4.011	132.52	134.49	-1.47
332.81	4.008	132.45	134.48	-1.51
332.80	4.005	132.52	134.48	-1.46
332.80	3.079	128.23	130.64	-1.84
332.79	3.083	128.41	130.67	-1.73
332.79	3.072	127.88	130.62	-2.10
354.96	4.007	95.65	95.77	-0.12
355.51	4.078	94.07	95.22	-1.21
355.94	4.155	93.35	94.94	-1.67
(b) Vapor phase				
343.49	1.142	13.78	13.71	0.54
343.51	1.137	13.74	13.71	0.24
343.52	1.136	13.63	13.71	-0.57
354.03	1.131	14.10	14.14	-0.26
354.03	1.129	14.13	14.14	-0.06
374.52	1.151	14.71	14.98	-1.83
374.53	1.153	15.06	14.98	0.49

Standard Uncertainties u are $u(T)=0.027$ K, $u(P)=0.003$ MPa, Expanded Uncertainty $u_c(\eta_{\text{exp}})=2.2\%$

*Calculated data from REFPROP (Huber et al., 2003)

**Deviation, $\Delta\eta = 100 \times \left(\frac{\eta_{\text{exp}} - \eta_{\text{cal}}}{\eta_{\text{cal}}} \right)$

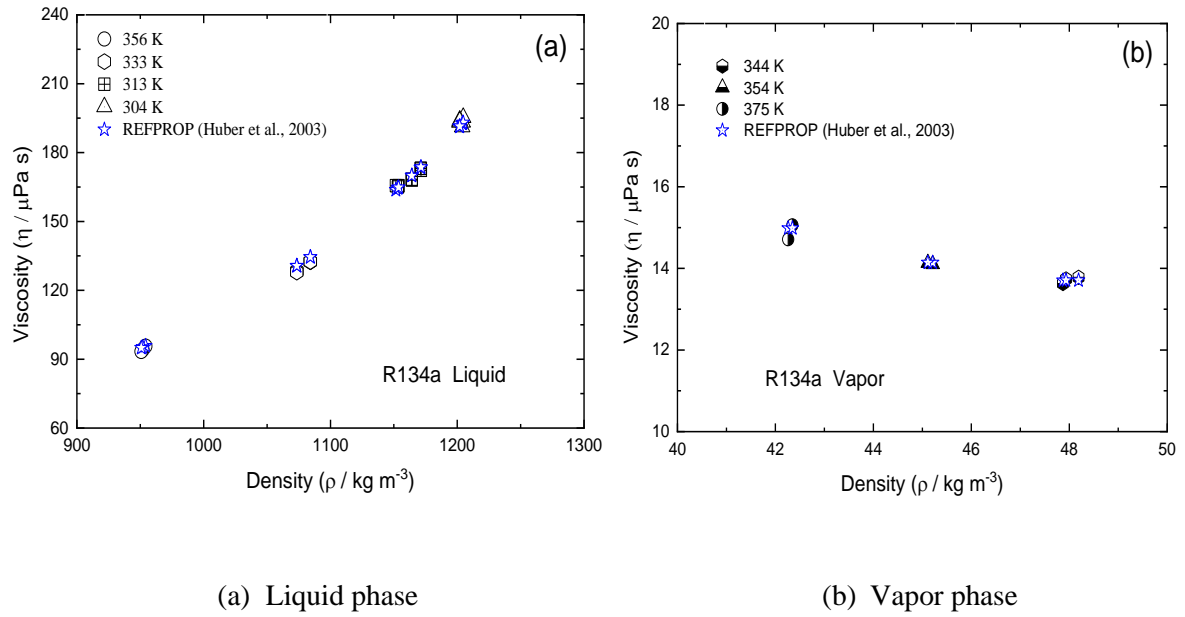


Fig. 3.1.4 Variation of viscosities of R134a with density

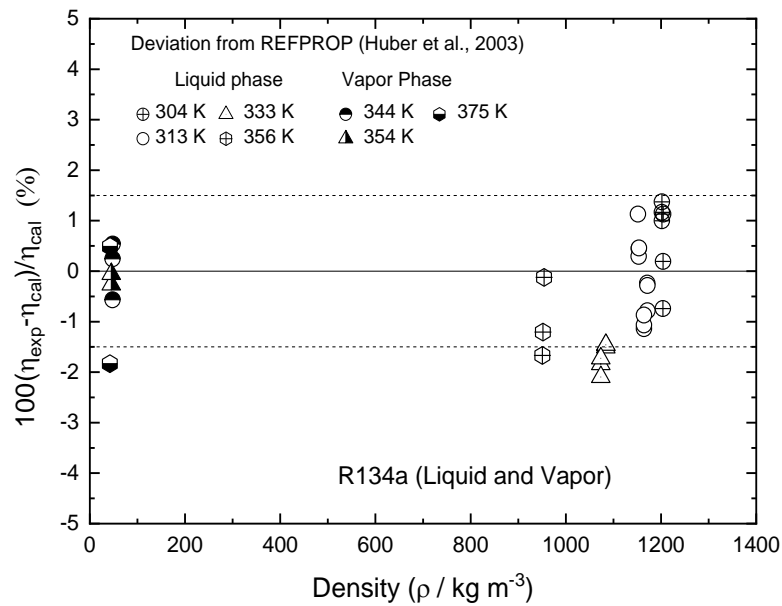


Fig. 3.1.5 Deviations between experimentally measured viscosity and REFPROP

3.1.4 Uncertainty calculation for viscosity measurement

The GUM method, which was revised in 2008 by Joint Committee for Guides in Metrology, was used to measure the uncertainty of viscosity data for the test fluids using the law of propagation (Bell, 2001; JCGM 100, 2008). The accuracy of viscosity measurements is influenced by several important parameters introduced by instruments during research. The most common input variables that cause uncertainty in the viscosity measurement include

inaccuracy owing to the diameter and length of the Pyrex capillary tube, pressure drop, flow rate, experimental pressure and temperature, and few other sources that induced negligible uncertainty. The uncertainties caused by the diameter of capillary tubes, the flow rate, and pressure drop of capillary tubes somehow have the greatest impact on calculating the measurement uncertainty than the other. The supercritical and vapor viscosity data have relatively more deviations than the liquid phase owing to the less consistent differential pressure and flow rates through the Pyrex capillary tubes.

The standard uncertainty $u(x_i)$ is defined as type-A and/ or type-B, depending on whether it is random or systematic, where type-A means random consideration or type-B as systematic. The standard uncertainty of input quantities x_i can be estimated by the following steps. Type-A evaluation comes from the measurement errors whereas type-B from the reading instrument or calibration. The arithmetic means of input quantities or average \bar{x} of the N observations can be expressed as

$$\bar{x} = \frac{1}{N} \sum_{i=1}^N x_i \quad (3.1.11)$$

The experimental standard deviation of input quantities x_i can be estimated as

$$s^2(x_i) = \frac{1}{N-1} \sum_{j=1}^N (x_j - \bar{x})^2 \quad (3.1.12)$$

Then the standard uncertainty of input quantities can be expressed as

$$u(x_i) = s(\bar{x}_i) = \sqrt{\frac{s^2(x_i)}{N}} \quad (3.1.13)$$

Again, type-B evaluation uncertainty for the reading instrument or calibration;

$$u(x_i)_B = \sqrt{\frac{\partial x^2}{12}} \quad (3.1.14)$$

The combined standard uncertainty $u_c(y)$ is the positive square root of the combined variance $u_c^2(y)$, generally written as Eq. (3.1.15) or (3.1.16) as follows,

$$u_c^2(y) = \left(\frac{\partial y}{\partial x_1} \right)^2 u^2(x_1) + \left(\frac{\partial y}{\partial x_2} \right)^2 u^2(x_2) + \dots \dots \dots \left(\frac{\partial y}{\partial x_N} \right)^2 u^2(x_N) \quad (3.1.15)$$

Or,

$$u_c^2(y) = \sum_{i=1}^N \left[\left(\frac{\partial y(x)}{\partial x_i} \right)^2 \cdot u^2(x_i) \right] \quad (3.1.16)$$

where $u^2(x_i)$ are the variances of several input parameters $x_i; i=1,2,\dots,N$. The standard uncertainty $u(x_i)$ is defined as type-A and/ or type-B, where type-A means random consideration or type-B as systematic. In this analysis, the combined standard uncertainty of viscosity of test refrigerants, based on the basic method of tandem capillary tubes, was calculated using the above equation which is expressed in Eq. (3.1.17).

$$u_c(\eta) = \sqrt{\left(\frac{\partial \eta}{\partial d} \right)^2 u^2(d) + \left(\frac{\partial \eta}{\partial L} \right)^2 u^2(L) + \left(\frac{\partial \eta}{\partial \Delta P} \right)^2 u^2(\Delta P) + \left(\frac{\partial \eta}{\partial q} \right)^2 u^2(q) + \left(\frac{\partial \eta}{\partial T} \right)^2 u^2(T) + \left(\frac{\partial \eta}{\partial P} \right)^2 u^2(P)} \quad (3.1.17)$$

The expanded uncertainty $U_e(\eta)$ for the viscosity measurement was calculated from the multiplication of the combined standard uncertainty by a coverage factor k that affects the confidence as well as trust level and usually ranges from 2 to 3 (Bell, 2001; JCGM 100, 2008). In this study, the expanded uncertainty was calculated using the following Eq (3.1.18) with $k = 2$ and a 95 % confidence level.

$$U_e(\eta) = k \cdot u_c(\eta) \quad (3.1.18)$$

Including all parameters, the expanded uncertainties and combined standard uncertainties for the viscosity measurement of the test refrigerants were calculated and summarized in Table 3.1.3. Moreover, the combined uncertainty due to the instrument is 1.09 %, excluding experimental conditions as fluctuation. The uncertainty calculation as an example for viscosity measurement has detailed in section 3.0 of the appendix.

Table 3.1.3 Summary of uncertainties for viscosity measurements

Test fluid	Combined Uncertainties (%)			Expanded Uncertainties (%) (k=2 and 95% Confidence Level)		
	Liquid	Vapor	SpCr*	Liquid	Vapor	SpCr*
R1336mzz(E)	1.13	1.15	1.16	2.26	2.30	2.32
3,3,4,4,5,5-HFCPE	1.12	1.47	-	2.24	2.94	-
R1123+R32	1.10	1.30	-	2.21	2.60	-

*SpCr–Supercritical Phase

3.2 Theory and Experimental Apparatus for Thermal Conductivity Measurement

The thermal conductivity measurement was conducted by the transient hot-wire method over a wide range of temperature and pressure. The liquid, vapor, and supercritical thermal conductivities were measured for the environmentally friendly refrigerants used as working fluids. In this method, the measuring cell was constructed using two thin ($15\mu\text{m}$ diameter) platinum wires that are vertically installed in parallel connection to minimize the effects due to axial heat conduction. In the following parts, the working principle of this procedure, a summary of the experimental apparatus, a reliability test as well as validation of the apparatus, and the measurement uncertainties are discussed.

3.2.1 Theory of the transient hot-wires (THW) method

The transient hot-wire method is a popular and precise technique to measure the thermal conductivity of liquids, solids, and gases. It is a very fast technique compared to the steady-state method. The hot wire method can be used in a variety of experimental settings. The resistance thermometer technique, the regular cross-array technique, and the parallel wires technique are the three techniques it distinguishes. In this study, the parallel wires technique is used to calculate the thermal conductivity of the working fluid. Two parallel platinum thin wires ($15\mu\text{m}$ diameter) are used vertically to construct the measurement cell for minimizing the effects due to axial heat conduction.

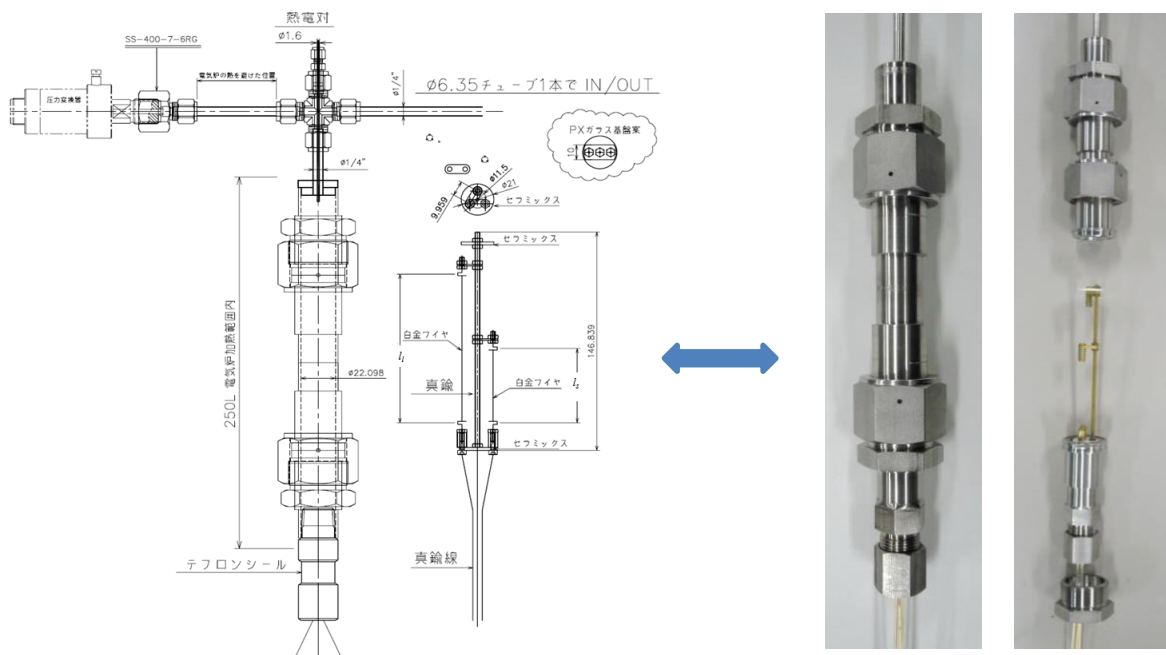


Fig. 3.2.1 The original viewpoint of the measuring cell as well as the pressure vessel of the apparatus

In our laboratory, we have developed two types of transient hot wires apparatus: (a) an electric heating system, and (b) an oil bath heating or nybrine cooling system. Figs. 3.2.1 and 3.2.2 show the original view of this apparatus, where Table 3.2.1 indicates the platinum wire dimensions.



(a)



(b)

Fig. 3.2.2 The original view of experimental apparatus to measure thermal conductivity of refrigerants (a) electric heating system (b) oil bath heating or nybrine cooling system

Table 3.2.1 Length of platinum thin wires

Type	Wire	Length (mm)
Electric (heating)	Long (l_L)	93.46
	Short (l_S)	44.89
Oil/nybrine(heating or cooling)	Long (l_L)	50.14
	Short (l_S)	19.54

The well-established THW method measures the thermal conductivity of test fluids from the temperature change caused by a linear heat source (hotwire) embedded in the tested material over a wide range of thermodynamic states in a known time interval. According to the Joule–Lenz theorem, the resistance of wire transforms electric current into heat by passing it through a linear heat source. It has been considered that producing a constant heat flux per unit length, Q as well as raising the temperature of the surrounding bed wherein all the electric current dissipated in the wire due to its resistance is converted to heat and transmitted to the testbed. Furthermore, as compared to the effects of convection and radiation, conduction plays a significant role. But, if there is present any convection effect it is difficult to get precise measurements. The main reason for making measurements difficult is the need to eliminate the effects of convection caused by the temperature gradient in the fluid in measuring the thermal conductivity of the fluid. In order to eliminate the influence of convection, it is necessary to finish the measurement before convection occurs, and it is necessary to measure in an environment where convection is unlikely to occur. For these reasons, the transient hot-wire method is becoming mainstream for measuring the thermal conductivity of liquids in recent years. The greatest feature of the transient hot-wire method is that the measurement time is short and the influence of convection can be experimentally eliminated.

The radial heat flow around the hot metallic wire (length/radius ratio >200) occurs when it is heated with constant heat flux, Q at time $t > 0$ and immersed in a homogeneous medium with uniform initial temperature. The temperature rises $\Delta T(t, r_o)$ of the heat source for stepwise heat transfer rate Q per unit length at time t in any distance r_o from the wire are expressed by Carslaw and Jaeger (1959) as

$$\Delta T(t, r_o) = \frac{Q}{4\pi\lambda} \left(\ln t + \ln \frac{4\alpha}{r_o^2 C} \right) \quad (3.2.1)$$

where λ is thermal conductivity ($\text{mW m}^{-1} \text{K}^{-1}$) and α is thermal diffusivity ($\text{m}^2 \text{s}^{-1}$), respectively, and Q is the heat flux per unit length ($\text{mW m}^{-1} \text{s}^{-1}$) with $C = \exp(\gamma)$, $\gamma = 0.5772$ is Euler's constant. The thermal conductivity λ of the test fluids at a temperature T (K) with the working pressure P (MPa) is calculated using the slope, $S = d(\Delta T)/d(\ln t)$ of the temperature rise against the logarithmic elapsed time as follows as Eq. (3.2.2), where ΔT is the experimental temperature rise.

$$\lambda = \frac{Q}{4\pi} \left/ \frac{d(\Delta T)}{d(\ln t)} \right. \quad (3.2.2)$$

The above Eq. (3.2.2) is derived by differentiating Eq. (3.2.1) with $\ln t$ and summarized as the followings;

$$\lambda = \frac{Q}{4\pi} \left(\frac{dE/dT}{dE/d \ln t} \right) \quad (3.2.3)$$

$$\text{where depending on the relation of the composition function: } \frac{dE}{d \ln t} = \frac{dE}{dT} \frac{d(\Delta T)}{d(\ln t)} \quad (3.2.4)$$

If a constant heat transfer rate per unit length, Q of the hot wire is obtained with respect to a constant time interval, Joule's law can be expressed as;

$$Q = \frac{RI^2 t}{l} = \frac{R_{L,0} + R_{S,0}}{(l_L + l_S)} \left(\frac{V_b}{R_3 + R_{L,0} + R_4 + R_{S,0}} \right)^2 \quad (3.2.5)$$

The non-equilibrium potential difference E of the bridge gives Eq. (3.2.6). Moreover, differentiating Eq. (3.2.6) with temperature, we get Eq. (3.2.7).

$$E = V_b \left(\frac{R_3 + R_L}{(R_3 + R_L) + (R_4 + R_S)} - \frac{R_1}{R_1 + R_2} \right) \quad (3.2.6)$$

$$\frac{dE}{dT} = V_b \frac{d}{dT} \left(\frac{R_3 + R_L}{(R_3 + R_L) + (R_4 + R_S)} \right) = \frac{V_b}{(R_3 + R_L) + (R_4 + R_S)} \left(\frac{dR_L}{dT} - \left(\frac{dR_L}{dT} + \frac{dR_S}{dT} \right) \frac{R_3 + R_L}{(R_3 + R_L) + (R_4 + R_S)} \right) \quad (3.2.7)$$

Therefore, considering from Eq. (3.2.3) to Eq. (3.2.6), the final form of the thermal conductivity equation is written as;

$$\lambda = \frac{R_{L,0} + R_{S,0}}{4\pi(l_L + l_S)} \left(\frac{V_b}{(R_3 + R_{L,0}) + (R_4 + R_{S,0})} \right)^2 \times \frac{V_b}{(R_3 + R_L) + (R_4 + R_S)} \left(\frac{dR_L}{dT} - \left(\frac{dR_L}{dT} + \frac{dR_S}{dT} \right) \frac{R_3 + R_L}{(R_3 + R_L) + (R_4 + R_S)} \right) \left/ \frac{dE}{d \ln t} \right. \quad (3.2.8)$$

3.2.2 Experimental apparatus for thermal conductivity measurement

The well-known transient hot-wire method is used in this work to measure the thermal conductivity of test refrigerants and this method is based on the temperature rise of vertical platinum wires when the voltage is applied to it. Fig. 3.2.3 represents the schematic illustration of the experimental apparatus which is used to measure the thermal conductivity of test fluid. The detailed explanations regarding the experimental procedures with the reliability check are reported elsewhere (Alam et al., 2018a, 2017; Kariya et al., 2017).

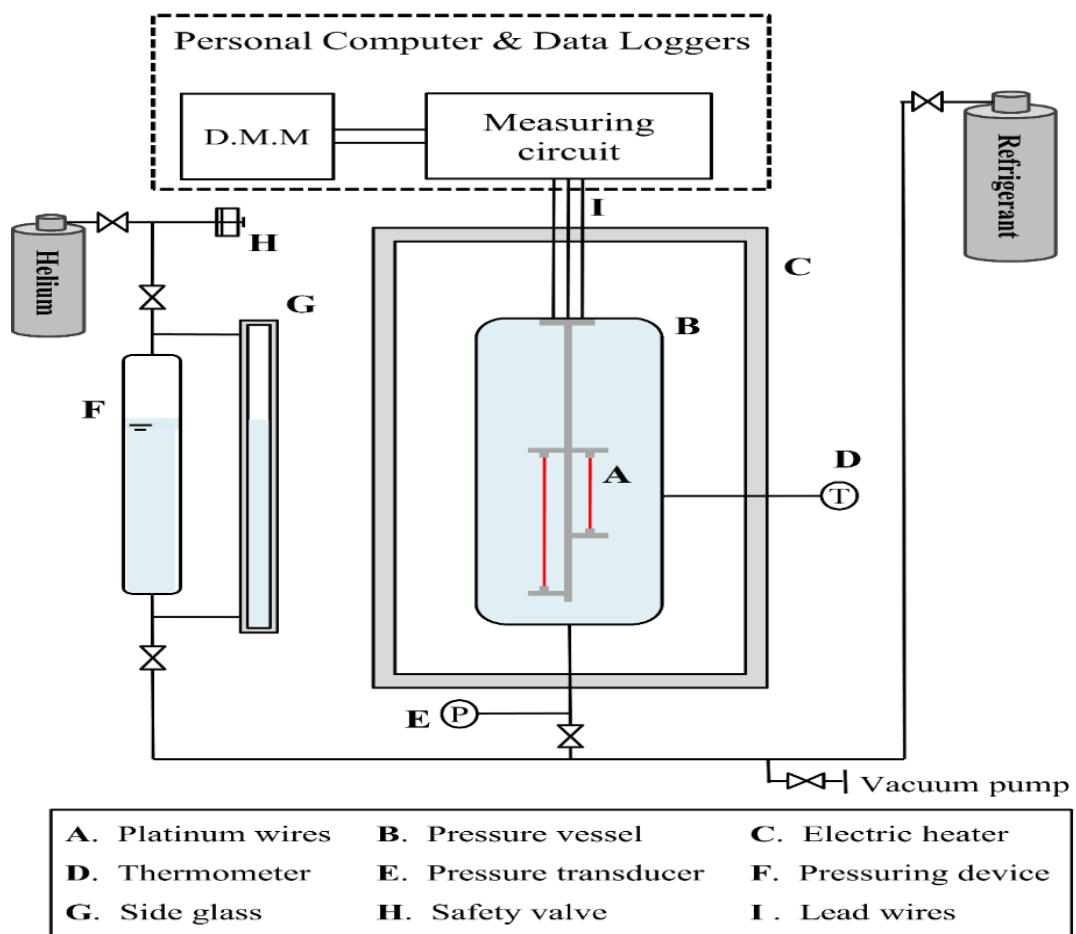


Fig. 3.2.3 Schematic illustration of the thermal conductivity measuring apparatus

In this apparatus, two platinum wires (A) are used in the measuring cell as the compensation system to get rid of the errors during the axial conduction. Two platinum wires of 15 μm diameter are placed in parallel connection inside a pressure vessel (B) act as long and short wires, respectively. The test refrigerant was charged in the pressure vessel (B) which was surrounded by an electric heater (C) and the temperature of the vessel was measured by a resistance thermometer pt100 (D) with a diameter of 3.2 mm. In order to maintain the desired

system pressure, helium gas was considered to pressurize the system through the pressurizing device (F). Moreover, the pressure of the system was obtained by a pressure transducer (E) of Model PG-100KU, KYOWA. A side glass (G) was attached with the pressuring device to ensure the liquid level into the measuring cell. A four-lead Wheatstone bridge circuit was utilized to get the temperature rise of the platinum wires. Finally, the data acquisition system, as well as its control, was coordinated by a personal computer consisting of two data loggers, one Keithley 2701 and another Agilent 34410A6.5, that would help to record the measurements of unbalanced voltage with time and also the other measurements, respectively.

3.2.3 Bridge circuit to measure the transient temperature rise

A four-lead Wheatstone bridge circuit was utilized to get the temperature rise of the platinum wires as detailed in Alam et al. (2019, 2018a, 2017). Besides, I have prepared an overview of this bridge shown in Fig. 3.2.4. Each arm of the bridge is designed to have a constant resistance of $100\ \Omega$, where R_1 and R_2 are the equal resistance of long and short wires, respectively. The long wire was placed on one arm with a composite of R_3 and a short wire on the other arm with a composite of R_4 to compensate for the end effect, respectively.

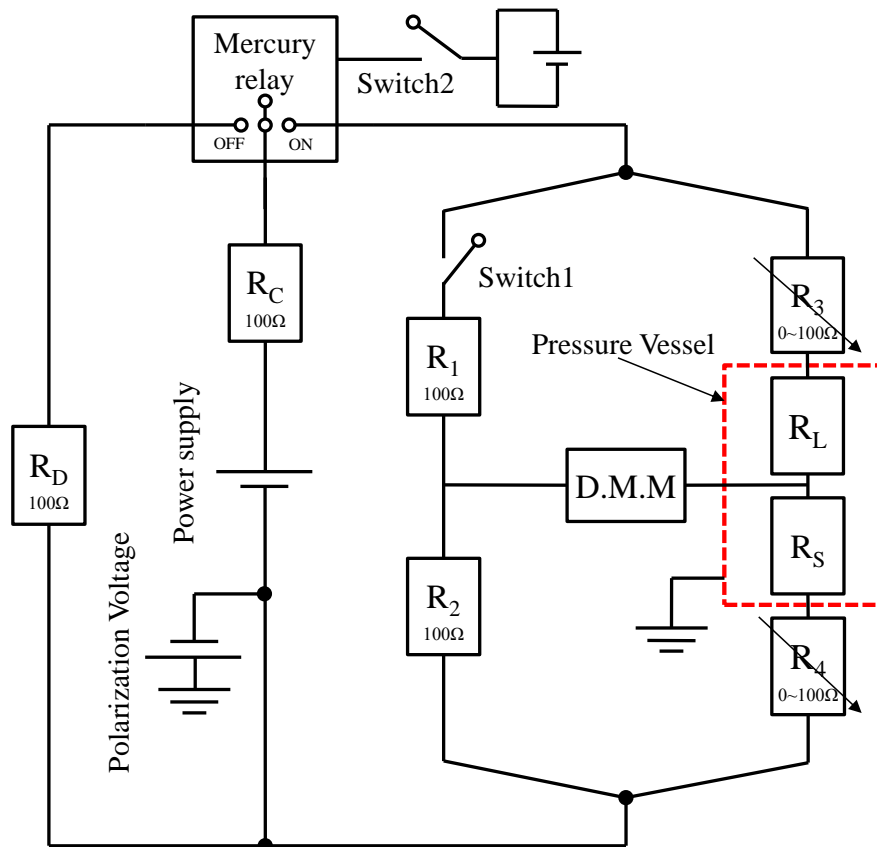


Fig. 3.2.4 A schematic diagram of the measuring bridge circuit

Before the measurement, the bridge circuit was balanced as close to null by regulating the variable resistances R_3 and R_4 as each arm has a resistance of $100\ \Omega$. A dummy circuit was used around the bridge, and hence, before supplying the power to the bridge, the mercury relay is shut off the dummy circuit and electricity passes through the dummy circuit to hold a steady and constant voltage of the power supply. Hence, a constant voltage was provided to the bridge circuit by changing the mercury relay and developed the unbalanced voltage across the bridge as a function of time that is recorded by a digital multimeter (D.M.M.) with an interval of 2.39 milliseconds for 6.0 seconds. The least-squares fitting of the data was used to calculate the slope of the temperature rise vs. time evolution on a logarithmic scale, in which it is important to locate a linear portion of the temperature rise curve.

3.2.4 Apparatus reliability and validity test for thermal conductivity measurement

The experimental results should be tested and compared with the reference fluid before the measurement of the test fluids to ensure the validity of the experimental apparatus as well as the accuracy of the measurements. R134a had been used as a reference fluid in this analysis to verify the reliability and stability of the measurements. For this purpose, the thermal conductivity data of R134a was measured from the temperature ranges of 313 to 354 K and pressure up to 4.2 MPa using this experimental setup by our research group. Fig. 3.2.5 shows the comparative study of thermal conductivity for R134a with the calculated values by REFPROP as well as reference values.

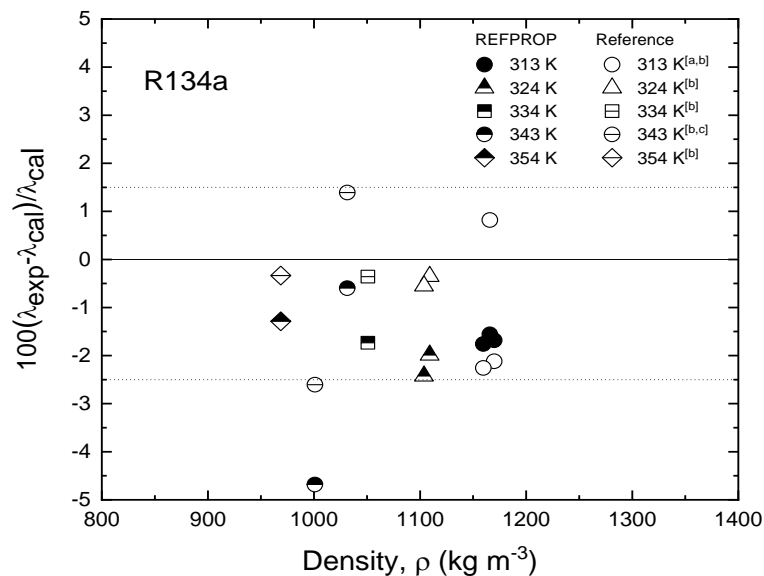


Fig. 3.2.5 Comparative study of thermal conductivity for R134a with the calculated values by REFPROP as well as reference values (^aAssael and Karagiannidis, 1993; ^bBaginsky and Shipitsyna, 2009; ^cLaesecke et al., 1992)

The maximum deviations of the experimentally measured data from the REFPROP calculated data (Lemmon et al., 2018; Perkins et al., 2000) and reference data (Assael and Karagiannidis, 1993; Baginsky and Shipitsyna, 2009; Laesecke et al., 1992) were found to be -4.7 % and -2.6 %, as well as the average absolute deviations (AAD) of 1.97 % and 1.20 %, respectively. Most of the data are agreed and accepted well within -2.5 % to +1.5 %. Using the expression of the propagation of uncertainties that may be suitable for the experimental apparatus, the uncertainty of thermal conductivity measurements of R134a was calculated at about 2.06 % (Alam et al., 2017). Such findings suggest proof of the reliability of both the measurement method and the apparatus.

Table 3.2.2 Thermal conductivity ($\text{mW m}^{-1} \text{K}^{-1}$) of R134a compared to REFPROP and reference data

T (K)	P (MPa)	λ_{exp}	λ_{cal}^*	λ_{ref}^*	$\Delta\lambda_1^{**}$	$\Delta\lambda_2^{**}$
313.37	3.61	75.84	77.04	75.23 (Baginsky and Shipitsyna, 2009)	-1.6	0.82
313.40	4.22	76.24	77.55	77.90 (Assael and Karagiannidis, 1993)	-1.7	-2.1
313.38	2.77	74.94	76.29	76.68 (Baginsky and Shipitsyna, 2009)	-1.8	-2.3
324.28	2.49	69.83	71.24	70.08 (Baginsky and Shipitsyna, 2009)	-2	-0.35
324.03	1.86	68.93	70.65	69.32 (Baginsky and Shipitsyna, 2009)	-2.4	-0.55
334.26	1.98	64.82	65.97	65.06 (Baginsky and Shipitsyna, 2009)	-1.7	-0.35
343.30	2.39	59.16	62.07	60.75 (Laesecke et al., 1992)	-4.7	-2.6
343.18	4.09	64.37	64.76	63.49 (Baginsky and Shipitsyna, 2009)	-0.6	1.4
353.57	4.19	59.31	60.08	59.51 (Baginsky and Shipitsyna, 2009)	-1.3	-0.34

Standard Uncertainties u are $u(T)=0.0237 \text{ K}$, $u(P)=0.0021 \text{ MPa}$, and Combined Standard Uncertainty $u_c(\lambda_{\text{exp}})=2.06 \%$

*calculated data from the REFPROP and references as λ_{cal} and λ_{ref}

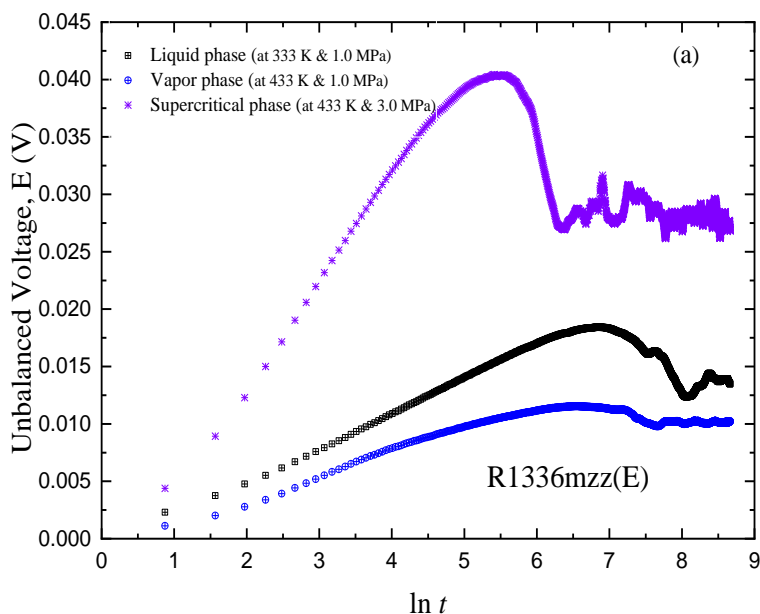
**Deviation, $\Delta\lambda_1 = 100 \times \left(\frac{\lambda_{\text{exp}} - \lambda_{\text{cal}}}{\lambda_{\text{cal}}} \right)$ **Deviation, $\Delta\lambda_2 = 100 \times \left(\frac{\lambda_{\text{exp}} - \lambda_{\text{ref}}}{\lambda_{\text{ref}}} \right)$

3.2.5 Polarization technique and typical data measurements

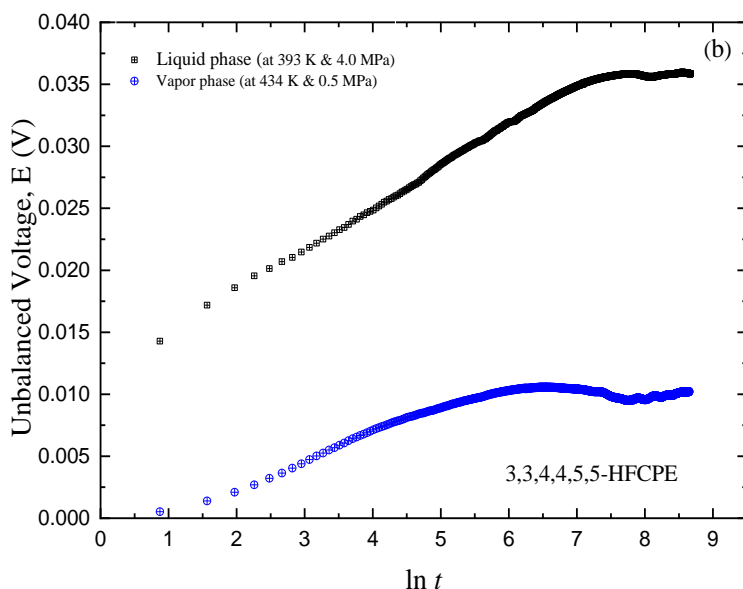
When the thermal conductivity of a polar liquid is measured using the THW method without electrical insulation, the measurement is suffered from the increase of uncertainty caused by a resistance drop between the hot wire and the cell wall. Following the polarization technique (Perkins et al., 1992), a polarization voltage was applied between the ground and power supply, as shown previously in Fig. 3.2.4.

Fig. 3.2.6 shows the examples of the variation of measured unbalanced voltage with respect to the logarithmic time. For R1336mzz(E), the unbalance voltage increases until $\ln t$ reached 5.5 to 7.0 and after that decreases due to the occurrence of convection. Again for 3,3,4,4,5,5-

HFCPE, the unbalance voltage increases until $\ln t$ reached 6.5 to 7.5 and after that decreases due to the occurrence of convection. By analysis of the data, the regression coefficient linearly $dE/d(\ln t)$ was obtained from the linear part of the data and the thermal conductivity was calculated. The present data were obtained by checking and removing the micro noise caused by the power source, electric circuit, and equipment carefully.



(a) R1336mzz(E): liquid phase (power supply: 14V, polarization voltage: 6V); vapor phase (power supply: 8V); and supercritical phase (power supply: 14V, polarization voltage: 6V)



(b) 3,3,4,4,5,5-HFCPE: liquid phase (power supply: 16V, polarization voltage: 8V); vapor phase (power supply: 8V)

Fig. 3.2.6 Variation of unbalanced voltage with logarithmic time

3.2.6 Uncertainty calculation for thermal conductivity measurement

The measurement uncertainty for thermal conductivity of the test refrigerants was estimated using the expression for the law of propagation of uncertainty by GUM (Bell, 2001; JCGM 100, 2008; Taylor and Kuyatt, 1994). In the measurement, the several input quantities such as the slope of the total resistance change with the temperature against the logarithmic time, platinum wire temperature coefficient, lengths of the platinum wires, resistances, heat input, experimental temperature, and other sources, include the measurement uncertainty. The dominant parameters for causing the uncertainty are the platinum wires temperature coefficient, heat input of the system, and the slope of total resistance change with the temperature against the logarithmic time, wherein other sources are to introduce the little uncertainty. Due to the temperature coefficient for the resistance of the platinum wire, the uncertainty was estimated at 0.0123 K^{-1} . Again, the uncertainties in the slope of total resistance changes as the variation of the temperature vs. natural logarithmic elapsed time $d\Delta T/d \ln t$ were estimated to be different for liquid, vapor, and supercritical regions, respectively. The uncertainty due to the slope fitting of a supercritical region is greater than that of vapor and liquid region because of the shorter available straight portion in the temperature rise vs. logarithmic time curve during the measurements. Similarly, the uncertainty of the vapor region is greater than the liquid region.

In general, the combined standard uncertainty $u_c(y)$ is the positive square root of the combined variance $u_c^2(y)$, generally written as Eq. (3.2.9) or (3.2.10) as follows,

$$u_c^2(y) = \left(\frac{\partial y}{\partial x_1} \right)^2 u^2(x_1) + \left(\frac{\partial y}{\partial x_2} \right)^2 u^2(x_2) + \dots \dots \dots \left(\frac{\partial y}{\partial x_N} \right)^2 u^2(x_N) \quad (3.2.9)$$

Or

$$u_c^2(y) = \sum_{i=1}^N \left[\left(\frac{\partial y(x)}{\partial x_i} \right)^2 \cdot u^2(x_i) \right] \quad (3.2.10)$$

where $u^2(x_i)$ are the variances of several input parameters x_i ; $i = 1, 2, \dots, N$. The standard uncertainty $u(x_i)$ is defined as type-A and/ or type-B, depending on whether it is random or systematic, whereas type-A means random consideration or type-B as systematic. In this measurement, the combined uncertainty for thermal conductivity measurements, based

on the transient hot-wire technique, was estimated using the above equation which is expressed as Eq. (3.2.11).

$$u_c(\lambda) = \sqrt{\left(\frac{\partial \lambda}{\partial T}\right)^2 u^2(T) + \left(\frac{\partial \lambda}{\partial (d\Delta T/d \ln t)}\right)^2 u^2(d\Delta T/d \ln t) + \left(\frac{\partial \lambda}{\partial l}\right)^2 u^2(l) + \left(\frac{\partial \lambda}{\partial R}\right)^2 u^2(R) + \left(\frac{\partial \lambda}{\partial \alpha'}\right)^2 u^2(\alpha') + \left(\frac{\partial \lambda}{\partial q_h}\right)^2 u^2(q_h)} \quad (3.2.11)$$

where R is the resistance of the platinum hot wire (Ω) and q_h is the system heat input. The expanded uncertainty $U_e(\lambda)$ for the thermal conductivity measurement was calculated from the multiplication of the combined standard uncertainty by a coverage factor k that affects the confidence as well as trust level and usually ranges from 2 to 3 (Bell, 2001; JCGM 100, 2008). In this study, the expanded uncertainty was calculated using the following Eq (3.2.12) with $k = 2$ and a 95 % confidence level.

$$U_e(\lambda) = k \cdot u_c(\lambda) \quad (3.2.12)$$

Including all parameters, the expanded uncertainties and combined standard uncertainties for the thermal conductivity measurements of the test refrigerants were calculated and summarized in Table 3.2.3. Moreover, the combined uncertainty due to the instrument is 1.38 %, excluding experimental conditions as fluctuation. The uncertainty calculation as an example for thermal conductivity measurement has detailed in section 3.0 of the appendix.

Table 3.2.3 Summary of uncertainties for thermal conductivity measurements

Test fluid	Combined Uncertainties (%)			Expanded Uncertainties (%) (k=2 and 95% Confidence Level)		
	Liquid	Vapor	SpCr*	Liquid	Vapor	SpCr*
R1336mzz(E)	1.53	1.58	1.62	3.06	3.16	3.23
3,3,4,4,5,5-HFCPE	1.54	1.76	-	3.08	3.52	-

*SpCr–Supercritical Phase

3.3 Theory for deviations in terms of AAD, MAD, and Bais

The deviations of the experimental viscosities and thermal conductivities from the predicted or calculated data using the correlations and existing models, REFPROP, and/or other research data are defined as follows:

$$\Delta \eta_i = \left(\frac{\eta_{\text{exp},i} - \eta_{\text{cal},i}}{\eta_{\text{cal},i}} \right) \times 100 \quad (3.3.1)$$

$$\Delta\lambda_i = \left(\frac{\lambda_{\text{exp},i} - \lambda_{\text{cal},i}}{\lambda_{\text{cal},i}} \right) \times 100 \quad (3.3.2)$$

where $\eta_{\text{exp},i}$ and $\lambda_{\text{exp},i}$ are the experimental viscosities and thermal conductivities, respectively. In while, $\eta_{\text{cal},i}$ and $\lambda_{\text{cal},i}$ are the calculated viscosities and thermal conductivities from any correlations and existing models, REFPROP, and/or other research data.

Again, the analysis of the deviations for viscosities and thermal conductivities in terms of the average absolute deviation (AAD %), the maximum absolute deviation (MAD %), and the average percentage deviation (Bias %) are defined as follows:

$$AAD = \frac{100}{N} \sum_{i=1}^N \left| \frac{\eta_{\text{exp},i} - \eta_{\text{cal},i}}{\eta_{\text{cal},i}} \right| \quad (3.3.3)$$

$$MAD = \max \left(100 \times \left| \frac{\eta_{\text{exp},i} - \eta_{\text{cal},i}}{\eta_{\text{cal},i}} \right| \right) \quad (3.3.4)$$

and

$$Bias = \frac{100}{N} \sum_{i=1}^N \left(\frac{\eta_{\text{exp},i} - \eta_{\text{cal},i}}{\eta_{\text{cal},i}} \right) \quad (3.3.5)$$

However, in this study, the data deviations of viscosities and thermal conductivities for eco-friendly refrigerants used as working fluids (e.g., R1336mzz(E), 3,3,4,4,5,5-HFCPE, R1132(E), and mixture (R1123+R32) are performed using the above-mentioned equation from Eq. (3.3.1) to Eq. (3.3.5).

References

- Alam, M.J., Islam, M.A., Kariya, K., Miyara, A., 2018a. Measurement of thermal conductivity and correlations at saturated state of refrigerant trans-1-chloro-3,3,3-trifluoropropene (R-1233zd(E)). *Int. J. Refrig.* 90, 174–180. <https://doi.org/10.1016/j.ijrefrig.2018.02.004>
- Alam, M.J., Islam, M.A., Kariya, K., Miyara, A., 2017. Measurement of thermal conductivity of cis-1,1,1,4,4,4-hexafluoro-2-butene (R-1336mzz(Z)) by the transient hot-wire method. *Int. J. Refrig.* 84, 220–227. <https://doi.org/10.1016/j.ijrefrig.2017.08.014>

- Alam, M.J., Miyara, A., Kariya, K., Kontomaris, K.K., 2018b. Measurement of Viscosity of cis-1,1,1,4,4,4-Hexafluoro-2-butene (R-1336mzz(Z)) by Tandem Capillary Tubes Method. *J. Chem. Eng. Data* 63, 1706–1712. <https://doi.org/10.1021/acs.jced.8b00036>
- Alam, M.J., Yamaguchi, K., Hori, Y., Kariya, K., Miyara, A., 2019. Measurement of thermal conductivity and viscosity of cis-1-chloro-2,3,3,3-tetrafluoropropene (R-1224yd(Z)). *Int. J. Refrig.* 104, 221–228. <https://doi.org/10.1016/j.ijrefrig.2019.05.033>
- Assael, M.J., Karagiannidis, E., 1993. Measurements of the Thermal Conductivity of R22, R123, and R134a in the Temperature Range 250-340 K at Pressures up to 30 MPa. *Int. J. Thermophys.* 14, 183–197.
- Baginsky, A.V., Shipitsyna, A.S., 2009. Thermal conductivity and thermal diffusivity of the R134a refrigerant in the liquid state. *Thermophys. Aeromechanics* 16, 267–273. <https://doi.org/10.1134/S0869864309020115>
- Bell, S., 2001. A Beginner's Guide to Uncertainty of Measurement, Measurement Good Practice Guide No. 11 (Issue 2), Centre for Basic, Thermal and Length Metrology, National Physical Laboratory. Teddington, Middlesex, United Kingdom, TW11 0LW.
- Carslaw, H.S., Jaeger, J.C., 1959. *Conduction of Heat in Solids*, 2nd ed. Oxford University Press, Oxford.
- Huber, M.L., Laesecke, A., Perkins, R.A., 2003. Model for the viscosity and thermal conductivity of refrigerants, including a new correlation for the viscosity of R134a. *Ind. Eng. Chem. Res.* 42, 3163–3178. <https://doi.org/10.1021/ie0300880>
- JCGM 100, 2008. Evaluation of measurement data-Guide to the expression of uncertainty in measurement, GUM 1995 with minor corrections.
- Kariya, K., Islam, M.A., Jahangir, A.M., Ishida, H., Miyara, A., 2017. Transport properties measurement on low GWP alternative refrigerants. *AIP Conf. Proc.* 1788. <https://doi.org/10.1063/1.4968251>
- Laesecke, A., Perkins, R.A., Nieto de Castro, C.A., 1992. Thermal conductivity of R134a. *Fluid Phase Equilib.* 80, 263–274. [https://doi.org/10.1016/0378-3812\(92\)87073-V](https://doi.org/10.1016/0378-3812(92)87073-V)
- Lemmon, E.W., Bell, I. H., Huber, M., L., McLinden, M.O., 2018. NIST Standard Reference

Database 23: Reference Fluid Thermodynamic Properties-REFPROP (DLL Version 10.0a), NIST, USA. NIST, USA.

- Miyara, A., Alam, M.J., Kariya, K., 2018. Measurement of viscosity of trans-1-chloro-3,3,3-trifluoropropene (R-1233zd(E)) by tandem capillary tubes method. *Int. J. Refrig.* 92, 86–93. <https://doi.org/10.1016/j.ijrefrig.2018.05.021>
- Miyara, A., Alam, M.J., Yamaguchi, K., Kariya, K., 2019. Development and Validation of Tandem Capillary Tubes Method to Measure Viscosity of Fluids. *Trans. Japan Soc. Refrig. Air Cond. Eng.* https://doi.org/10.11322/tjsrae.18-47_EM_OA
- Mondal, D., Hori, Y., Kariya, K., Miyara, A., 2019. Measurement of vapor viscosity of R1123/R32 mixture refrigerant by tandem capillary tubes method, in: *Proceedings of the 12th Asian Thermophysical Properties Conference (ATPC 2019)*. Xi'an Jiaotong University, Xi'an, China.
- Mondal, D., Hori, Y., Kariya, K., Miyara, A., Alam, M.J., 2020. Measurement of Viscosity of a Binary Mixture of R1123+R32 Refrigerant by Tandem Capillary Tube Method. *Int. J. Thermophys.* 41, 83 (1–20). <https://doi.org/10.1007/s10765-020-02653-4>
- Perkins, R.A., Laesecke, A., de Castro, C.A.N., 1992. Polarized transient hot wire thermal conductivity measurements. *Fluid Phase Equilib.* 80, 275–286. [https://doi.org/10.1016/0378-3812\(92\)87074-W](https://doi.org/10.1016/0378-3812(92)87074-W)
- Perkins, R.A., Laesecke, A., Howley, J., Ramires, M., L. V., Gurova, A.N., Cusco, L., 2000. Experimental Thermal Conductivity Values for the IUPAC Round- Robin Sample of 1, 1, 1, 2-Tetrafluoroethane (R134a). NISTIR 6605, National Institute of Standards and Technology, Boulder, Colorado 80305-3328. <https://doi.org/10.6028/NIST.IR.6605>
- Taylor, B.N., Kuyatt, C.E., 1994. Guidelines for Evaluating and Expressing the Uncertainty of NIST Measurement Results, NIST Technical Note 1297, National Institute for Standards and Technology (NIST).
- Viswanath, D.S., Ghosh, T.K., Prasad, D.H.L., Dutt, N.V.K., Rani, K.Y., 2007. *Viscosity of Liquids: Theory, Estimation, Experiment, and Data*, Springer Editions, Dordrecht, Netherlands.

Chapter 4

Experimental Measurement and Results

This chapter describes the experimental measurement and results, and comparison of the measured data with the estimated data for transport properties of low-GWP refrigerants. The measured viscosities by the method tandem capillary tubes and thermal conductivities by the transient hot-wire method are recorded sequentially with estimating the measurement uncertainties. The experimental data are correlated with the other researchers and the simplified correlations at saturation conditions are developed. The test fluids collection, the experimental viscosity measurement, and the experimental thermal conductivity measurement are discussed in the following sections.

4.1 Test Fluids

The Chemours Company, located in the USA, provided the sample fluid of R1336mzz(E). The sample's designated purity was 99.99% in mass fraction based on the analysis by the supplier. The Chemical Abstracts Service Registration Number (CASRN) number of the sample fluid is 66711-86-2. Another test fluid 3,3,4,4,5,5-HFCPE was supplied by the National Institute of Advanced Industrial Science and Technology (AIST), Japan with the purity of >99.9 % mass fraction by supplier's analysis. The CASR of 3,3,4,4,5,5-HFCPE is 1005-73-8. Again, the other test fluid R1132(E) was provided by Daikin Industries, LTD., Japan. The CASR of R1132(E) is 1630-78-0. The designated purity of this sample is 99.9 % or more in mass fraction based on the analysis by the supplier, which is the same sample of Akasaka et al. (2020). The impurity contained with HFO1132 (E) is 0.002% acetylene. Another test fluid mixture of R1123+R32 was supplied by AGC Inc., Japan. The indicated composition of R1123 and R32 are 40% and 60% in mass fraction by supplier's analysis, which is the same sample of Higashi and Akasaka (2016) and Fukushima and Hashimoto (2016). Moreover, the reference refrigerant R134a is used with more than 99.5% purity supplied by Chemours-Mitsui Fluoroproducts Co. Ltd. The CASR of the reference fluid of R134a is 811-97-2. However, the test fluids supplied by various

companies at the indicated purity by mole fraction are listed in Table 4.1.1, where Fig. 4.1.1 shows the pressure vs. temperature curve for these refrigerants. Moreover, these test fluids were used to investigate the measurements without any examination for further purification.

Table 4.1.1 Sample information

(a) Pure test fluids			
Sample	CASRN	Purity (%)	Supplier/ Manufacturer
R1336mzz(E)	66711-86-2	99.99	Chemours Company, USA
3,3,4,4,5,5-HFCPE	1005-73-8	>99.9	National Institute of Advanced Industrial Science and Technology (AIST), Japan
R1132(E)	1630-78-0	99.9	Daikin Industries, LTD., Japan
R134a	811-97-2	99.50	Chemours-Mitsui Fluoroproducts Co. Ltd.
(b) Mixture test fluids			
Sample	CASRN	Mass fraction (%)	Supplier/ Manufacturer
R1123	359-11-5	40	AGC Inc., Japan
R32	75-10-5	60	AGC Inc., Japan
R1123+R32		100	AGC Inc., Japan

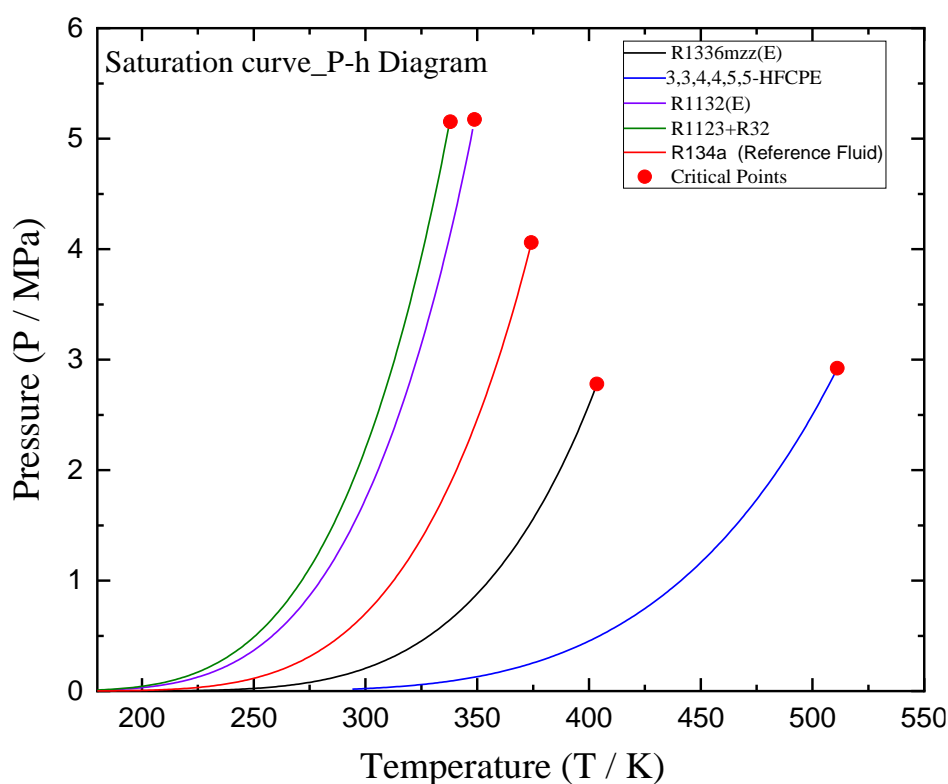


Fig. 4.1.1 Pressure vs. temperature curve of test fluids used to investigate the measurements

4.2 Experimental Viscosity Measurement

The viscosity measurements were conducted by the method of the tandem capillary tubes, where the measurement cell known as viscometer was constructed using almost the same diameter but different lengths of two capillary tubes. These tubes are installed horizontally to the measurement cell by the connection in series for eliminating the end effects of capillary tubes. The viscosities were measured over a wide range of temperature and pressure for the working fluids R1336mzz(E), 3,3,4,4,5,5-HFCPE, R1132(E), and a mixture of R1123+R32. The experimental viscosity data with measurement uncertainties, comparison with other research data or existing model or REFPROP, and saturation correlations to predict the saturated viscosities are discussed in the following sections.

4.2.1 Viscosity measurement of R1336mzz(E)

4.2.1.1 Overview of R1336mzz(E)

As one of the hydrofluoroolefins, trans-1,1,1,4,4,4-hexafluoro-2-butene (R1336mzz(E)) is treated as a novel working substance for the organic Rankine cycles and the heat pumps, the main targets of this study are to measure the viscosity of this refrigerant in liquid, vapor, and supercritical regions by the method of tandem capillary tubes and to develop the simplified correlations for estimating the saturated liquid and vapor viscosities. The environmental concern regarding the high global warming potential (GWP) of conventional working fluids has accelerated the interests of researchers to search the alternatives with suitable properties in the context of environmental issues. With the awareness of the environmental issues, the reduction of greenhouse gas emissions in accordance with the Kyoto Protocol is more familiarized to meet the new outcomes of next-generation refrigerants. Transport properties are important particularly for refrigerants in modern technology of refrigeration, air conditioning, and heat pumps. Recently, promising alternatives such as hydrofluoroolefins (HFOs) as well as hydrochlorofluoroolefins (HCFOs) have been the key focus due to the zero or very low ozone-depleting potential (ODP) and lower GWP. The HFO refrigerant trans-1,1,1,4,4,4-hexafluoro-2-butene (R1336mzz(E)) is expected as a probable working fluid for organic Rankine cycles (ORCs) as well as for high-temperature heat pumps (HTHPs). It will be a replacement for R245fa as a working fluid applicable to both ORCs and HTHPs platforms for the heat recovery approach from different sources (Juhasz, 2017; Tanaka et al., 2017b). It has a zero ODP and GWP of 18 (Juhasz, 2017) for a time horizon of 100 years. It is indicated as a

working fluid by the safety classification of A1 (Yang et al., 2019) in the ASHRAE Standard 34, due to its low toxicity, non-flammability, and high thermal stability.

Fig. 4.2.1.1 shows the molecular structure of R1336mzz(E), and the fundamental information is summarized in Table 4.2.1.1. The critical density, pressure, and temperature of this refrigerant were measured by Sakoda et al. (2021); they are 513.33 kg m^{-3} , 2.779 MPa, and 403.53 K respectively. The boiling point temperature of this refrigerant is 280.58 K (Tanaka et al., 2017b), which could be suitable for the ORCs, HTHPs, and chiller applications. The fundamental information indicates strong evidence for the negligible environmental impact of R1336mzz(E).

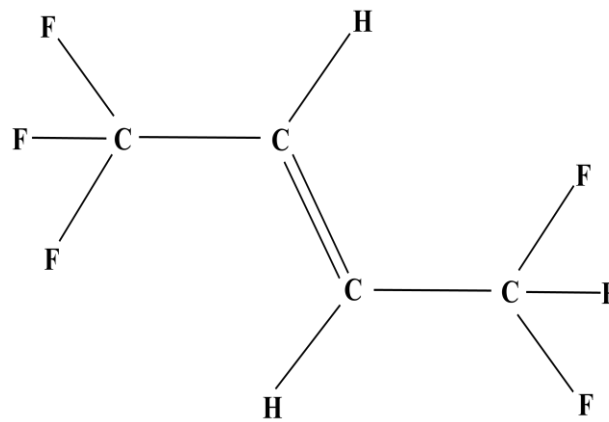


Fig. 4.2.1.1 Molecular structures of R1336mzz(E)

Table 4.2.1.1 Fundamental information of R1336mzz(E)

Parameters	R1336mzz(E)	Reference
Chemical formula	Trans $\text{CF}_3\text{-CH=CH-CF}_3$	
CASRN	66711-86-2	
Critical temperature (K)	403.53	Sakoda et al. (2021)
Critical pressure (MPa)	2.779	Sakoda et al. (2021)
Critical density (kg m^{-3})	513.33	Sakoda et al. (2021)
Molecular weight (g mol^{-1})	164.05	Tanaka et al. (2017b)
Flammability limits	Non-flammable	
Boiling point (K)	280.58	Tanaka et al. (2017b)
ODP	0	
GWP (100 year)	18	Juhasz (2017)

The thermophysical properties are key tools to design and implement efficient energy systems. A few of the thermodynamic properties of R1336mzz(E) are currently published in the open literature. Sakoda et al. (2021) and Tanaka et al. (2017b, 2017c) measured the $P\rho T$ properties, critical parameters, vapor pressures of this refrigerant. Based on these measurements a Helmholtz energy equation of state (EoS) was developed by Akasaka (2019a, 2019b) for this refrigerant. The experimentally measured viscosity data of R1336mzz(E) are still not available in the literature. Recently, some of the viscosity data of this refrigerant were measured and the thermal conductivity data of this refrigerant were measured and published by our research group (Amakusa et al., 2021; Miyoshi et al., 2020; Mondal et al., 2021a; Tuhin et al., 2021).

In this part of the work, the viscosity of R1336mzz(E) was measured by the method of the tandem capillary tubes up to pressure up to 4.0 MPa over the temperatures from 314 to 394 K for liquid, 353 to 453 K for vapor, and 413 to 453 K at the supercritical phases, respectively. In addition, simple correlations were developed by the extrapolation method from the experimental data up to the liquid-vapor saturation conditions to get the saturated liquid and vapor viscosity.

4.2.1.2 Measured viscosities of R1336mzz(E)

The viscosity measurement of R1336mzz(E) was conducted by the method of tandem capillary tubes for a wide range of pressures and temperatures. Fig. 4.2.1.2 shows the measurement conditions on a P - T diagram. Akasaka (2019a, 2019b) developed a preliminary Helmholtz energy EoS, which was used to draw the liquid-vapor saturation line. For reproducibility, the measurement was repeated three times for a given temperature and pressure (Yao et al., 2014). Differences in three repeatable tests are within ± 0.6 %. Half-hour interval was made at least, between two successive measurements, where the pressure and temperature changed slightly.

The viscosity measurement was made at temperatures from 314 to 394 K and pressures from 1.0 to 4.0 MPa for the liquid phase, and at temperatures from 353 to 453 K and pressures up to 2.0 MPa for the vapor phase. The supercritical viscosity was measured at temperatures from 413 to 453 K and pressures from 3.0 to 4.0 MPa. Tables 4.2.1.2, 4.2.1.3, and 4.2.1.4 summarize all experimental data for the liquid, vapor, and supercritical regions. The estimated expanded uncertainties in the viscosity measurements are presented at the bottom of the tables with the pressure and temperature uncertainties.

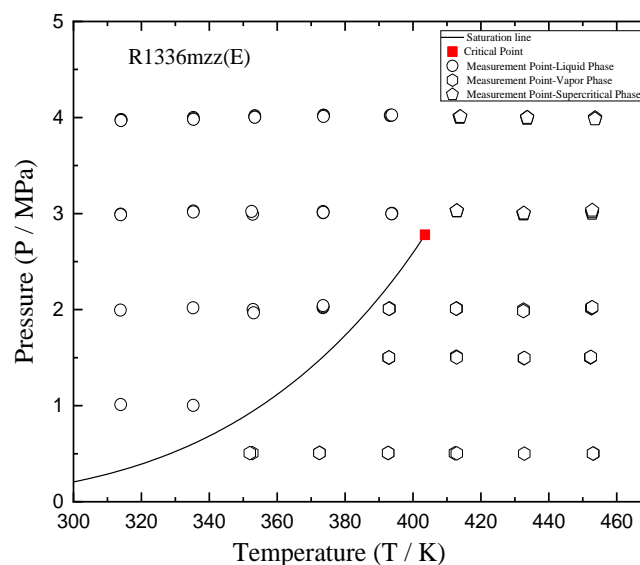


Fig. 4.2.1.2 Distribution of the measurements for the viscosity of R1336mzz(E)

Table 4.2.1.2 Experimental data for the liquid viscosity, η ($\mu\text{Pa s}$) of R1336mzz(E)

T (K)	P (MPa)	η ($\mu\text{Pa s}$)	T (K)	P (MPa)	η ($\mu\text{Pa s}$)
314.03	3.979	251.26	352.47	3.023	157.30
314.03	3.975	251.37	352.93	1.992	152.64
314.00	3.969	251.20	352.92	2.000	152.12
313.90	2.993	249.58	353.07	1.967	152.57
313.90	2.988	249.29	373.66	4.023	124.55
313.84	1.995	245.58	373.66	4.021	123.83
313.90	1.012	242.93	373.64	4.011	124.68
335.33	4.000	199.47	373.52	3.009	116.26
335.32	3.987	199.58	373.54	3.021	116.27
335.33	3.981	198.03	373.57	3.012	117.44
335.29	3.026	190.70	373.49	2.020	111.03
335.30	3.017	190.03	373.56	2.029	110.65
335.24	2.019	185.32	373.54	2.041	112.20
335.25	2.018	185.03	393.29	4.021	92.23
335.28	1.003	184.77	393.45	4.022	91.47
353.41	4.018	160.66	393.75	4.025	92.07
353.43	4.006	160.83	393.79	3.002	79.14
353.39	4.003	160.67	393.75	2.998	78.89
352.77	2.993	157.12	393.72	2.999	79.55

Standard uncertainties due to pressure and temperature are $u(P) = 0.0037$ MPa and $u(T) = 0.020$ K

Combined standard uncertainty $u_c(\eta) = 1.13$ %; Expanded uncertainty $U_c(\eta) = 2.26$ % with $k=2$ and 95 % confidence level

Table 4.2.1.3 Experimental data for the vapor viscosity, η ($\mu\text{Pa s}$) of R1336mzz(E)

T (K)	P (MPa)	η ($\mu\text{Pa s}$)	T (K)	P (MPa)	η ($\mu\text{Pa s}$)
352.68	0.506	10.78	412.82	2.012	15.79
351.93	0.506	11.04	412.80	2.011	15.68
372.47	0.509	12.05	412.73	2.010	15.68
372.46	0.508	12.08	432.79	0.501	14.80
392.71	0.508	12.27	432.69	1.494	15.96
392.71	0.508	12.15	432.80	1.497	16.21
392.69	0.508	12.47	432.62	1.992	16.21
392.89	1.502	14.96	432.55	2.001	16.36
392.90	1.501	14.95	432.52	1.985	15.97
392.91	1.503	14.94	453.13	0.502	15.07
393.06	2.014	15.76	453.01	0.502	14.97
393.00	2.008	15.53	453.02	0.502	14.99
392.96	2.009	15.78	452.30	1.505	16.01
412.36	0.506	13.87	452.23	1.503	15.86
412.89	0.503	14.44	452.35	1.508	15.97
412.77	1.511	14.74	452.55	2.013	16.08
412.85	1.503	14.89	452.65	2.023	16.20
412.86	1.503	14.73	452.78	2.025	16.23

Standard uncertainties due to pressure and temperature are $u(P) = 0.0027$ MPa and $u(T) = 0.026$ K

Combined standard uncertainty $u_c(\eta) = 1.15$ %; Expanded uncertainty $U_c(\eta) = 2.30$ % with $k=2$ and 95 % confidence level

Table 4.2.1.4 Experimental data for the supercritical viscosity, η ($\mu\text{Pa s}$) of R1336mzz(E)

T (K)	P (MPa)	η ($\mu\text{Pa s}$)	T (K)	P (MPa)	η ($\mu\text{Pa s}$)
413.78	3.999	53.66	432.55	2.994	18.16
413.76	4.007	52.61	432.57	3.000	18.34
413.97	4.008	53.35	432.65	3.004	18.38
412.90	3.026	21.95	453.69	3.992	21.41
412.91	3.028	21.72	453.61	3.997	21.66
412.92	3.029	21.96	453.61	3.985	21.49
433.62	4.001	25.72	452.76	3.001	18.22
433.62	3.990	25.61	452.73	3.017	18.13
433.65	3.998	25.59	452.78	3.033	18.10

Standard uncertainties due to pressure and temperature are $u(P) = 0.0043$ MPa and $u(T) = 0.021$ K

Combined standard uncertainty $u_c(\eta) = 1.16$ %; Expanded uncertainty $U_c(\eta) = 2.32$ % with $k=2$ and 95 % confidence level

Fig. 4.2.1.3 shows a plot of the liquid viscosity data on a η - ρ diagram. The experimental viscosity measurement for R1336mzz(E) was performed covering a temperature range from 314 to 394 K and pressure from 1.0 to 4.0 MPa. The liquid viscosities range from 79.6 to 251.3 $\mu\text{Pa s}$. The viscosities increase with increasing pressure at constant temperature and decrease with increasing temperature at constant pressure. The viscosities also increase exponentially with increasing density. The liquid viscosity data were correlated with the ECS model coupled with the EoS (Akasaka, 2019a, 2019b). The ECS model indicates a similar trend but relatively higher deviations over experimental uncertainties at lower temperatures than higher temperatures for all corresponding pressure. The expanded uncertainty is calculated to 2.26 % with $k=2$ and 95 % confidence level.

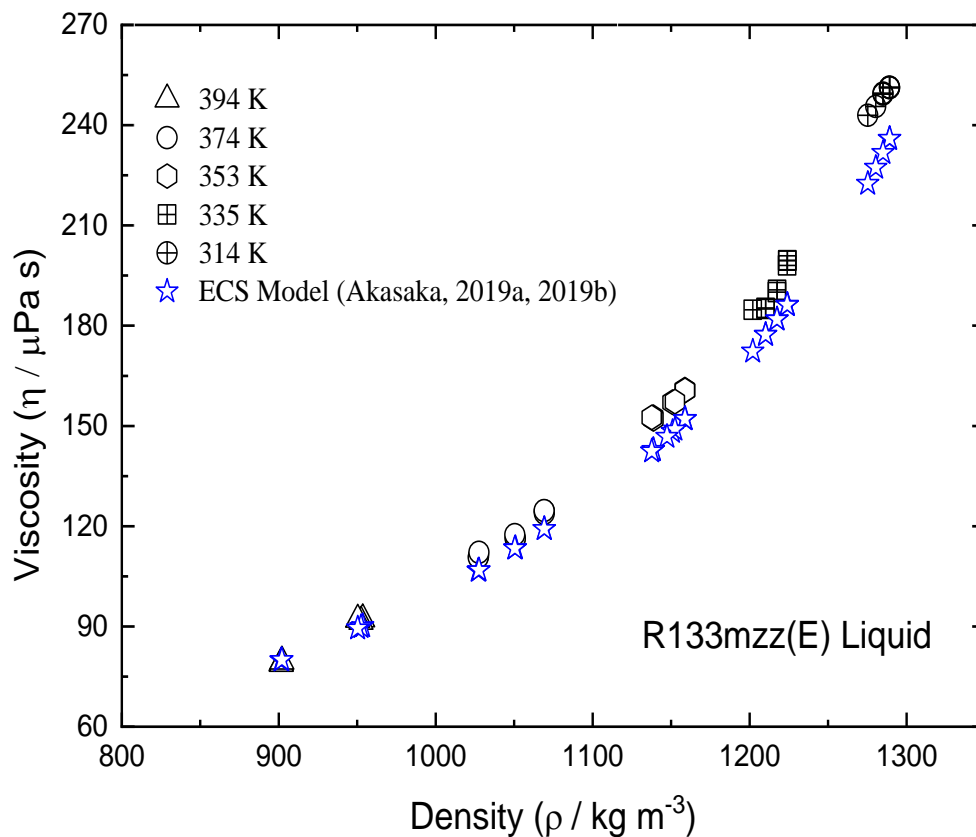


Fig. 4.2.1.3 Variation of the liquid viscosity of R1336mzz(E) with density

Fig. 4.2.1.4 plots the viscosities of the vapor phase versus density at different pressures and temperatures. The vapor viscosity data of this refrigerant was measured over temperatures ranging from 353 to 453 K whereas pressure varies from 0.5 to 2.0 MPa. The vapor viscosities become higher with increasing pressure at constant temperature and also become higher with increasing temperature at constant pressure; this is an opposite trend to the liquid viscosities.

The vapor viscosities of R1336mzz(E) were measured from 10.8 to 16.2 $\mu\text{Pa s}$, and they are more scattered than the liquid phase data owing to less consistent flow rate as well as differential pressures in Pyrex capillary tubes. At 0.5 MPa, the viscosities are most scattered comparable to those at other pressures.

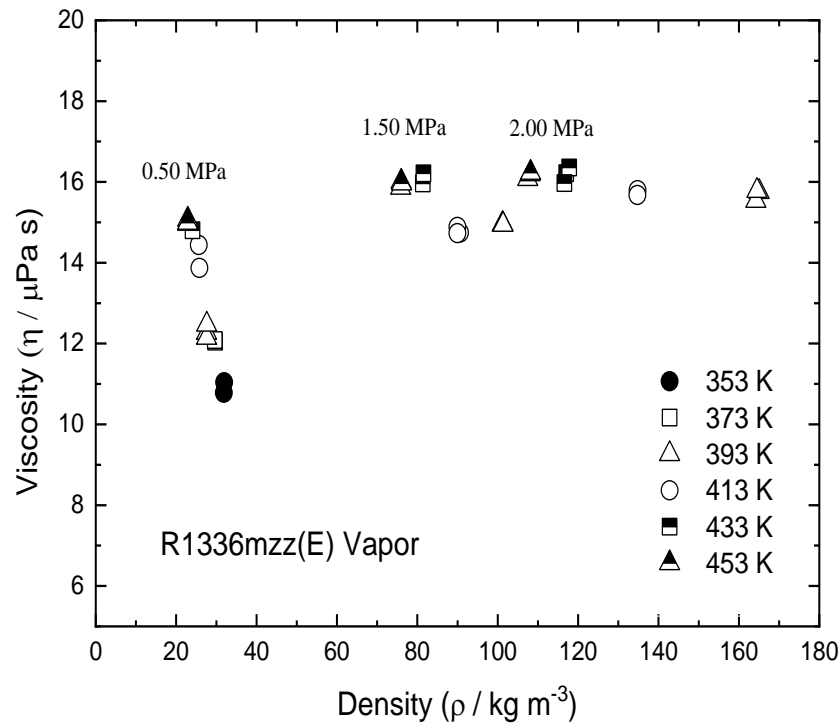


Fig. 4.2.1.4 Variation of the vapor viscosity of R1336mzz(E) with density

Fig. 4.2.1.5 represents the viscosities of R1336mzz(E) in the supercritical region. The viscosity data in the supercritical region were located at temperatures from 413 to 453 K and pressures from 3.0 to 4.0 MPa. For all corresponding temperatures, the viscosities were significantly increased with increasing pressure and density. In the supercritical region, there are exist three sub-regions named liquid-like supercritical, pseudocritical, and vapor-like supercritical, respectively (Imre et al., 2015; Saravi and Tassou, 2019). The experimental data at 414 K and 4.0 MPa show the behavior as the liquid-like supercritical, and therefore, this point data is considerably higher than the other points that indicate the data as the trend of the liquid phase.

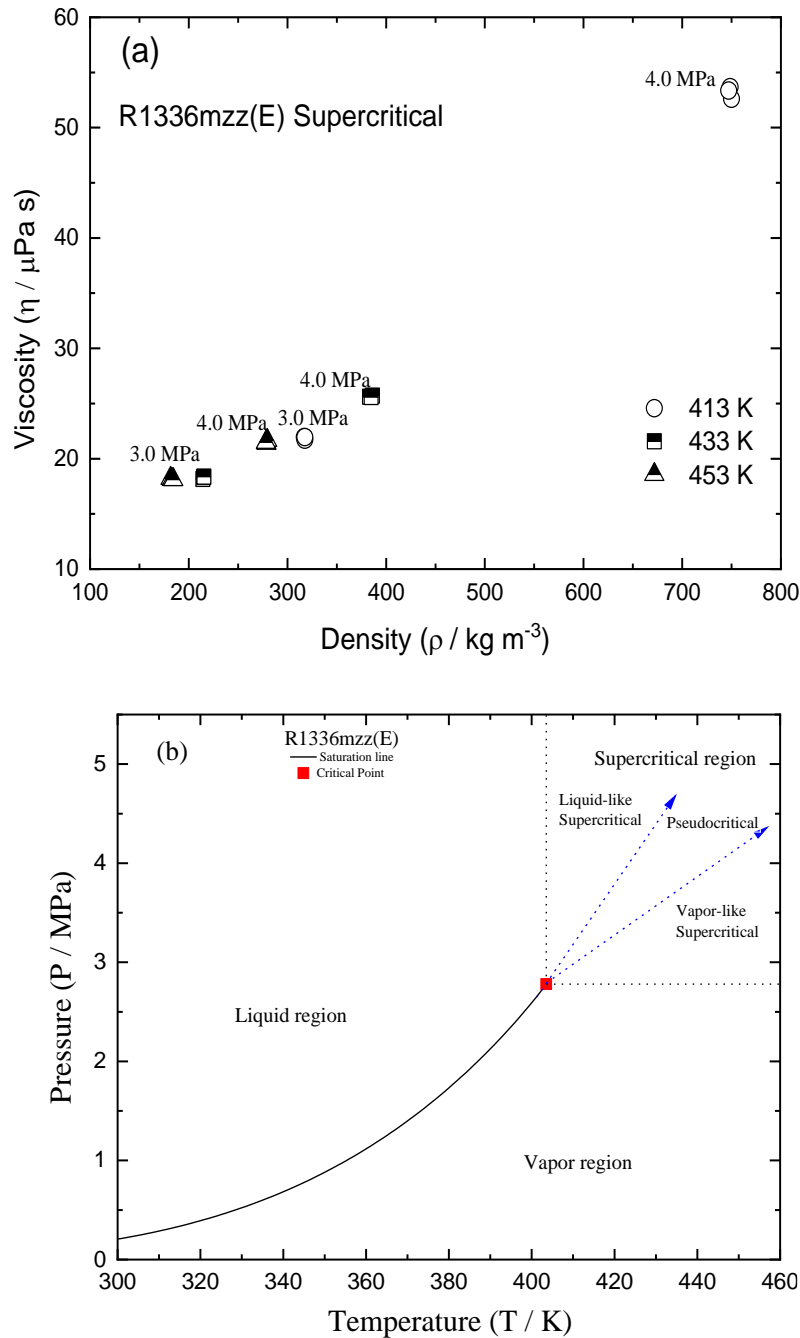


Fig. 4.2.1.5 (a) Variation of the viscosity of supercritical R1336mzz(E) with density, and (b) P-T diagram with defined sub-regions of supercritical phase: liquid-like, pseudocritical, and vapor-like.

Figs. 4.2.1.6 and 4.2.1.7 demonstrate all experimental viscosity data of R1336mzz(E) for the liquid, vapor, and supercritical phases with the temperature ranging from 314 to 453 K over the pressure up to 4.0 MPa. The vapor phase data are scattered to a great extent than the liquid phase owing to the less consistent differential pressure and flow rates through the pyrex capillary tubes. Therefore, the measured supercritical data are somewhat scattered significantly

among them than that of measured data for liquid and vapor due to the above critical conditions as well as relatively high temperature, pressure. The expanded uncertainty of the supercritical phase was estimated at 2.32 % which is greater than the liquid and vapor phase.

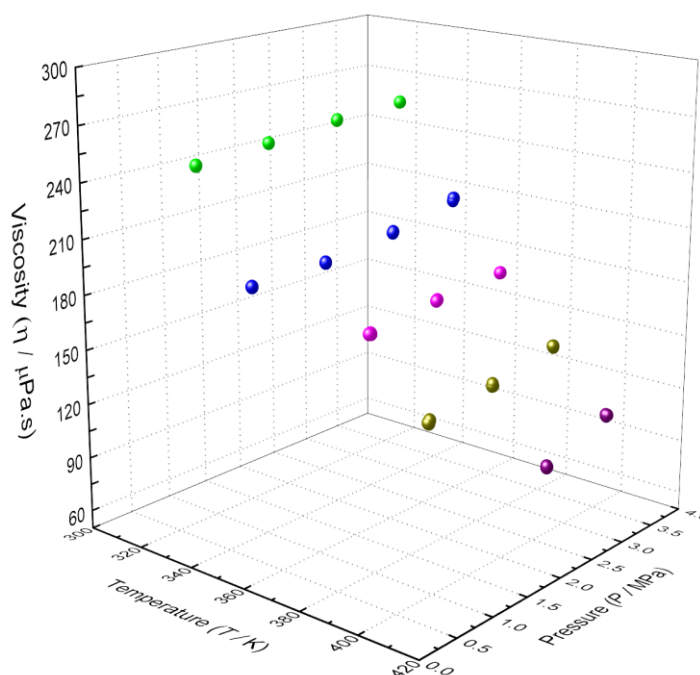
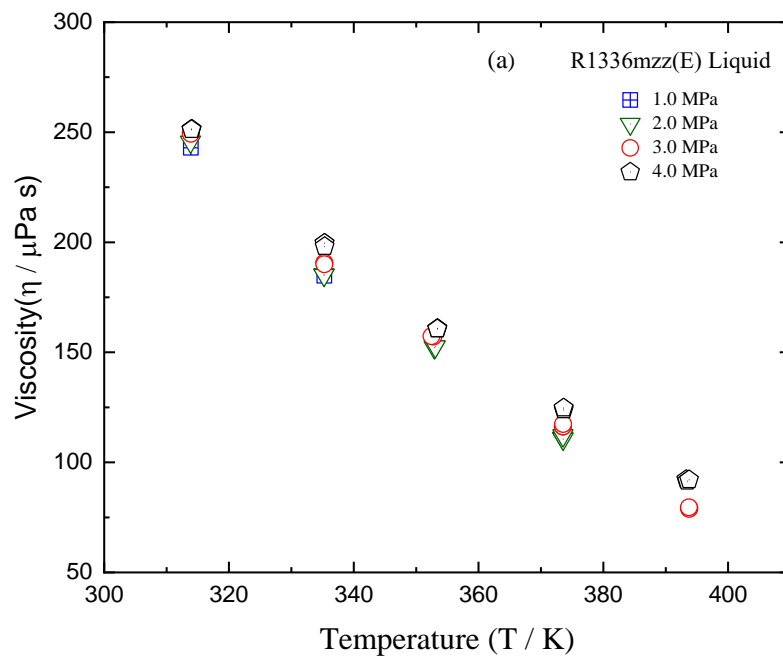


Fig. 4.2.1.6 Variation of liquid viscosities of R1336mzz(E) with temperature and pressure

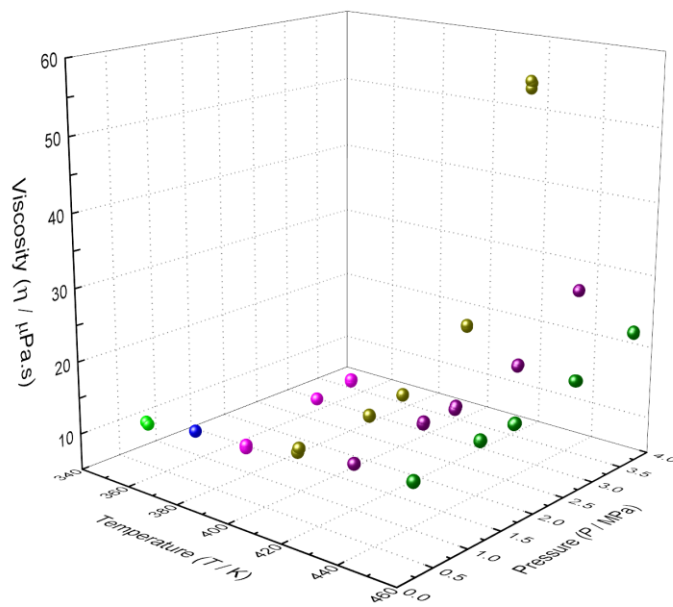
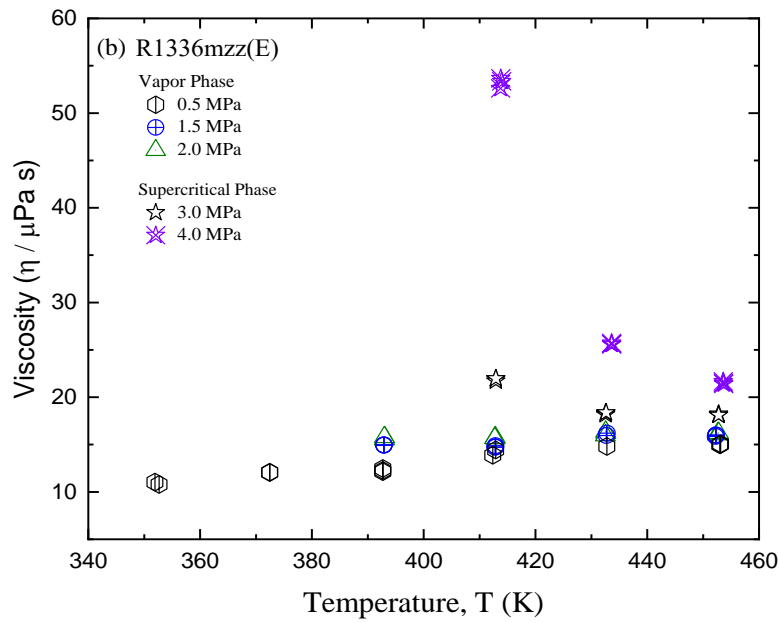


Fig. 4.2.1.7 Variation of vapor and supercritical viscosities of R1336mzz(E) with temperature and pressure

Fig. 4.2.1.8 shows the comparison of viscosity data of R1336mzz(E) with other green refrigerants. The measured viscosity data of liquid R1336mzz(E) were compared with R1336mzz(Z) (Alam et al., 2018), R1233zd(E) (Miyara et al., 2018a), and R1234ze(Z) (Alam et al., 2021). It is observed that the viscosities of liquid R1336mzz(E) are lower than that of R1336mzz(Z) and R1233zd(E) in a similar temperature region. Again in comparison with

R1234ze(Z), the viscosities of R1336mzz(E) are a little higher in the same temperature region and the difference decreases with the increase of temperature.

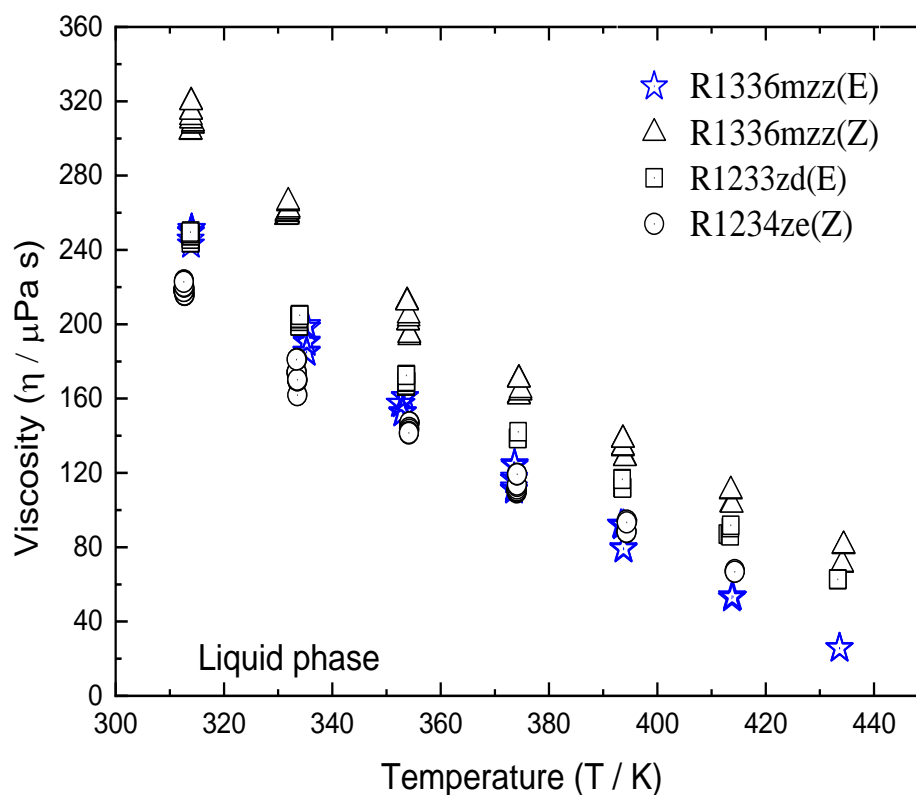


Fig. 4.2.1.8. Comparison of viscosity data of liquid R1336mzz(E) with other green refrigerants: R1336mzz(Z) (Alam et al., 2018), R1233zd(E) (Miyara et al., 2018a), and R1234ze(Z) (Alam et al., 2021).

4.2.1.3 Data deviations of R1336mzz(E)

Figs. 4.2.1.9 and 4.2.1.10 show the deviations in experimental liquid, vapor, and supercritical viscosities from the estimated values by the ECS model. In the liquid phase shown in Fig. 4.2.1.9, the measured data agreed well in the range from -1.5% to $+8.5\%$ deviations. The deviations become larger with the decrease in temperature. At 313.9 K, the maximum deviation (9.19 %) is observed. In the vapor and supercritical phases shown in Fig. 4.2.1.10, the measured data agreed well the deviations range from -8.5% to -17.5% . The measurements appear to show systematic negative deviation that reaches down to -22.68% at temperature 352.7 K for the vapor phase, and down to -17.2% at temperature 452.8 K for the supercritical phase.

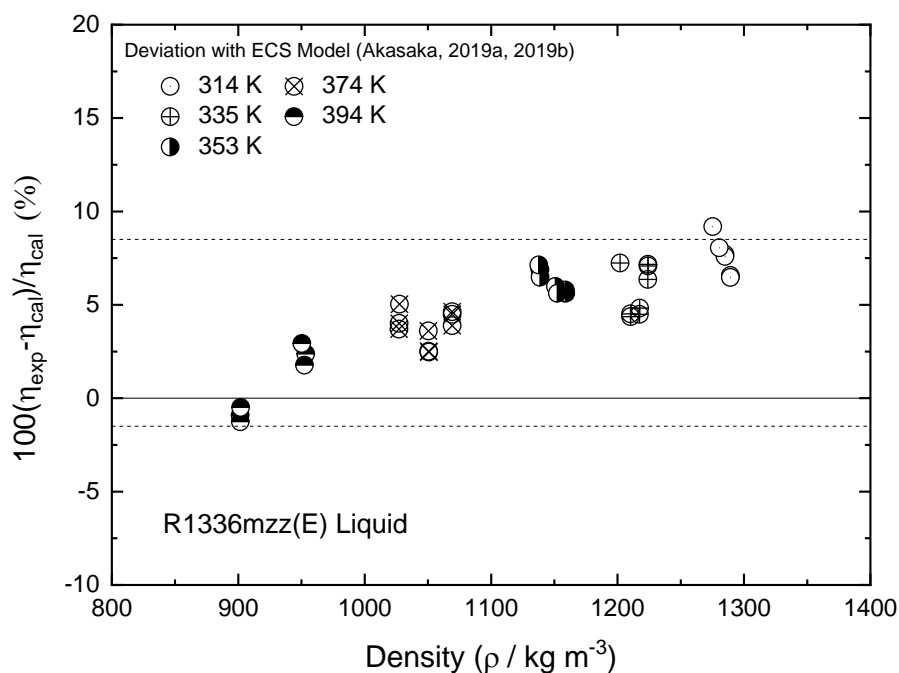


Fig. 4.2.1.9 Comparison of the experimental viscosity data in the liquid phase with predicted values by the ECS model

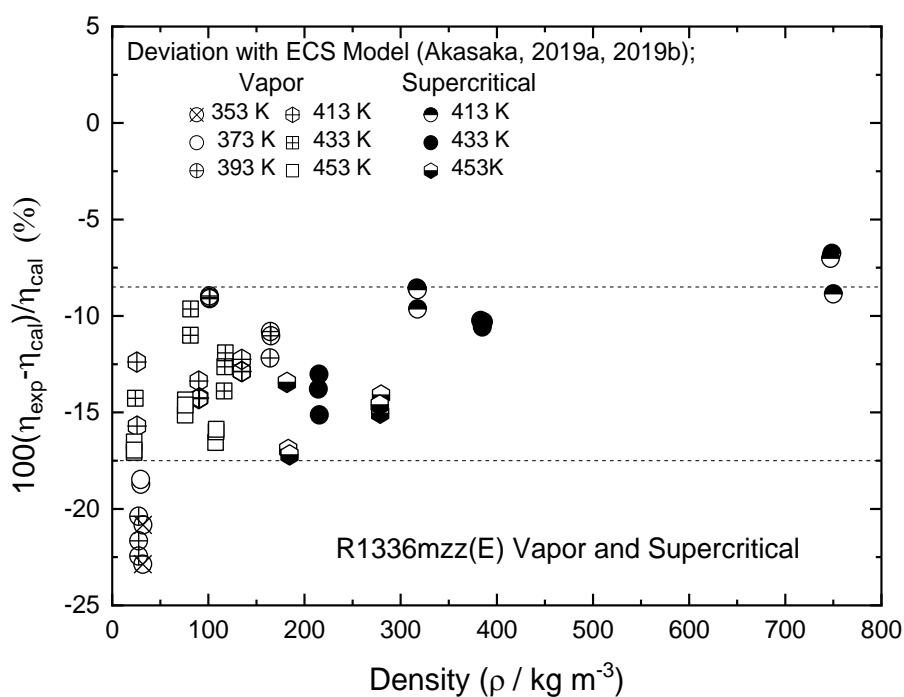


Fig. 4.2.1.10 Comparison of the experimental viscosity data in the vapor and supercritical regions with predicted values by the ECS model

Deviations $\Delta\eta_i$ in viscosity data are calculated from predicted values by the ECS model coupled with the EoS (Akasaka, 2019a, 2019b). The average absolute deviation in the

measurements is 5.04 % for the liquid phase, while for the vapor and supercritical phases; they are 14.75 % and 11.88 %, respectively. The analyses of viscosity deviations are summarized in Table 4.2.1.5, where the average absolute deviation (AAD %), maximum absolute deviation (MAD %), and average percentage deviation (Bias %) are shown as follows:

Table 4.2.1.5 Statistical analyses of the viscosity deviations in terms of AAD, MAD, and Bias

Phases	Parameters	ECS Model*
Liquid	AAD (%)	5.04
	MAD (%)	9.19
	Bias (%)	4.89
Vapor	AAD (%)	14.75
	MAD (%)	22.86
	Bias (%)	-14.75
Supercritical	AAD (%)	11.88
	MAD (%)	17.20
	Bias (%)	-11.88

*Calculated with the help of ECS model coupled with the EoS developed by Akasaka (2019a, 2019b)

4.2.1.4 Correlations for the saturated viscosity of R1336mzz(E)

The extrapolating approach is used to establish correlations to predict the saturated viscosity of R1336mzz(E), which can be used for the design and simulation of the energy system. The preliminary Helmholtz energy equation of state (EoS) developed by Akasaka (2019a, 2019b) for this refrigerant was used to calculate the properties at saturation conditions. For the liquid phase, Fig. 4.2.1.11 shows the extrapolation to the saturated liquid viscosity of R1336mzz(E) from the measured data along isothermals. Only at 387.20 K, the saturated values were extrapolated along an isobar. A correlation for the saturated liquid viscosity, $\eta_{sat,L}$, was then determined by the linear fitting of the extrapolated data in terms of the saturation temperature, as Eq. (4.2.1.1). A similar manner was applied to the saturated vapor viscosities, and a correlation for the saturated vapor viscosity of R1336mzz(E), $\eta_{sat,V}$, was developed as Eq. (4.2.1.2). Figure 4.2.1.12 shows the extrapolated data and calculated values by linear fitting given by Eqs. (4.2.1.1) and (4.2.1.2) both for the saturated liquid and vapor. Table 4.2.1.6 summarizes numerical values for extrapolated data and calculated values for the liquid and vapor viscosities at saturation conditions.

$$\eta_{sat,L} = -2.091T_{sat} + 889.34 \quad (4.2.1.1)$$

$$\eta_{sat,V} = 0.0981T_{sat} - 22.25 \quad (4.2.1.2)$$

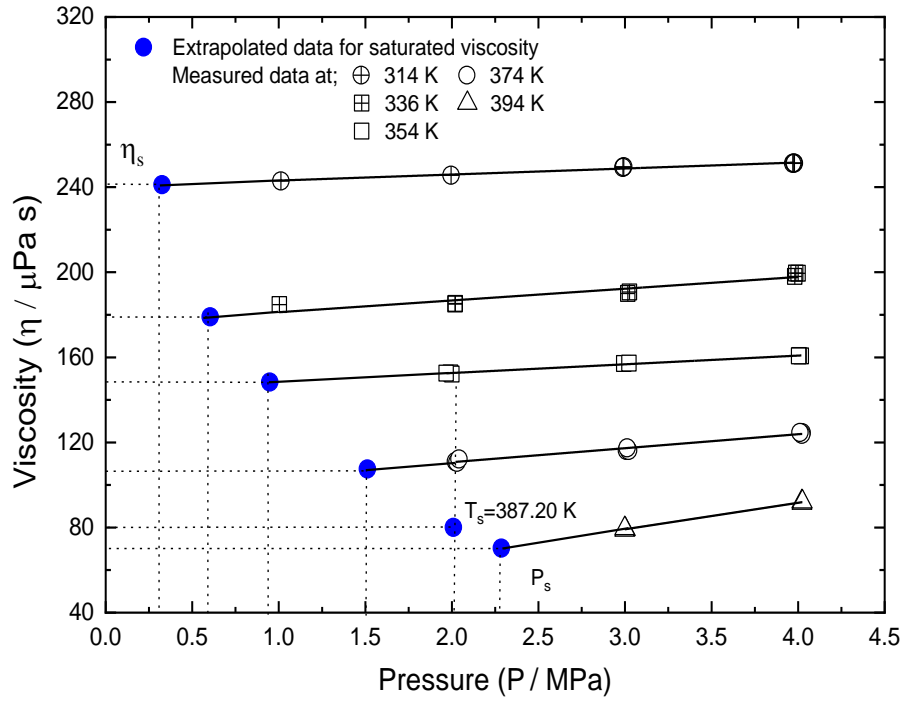


Fig. 4.2.1.11 Extrapolated data for the liquid viscosity at the saturated conditions

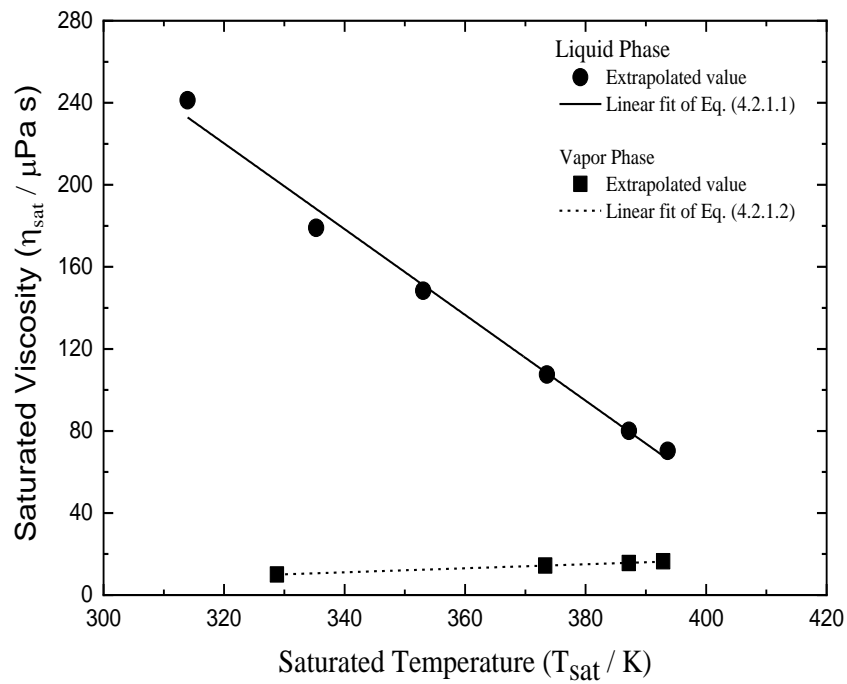


Fig. 4.2.1.12 Saturated viscosity vs. temperature

Table 4.2.1.6 Saturated viscosity, η_{sat} ($\mu\text{Pa s}$) of R1336mzz(E)

(a) Liquid phase			
T (K)	P (MPa)	$\eta_{sat,L}$ (Extrapolated)	$\eta_{sat,L}$ (Eq. 4.2.1.1)
313.94	0.326	241.20	232.89
335.29	0.604	179.03	188.24
353.05	0.948	148.34	151.12
373.58	1.512	107.51	108.19
387.20	2.009	80.06	79.71
393.62	2.286	70.31	66.27
(b) Vapor phase			
T (K)	P (MPa)	$\eta_{sat,V}$ (Extrapolated)	$\eta_{sat,V}$ (Eq. 4.2.1.2)
328.78	0.505	10.02	10.00
373.29	1.503	14.37	14.37
387.18	2.009	15.60	15.73
392.87	2.251	16.42	16.29

4.2.1.5 Conclusion

In this part of this study, the viscosity measurement was conducted for R1336mzz(E) by the method of tandem capillary tubes. The measurement was performed at pressures from 0.5 MPa to 4.0 MPa and temperatures from 314 to 394 K for the liquid, 353 to 453 K for the vapor, and 413 to 453 K for the supercritical phases, respectively. The measured liquid, vapor, and supercritical viscosity data of R1336mzz(E) are located at a range of 79.6 to 251.3 $\mu\text{Pa s}$, 10.8 to 16.2 $\mu\text{Pa s}$, and 18.1 to 53.6 $\mu\text{Pa s}$, respectively. The expanded uncertainties in the viscosity measurement are calculated as 2.26 % for the liquid, 2.30 % for the vapor, and 2.32 % for the supercritical phase using $k=2$ and a 95 % confidence level. The experimental data are correlated with the ECS model. The AADs in correlated values are 5.04 % for the liquid, 14.75 % for the vapor, and 11.88 % for the supercritical phases, respectively. Due to a less consistent flow rate and differential pressures in Pyrex capillary tubes, the experimental results for the vapor phase are a little more scattered with systemic negative deviations comparable to those for the liquid. As a consequence of the above critical conditions, as well as the comparatively high temperature and pressure, the experimental data of the supercritical phase is somewhat dispersed to a great extent in contrast to the liquid and vapor phases. The extrapolation from the experimental data to saturation conditions was used to approximate saturated viscosities. Simple correlations as a function of temperature are established to predict the saturated viscosity for liquid and vapor phases for industrial design and simulation.

4.2.2 Kinematic viscosity measurement of 3,3,4,4,5,5-HFCPE

4.2.2.1 Overview of 3,3,4,4,5,5-HFCPE

Kinematic viscosity is also an important tool to identify the feasibility to be used in the engineering or commercial area of any working fluid. The major goals of the present work are to measure the kinematic viscosity of 1H, 2H-Hexafluorocyclopentene, shortly 3,3,4,4,5,5-HFCPE, both for liquid and vapor phases and to develop the simplified correlations of the extracted data at saturation conditions for industrial design and simulation. Special awareness regarding climate change, the potential impact of refrigerants with low GWP are the key focus all over the world. The rapid change of the earth's climate is responsible for the human lives threatened, which is the consequence of global warming. Conventional refrigerants, such as hydrofluorocarbons (HFCs) and hydrochlorofluorocarbons (HCFCs) having high GWP values, are the major reasons for global warming and consequently, the Montreal Protocol and Kyoto Protocol have been introduced to control these harmful gases (UNEP, 2014). Therefore, more environmentally acceptable alternatives to conventional refrigerants are needed for usage in popular applications such as heat pumps and Organic Rankine Cycles (ORCs) (McLinden, 2009; Richter et al., 2011). To achieve the challenge, a newly developed refrigerant of 3,3,4,4,5,5-HFCPE is an interesting working fluid that has suitably low toxicity and low flammability properties, a zero ODP value, and a lower GWP value. The 3,3,4,4,5,5-HFCPE does not belong to the hydro-fluoro-olefins (HFOs), but having above friendly properties, it is considered as a suitable substitution of HFCs similarly to HFOs. The molecular structure and the fundamental properties of 3,3,4,4,5,5-HFCPE are shown in Fig. 4.2.2.1 and summarized in Table 4.2.2.1, respectively.

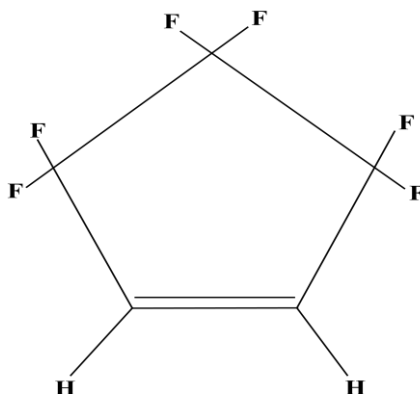


Fig. 4.2.2.1 Molecular structure of 3,3,4,4,5,5-HFCPE

The predicted critical temperature is 511.15 K (Lydersen, 1955; Wajima et al., 2017) and the critical pressure is estimated at 2.923 MPa by the method of Lydersen (1955), respectively. It has zero ODP and GWP value of 33 (Wajima et al., 2017) that indicates the eco-friendly behaviors as a working fluid. The thermodynamic properties and the transport properties of the working fluid are the most important factors for designing energy systems, practical appliances, and simulations. The transport properties of 3,3,4,4,5,5-HFCPE, like thermal conductivity and viscosity, have become of growing interest for designing practical applications. There are no experimental data for the thermodynamic properties and the transport properties of 3,3,4,4,5,5-HFCPE available yet in the open literature. Although some data of the thermal conductivity and kinematic viscosity data are reported in conferences by our research group (Mondal et al., 2021b; Tuhin et al., 2020), a sufficient number of data was not reported. In this study, the kinematic viscosities measurements of 3,3,4,4,5,5-HFCPE were conducted by the method of tandem capillary tubes at a temperature range from 332 to 494 K over a pressure range from 0.5 to 4.0 MPa for the liquid state, while in the vapor state from 413 to 514 K at pressures up to 2.0 MPa. Also, the combined and expanded uncertainties for the kinematic viscosity measurement of 3,3,4,4,5,5-HFCPE were estimated using the propagation law for uncertainties by the GUM method (Bell, 2001; JCGM 100, 2008; Taylor and Kuyatt, 1994). The simplified correlations were achieved from extrapolating the measured data by expressing the saturation kinematic viscosities in terms of saturation temperature.

Table 4.2.2.1 Fundamental properties of 3,3,4,4,5,5-HFCPE

Parameters	Value	Reference
Name	1H, 2H-Hexafluorocyclopentene	
Chemical formula	C ₅ H ₂ F ₆	
CASRN	1005-73-8	AIST (2020)
Critical temperature (K)	511.15	Lydersen (1955); Wajima et al. (2017)
Critical pressure (MPa)	2.923	Lydersen (1955)
Molecular weight (g mol ⁻¹)	176.06	AIST (2020)
Flammability (Vol%, 35 °C wet)	4-9	AIST (2020)
Boiling point (K)	341.15	Wajima et al. (2017)
ODP	0	
GWP (100 year)	33	Wajima et al. (2017)

4.2.2.2 Measured kinematic viscosities of 3,3,4,4,5,5-HFCPE

The kinematic viscosity measurements of 3,3,4,4,5,5-HFCPE were performed by the method of the tandem capillary tubes both for liquid and vapor phases with a wide range of pressures and temperatures. Each point measurement was conducted repeatedly three times carefully after getting the stable condition of the apparatus. The repeated measurement results did not exceed $\pm 0.65\%$, where the time interval of two successive measurements was at least 30 minutes. Hence, the experimental temperatures and pressures changed a little bit. Fig. 4.2.2.2 shows the measurement points of 3,3,4,4,5,5-HFCPE covering the area by P - T diagram. The critical temperature of 3,3,4,4,5,5-HFCPE is found as 511.15 K (Lydersen, 1955; Wajima et al., 2017) and also the critical pressure is estimated as 2.923 MPa by the method of Lydersen (1955). The vapor-liquid saturation line was drawn by utilizing the Riedel-Plank correlations (Poling et al., 2000; Riedel, 1954; Vetere, 1991). The liquid kinematic viscosities of 3,3,4,4,5,5-HFCPE were measured at a temperature range from 332 to 494 K up to 4.0 MPa and for vapor kinematic viscosities from 413 to 514 K at pressures up to 2.00 MPa. The measured kinematic viscosity data of liquid and vapor states are presented in Tables 4.2.2.2 and 4.2.2.3, respectively. The measurement uncertainties of 3,3,4,4,5,5-HFCPE both for the liquid and vapor are stated below in the Tables.

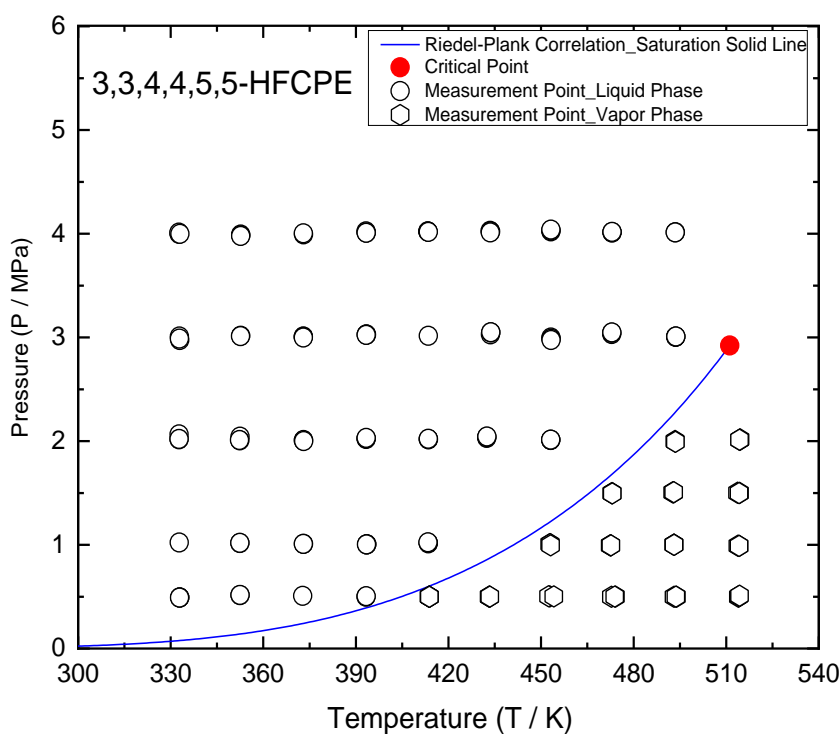


Fig. 4.2.2.2 Experimentally measurement points of 3,3,4,4,5,5-HFCPE

Table 4.2.2.2 Experimental liquid kinematic viscosities, ν_{exp} ($\text{cm}^2 \text{s}^{-1}$) of 3,3,4,4,5,5-HFCPE

T (K)	P (MPa)	ν_{exp}	T (K)	P (MPa)	ν_{exp}
332.73	3.999	0.00408	393.34	2.025	0.00224
332.67	4.010	0.00409	393.35	2.030	0.00224
332.99	3.999	0.00411	393.59	1.005	0.00219
332.92	2.975	0.00403	393.52	1.003	0.00219
332.86	3.008	0.00405	393.48	1.003	0.00220
332.82	2.987	0.00403	393.30	0.500	0.00202
332.73	2.065	0.00397	393.36	0.504	0.00197
332.74	2.017	0.00398	413.32	4.022	0.00214
332.74	2.021	0.00393	413.36	4.021	0.00213
332.79	1.022	0.00388	413.47	4.017	0.00213
332.78	1.022	0.00389	413.51	3.015	0.00196
332.78	1.022	0.00388	413.50	3.015	0.00196
332.93	0.491	0.00364	413.50	3.015	0.00196
332.92	0.492	0.00363	413.55	2.016	0.00192
332.88	0.492	0.00363	413.50	2.019	0.00192
352.68	3.991	0.00337	413.49	2.022	0.00192
352.69	3.983	0.00337	413.50	1.013	0.00184
352.68	3.978	0.00337	413.48	1.020	0.00184
352.67	3.015	0.00329	413.37	1.023	0.00184
352.62	3.011	0.00332	433.52	4.028	0.00179
352.62	3.011	0.00331	433.66	4.020	0.00179
352.47	2.042	0.00327	433.58	4.011	0.00179
352.40	2.008	0.00327	433.65	3.029	0.00170
352.33	2.010	0.00327	433.74	3.047	0.00171
352.43	1.018	0.00312	433.73	3.050	0.00170
352.44	1.019	0.00314	432.42	2.031	0.00164
352.49	0.515	0.00282	432.44	2.039	0.00166

352.50	0.515	0.00281	432.46	2.044	0.00165
352.47	0.516	0.00283	453.19	4.021	0.00149
373.04	3.993	0.00286	453.20	4.030	0.00149
373.02	4.003	0.00287	453.21	4.039	0.00149
372.99	3.009	0.00283	453.22	2.999	0.00148
372.97	3.004	0.00283	453.29	2.986	0.00147
372.98	2.998	0.00282	453.27	2.975	0.00147
373.01	2.005	0.00270	453.14	2.011	0.00143
373.07	2.011	0.00270	453.16	2.012	0.00144
373.08	2.001	0.00272	453.15	2.013	0.00143
373.11	2.000	0.00270	473.05	4.011	0.00126
373.03	1.008	0.00258	473.00	4.015	0.00126
373.00	1.009	0.00257	473.03	4.017	0.00126
372.76	0.508	0.00245	472.90	3.033	0.00121
372.77	0.508	0.00246	472.90	3.043	0.00122
393.27	4.022	0.00244	472.98	3.048	0.00122
393.38	4.010	0.00246	493.53	4.013	0.00105
393.35	4.009	0.00244	493.53	4.013	0.00105
393.42	3.028	0.00238	493.50	4.011	0.00105
393.46	3.026	0.00238	493.64	3.005	0.00096
393.38	3.023	0.00237	493.67	3.007	0.00095
393.36	2.021	0.00224	493.70	3.008	0.00096

Standard uncertainties due to pressure and temperature are $u(P)=0.0036$ MPa and $u(T)=0.029$ K
Combined standard uncertainty $u_c(v)=1.12\%$; Expanded uncertainty $U_c(v)=2.24\%$ with $k=2$ and 95 % confidence level

Table 4.2.2.3 Experimental vapor kinematic viscosities, ν_{exp} ($\text{cm}^2 \text{s}^{-1}$) of 3,3,4,4,5,5-HFCPE

T (K)	P (MPa)	ν_{exp}	T (K)	P (MPa)	ν_{exp}
413.82	0.500	0.00424	493.85	0.500	0.00654
413.78	0.499	0.00434	493.71	0.500	0.00657
413.76	0.500	0.00435	493.05	1.002	0.00340
413.81	0.499	0.00444	493.13	1.001	0.00338
433.20	0.500	0.00493	493.09	1.000	0.00338
433.31	0.500	0.00500	492.69	1.506	0.00208
433.39	0.501	0.00508	492.97	1.507	0.00208
452.81	0.502	0.00567	492.99	1.508	0.00207
452.82	0.502	0.00585	493.41	2.001	0.00141
454.13	0.503	0.00570	493.41	1.997	0.00140
452.85	1.007	0.00265	493.52	1.993	0.00142
452.99	1.007	0.00263	513.94	0.499	0.00716
453.10	0.995	0.00266	514.16	0.505	0.00714
472.83	0.499	0.00598	514.33	0.509	0.00715
474.10	0.500	0.00609	514.20	0.991	0.00382
473.91	0.500	0.00601	513.79	0.991	0.00382
472.44	0.995	0.00296	514.20	0.990	0.00382
472.57	0.994	0.00294	513.68	1.502	0.00229
472.62	0.994	0.00295	514.32	1.501	0.00229
473.01	1.500	0.00175	514.16	1.500	0.00230
472.96	1.497	0.00175	514.50	2.018	0.00153
473.09	1.495	0.00176	514.42	2.013	0.00154
493.10	0.499	0.00660	514.34	2.013	0.00155

Standard uncertainties due to pressure and temperature are $u(P)=0.0028$ MPa and $u(T)=0.034$ K

Combined standard uncertainty $u_c(\nu)=1.47$ %; Expanded uncertainty $U_c(\nu)=2.94$ % with $k=2$ and 95 % confidence level

Fig. 4.2.2.3 demonstrates the variation of experimental liquid kinematic viscosities of 3,3,4,4,5,5-HFCPE with temperature. The liquid kinematic viscosities were measured at a range of temperature from 332 to 494 K and pressures from 0.5 to 4.0 MPa. The measured liquid kinematic viscosities are decreased with increasing the temperature for all corresponding pressures but increased with rising the pressure if the temperature remains constant. The expanded uncertainty of the liquid kinematic viscosity measurement was calculated at 2.24% with $k=2$ and 95% confidence level.

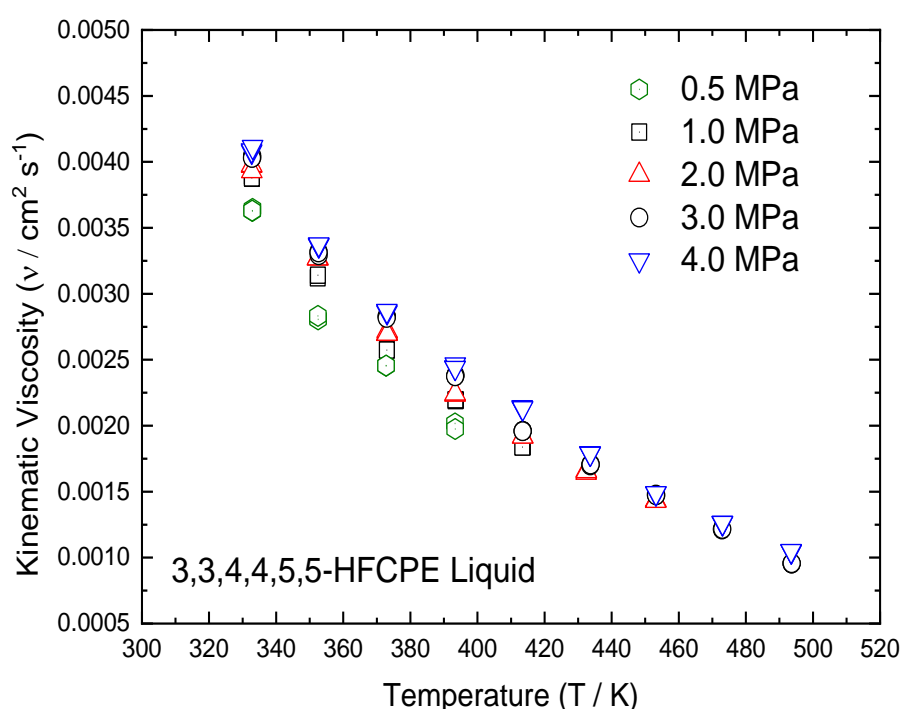


Fig. 4.2.2.3 Variation of liquid kinematic viscosities of 3,3,4,4,5,5-HFCPE with temperature

Fig. 4.2.2.4 represents the vapor kinematic viscosities of 3,3,4,4,5,5-HFCPE at a range of temperature from 413 to 514 K and pressure from 0.5 to 2.0 MPa. The vapor kinematic viscosities are increased with increasing the temperature for all pressures but a reduction of kinematic viscosity is found with rising the pressure if the temperature is constant. The vapor kinematic viscosities pattern is opposite to the liquid phase. The vapor kinematic viscosities deviated a little more than liquid kinematic viscosities for the less consistent flow rate of refrigerant and the differential pressure through the long and short Pyrex capillary tubes. The expanded uncertainty for vapor kinematic viscosities measurement was calculated at 2.94% with $k=2$ and 95% confidence level.

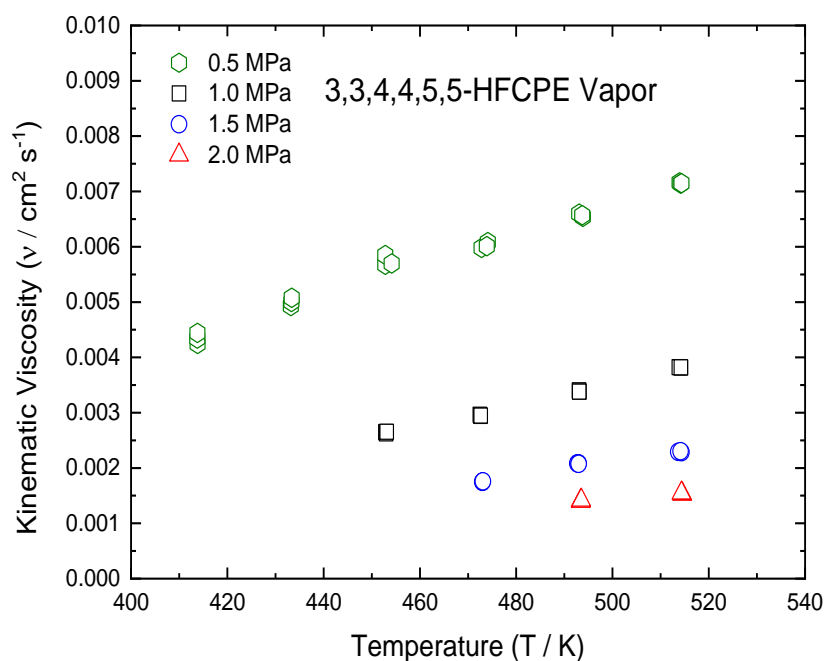
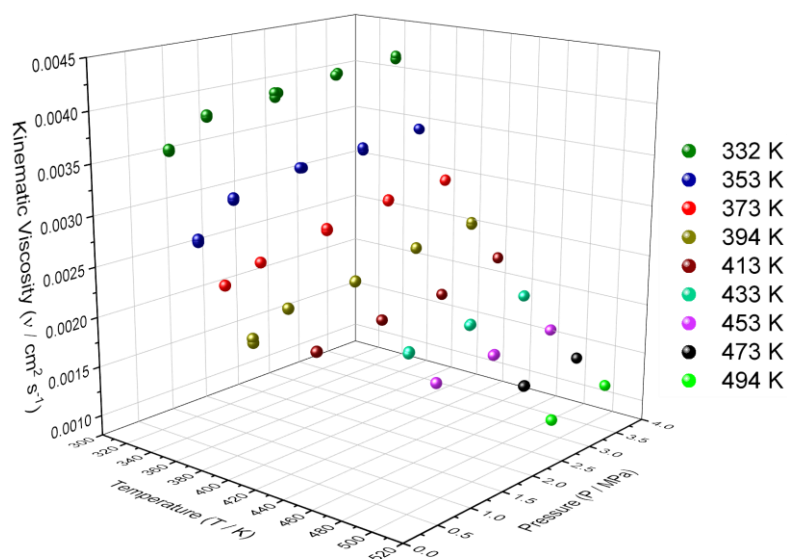


Fig. 4.2.2.4 Variation of vapor kinematic viscosities of 3,3,4,4,5,5-HFCPE with temperature

Fig. 4.2.2.5 demonstrates the 3D presentation for all experimental kinematic viscosities of 3,3,4,4,5,5-HFCPE both for liquid and vapor phases at temperatures from 332 to 514 K and pressures from 0.5 to 4.0 MPa. Therefore, the measured vapor phase data have deviated significantly among them than the liquid phase owing to the less consistent differential pressure and flow rates through the Pyrex capillary tubes. The expanded uncertainty for vapor phase kinematic viscosity measurement was calculated at 2.94 % which is higher than the liquid phase measurement at 2.24 % with $k=2$ and 95 % confidence level.



(a) Liquid 3,3,4,4,5,5-HFCPE

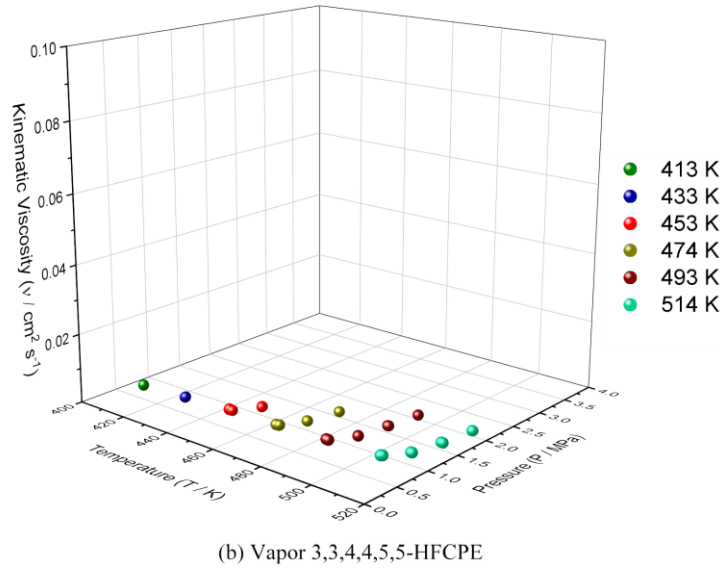


Fig. 4.2.2.5 3D Presentation of the kinematic viscosities of 3,3,4,4,5,5-HFCPE with temperature and pressure

Again, Fig. 4.2.2.6 shows the comparison of kinematic viscosities of 3,3,4,4,5,5-HFCPE over the known working fluids (cyclopentane, pentane, and cyclohexane). This figure indicates the data trend of 3,3,4,4,5,5-HFCPE for pressures at 4.0 MPa and 1.0 MPa in the liquid and vapor phases. A similar data trend for this working fluid is found both for liquid and vapor phases compare to the known working fluids. In the liquid phase, the measured data of this fluid are almost similar to cyclopentane and pentane, but lower than cyclohexane. While in the vapor phase, the measured data are quite lower than the mentioned three fluids, but the data trend is the same as them. These findings imply that the measured data are acceptable.

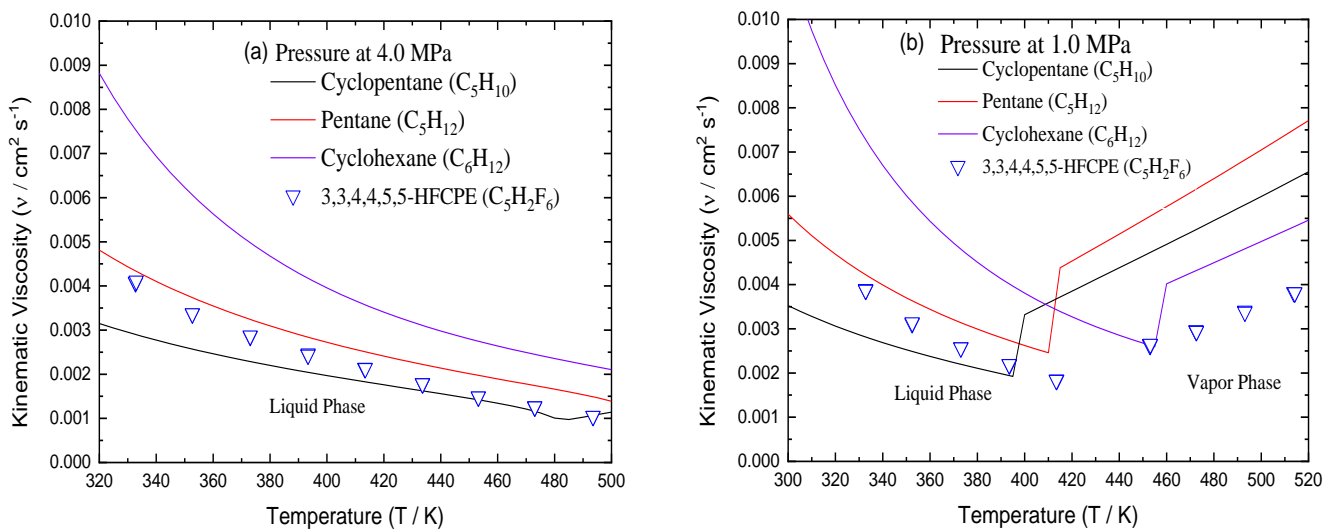


Fig. 4.2.2.6. Comparison of liquid kinematic viscosities of 3,3,4,4,5,5-HFCPE for pressures at 4.0 MPa and 1.0 MPa (kinematic viscosities of cyclopentane, pentane, and cyclohexane are taken from Huber (2018))

4.2.2.3 Correlations at saturation conditions for kinematic viscosity of 3,3,4,4,5,5-HFCPE

The extrapolating approach was used to establish the correlations to predict the saturated kinematic viscosities of 3,3,4,4,5,5-HFCPE, which indicates the best design and simulation of the energy system. The saturation properties of this refrigerant were attained from the Riedel-Plank correlations. Therefore, the simplified saturated correlations were established by extrapolating the measured data up to saturation conditions both of liquid and vapor phases, respectively. In the liquid phase, the extrapolated kinematic viscosities at saturation conditions were obtained from extrapolating the measured data of liquid 3,3,4,4,5,5-HFCPE by identical temperature which is understandable from Fig. 4.2.2.7. While in the vapor phase, the saturated kinematic viscosity was extrapolated at both identical pressure and temperature. Then correlation equations both for liquid and vapor saturated kinematic viscosities were derived by the polynomial fitting from the extrapolated data in terms of saturated temperature. Fig. 4.2.2.8 shows the polynomial fitting of extrapolated data as well as the variation of saturated kinematic viscosities both for liquid and vapor phase of 3,3,4,4,5,5-HFCPE with the saturation temperature. The saturation kinematic viscosity correlation for liquid 3,3,4,4,5,5-HFCPE was developed as Eq. (4.2.2.1) where the vapor saturation kinematic viscosity correlation was expressed as Eq. (4.2.2.2). From room temperature to high temperature, the correlations to determine the kinematic viscosities at saturation conditions for both liquid and vapor 3,3,4,4,5,5-HFCPE showed good results. Table 4.2.2.4 summarizes the extrapolated data and calculated data from correlations both for the liquid and vapor kinematic viscosities of 3,3,4,4,5,5-HFCPE at saturated conditions.

$$\nu_{sat,L} = 4.585 \times 10^{-8} T_{sat}^2 - 5.215 \times 10^{-5} T_{sat} + 0.0155 \quad (4.2.2.1)$$

$$\nu_{sat,V} = 4.143 \times 10^{-7} T_{sat}^2 - 4.127 \times 10^{-4} T_{sat} + 0.10397 \quad (4.2.2.2)$$

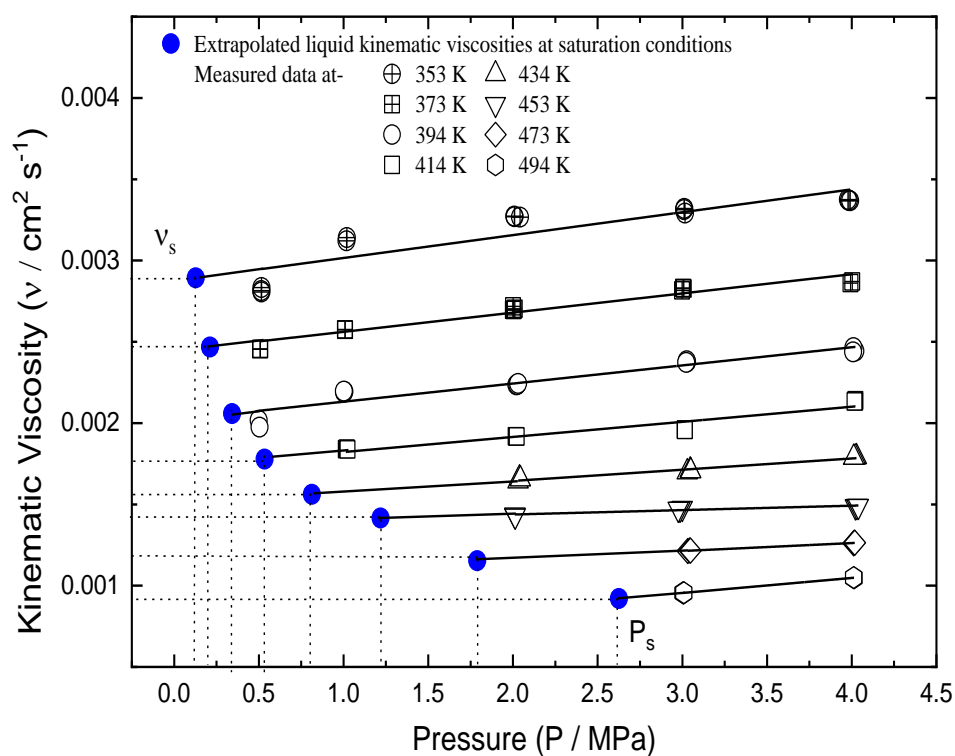


Fig. 4.2.2.7 Extrapolated liquid kinematic viscosities at saturation conditions

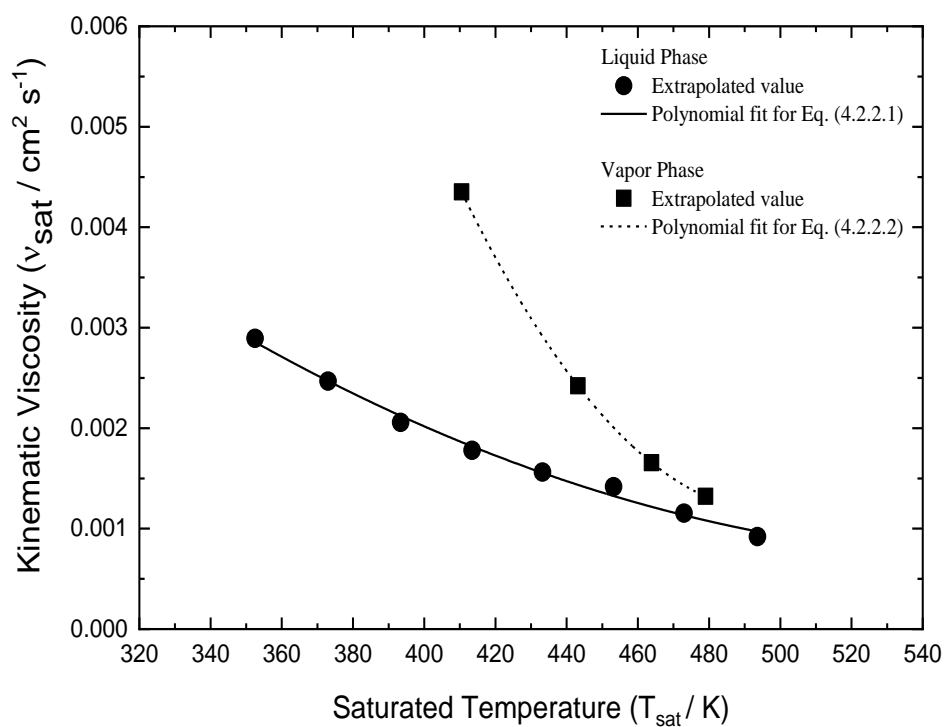


Fig. 4.2.2.8 Variation of saturated kinematic viscosities with the saturation temperature

Table 4.2.2.4 Saturated kinematic viscosity, ν_{sat} ($\text{cm}^2 \text{s}^{-1}$) of 3,3,4,4,5,5-HFCPE

(a) Liquid			
T (K)	P (MPa)	$\nu_{sat,L}$ Extrapolated	$\nu_{sat,L}$ Eq. (4.2.2.1)
352.54	0.128	0.00289	0.00281
372.99	0.212	0.00247	0.00243
393.40	0.342	0.00206	0.00208
413.46	0.534	0.00178	0.00178
433.24	0.813	0.00156	0.00151
453.20	1.219	0.00142	0.00128
472.98	1.790	0.00115	0.00109
493.60	2.626	0.00092	0.00093
(b) Vapor			
T (K)	P (MPa)	$\nu_{sat,V}$ Extrapolated	$\nu_{sat,L}$ Eq. (4.2.2.2)
410.50	0.501	0.00435	0.00437
443.18	0.997	0.00242	0.00244
463.84	1.502	0.00166	0.00168
479.01	2.006	0.00132	0.00134

4.2.2.4 Conclusion

In this part of the study, the kinematic viscosity measurements of 3,3,4,4,5,5-HFCPE were conducted over the wider temperatures and pressures both for liquid and vapor phase by the method of tandem capillary tubes. The kinematic viscosities of this refrigerant were measured for liquid at temperatures from 332 to 494 K over the pressures from 0.5 to 4.0 MPa and for vapor at temperatures from 413 to 534 K over the pressures from 0.5 to 2.0 MPa. The measured liquid and vapor kinematic viscosities were found as 0.0009 to 0.0041 $\text{cm}^2 \text{s}^{-1}$, and 0.0014 to 0.0065 $\text{cm}^2 \text{s}^{-1}$, respectively. The measurement uncertainties are calculated using the propagation law of uncertainties by the GUM method. The expanded uncertainties are estimated at 2.24 % for liquid and 2.94 % for vapor phases with $k=2$ and 95 % confidence levels, respectively. Therefore, the measured vapor phase data deviated a little more than the liquid phase owing to the less consistent differential pressure and flow rates through the Pyrex capillary tubes. Simplified correlations are developed to estimate the saturated liquid and vapor kinematic viscosities using the extrapolation approach from the experimental data as identical temperature and pressure up to saturation conditions.

4.2.3 Viscosity measurement of R1132(E)

4.2.3.1 Overview of R1132(E)

Transport properties are important in today's modern technology. In the context of environmental issues, the global warming potential (GWP) of conventional working fluids has accelerated the interests of researchers to search the alternatives having suitable properties. In this part, the principal goals are to measure the viscosity of trans-1,2-difluoroethene (R1132(E)) for liquid and vapor phases by the method of tandem capillary tubes and to correlate with the well-known model. In recently, promising alternatives such as hydrofluoroolefins (HFOs) and hydrochlorofluoroolefins (HCFOs) are the key focus owing to the zero ODP and lower GWP, but HCFOs have ODP, not zero ODP. The trans-1,2-difluoroethene (R1132(E); C₂H₂F₂, CAS 1630-78-0) is one possible low GWP refrigerant with a lower boiling point temperature. It is an olefin-based refrigerant with a carbon double bond, having a simpler molecular structure and a molecular weight of 64.035 g mol⁻¹. It is considered a next-generation refrigerant with promising properties to substitute difluoromethane (R32). It is expected that its mixtures with R32 will be highly probable working fluid for the use of residential air conditioners. Although a thermodynamic property model with reasonable accuracies is needed to evaluate the performance of the mixtures, even the experimental data for pure R1132(E) are currently very limited. Fig. 4.2.3.1 shows the molecular structure of R1132(E) whereas the basic information is demonstrated in Table 4.2.3.1.

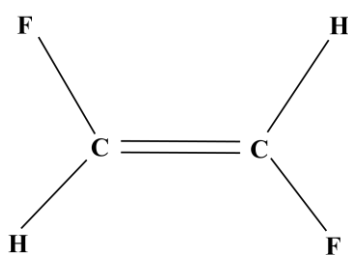


Fig. 4.2.3.1 Molecular structure of R1132(E)

The critical temperature and the critical density of this refrigerant were measured and reported by Higashi et al. (2020) as 348.72 K and 438 kg·m⁻³, respectively. In the meanwhile, the critical pressure is chosen as 5.1737 MPa by Akasaka (2021). The boiling point was calculated and reported at 220.1 K by Craig and Entemann (1961) using Clausius-Clapeyron equations fitted to experimental vapor pressure data. But, Akasaka (2021) used the boiling point of 220.51 K in his work. From the AIST, Japan, the author Tokuhashi et al. (2019) reported atmospheric

lifespan and GWP values for this refrigerant; they are 1.2 days and 0.0056, respectively. In another study, Domanski et al. (2017) reported the GWP value of 1 for this refrigerant. The basic information indicates strong evidence for the negligible environmental impact of R1132(E).

Table 4.2.3.1 Basic information of R1132(E)

Parameters	R1132(E)	Reference
Chemical formula	Trans CHF=CHF (i.e., C ₂ H ₂ F ₂)	
CASRN	1630-78-0	
Critical temperature (K)	348.82	Higashi et al. (2020)
Critical pressure (MPa)	5.1737	Akasaka (2021)
Critical density (kg m ⁻³)	438	Higashi et al. (2020)
Molecular weight (g mol ⁻¹)	64.035	
Boiling point (K)	220.1	Craig and Entemann (1961)
	/220.51	/Akasaka (2021)
Atmospheric lifetime (days)	1.2	Tokuhashi et al. (2019)
ODP		
GWP (100 years)	0.0056	Tokuhashi et al. (2019)
	/ 1	/Domanski et al. (2017)

As thermodynamic and thermophysical properties of the working fluid are the key attentions to design and implement efficient energy systems for ORCs and high-temperature heat pumps, it is mandatory to have vast knowledge regarding these issues. However, few reports of measured values of the thermodynamic and no reports for transport properties were found in the open literature. In a consequence, the thermodynamic properties of trans-1,2-difluoroethene (R1132(E)) as saturated liquid and vapor densities and critical parameters (Akasaka et al., 2020); saturation vapor pressure, and critical pressure (Perera et al., 2021, 2020); and others (Sakoda and Higashi, 2021) were reported separately in the various conferences. Higashi et al. (2020) experimentally measured and reported the critical temperature and the critical density of R1132(E); they are 348.72 K and 438 kg·m⁻³, respectively. The *PvT* property of R1132(E) was investigated by Akasaka et al. (2020) with the isochoric method and an equation of state (EoS) for this refrigerant was also developed by this author. Besides, Nakamura et al. (2020) measured and reported the triple point and surface tension for this refrigerant over a wide range of temperatures. But, there are no experimental

data for viscosity and thermal conductivity of this refrigerant in the open literature. Therefore, in this part of the study, the viscosity measurements were conducted over the temperature range of 302 to 335 K at pressures of 3.0 to 4.0 MPa for the liquid phase and 323 to 345 K at pressures of 2.5 to 4.0 MPa for the vapor phase, respectively.

4.2.3.2 Measured viscosities of R1132(E)

The viscosity of R1132(E) was measured by the tandem capillary tube method over a wide range of temperatures and pressures. Fig. 4.2.3.2 illustrates the measurement conditions covering the region for temperatures and pressures wherein the vapor-liquid saturation solid line was drawn using the equation of state (EoS) by Akasaka and co-authors (2021; 2020). The critical temperature and pressure of R1132(E) were found as 348.82 K and 5.1737 MPa, respectively. For the reproducibility, each measurement result at corresponding temperature and pressure was repeated 3 times (Yao et al., 2014) and the scatter of the three repeatable measurements did not exceed $\pm 0.65\%$. Nevertheless, the time duration between the two measurements was at least 30 minutes where the temperature and pressure changed slightly.

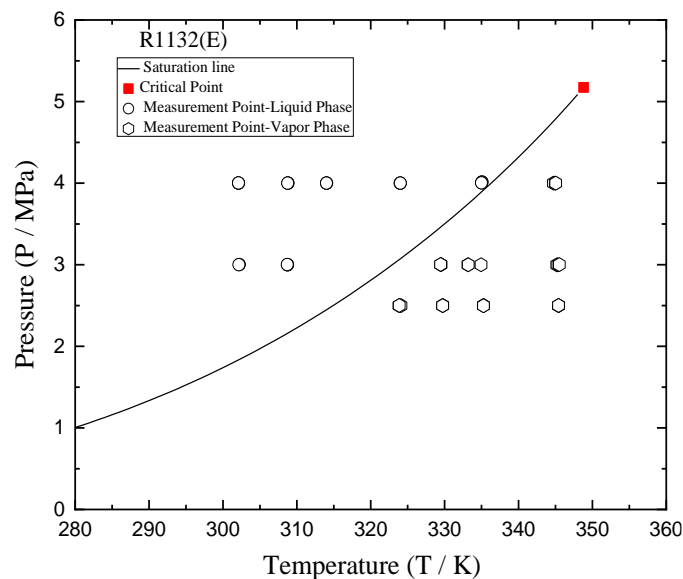


Fig. 4.2.3.2 Temperature and pressure ranges for the experimental points of R1132(E)

Therefore, the viscosity of R1132(E) was reported over the temperatures from 302 to 335 K and pressure from 3.0 to 4.0 MPa for the liquid phase and from 323 to 345 K over the pressure from 2.50 to 4.0 MPa in the vapor phase, respectively. All the experimental viscosity data of R1132(E) are listed in Tables 4.2.3.2 to 4.2.3.3.

Table 4.2.3.2 Experimental viscosity, η ($\mu\text{Pa s}$) of R1132(E) at the liquid phase

T (K)	P (MPa)	η ($\mu\text{Pa s}$)	η_{cal}^* ($\mu\text{Pa s}$)	$\Delta\eta^{**}$
302.12	4.000	114.54	129.21	-11.35
302.11	4.000	114.00	129.22	-11.78
302.11	4.002	112.59	129.23	-12.87
302.23	3.002	107.21	125.95	-14.88
302.16	3.000	106.61	126.08	-15.45
308.82	4.001	104.36	117.77	-11.38
308.78	4.000	104.46	117.84	-11.36
308.77	4.000	104.63	117.86	-11.22
308.77	3.000	93.58	114.54	-18.30
308.74	2.999	92.65	114.58	-19.15
308.71	3.001	94.19	114.63	-17.83
314.02	4.000	94.41	109.11	-13.47
314.05	4.000	94.10	109.05	-13.71
314.01	3.999	92.18	109.12	-15.52
324.01	3.999	77.93	92.49	-15.74
324.00	3.999	78.69	92.51	-14.94
324.01	4.000	79.91	92.50	-13.61
335.06	4.012	63.82	72.15	-11.55
335.07	4.014	63.78	72.14	-11.60
335.01	4.004	64.10	72.20	-11.23
335.00	4.004	64.26	72.22	-11.02

*Akasaka and co-authors (Akasaka, 2021; Akasaka et al., 2020)

**Deviation, $\Delta\eta = 100 \times \left(\frac{\eta - \eta_{cal}}{\eta_{cal}} \right)$

Table 4.2.3.3 Experimental viscosity, η ($\mu\text{Pa s}$) of R1132(E) at vapor phase

T (K)	P (MPa)	η ($\mu\text{Pa s}$)	η_{cal}^* ($\mu\text{Pa s}$)	$\Delta\eta^{**}$
323.82	2.499	12.54	15.09	-16.93
324.10	2.499	12.78	15.10	-15.41
323.87	2.501	12.45	15.09	-17.53
329.74	2.499	13.12	15.35	-14.49
329.75	2.501	13.21	15.35	-13.93

329.74	2.500	13.30	15.35	-13.31
329.48	3.002	13.86	15.80	-12.28
329.52	3.002	13.78	15.80	-12.77
329.46	3.003	13.50	15.80	-14.52
335.26	2.500	13.85	15.59	-11.16
335.26	2.501	13.98	15.59	-10.34
335.28	2.497	13.15	15.59	-15.64
333.17	2.999	14.10	15.92	-11.39
333.21	2.999	13.96	15.92	-12.29
334.94	3.001	14.18	15.98	-11.25
345.45	2.499	14.12	16.05	-12.03
345.41	2.499	14.11	16.04	-12.03
345.43	2.500	14.19	16.05	-11.54
345.19	2.999	14.72	16.37	-10.10
345.33	3.000	14.69	16.38	-10.33
345.54	3.002	14.44	16.39	-11.89
344.73	3.999	15.23	17.68	-13.81
345.00	3.999	15.13	17.68	-14.38
345.04	3.999	14.92	17.68	-15.60

*Akasaka and co-authors (Akasaka, 2021; Akasaka et al., 2020)

**Deviation, $\Delta\eta = 100 \times \left(\frac{\eta - \eta_{cal}}{\eta_{cal}} \right)$

In the liquid phase, the experimental viscosity of R1132(E) was measured covering the temperature from 302 to 335 K and pressure from 3.0 to 4.0MPa. Fig. 4.2.3.3 demonstrates the variation of measured liquid viscosity data of R1132(E) as well as estimated values from Akasaka and co-authors (2021; 2020) by indicating the typical changes with density and temperature. Distinct symbols are used to identify the measured temperatures. It was observed that the liquid R1132(E) shows a reduction in viscosity with increasing temperature. In other words, the liquid viscosity was increased exponentially by rising the density as well. In this work, the measured liquid viscosity was recorded at a range of 63.8 to 114.5 $\mu\text{Pa s}$. The obtained liquid viscosity data are compared with the estimated values by the ECS model from Akasaka and co-authors (2021; 2020), which indicate a similar trend result, but found relatively higher deviations at a lower temperature than the higher temperature for all corresponding pressure.

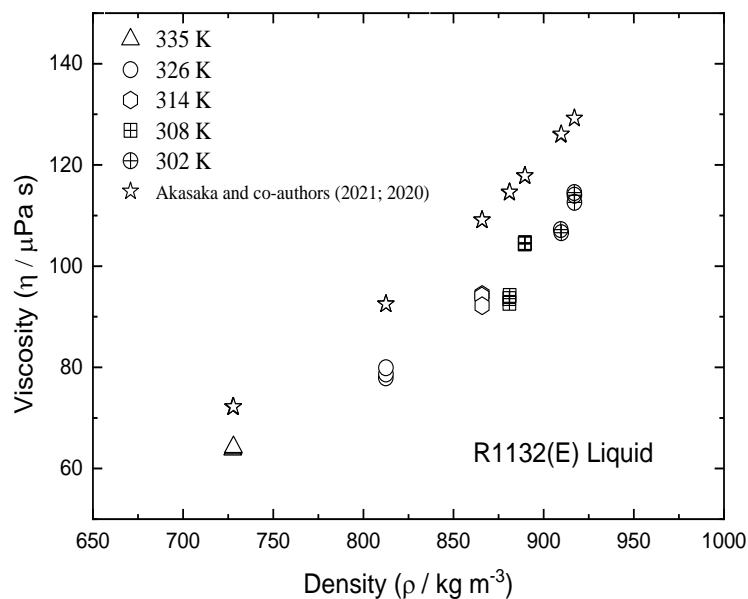


Fig. 4.2.3.3 Variation of the viscosity of liquid R1132(E) with density

Fig. 4.2.3.4 illustrates the density effects on the viscosity of the vapor phase with changing the temperature and pressure. The experimental viscosity data of vapor R1132(E) was measured over a temperature range from 323 to 345 K whereas pressure varies from 2.5 to 4.0 MPa. The measured data shows a reduction in viscosity with decreasing the temperature for all corresponding pressures. In other words, the viscosity data was decreased with increasing the density of the test fluid for all corresponding pressures. The vapor viscosity of R1132(E) was reported from 12.5 to 15.2 $\mu\text{Pa s}$.

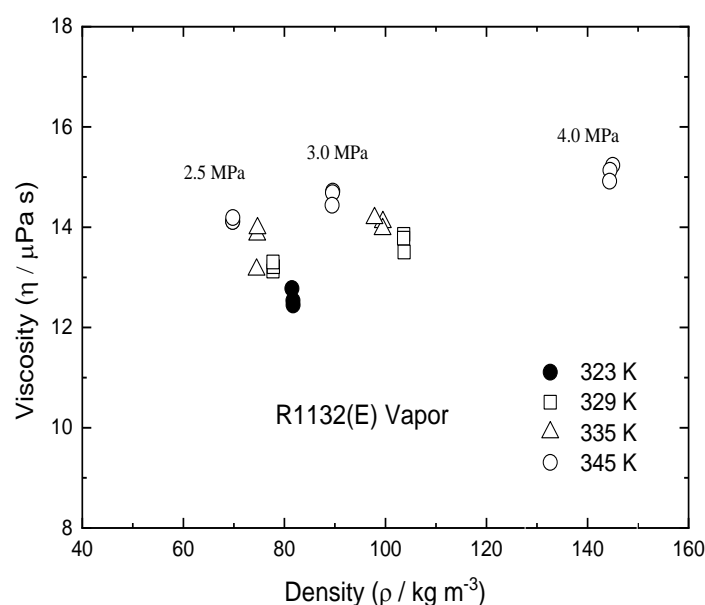


Fig. 4.2.3.4 Variation of the viscosity of vapor R1132(E) with density

Therefore, Fig. 4.2.3.5 demonstrates all experimental viscosity data for liquid R1132(E) with the temperature from 302 to 335 K over the pressure up to 4.0 MPa. In this figure, the liquid viscosities are illustrated in (a) two-dimensional view and (b) three-dimensional view to better understand the nature of viscosities variation with temperature and pressure. While in Fig. 4.2.3.6 shows all experimental vapor viscosity data of R1132(E) representing both a) two-dimensional view and (b) three-dimensional view. The vapor viscosities are measured for a temperature range from 323 to 345 K at pressure up to 4.0 MPa. Therefore, the vapor phase data are scattered to a great extent among them than the liquid phase owing to the less consistent differential pressure and flow rates of Pyrex capillary tubes.

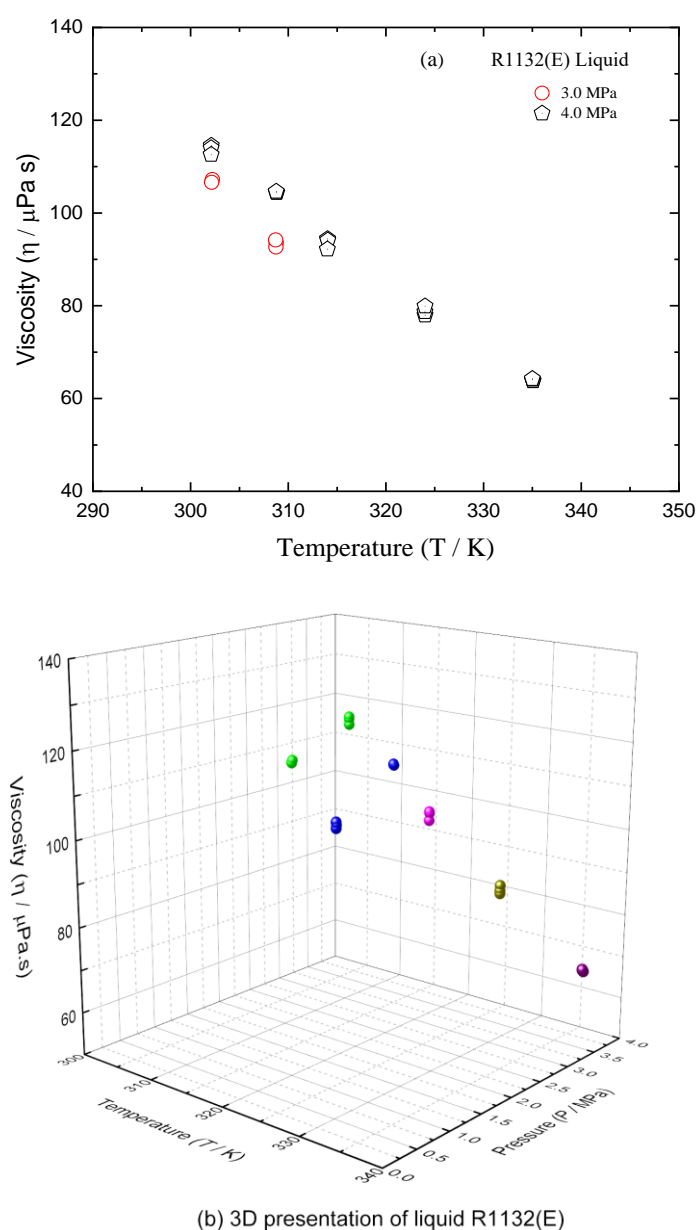


Fig. 4.2.3.5 Variation of the liquid viscosities of R1132(E) with temperature and pressure

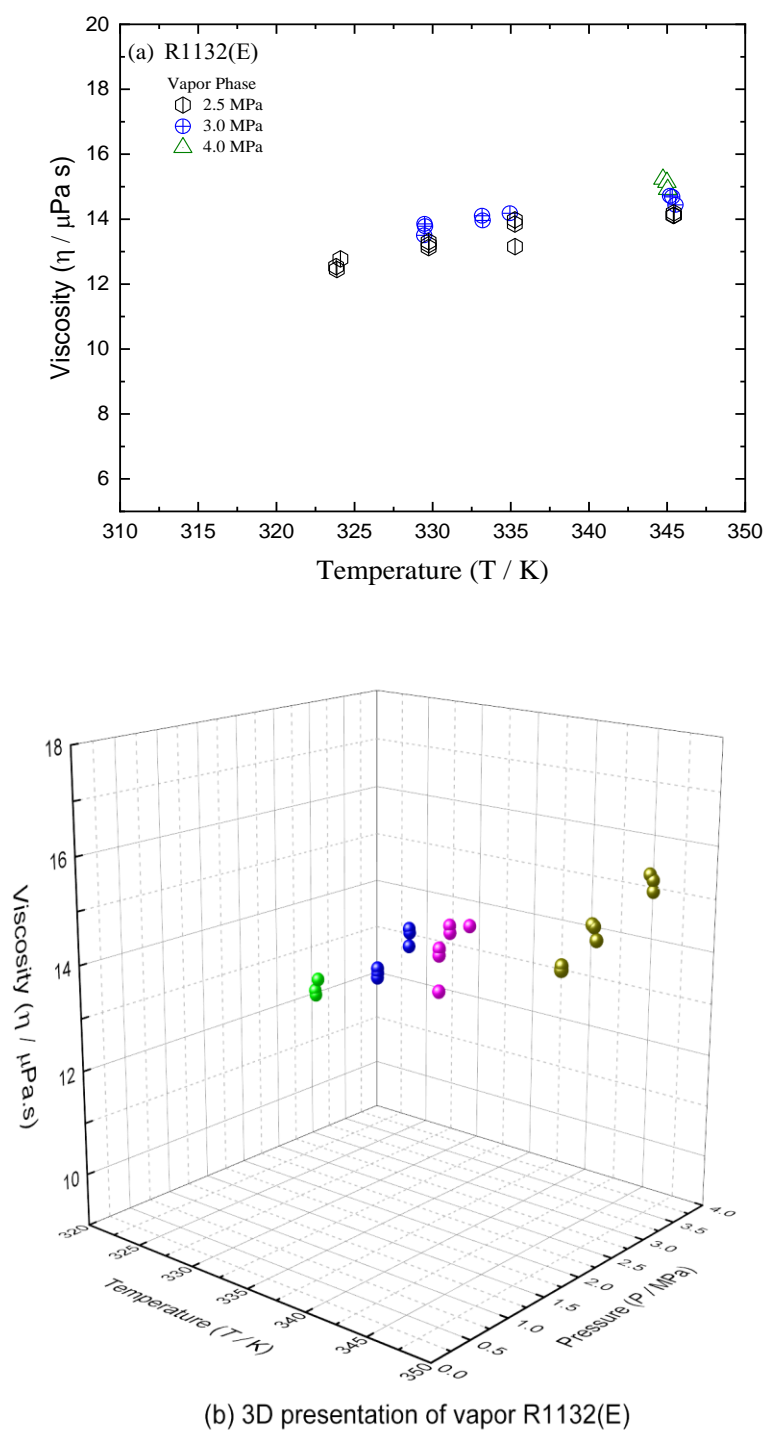


Fig. 4.2.3.6 Variation of the vapor viscosities of R1132(E) with temperature and pressure

4.2.3.3 Data deviations of R1132(E)

Figs. 4.2.3.7 and 4.2.3.8 show the deviation of the experimentally measured liquid and vapor viscosity data from the estimated data by the ECS model. In the liquid phase shown in Fig.

4.2.3.7, the measured data agreed and accepted well in the range from -10.5% to -18.5% deviations. At 308 K & 3.0 MPa , the measurements appear to have a systematic deviation that peaks at -19.15% by the ECS model. While in the vapor phase shown in Fig. 4.2.3.8, the deviations range from -10 to -16% . The measurements appear to show systematic negative deviation that reaches a peak of -17.53% at temperature 323.87 K .

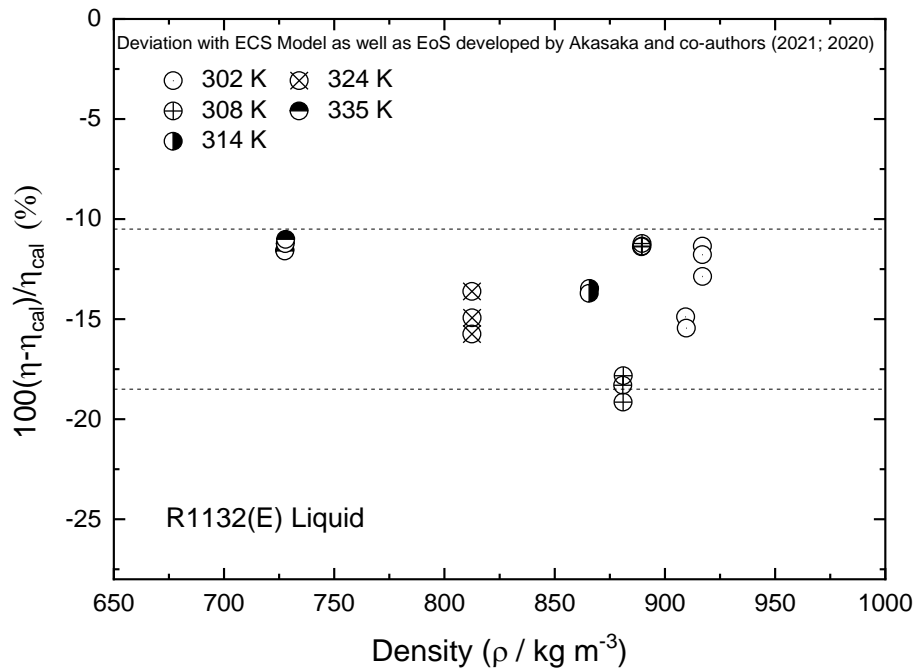


Fig. 4.2.3.7 Comparative study of viscosity data deviations for liquid R1132(E)

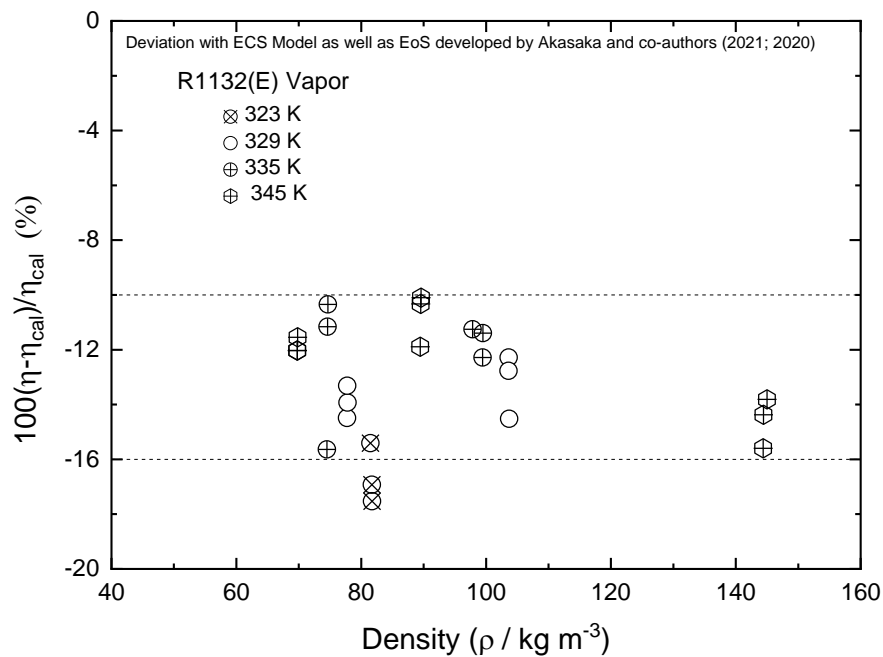


Fig. 4.2.3.8 Comparative study of viscosity data deviations for vapor R1132(E)

For the measurement of R1132(E), the deviations of viscosity data are calculated from the predicted data by the ECS model Akasaka and co-authors (2021; 2020). The average absolute deviation of the measurement at the liquid phase is found as 13.71 %, while in the vapor is observed as 13.12 %, respectively. The viscosity deviations are summarized in Table 4.2.3.4 that indicates the average absolute deviation (AAD %), maximum absolute deviation (MAD %), and average percentage deviation (Bias %), as follows:

Table 4.2.3.4 Study comparison of the viscosity deviations in terms of AAD, MAD, and Bais

Phases	Parameters	ECS Model*
Liquid	AAD (%)	13.71
	MAD (%)	19.15
	Bias (%)	-13.71
Vapor	AAD (%)	13.12
	MAD (%)	17.53
	Bias (%)	-13.12

*Calculated with the help of the ECS Model as well as EoS developed by Akasaka and co-authors (2021; 2020)

4.2.3.4 Conclusion

In this part of the study, the viscosity measurements of R1132(E) are conducted by the method of tandem capillary tubes. The measurements are performed over the pressure up to 4.0 MPa at a temperature range from 302 to 335 K for liquid and 323 to 345 K for vapor phases, respectively. Corresponding to the above pressure and temperature, the measured liquid and vapor viscosities of R1132(E) are reported at a range of 63.8 to 114.5 $\mu\text{Pa s}$, and 12.5 to 15.2 $\mu\text{Pa s}$, respectively. The experimental data are correlated with the ECS model obtaining the AAD of 13.71 % for the liquid phase and 13.12 % for the vapor phase. Owing to less consistent flow rate as well as differential pressure of Pyrex capillary tubes, the experimental results for the vapor phase are more dispersed among them, with systemic negative variations, comparable to liquid. Surprisingly, the data deviations phase in terms of AAD and MAD for the liquid are found somewhat larger than the vapor phase.

4.2.4 Viscosity measurement of the binary mixture of R1123+R32

4.2.4.1 Overview of a binary mixture of R1123+R32

A new challenge for refrigeration industries is to find out the potential working fluids having more environmentally friendly properties and sustainable replacement ability for use in standard applications, including refrigeration systems, heat pumps, and organic Rankine cycles. The key attentions of this study are to measure the viscosities of a binary mixture of R1123+R32 and correlated these data with other research data. Recently, hydro-fluoro-olefins (HFOs) and hydro-chlorofluoro-olefins (HCFOs) are two of the most promising alternatives to low-GWP fluids. Although some HFOs including R1234yf, R1234ze(E), R1233zd(E), R1224yd(Z) have been produced and expected as the alternatives for room air conditioners and the heat pumps, applicable equipment is limited because of their limited thermophysical properties (Higashi and Akasaka, 2016; Lemmon et al., 2009). On the other hand, hydrofluorocarbons (HFCs) have high GWP and, thus, there is a vital need to replace them to decrease HFC emissions. As of now, R32 (difluoromethane) is treated as the most prominent refrigerant of R22 or R410A alternatives due to its relatively lower GWP and excellent thermodynamic properties for high system performance. However, the usage amount of R32 has to be reduced according to the Kigali Amendment to the Montreal Protocol. Higashi and Akasaka (2016) and Tanaka et al. (2014) describe that R1123 (trifluoroethylene; $\text{CF}_2=\text{CHF}$; Molar mass is $82.0245 \text{ g}\cdot\text{mol}^{-1}$) belongs to the HFO family and has been appeared by the Japanese refrigerant company. It is expected as close to the thermophysical properties of R32. R1123 has zero ODP, and GWP is 0.3 on 100 years basis. The critical temperature and pressure of R1123 are 331.73 K and 4.546 MPa, respectively, and unsaturated carbon bond effects on an atmospheric lifetime of 1.6 days (AGC, 2016; Higashi and Akasaka, 2016). The normal boiling point of R1123 and R32 are 214.06 K and 221.50 K, respectively, wherein AMOLEA 400X is a blend of R1123 and R32 and the normal boiling point is 216.75 K. As per AGC Chemicals (AGC, 2016) and Akasaka et al. (2016), AMOLEA 400X has higher performance and temperature glide of 1.4 K at 1.8 MPa. It is well known that a large temperature glide of the refrigerant will cause the deterioration of the heat exchange rate in heat exchangers of air conditioners. Therefore, a mixture with a small temperature glide should be chosen to maintain the refrigeration performance. Although the R1123 has the potential to disproportionate explosively as does tetrafluoroethylene, it was proposed to reduce the risk of explosive self-decomposition reaction by mixing it with R32, vinylidene fluoride, and so

on (Hashimoto et al., 2019; Lisochkin and Poznyak, 2006). In fact, under the experimental conditions employed, no disproportionation propagation occurred in the mixture containing lower than 45 wt% of R1123 (Hashimoto et al., 2019; Otsuka et al., 2018). Conversely, mixtures containing 55 wt% or more R32 have no propagation that means increasing the concentration of R32 makes disproportionation propagation in a mixture more difficult to be initiated. Compared to other HFO+HFC mixtures, the 40/60 wt% mixture of R1123+R32 will be a good selection not only for safety assurance (Hashimoto et al., 2019) but also for the low GWP and refrigeration performance. The alternative working fluids should have low toxicity, low flammability, reasonable atmospheric lifetime, near-zero ODP, and ultra-low GWP (Miyara et al., 2018a, 2018b). The molecular structure and the basic thermophysical properties of pure refrigerants are presented in Fig. 4.2.4.1 and are listed in Table 4.2.4.1, respectively. Therefore, the mixture of R1123+R32 has zero ODP, a reasonable atmospheric lifetime, and a GWP of 406 on 100 years basis (AGC, 2016; AIST, 2016). These are the basic thermophysical properties introducing strong evidence of the smaller environmental impact of the R1123+R32 mixture.

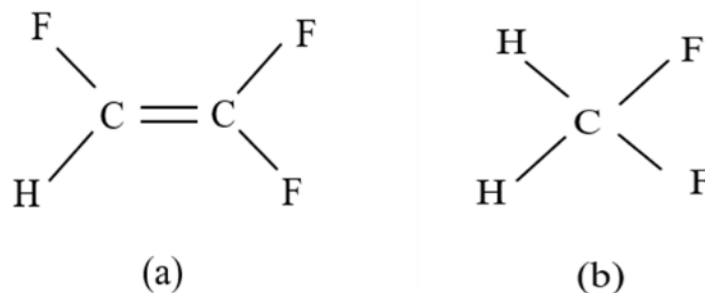


Fig. 4.2.4.1 Molecular structure of (a) R1123 and (b) R32

As a consequence, the experimental thermophysical properties of R1123 and R32 are required to evaluate their feasibility as a working fluid in commercial systems and appliances. The $P\rho T$ properties, critical parameters, vapor pressures, saturated vapor, and liquid densities, and vapor-liquid coexistence curve near the critical point of R1123 and R1123+R32 mixture were measured by the different experiments and described in Higashi and Akasaka (2016). In addition, Akasaka et al. (2016) developed a Helmholtz energy equation of state for R1123. In the design of the heat exchangers to describe its flow behavior, convection characteristics as well as two-phase heat transfer and pressure drop, it is necessary to utilize the proper knowledge of viscosity and thermal conductivity of test fluid (Kim et al., 2004).

Table 4.2.4.1 Fundamental properties of R1123 and R32

Parameters	R1123	R32
Chemical formula	CF ₂ =CHF	CH ₂ F ₂
CASRN	359-11-5	75-10-5
Critical temperature (K)	331.73 ^[g]	351.26 ^[a, f]
Critical pressure (MPa)	4.546 ^[g]	5.785 ^[a, e]
Critical density (kg m ⁻³)	492 ^[c, e]	424 ^[a, f]
Molecular weight (g mol ⁻¹)	82.0245	52.024
Flammability limits (vol%)	10.4-29.3 ^[b, e]	14.4-29.3 ^[e]
Normal Boiling point (K)	214.06 ^[c]	221.50 ^[e]
Atmospheric lifetime (days)	1.6 ^[a, b]	4.9 ^[a]
ODP	0 ^[b, e]	0 ^[a]
GWP (100 year)	0.3 ^[a, b]	677 ^[a]
ASHRAE Classification	A2L (Expected) ^[d, e]	A2L ^[e, d]

^aAGC (2016); ^bAIST (2016); ^cAkasaka et al. (2016); ^dASHRAE (2016); ^eHashimoto et al. (2019); ^fHigashi (1994); ^gHigashi and Akasaka (2016)

In addition to the thermodynamic properties, the transport properties of R1123+R32 are essential for the optimum design of energy systems, efficient processes, selection of the refrigerant, and accurate design in the components of HVAC systems. Transport properties of the other mixture of R1234yf with R32 and R125 had been measured by Dang et al. (2015a, 2015b). However, the measured data of the transport properties of the R1123+R32 mixture are very limited. Our research group (Hori et al., 2018; Mondal et al., 2019) reported some limited data of liquid and vapor viscosity of R1123+R32 at the conference. After that, all of the liquid and vapor viscosity data of a binary mixture of R1123+R32 are reported by Mondal et al., (2020). There are a few other experimentally measured viscosity data of R1123+R32 available in the open literature. In this part of the study, the viscosity of the R1123+R32 mixture was measured by the tandem capillary tube method over wider measurement ranges. For the liquid phase, the temperature range was from 250.64 K to 312.61 K and pressure was up to 4.0 MPa. For the vapor phase, the temperature range was from 323.35 K to 382.88 K at pressures up to 4.5 MPa. The measured liquid and vapor viscosity data were correlated with the Grunberg-Nissan method and Wilke mixture correlation, respectively. The deviations of the experimental data from the calculated values using the ECS model and the correlations were determined. Uncertainties of viscosity measurements were evaluated following the law of propagation of uncertainties (Bell, 2001; JCGM 100, 2008; Taylor and Kuyatt, 1994).

4.2.4.2 Measured viscosities of a binary mixture of R1123+R32 and correlation

In the present work, the viscosity of R1123+R32 was measured using the tandem capillary tube method along with a wide range of temperatures and pressures for liquid and vapor states, respectively. The measurements covering the region for temperature and pressure are shown in Fig. 4.2.4.2. In this figure, the vapor-liquid saturation line was drawn using the equation of state of Akasaka et al. (2016) as well as Higashi and Akasaka (2016). The mixture refrigerant was withdrawn from the sample cylinder into the apparatus in the liquid state. As the withdrawal procedure was in the liquid state, the bulk composition in the apparatus would be equal to the bulk composition of the cylinder. However, the composition change would also be expected. Therefore, the mass fraction of R1123+R32 was measured using gas chromatography (GC-2014AT 100V). The calibrated uncertainty of gas chromatography was within $\pm 0.2\%$ so that the accuracy of mass fraction calculated from the calibration curve is well agreed. In this work, the measurements were carried out of the R1123/R32 mixture for the mass fraction 0.428/0.572 in the liquid phase and 0.425/0.575 in the vapor phase. The critical temperature and pressure of the R1123+R32 mixture were measured by Higashi and Akasaka (2016) corresponding to the mass fraction of 0.401/0.599. According to their measurement, the critical temperature and pressure were reported as 338.01 K and 5.152 MPa, respectively.

Fig. 4.2.4.2 shows the experimental conditions covering the temperature and pressures for viscosity measurements of R1123+R32. In most cases, it had been measured approximately three times for each measurement. The time duration between the two measurements was at least 30 minutes, wherein the temperature and pressure changed slightly. Therefore, the viscosity of liquid was recorded over the temperature range from 250.64 K to 312.61 K at pressure up to 4.0 MPa and in the vapor phase from 323.35 K to 382.88 K at pressure up to 4.5 MPa. All the experimentally measured data are listed in Tables 4.2.4.2 and 4.2.4.3. The expanded uncertainties of viscosity measurements for both liquid and vapor phases are 2.10 % and 2.60 %, respectively, which are shown at the bottom of the tables with the other standard uncertainties.

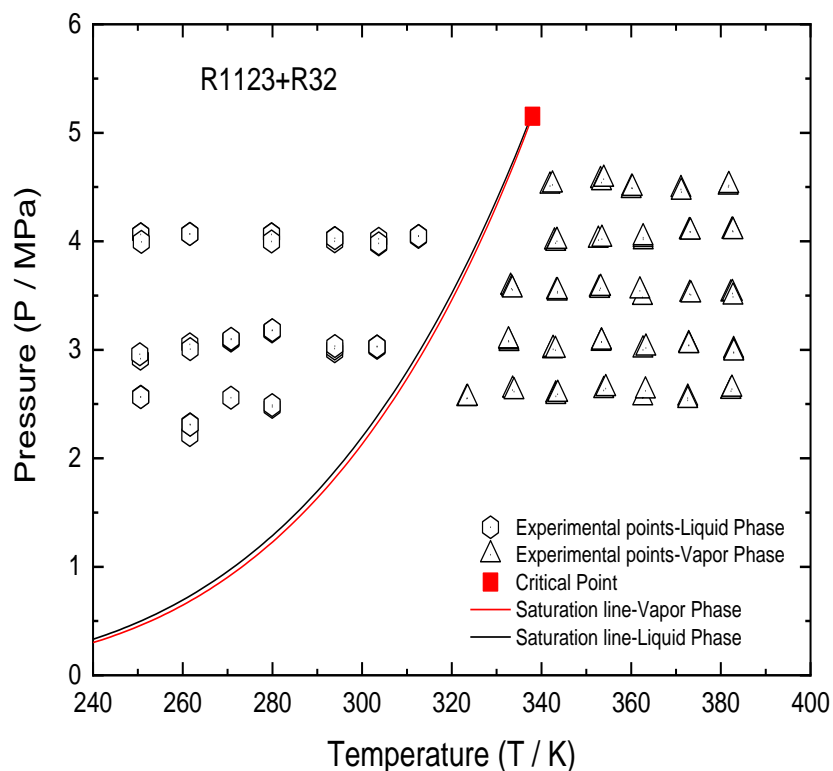


Fig. 4.2.4.2 Temperature and pressure ranges for the binary mixture of R1123+R32

Table 4.2.4.2 Experimental viscosity, η_{exp} ($\mu\text{Pa s}$) of R1123+R32 mixture at liquid phase^d

T (K) ^a	P (MPa) ^b	η_{exp} ($\mu\text{Pa s}$) ^c	$\Delta\eta_1$ ^f (%)	$\Delta\eta_2$ ^g (%)
250.64	4.065	199.59	4.19	-2.67
250.65	4.063	199.78	4.30	-2.56
250.77	3.995	200.44	4.87	-2.00
250.56	2.919	199.22	5.09	-1.80
250.43	2.959	198.77	4.63	-2.26
250.64	2.567	198.54	5.20	-1.67
250.66	2.564	198.58	5.24	-1.63
261.60	4.069	179.49	6.87	1.59
261.60	4.068	179.17	6.68	1.42
261.60	4.066	179.08	6.63	1.37
261.58	3.051	176.15	6.06	0.86
261.58	3.050	175.68	5.78	0.59
261.67	3.007	176.43	6.41	1.21

261.60	2.213	175.75	6.88	1.68
261.63	2.313	175.57	6.69	1.50
261.67	2.309	175.95	6.98	1.77
270.76	3.085	154.46	3.77	0.14
270.77	3.095	155.22	4.27	0.62
270.78	3.101	154.60	3.86	0.23
270.74	2.558	152.71	3.28	-0.31
279.81	4.065	137.10	1.19	-0.98
279.82	4.064	137.38	1.40	-0.78
279.82	3.998	136.82	1.08	-1.08
279.90	3.169	136.84	2.45	0.32
279.93	3.179	136.02	1.86	-0.26
279.97	3.180	135.52	1.52	-0.58
279.96	2.474	136.93	3.68	1.57
279.96	2.490	137.76	4.28	2.16
293.89	4.030	112.07	-1.86	-1.83
293.90	4.000	112.50	-1.41	-1.39
293.92	4.029	112.48	-1.46	-1.43
293.89	2.987	110.84	-0.89	-0.78
293.91	3.012	110.43	-1.29	-1.19
293.95	3.034	110.73	-1.02	-0.91
303.70	3.971	96.99	-3.32	-1.88
303.71	4.023	98.05	-2.37	-0.92
303.71	3.980	97.44	-2.87	-1.43
303.33	3.019	97.71	-0.66	0.89
303.34	3.031	98.90	0.53	2.10
303.34	3.029	99.74	1.40	2.99
312.54	4.041	85.51	-3.13	-0.50
312.58	4.049	84.27	-4.51	-1.91
312.61	4.047	84.45	-4.25	-1.65

^a Standard uncertainty of temperature is $u(T) = 0.029$ K; ^b Standard uncertainty of the pressure is $u(P) = 0.004$ MPa

^c Combined standard uncertainty is $u_c(\eta) = 1.10$ %; ^e Expanded uncertainty $U_c(\eta) = 2.21$ % with $k=2$ and 95 % confidence level

^d Mass fraction in the liquid phase of R1123/R32 = 0.428/0.572 by mass

^f $\Delta\eta_1$ is defined as the deviation between the experimental and calculated viscosity using the ECS model (Huber, 2018; Lemmon et al., 2018)

^g $\Delta\eta_2$ is defined as the deviation between the experimental and calculated viscosity using the G-N (Grunberg and Nissan, 1949; Viswanath et al., 2007) method; (Eq. 4.2.4.1)

In the case of the liquid phase, the experimental data can also be correlated with the method proposed by Grunberg and Nissan (G-N) (1949), which optimizes applicability and simplicity (Jung and Didion, 1990):

$$\ln \eta_{mix} = m_1 \ln \eta_1 + m_2 \ln \eta_2 + 2m_1m_2Z_{12} \quad (4.2.4.1)$$

where m_1 and m_2 are the mass fractions of the component, η_{mix} is the mixture viscosity in $\mu\text{Pa s}$, and Z_{12} is an interaction coefficient which is dependent on temperature, but independent of composition (Viswanath et al., 2007). The interaction coefficient is a function of components 1 and 2 as well as the temperature. For the pure refrigerant, the interaction coefficient is zero. But when one refrigerant is mixed with another refrigerant then introduced this coefficient due to optimizing the scarcity of the component as well as the component's proportion (Poling et al., 2000; Viswanath et al., 2007). For this measurement, the interaction coefficient was obtained by the least-square method from the measured mixture viscosity data and using the Eq. (4.2.4.1). Then correlation equation can be found by linear fitting of Z_{12} values as the function of temperature. Therefore, the interaction coefficient (Z_{12}) can be obtained from the correlation Eq. (4.2.4.2) as well as Fig. 4.2.4.3.

$$Z_{12} = -0.003T + 0.7168 \quad (4.2.4.2)$$

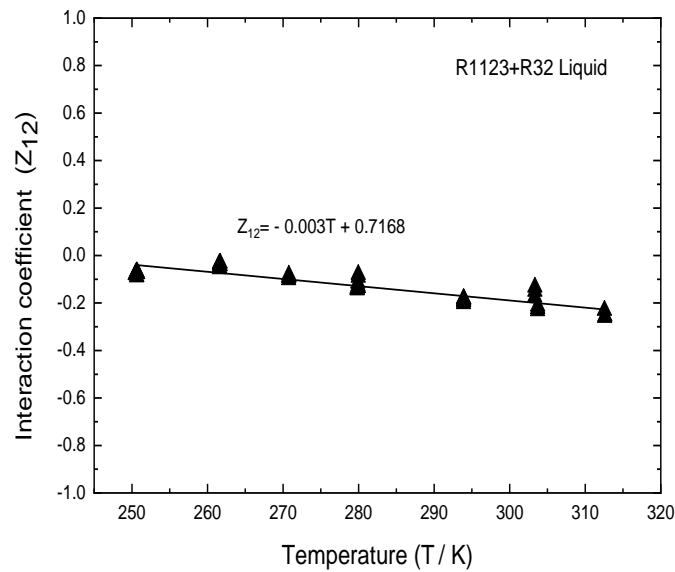


Fig. 4.2.4.3 Variation of interaction coefficient as a function of temperature at the liquid phase

To estimate correlations for the viscosities of the vapor phase mixtures, the relation was developed by Wilke (1950), which was used by other researchers (Dang et al., 2015a; Davidson, 1993), as defined as:

$$\eta_{mix} = \frac{m_1 \eta_1}{m_1 + m_2 \phi_{12}} + \frac{m_2 \eta_2}{m_2 + m_1 \phi_{21}} \quad (4.2.4.3)$$

where ϕ_{12} , and ϕ_{21} are the Sutherland coefficients (Cheung, 1958; Sutherland, 1895), as defined by:

$$\phi_{12} = \frac{\left[1 + (\eta_1 / \eta_2)^{0.5} (M_2 / M_1)^{0.25} \right]^2}{\left[8 \{ 1 + (M_1 / M_2) \} \right]^{0.5}} \quad (4.2.4.4)$$

$$\phi_{21} = \frac{\eta_2}{\eta_1} \frac{M_1}{M_2} \phi_{12} \quad (4.2.4.5)$$

where M_1 , and M_2 are the molecular weight of pure refrigerant in kg.mol⁻¹. The measured liquid and vapor data are correlated by using the above equation from Eq. (4.2.4.1) to Eq. (4.2.4.5), whereas the viscosity of each component (η_1 of R1123 and η_2 of R32) was calculated by the ECS model (Huber, 2018; Lemmon et al., 2018). The deviations of the experimental data from the calculated values using the ECS model and the correlations are demonstrated in Tables 4.2.4.2 and 4.2.4.3, and Figs. 4.2.4.8 and 4.2.4.9.

Table 4.2.4.3 Experimental viscosity, η_{exp} ($\mu\text{Pa s}$) of R1123+R32 mixture at vapor phase^d

T (K) ^a	P (MPa) ^b	η_{exp} ($\mu\text{Pa s}$) ^c	$\Delta\eta_1$ ^f (%)	$\Delta\eta_2$ ^g (%)
323.35	2.552	14.63	-3.39	-4.16
323.50	2.552	15.13	-0.14	-0.94
333.57	2.629	15.43	-1.18	-1.91
333.86	2.614	15.32	-1.90	-2.61
332.78	3.059	15.49	-2.40	-3.58
332.70	3.074	15.46	-2.67	-3.87
332.63	3.084	15.54	-2.21	-3.43
333.13	3.578	16.16	-1.50	-3.65
333.36	3.563	15.97	-2.56	-4.63
333.49	3.552	15.94	-2.70	-4.73
343.19	2.584	15.98	-0.12	-0.75
343.21	2.570	15.72	-1.73	-2.34
343.62	2.590	15.95	-0.43	-1.05
342.49	2.992	15.55	-3.97	-4.89
342.58	3.004	15.52	-4.25	-5.17
343.12	2.996	15.79	-2.70	-3.62
343.35	3.536	16.11	-3.17	-4.67
343.53	3.525	16.23	-2.39	-3.89
343.56	3.537	16.01	-3.79	-5.28
342.91	3.996	16.63	-2.84	-5.19
343.18	3.982	16.64	-2.67	-4.97
343.46	4.000	16.55	-3.37	-5.67
341.91	4.509	17.01	-5.21	-9.43
342.45	4.520	17.02	-5.23	-9.36
353.90	2.624	15.96	-3.11	-3.69
354.32	2.643	15.92	-3.49	-4.08
353.31	3.061	16.26	-2.44	-3.30
353.36	3.072	16.46	-1.32	-2.21
353.41	3.071	16.36	-1.93	-2.81
352.90	3.559	16.80	-1.04	-2.36
352.98	3.549	16.29	-4.02	-5.29

353.21	3.566	16.79	-1.18	-2.49
352.69	4.011	17.23	-0.72	-2.60
353.48	4.019	16.88	-2.91	-4.72
353.16	4.561	17.16	-4.63	-7.35
353.41	4.542	17.31	-3.67	-6.36
353.89	4.572	17.01	-5.61	-8.27
362.61	2.559	16.24	-3.45	-3.96
363.19	2.622	15.91	-5.72	-6.25
362.65	2.999	16.70	-1.89	-2.65
363.30	3.017	16.79	-1.57	-2.34
362.54	3.484	16.84	-2.58	-3.66
361.95	3.543	16.81	-2.81	-3.94
362.71	3.997	17.33	-1.78	-3.32
362.67	4.017	17.47	-1.11	-2.68
362.66	4.034	17.45	-1.30	-2.88
360.01	4.470	17.23	-4.30	-6.45
360.11	4.489	17.41	-3.42	-5.61
360.27	4.488	17.47	-3.12	-5.31
372.63	2.554	17.06	-1.12	-1.63
372.63	2.534	16.66	-3.36	-3.84
372.84	3.048	17.00	-2.67	-3.40
372.86	3.042	17.13	-1.93	-2.66
372.86	3.039	17.23	-1.30	-2.04
373.08	3.511	17.38	-1.86	-2.87
373.31	3.507	17.57	-0.85	-1.86
372.97	4.089	17.94	-0.71	-2.15
373.11	4.088	17.96	-0.63	-2.07
373.22	4.085	17.93	-0.78	-2.21
371.12	4.477	18.10	-1.14	-2.97
371.16	4.453	18.10	-1.04	-2.84
382.20	2.618	16.97	-4.04	-4.54
382.25	2.618	16.94	-4.21	-4.71
382.48	2.637	17.14	-3.16	-3.67

382.86	2.994	17.25	-3.41	-4.07
382.88	2.979	17.47	-2.14	-2.81
382.88	2.971	17.20	-3.64	-4.29
382.23	3.515	17.74	-1.84	-2.78
382.57	3.518	17.28	-4.49	-5.40
382.71	3.488	17.84	-1.34	-2.27
382.46	4.094	18.28	-0.73	-2.04
382.64	4.095	18.24	-0.97	-2.28
382.71	4.090	18.24	-0.94	-2.25
381.64	4.500	18.91	1.34	-0.32
381.77	4.515	19.09	2.27	0.58

^a Standard uncertainty of temperature is $u(T) = 0.054$ K; ^b Standard uncertainty of the pressure is $u(P) = 0.0056$ MPa

^c Combined standard uncertainty is $u_c(\eta) = 1.30$ %; ^e Expanded uncertainty $U_c(\eta) = 2.60$ % with $k=2$ and 95 % confidence level

^d Mass fraction in vapor phase of R1123/R32 = 0.425/0.575 by mass

^f $\Delta\eta_1$ is defined as the deviation between the experimental and calculated viscosity using the ECS model (Huber, 2018; Lemmon et al., 2018)

^g $\Delta\eta_2$ is defined as the deviation between the experimental and calculated viscosity using the Wilke correlation (Wilke, 1950); (Eq. 4.2.4.3)

The variation of experimental viscosity of the liquid R1123+R32 mixture is reported in Fig. 4.2.4.4 as a function of density, which was determined from the measured temperature and pressures. The viscosity of R1123+R32 was measured over a temperature range from 250.64 K to 312.61 K and pressure up to 4.0 MPa for the liquid phase. Distinct symbols were used to identify the measured temperatures.

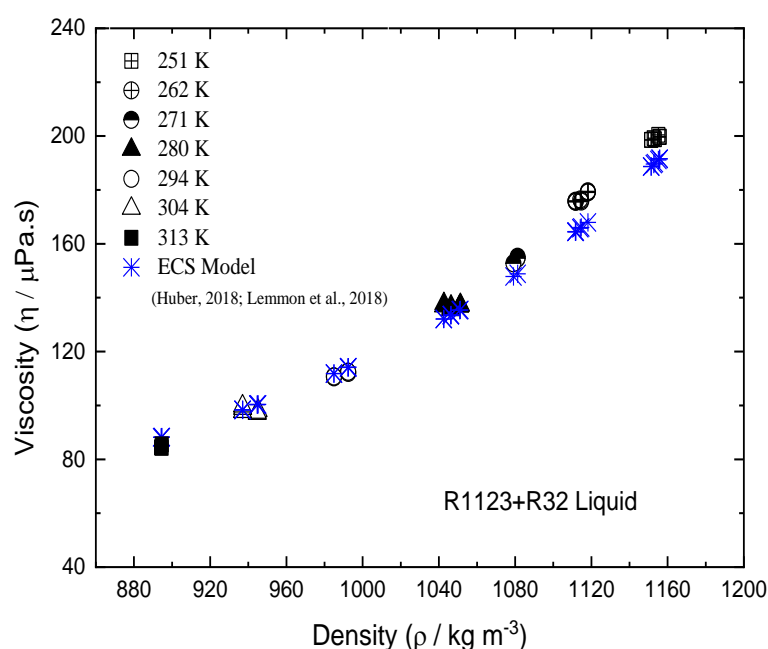


Fig. 4.2.4.4 Variation of viscosity data of liquid R1123+R32 mixture as a function of density

A typical change in viscosity was observed in the figure with temperature and density. It was noticed that the liquid R1123+R32 shows a reduction in viscosity with increasing the temperature, having a similar trend to the estimated values of the ECS model (Huber, 2018; Lemmon et al., 2018) that are also demonstrated in Fig. 4.2.4.4. In addition, the experimentally measured viscosity data of liquid R1123+R32 was correlated with the G-N empirical equation (Grunberg and Nissan, 1949; Viswanath et al., 2007).

On the other hand, the experimental viscosity data of the vapor R1123+R32 mixture as a function of density is presented in Fig. 4.2.4.5 over a temperature range from 323.35 K to 382.88 K and pressure up to 4.5 MPa. It was observed that the viscosity of vapor R1123+R32 decreases with the decrease in temperature, getting the same trend of predicted values by the ECS model. In this measurement, the viscosity data at 4.5 MPa pressure are exceedingly scattered among them up to 9.43% compared to other pressures due to the high-pressure measurement. Additionally, the experimentally measured viscosity data of vapor R1123+R32 was correlated with the Wilke mixture empirical correlation (Wilke, 1950).

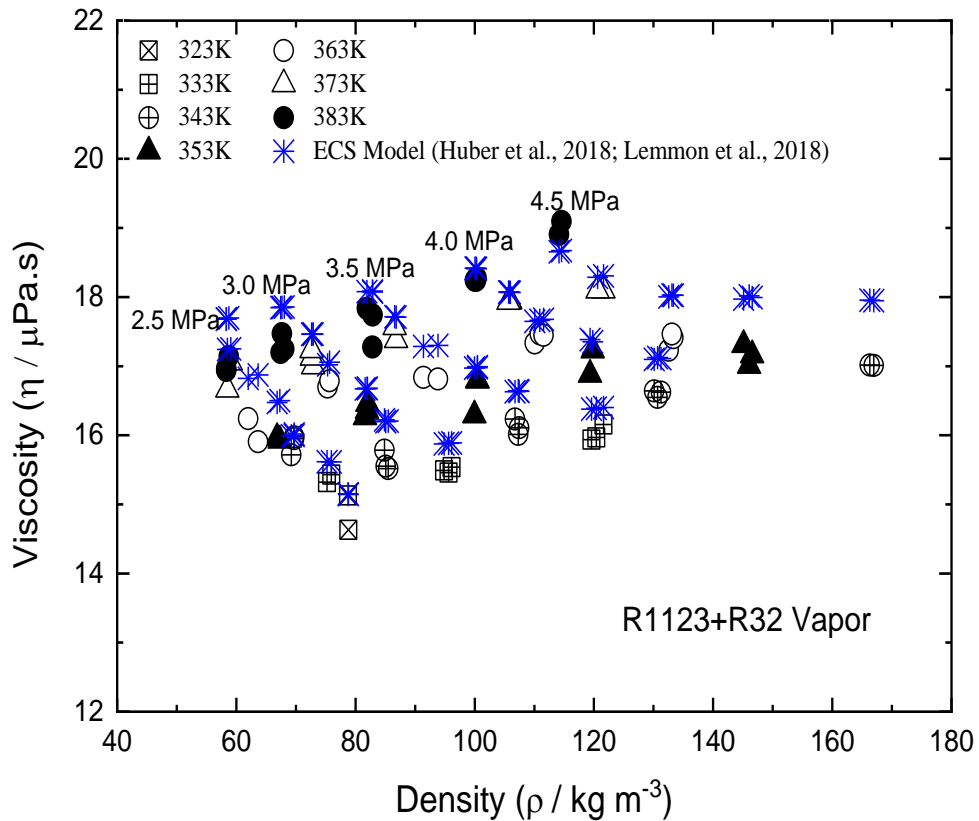


Fig. 4.2.4.5 Variation of viscosity data of vapor R1123+R32 mixture as a function of density

Finally, Figs. 4.2.2.6 and 4.2.2.7 demonstrate all experimental viscosities of a binary mixture of R1123+R32 for the liquid and vapor phases with the temperature ranging from 250.64 to 382.88 K over the pressure up to 4.5 MPa, which helps us to understand properly about the data trend both of liquid and vapor phases. Therefore, the measured vapor phase data are scattered to a great extent than the liquid phase owing to the less consistent differential pressure and flow rates through the Pyrex capillary tubes. The expanded uncertainty of the vapor phase was estimated at 2.60 % (with $k=2$ and 95 % confidence level) which is greater than the liquid phase's uncertainty of 2.21 %.

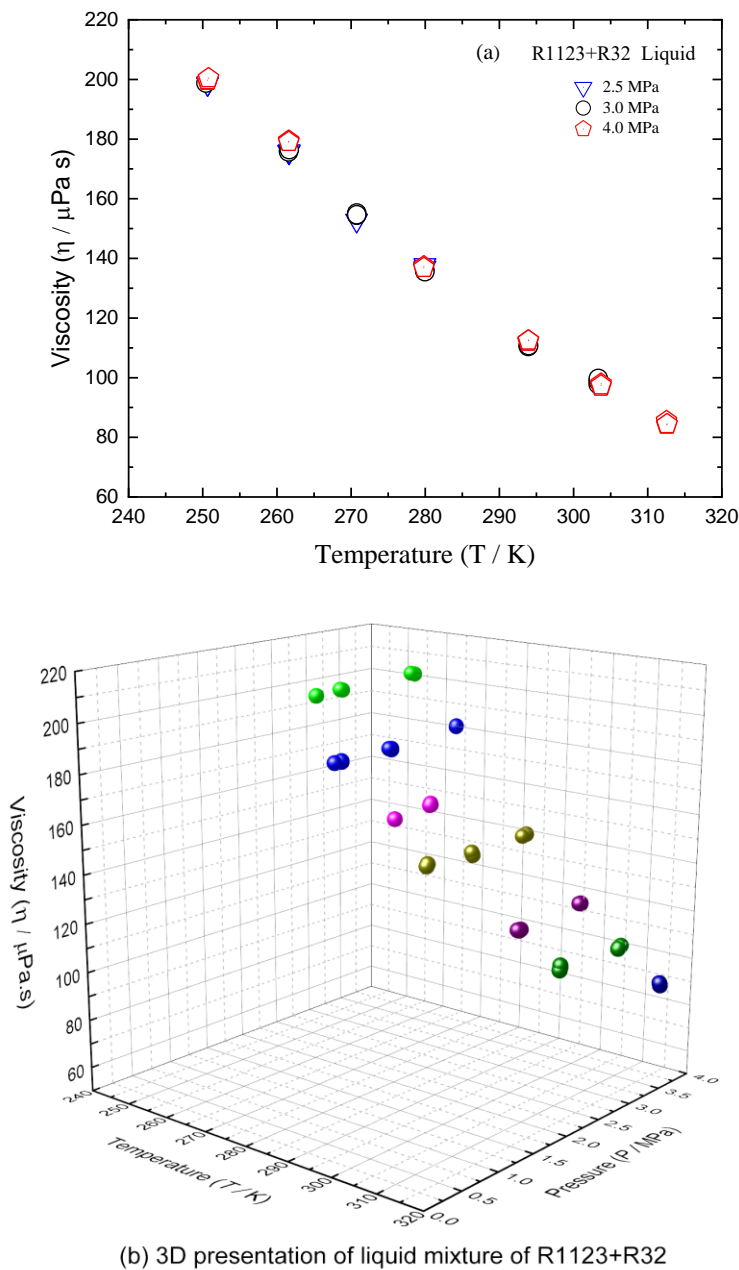
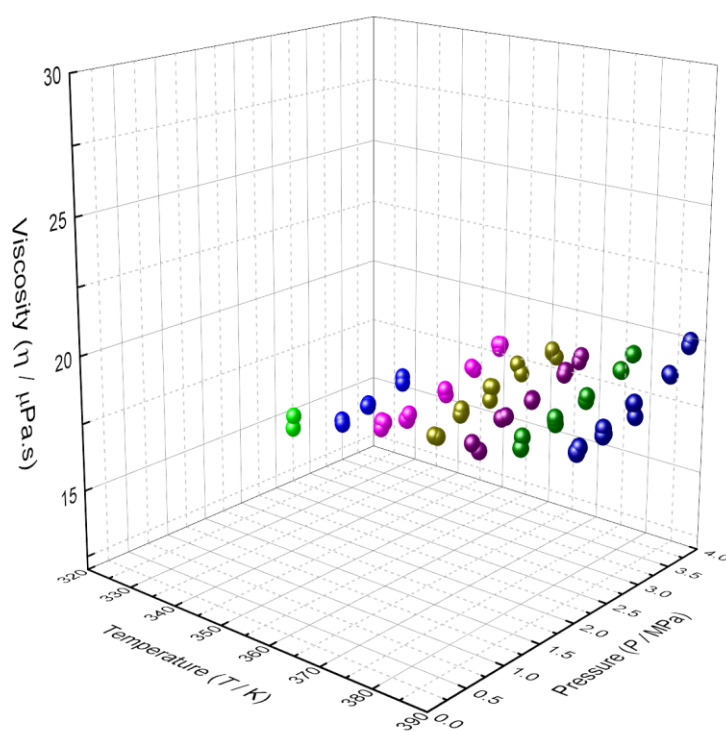
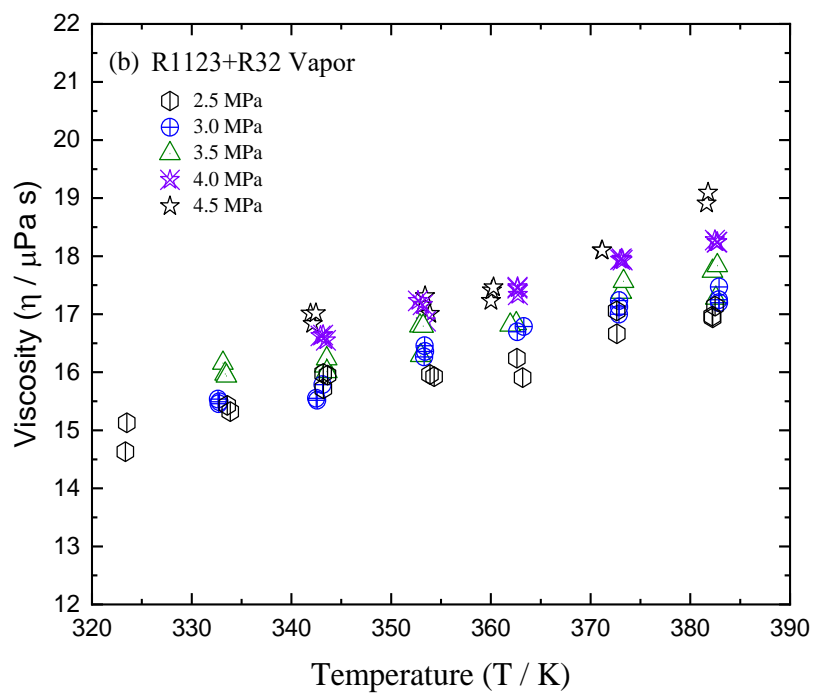


Fig. 4.2.4.6 Variation of the liquid viscosities of R1123+R32 with temperature and pressure



(b) 3D presentation of vapor mixture of R1123+R32

Fig. 4.2.4.7 Variation of the vapor viscosities of R1123+R32 with temperature and pressure

4.2.4.3 Data deviations of R1123+R32

Fig. 4.2.4.8 demonstrates the deviations of the experimental viscosity of the liquid phase against the calculated values of the ECS model and the Grunberg-Nissan correlation. Therefore, most of the data agreed well within a deviation of $\pm 4.5\%$, even if with a clear trend to increase with temperature. As shown in Fig. 4.2.4.8, the measurements seem to exhibit a systematic deviation which reaches a maximum of 6.98% at 262 K. The average absolute deviation of the measurement at the liquid phase was found as 3.63% for the ECS model and 1.33% for the Grunberg-Nissan correlation. The Grunberg-Nissan method, therefore, showed a good agreement with the experimental measurements of the liquid mixture than the ECS model.

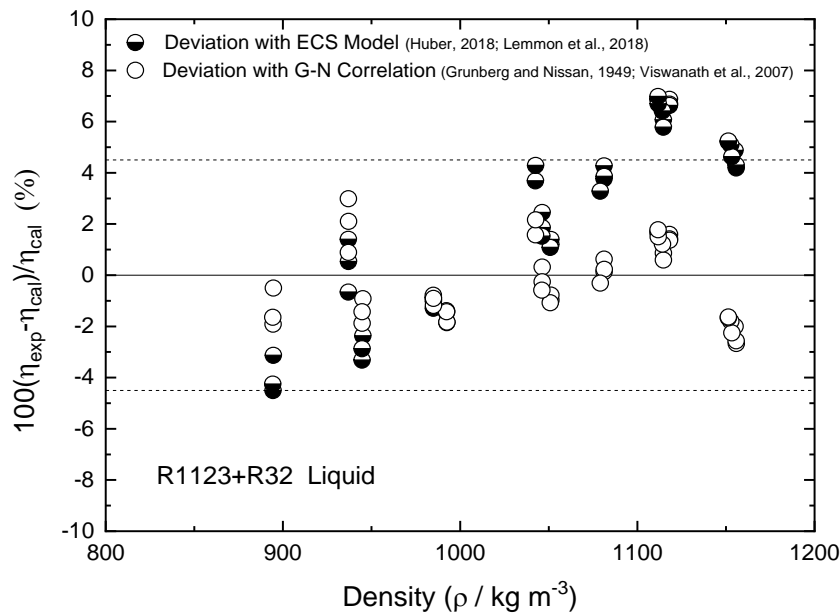


Fig. 4.2.4.8 Deviations of experimental viscosity from calculated values for the liquid R1123+R32

Fig. 4.2.4.9 illustrates the comparison of experimentally measured vapor viscosity data with the calculated values of the ECS model and the Wilke mixture correlation. The deviations of experimental data are evaluated and most of the data fall within deviation from -6.0% to $+1.5\%$. The average absolute deviation of the measured viscosity of vapor R1123+R32 was observed as 2.45% for the ECS model and 3.69% for the Wilke correlation. In the case of vapor viscosity, the deviations of experimental data from the ECS model are quite well than the Wilke correlation. Therefore, the experimental viscosity data of the vapor phase are scattered among them comparable to liquid due to less stable flow and differential pressure of short and long capillary tubes, with some systematic negative deviation from the ECS model

and correlations. The expanded uncertainty of measurements at the liquid phase was estimated to be less than 2.21 %, whereas less than 2.60 % for the vapor phase.

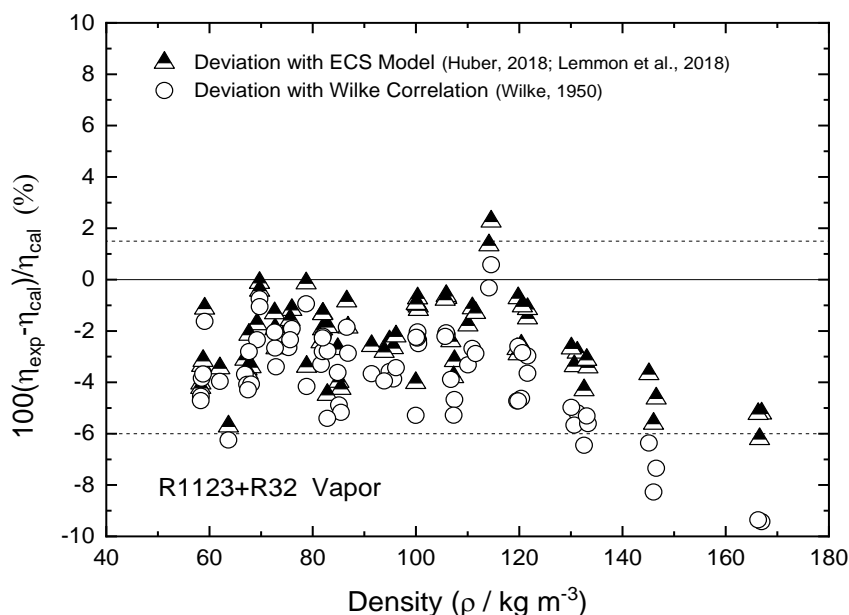


Fig. 4.2.4.9 Deviations of experimental viscosity from calculated values for the vapor R1123+R32

Table 4.2.4.4 summarizes the analysis of the deviations of viscosities in terms of the average absolute deviation (AAD %), the maximum absolute deviation (MAD %), and the average percentage deviation (Bias %) that are defined as follows:

Table 4.2.4.4 Comparison of the experimental viscosity of R1123+R32 with the calculated data

	Liquid Phase			Vapor Phase		
	AAD (%)	MAD (%)	Bias (%)	AAD (%)	MAD (%)	Bias (%)
*ECS model	3.63	6.98	2.28	2.45	5.72	-2.35
**Correlations	1.33	2.99	-0.26	3.69	9.43	-3.68

*ECS model developed by Huber (2018) and Lemmon et al. (2018)

** For liquid phase used Grunberg and Nissan (G-N) method (Grunberg and Nissan, 1949; Viswanath et al., 2007) and in vapor phase used Wilke correlation (1950)

4.2.4.4 Correlations at saturation conditions for R1123+R32

The simplified correlations for saturated viscosity were developed by extrapolating experimental data up to saturation conditions both of liquid and vapor phases. The extrapolation to get saturated viscosity of liquid R1123+R32 by identical temperature is understandable from Fig. 4.2.4.10. In the case of vapor, the saturated viscosity was extracted

by identical pressure and temperature. Then correlation equations can be found by linear fitting of saturated viscosity data in the function of temperature. The saturated viscosity of liquid R1123+R32 mixture, $\eta_{sat,L}$, can be obtained from Eq. (4.2.4.6) as a function of saturation temperature T_{sat} . Meanwhile, the viscosity of saturation vapor R1123+R32 mixture, $\eta_{sat,V}$, can be calculated by using Eq. (4.2.4.7). It is summarized that both saturated liquid and vapor correlations could be showed good results from room to high temperature. Fig. 4.2.4.11 demonstrates all extrapolated values, calculated values by Eqs. (4.2.4.6) and (4.2.4.7), and estimated values of the ECS model for saturated liquid and vapor viscosity of R1123+R32 which are listed in Table 4.2.4.5.

$$\eta_{sat,L} = -1.877T_{sat} + 664.41 \quad (4.2.4.6)$$

$$\eta_{sat,V} = 0.086T_{sat} - 12.11 \quad (4.2.4.7)$$

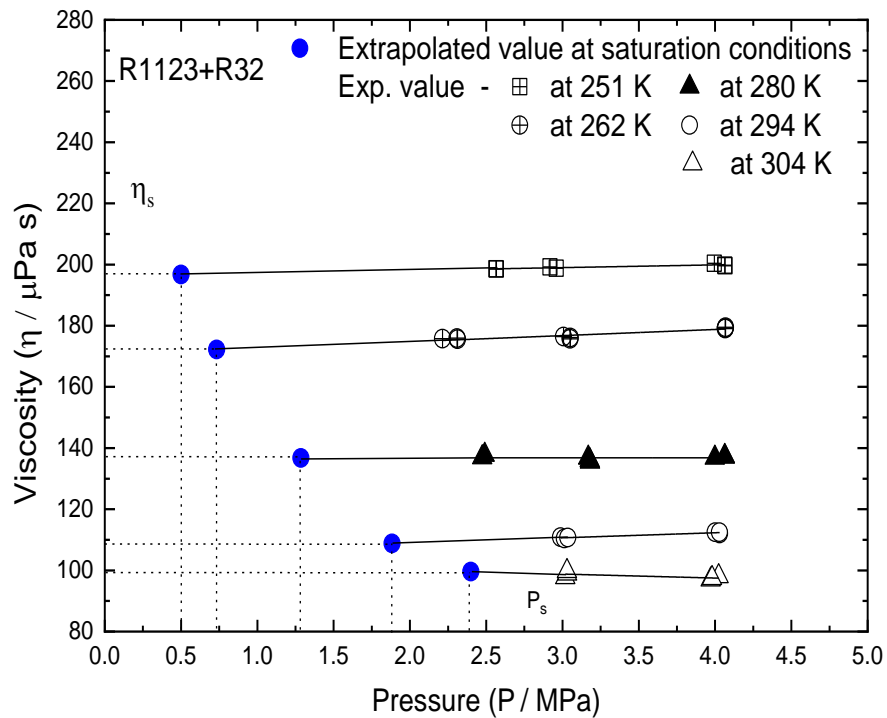


Fig. 4.2.4.10 Extrapolated value of liquid phase viscosity at saturation conditions

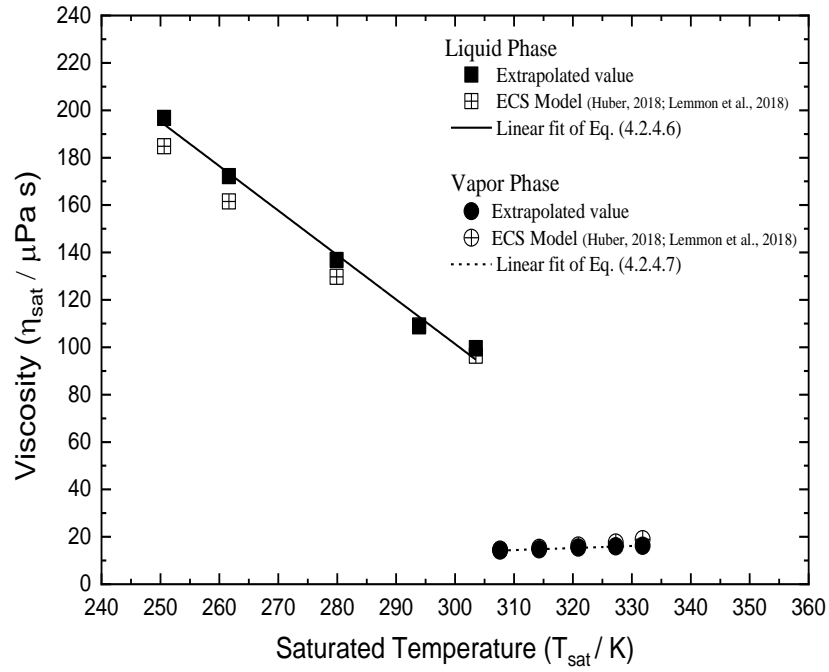


Fig. 4.2.4.11 Saturated viscosity vs. temperature

Table 4.2.4.5 Saturated viscosities, η_{sat} ($\mu\text{Pa s}$) of R1123+R32

(a) Liquid					
T (K)	P (MPa)	$\eta_{sat,L}$ Extrapolated	$\eta_{sat,L}$ Eq. (4.2.4.6)	$\eta_{sat,L}$ ECS Model	
250.62	0.500	196.77	193.99	184.79	
261.61	0.733	172.22	173.36	161.53	
279.90	1.286	136.77	139.05	129.69	
293.91	1.883	108.80	112.75	109.21	
303.52	2.399	99.59	94.70	96.37	
(b) Vapor					
T (K)	P (MPa)	$\eta_{sat,V}$ Extrapolated	$\eta_{sat,V}$ Eq. (4.2.4.7)	$\eta_{sat,V}$ ECS Model	
307.64	2.581	14.21	14.35	14.58	
314.30	3.029	14.70	14.92	15.32	
320.92	3.533	15.47	15.49	16.28	
327.28	4.077	15.97	16.04	17.57	
331.84	4.508	16.19	16.43	18.95	

4.2.4.5 Conclusion

In this work, the experimental viscosity data of mixture R1123+R32 are reported covering liquid and vapor phases using the tandem capillary tube method, respectively. These measured viscosity data are required for the design of efficient chemical processes, equipment, and simulation for refrigeration systems, organic Rankine cycle, and heat pumps. The liquid viscosity was measured for the mixture of R1123+R32 at a temperature from 250.64 K to 312.61 K for pressures up to 4.0 MPa, and in vapor mixture data were measured from temperature 323.35 K to 382.88 K at pressure up to 4.5 MPa. These measured data were compared with the estimated value of the ECS model, and the average absolute deviations were found at 3.63% for the liquid phase and 2.45% for the vapor phase, respectively. Also, the measured liquid and vapor viscosity data were correlated with the Grunberg-Nissan method and Wilke mixture correlation, respectively, while the AAD was 1.33% for liquid and 3.69% for vapor phases. Therefore, the experimental data of the vapor phase are scattered than the liquid due to less stability of flow rate and differential pressure of short and long tubes. The trifluoroethylene (R1123) with the mixture of the R32 is a useful alternative as the next generation refrigerant due to its lower GWP and refrigeration performance than that of those ordinarily used. The expanded uncertainties of viscosity measurements for R1123+R32 were estimated at 2.21 % and 2.60 % of the liquid and vapor phases, respectively. Also, the simplified correlations for saturation conditions in terms of saturated temperature are developed for both liquid and vapor phases by the extrapolation method.

4.3 Experimental Thermal Conductivity Measurement

The transient hot-wire method is a popular and precise technique to measure the thermal conductivity of liquids, solids, and gases. In this part of the study, the thermal conductivity measurement was conducted by the transient hot-wire method, where the two platinum hot wires were connected in the measurement cell to eliminate the end effects. The thermal conductivities were measured over a wide range of temperature and pressure for the working fluids R1336mzz(E) and 3,3,4,4,5,5-HFCPE. The experimental thermal conductivities data, with measurement uncertainties, comparison with other research data or existing models, and saturation correlations to predict the data are discussed in the following sections.

4.3.1 Thermal conductivity measurement of R1336mzz(E)

4.3.1.1 Overview of R1336mzz(E)

Measurements of thermal conductivities of the trans-1,1,1,4,4,4-hexafluoro-2-butene (R1336mzz(E)) in liquid, vapor, and supercritical phases are the key attention of this study, and the simple correlations at saturated state are developed to estimate the thermal conductivity for industrial design and simulation. As improved awareness of the environmental impact and governing pressures for the decline of greenhouse gas emissions by the Kyoto Protocol, more emphasis will be focused on alternatives that meet the new goals. Consequently, it is so significant to achieve novel substitutes with lower GWP and zero ODP value than conventional fluids. In recent, two fruitful alternatives as hydro-fluoro-olefins (HFOs) and hydro-chloro-fluoro-olefins (HCFOs) are growing a vital focus for their low GWP values that HCFOs have ODP, not zero ODP. The novel working fluids of HFOs are being established, as R1336mzz(E) and R1336mzz(Z), to meet the more stringent guidelines of low GWP and zero ODP and they exhibit the known attributes of good working fluids (Juhász, 2017). The suitable working fluid R1336mzz(E) is a non-flammable compound, high thermal stability, low GWP, and as expected in the application of waste heat recovery including high-temperature heat pumps (HTHP) and organic Rankine cycles (ORCs). It will be a replacement for R-245fa as a refrigerant enabling both HTHP and ORCs platforms to restore heat from several sources (Juhász, 2017; Tanaka et al., 2017b). It has a GWP value of 18 as well as zero ODP (Juhász, 2017) and is expected as a working fluid by the safety classification of A1 (Akasaka, 2019a; Yang et al., 2019) in ASHRAE Standard 34, due to its low toxicity and non-flammability. R1336mzz(E) is a hexafluoro-2-butene with an unsaturated bond similar to R1336mzz(Z). The

main difference between the trans- and cis- isomer is evident not only by the critical temperature and pressure but also by the boiling temperature and vapor pressure when looking at Table 4.3.1.1. The boiling point, critical temperature, and critical pressure of R1336mzz(E) were measured and reported by Tanaka et al. (2017b) and Sakoda et al. (2021) as 280.58 K, 403.53 K, and 2.779 MPa, respectively. Elsewhere, R1336mzz(Z) has a slightly higher boiling point of 306.55 K (Kontomaris, 2014). Again, the critical temperature and critical pressure of R1336mzz(Z) were measured and reported as 444.50 K and 2.90 MPa, respectively (Juhasz, 2017; Tanaka et al., 2017a). Therefore, the basic properties are summarized in Table 4.3.1.1 whereas the molecular geometry is illustrated in Fig. 4.3.1.1.

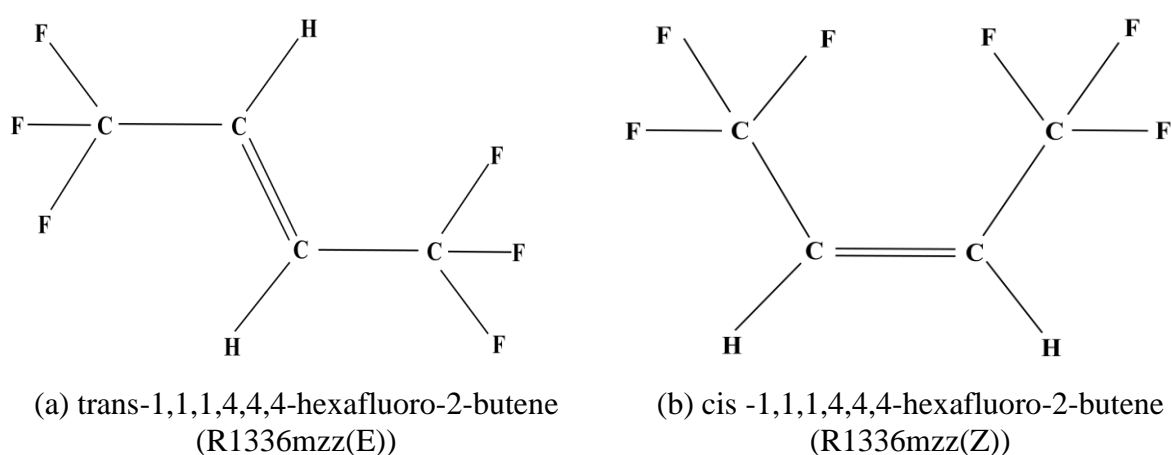


Fig. 4.3.1.1 Molecular geometry of R1336mzz(E) and R1336mzz(Z)

Table 4.3.1.1 Basic properties of HFO refrigerants R1336mzz(E) and R1336mzz(Z)

Parameters	R1336mzz(E)	R1336mzz(Z)
Chemical formula	Trans $\text{CF}_3\text{-CH=CH-CF}_3$	Cis $\text{CF}_3\text{-CH=CH-CF}_3$
CASRN	66711-86-2	692-49-9
Critical temperature (K)	403.53 (Sakoda et al., 2021)	444.50 (Tanaka et al., 2017a)
Critical pressure (MPa)	2.779 (Sakoda et al., 2021)	2.90 (Tanaka et al., 2017a)
Critical density (kg/m^3)	513.33 (Sakoda et al., 2021)	507 (Tanaka et al., 2017a)
Molecular weight (g/mol)	164.05 (Tanaka et al., 2017b)	164.056 (Kontomaris, 2014)
Flammability limits	Non-flammable	Non-flammable (ASTM, 2004)
Boiling point (K)	280.58 (Tanaka et al., 2017b)	306.55 (Kontomaris, 2014)
ODP	0	0
GWP (100 year)	18 (Juhasz, 2017)	2 (Myhre et al., 2013)

The thermodynamic properties, as well as transport properties of the working fluid, are key tools to design an energy system efficiently and to select a refrigerant for the practical appliances and simulations. Consequently, the transport properties of R1336mzz(E) are essential to evaluate its practicability as an alternative in commercial appliances and systems. A few of the thermodynamic properties of R1336mzz(E) has been disclosed herein the literature, especially the critical parameters, vapor pressures at saturation conditions, and the $P\rho T$ properties were measured and reported by Sakoda et al. (2021) and Tanaka et al. (2017c, 2017b). Also, a Helmholtz energy equation was delivered by Akasaka (2019a, 2019b) for R1336mzz(E). On contrary, the $P\rho T$ properties, temperature, and pressure for the critical conditions, vapor pressure, and saturated liquid and vapor density of R1336mzz(Z) were measured by Tanaka et al. (2017a, 2016). In a separate study, the viscosity and thermal conductivity of R1336mzz(Z) were presented by Alam et al. (2018, 2017). However, some of the thermal conductivity data for this refrigerant had been measured by our research group (Amakusa et al., 2021; Miyoshi et al., 2020; Mondal et al., 2021a; Tuhin et al., 2021). There are no experimental viscosity data, and very few thermal conductivity of R1336mzz(E) available yet in the literature. Therefore, in this part of the work, the thermal conductivity of R1336mzz(E) was measured by the technique of transient hot-wire for the liquid state at temperature ranges from 313 to 393 K at pressure up to 4.0 MPa and in vapor state from 313 to 453 K whereas the pressure at 0.25 to 2.5 MPa, respectively. The thermal conductivity in a supercritical region was also measured at temperature ranges from 413 to 453 K, and the pressure at 3.0 to 4.0 MPa. The experimentally measured thermal conductivity of R1336mzz(E) at the liquid and vapor states were compared with the measured values for R1336mzz(Z) as experimental setup, as well as measurement conditions, were almost similar to Alam et al. (2017). Moreover, the correlations at the saturated state were developed to predict the thermal conductivity by extrapolating the experimental data until the saturation conditions for both liquid and vapor states. The uncertainties for thermal conductivity measurements of R1336mzz(E) were estimated using the propagation law for uncertainties (Bell, 2001; JCGM 100, 2008; Taylor and Kuyatt, 1994).

4.3.1.2 Measured thermal conductivities of R1336mzz(E)

The thermal conductivity of R1336mzz(E) was measured by the transient hot-wire method over a wide range of temperatures and pressures. Fig. 4.3.1.2 illustrates the measurement conditions

covering the regions for temperatures and pressures wherein the saturation line was sketched utilizing the equation of state by Akasaka (2019a, 2019b). The critical temperature and pressure of R1336mzz(E) were measured and reported by Sakoda et al. (2021) and Tanaka et al. (2017b) as 403.53 K and 2.779 MPa, respectively. The thermal conductivity was reported for the liquid state at the temperatures of 313 to 393 K over the pressures up to 4.0 MPa and for the vapor state at 313 to 453 K and pressures from 0.25 to 2.5 MPa, respectively. Also, the thermal conductivity in a supercritical region was measured from the temperature range 413 to 453 K at pressures 3.0 to 4.0 MPa. At the corresponding temperature and pressure, each measurement was conducted 3 times (Yao et al., 2014) for the reproducibility of test results, and also the repeatable measurements didn't exceed $\pm 0.5\%$ scatter limits. Nevertheless, the time duration between two successive measurements was a minimum of half-hour wherein the temperature and pressure altered a little. Therefore, all the experimental thermal conductivity of R1336mzz(E) are listed in Tables 4.3.1.2, 4.3.1.3, and 4.3.1.4. The uncertainties of thermal conductivity measurements for the liquid, vapor and supercritical states are listed below on those tables.

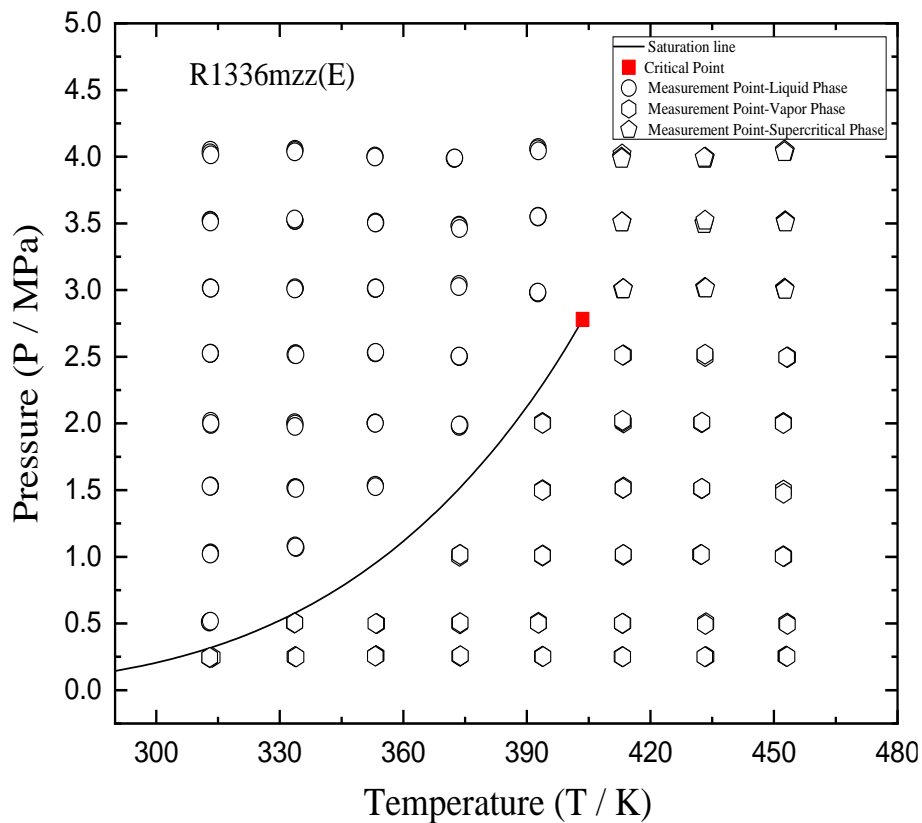


Fig. 4.3.1.2 Measurement points of R1336mzz(E)

Table 4.3.1.2 Experimental liquid thermal conductivity, λ (mW m⁻¹ K⁻¹) of R1336mzz(E)

T /(K)	P (MPa)	λ	T (K)	P (MPa)	λ
313.14	4.047	70.23	333.96	1.069	64.52
313.10	4.028	70.23	333.86	1.073	64.51
313.28	4.013	70.24	353.17	4.000	61.56
313.11	3.523	70.03	353.13	4.004	61.54
313.18	3.519	70.04	353.12	3.997	61.55
313.17	3.510	70.05	353.25	3.509	61.15
313.28	3.014	69.80	353.33	3.504	61.13
313.15	3.017	69.78	353.23	3.502	61.14
313.21	3.014	69.79	353.31	3.016	60.89
313.17	2.523	69.51	353.22	3.011	60.88
313.16	2.526	69.52	353.30	3.013	60.89
313.15	2.526	69.53	353.23	2.529	60.71
313.20	2.015	69.34	353.22	2.530	60.71
313.26	1.991	69.33	353.30	2.532	60.70
313.28	1.999	69.32	353.16	2.004	60.41
313.16	1.528	69.06	353.18	2.001	60.42
313.21	1.532	69.07	353.22	2.001	60.41
313.09	1.528	69.06	353.26	1.532	60.10
313.16	1.028	68.76	353.18	1.535	60.09
313.24	1.023	68.76	353.26	1.526	60.09
313.13	1.020	68.75	372.37	3.987	57.03
312.92	0.511	68.40	372.47	3.988	57.02
312.92	0.512	68.41	372.47	3.990	57.04
313.18	0.516	68.40	373.55	3.486	56.61
333.72	4.056	66.43	373.52	3.480	56.61
333.71	4.047	66.43	373.67	3.460	56.61
333.66	4.037	66.42	373.56	3.042	56.27
333.70	3.521	66.12	373.49	3.025	56.25
333.69	3.523	66.12	373.50	2.503	55.77
333.61	3.532	66.13	373.66	2.502	55.76

333.81	3.011	65.84	373.58	2.505	55.76
333.72	3.017	65.85	373.59	1.977	55.36
333.68	3.008	65.85	373.77	1.987	55.35
333.82	2.523	65.52	373.61	1.988	55.36
333.73	2.515	65.54	392.73	4.069	52.81
333.94	2.515	65.53	392.62	4.059	52.80
333.61	2.005	65.12	392.81	4.043	52.82
333.74	1.995	65.12	392.74	3.553	52.43
333.70	1.977	65.13	392.72	3.547	52.44
333.66	1.519	64.65	392.73	3.550	52.43
333.89	1.518	64.66	392.68	2.978	52.02
333.87	1.511	64.65	392.59	2.982	52.02
333.71	1.081	64.51	392.67	2.984	52.01

Standard uncertainties due to pressure and temperature are $u(P)=0.0017$ MPa and $u(T)=0.0189$ K
Combined standard uncertainty $u_c(\lambda)=1.53$ %; Expanded uncertainty $U_c(\lambda)=3.06$ % with $k=2$ and 95 % confidence level

Table 4.3.1.3 Experimental vapor thermal conductivity, λ ($\text{mW m}^{-1} \text{K}^{-1}$) of R1336mzz(E)

T (K)	P (MPa)	λ	T (K)	P (MPa)	λ
313.63	0.246	12.64	413.40	1.017	16.95
313.01	0.243	12.63	413.34	1.512	17.74
313.01	0.245	12.63	413.48	1.523	17.75
333.74	0.250	13.26	413.36	1.515	17.74
333.69	0.252	13.26	413.44	2.004	18.37
333.97	0.249	13.25	413.27	2.014	18.37
333.54	0.503	13.50	413.24	2.023	18.38
333.68	0.506	13.51	413.47	2.513	20.40
333.66	0.505	13.51	413.38	2.513	20.39
353.41	0.259	13.89	413.24	2.512	20.41
353.30	0.258	13.89	433.52	0.253	17.51
353.20	0.255	13.88	433.29	0.250	17.51
353.54	0.499	14.24	433.22	0.250	17.50
353.52	0.501	14.25	433.42	0.497	17.79
353.35	0.500	14.25	433.49	0.506	17.81
373.81	0.256	14.71	433.36	0.494	17.80

373.69	0.256	14.70	432.18	1.018	18.06
373.85	0.258	14.71	432.30	1.018	18.07
373.71	0.505	14.95	432.39	1.018	18.08
373.75	0.497	14.95	432.53	1.511	18.58
373.83	0.506	14.96	432.38	1.510	18.57
373.72	1.019	15.20	432.46	1.513	18.58
373.64	1.004	15.19	432.46	2.006	19.38
373.79	1.018	15.20	432.45	2.005	19.39
393.80	0.255	15.51	432.53	2.010	19.39
393.80	0.252	15.50	433.20	2.513	20.62
393.91	0.252	15.50	433.32	2.501	20.61
392.87	0.504	15.79	433.27	2.519	20.61
392.80	0.509	15.79	452.88	0.255	18.54
392.79	0.502	15.78	453.00	0.255	18.54
393.78	1.005	16.06	453.17	0.253	18.53
393.86	1.015	16.07	453.18	0.503	18.81
393.80	1.009	16.06	453.10	0.501	18.81
393.83	1.500	16.74	453.28	0.493	18.80
393.80	1.502	16.74	452.30	1.009	19.15
393.76	1.497	16.73	452.41	1.002	19.16
393.88	2.004	17.32	452.25	1.002	19.15
393.75	2.008	17.32	452.29	1.498	19.67
393.79	2.000	17.31	452.31	1.501	19.68
413.29	0.250	16.45	452.30	1.476	19.67
413.14	0.252	16.45	452.23	2.007	20.43
413.30	0.251	16.44	452.35	2.005	20.44
413.18	0.501	16.68	452.27	2.000	20.44
413.32	0.502	16.69	453.24	2.494	21.63
413.21	0.502	16.68	453.31	2.499	21.64
413.40	1.017	16.95	453.16	2.498	21.62
413.39	1.011	16.94	453.09	2.497	21.62

Standard uncertainties due to pressure and temperature are $u(P)=0.0019$ MPa and $u(T)=0.0242$ K
Combined standard uncertainty $u_c(\lambda)=1.58\%$; Expanded uncertainty $U_c(\lambda)=3.16\%$ with $k=2$ and 95 % confidence level

Table 4.3.1.4 Experimental supercritical thermal conductivity of HFO refrigerant R1336mzz(E)

T (K)	P (MPa)	λ	T (K)	P (MPa)	λ
413.26	3.005	26.79	433.26	3.521	23.52
413.43	3.007	26.78	433.28	3.993	27.49
413.42	3.006	26.78	433.21	3.984	27.50
413.12	3.508	40.07	433.08	3.992	27.51
413.07	3.508	40.06	452.57	3.011	22.19
413.07	3.508	40.06	452.60	3.005	22.20
413.12	4.016	45.46	452.71	3.002	22.19
412.97	3.993	45.45	452.71	3.516	24.02
413.02	3.984	45.46	452.79	3.512	24.01
433.32	3.014	21.51	452.82	3.508	24.02
433.16	3.015	21.52	452.64	4.036	25.90
433.37	3.013	21.51	452.75	4.039	25.91
433.04	3.501	23.51	452.52	4.046	25.92
433.06	3.495	23.50	452.54	4.035	25.92

Standard uncertainties due to pressure and temperature are $u(P)=0.0029$ MPa and $u(T)=0.0278$ K
Combined standard uncertainty $u_c(\lambda)=1.62\%$; Expanded uncertainty $U_c(\lambda)=3.23\%$ with $k=2$ and 95 % confidence level

Fig. 4.3.1.3 demonstrates the variation of measured thermal conductivity of liquid HFO refrigerant R1336mzz(E) indicating typical changes with density and temperature. The liquid thermal conductivity of R1336mzz(E) was measured within the temperature from 313 to 393 K and pressure up to 4.0MPa. It was observed from this figure that the liquid R1336mzz(E) appears a diminishment in thermal conductivity with expanding the temperature identifying by different symbols. In different words, liquid thermal conductivity was increased exponentially by rising the density as well. For liquid measurements, the only temperature at 393 K indicates slightly scattered data among the other measurement points due to nearer at the critical point. The expanded uncertainty was estimated to be less than 3.06 % over the liquid thermal conductivity measurements. Also, the measured liquid thermal conductivity was compared with Alam et al. (2017) measured liquid data for R1336mzz(Z), having an almost similar trend of data deviations.

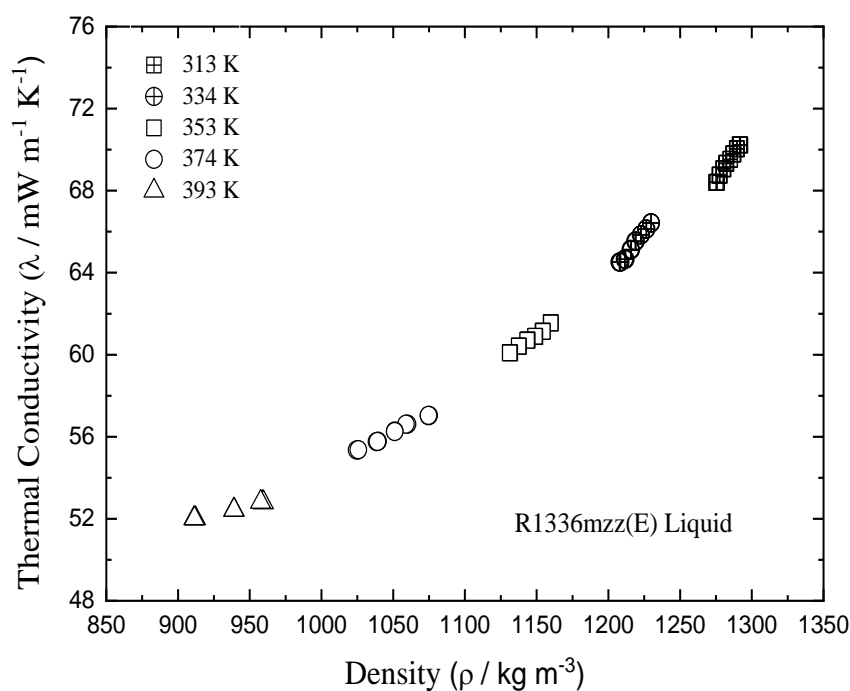


Fig. 4.3.1.3 Experimental thermal conductivity of R1336mzz(E) with density in a liquid region

Fig. 4.3.1.4 illustrates the effects of density on the vapor thermal conductivity of R1336mzz(E) with altering the temperature and pressure. The thermal conductivity of vapor R1336mzz(E) was measured within the temperature from 313 to 453 K whereas pressure varies at 0.25 to 2.50 MPa. This measured thermal conductivity was compared with the data of Alam et al. (2017) for the vapor R1336mzz(Z) and observed the same pattern of data deviations corresponding to the density. The measured vapor data of R1336mzz(E) appears a diminishment in thermal conductivity with reducing the temperature for all corresponding pressures. In other words, the vapor thermal conductivity data was decreased with increasing the density of the test fluid for all corresponding pressures. During the vapor measurements only at temperature 413 K and pressure of 2.50 MPa, some measurement difficulties were faced due to very nearer at the critical conditions corresponding to the other measurements.

Also, the thermal conductivity data in a supercritical region was recorded at temperatures ranging from 413 to 453 K and pressure of 3.0 to 4.0 MPa. Fig. 4.3.1.5 describes the supercritical data variations wherein the thermal conductivity data was suddenly increased with expanding the pressure as well as the density for each temperature. It was a very challenging task to determine the thermal conductivity at the supercritical phase because all the measurement points resided above the critical conditions as well as relatively high temperature

and pressure, getting more scattered data among the other measurements. Besides, there was a limitation of the experimental apparatus that can't sustain system pressure more than 5.00 MPa. Therefore, the thermal conductivity data of the supercritical phase was not pretty well either liquid or vapor phases.

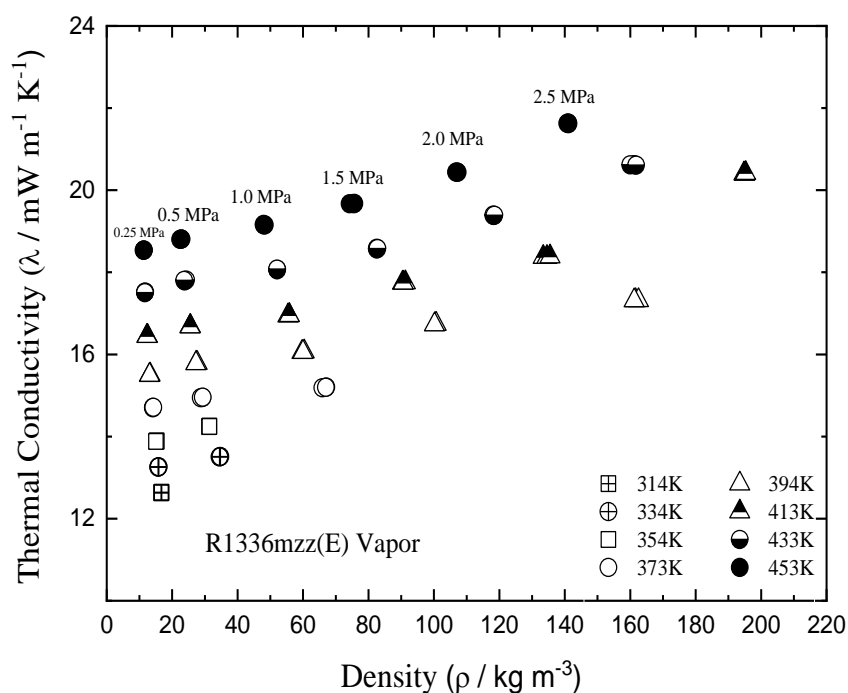


Fig. 4.3.1.4 Experimental thermal conductivity of R1336mzz(E) with density in a vapor region

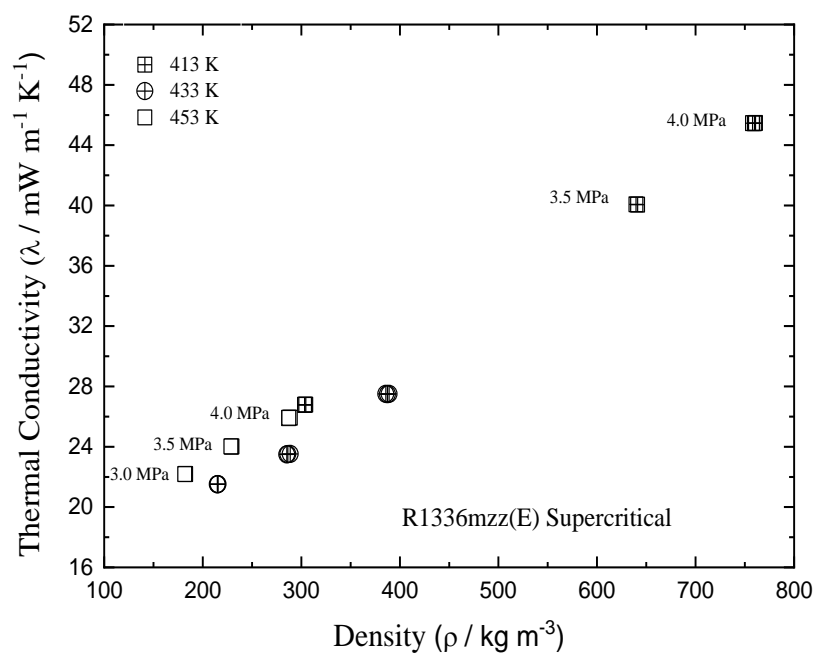


Fig. 4.3.1.5 Experimental thermal conductivity of R1336mzz(E) with density in a supercritical region

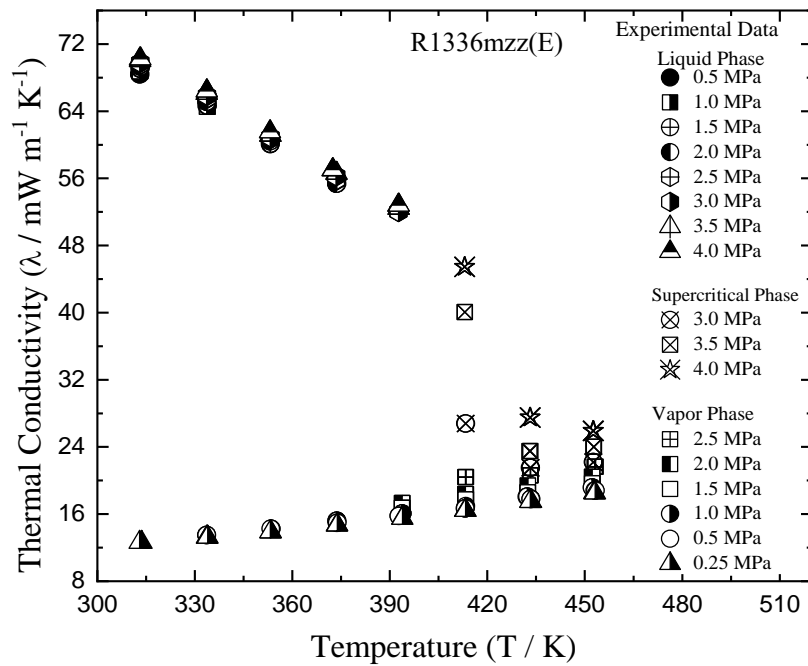
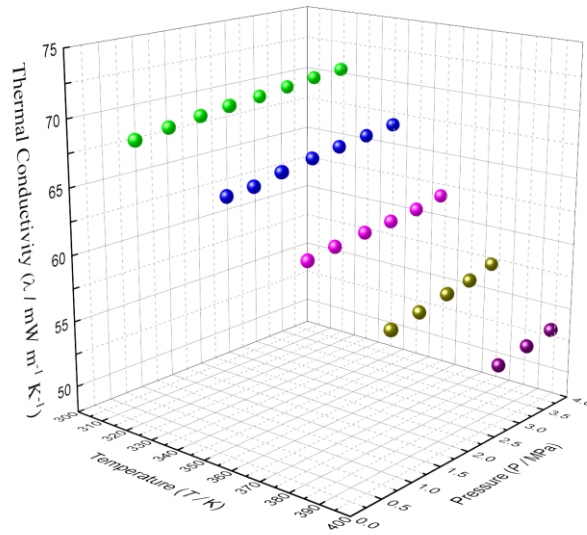


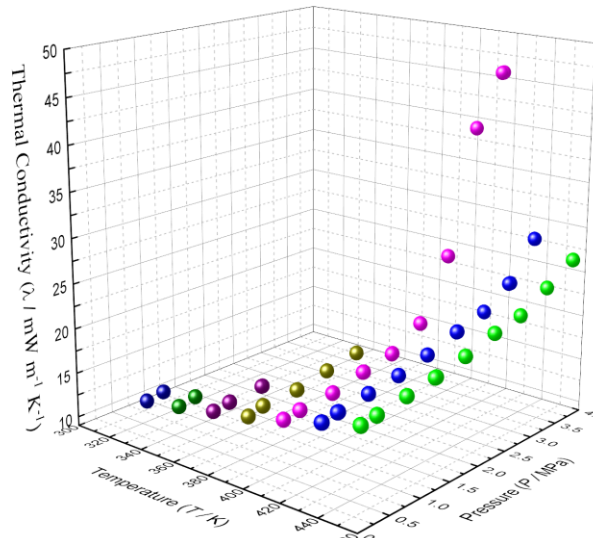
Fig. 4.3.1.6 Experimental thermal conductivity of R1336mzz(E) with temperature

Fig. 4.3.1.6 demonstrates the variation of all experimental thermal conductivity of R1336mzz(E) within the temperature varies from 313 to 453 K, and the pressure up to 4.0 MPa for not only the liquid and vapor but also the supercritical phases. The thermal conductivity data of the supercritical state are somewhat scattered to a great extent than the liquid and vapor states due to the above critical conditions as well as relatively high temperature, pressure, and getting a very smaller portion of an accessible straight line in the slope fitting of the temperature rise vs. logarithmic elapsed time curve. In addition, the effect of convection is more dominant at supercritical and vapor states than liquid. Therefore, the expanded uncertainty of the supercritical state was estimated to be 3.23 % which is greater than the liquid and vapor states due to the smaller linear part during the slope fitting of the temperature rise curve.

Fig. 4.3.1.7 demonstrates the 3D presentation for all experimental thermal conductivities of R1336mzz(E). This figure indicates the data trend of liquid, vapor, and supercritical thermal conductivities of R1336mzz(E) that are clearly understood by the figures. As the supercritical data are more scattered than the liquid as well as vapor data and some data of supercritical phase are located in the liquid-like supercritical sub-zone, these are far from the other data.



(a) Liquid R1336mzz(E)



(b) Vapor and Supercritical R1336mzz(E)

Fig. 4.3.1.7 3D presentation of thermal conductivities of R1336mzz(E) with temperature and pressure

4.3.1.3 Comparison with related research and data deviations of R1336mzz(E)

The measured thermal conductivities of R1336mzz(E) are compared with the other researchers. After that, the measured data are also correlated with the calculated data from the ECS model. Figs. 4.3.1.8 and 4.3.1.9 represent the comparison of experimentally measured liquid and vapor thermal conductivity data of R1336mzz(E) with the data measured by Alam et al. (2017) for R1336mzz(Z) with temperature and pressure. As the experimental apparatus is almost the same as Alam et al. (2017), it is compared the measured thermal conductivity data for gathering

a vast knowledge regarding the trans- and cis- isomer of R1336mzz having different critical temperatures and pressure, boiling point, and vapor pressures. In the liquid thermal conductivity measurement, the data of HFO refrigerant R1336mzz(E) are found an almost similar trend to temperature as well as pressure. Most of our experimental data are agreed well and found slightly lower than the data measured by Alam et al. (2017). At the vapor phase, the measured data of R1336mzz(E) are having also a similar trend but observing significantly lower than the data measured by Alam et al. (2017). It is noticed from the figures that the vapor thermal conductivity data are significantly scattered to a great extent than the data at liquid state.

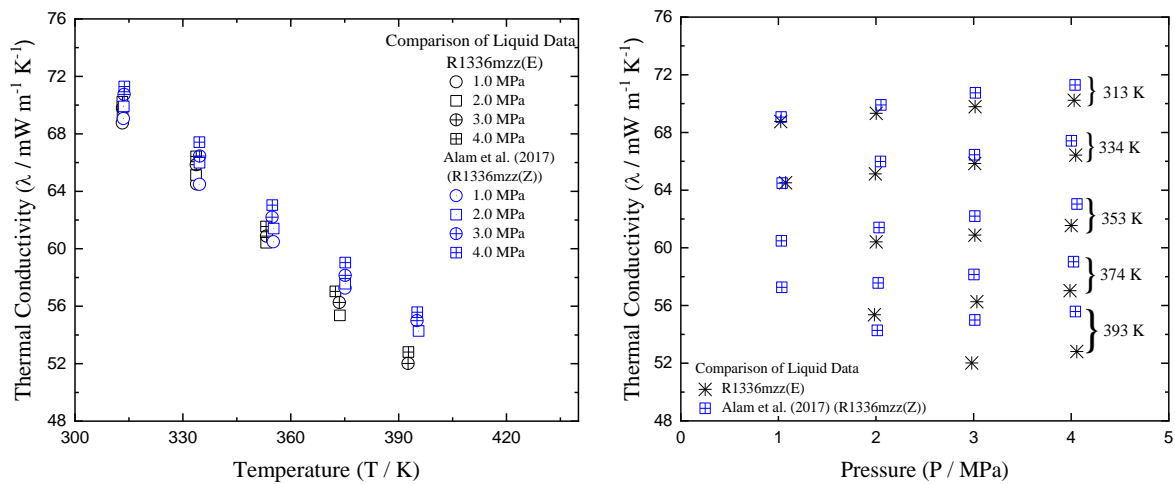


Fig. 4.3.1.8 Comparative liquid thermal conductivity of R1336mzz(E) and R1336mzz(Z) (Alam et al., 2017) concerning the temperature and pressure, respectively

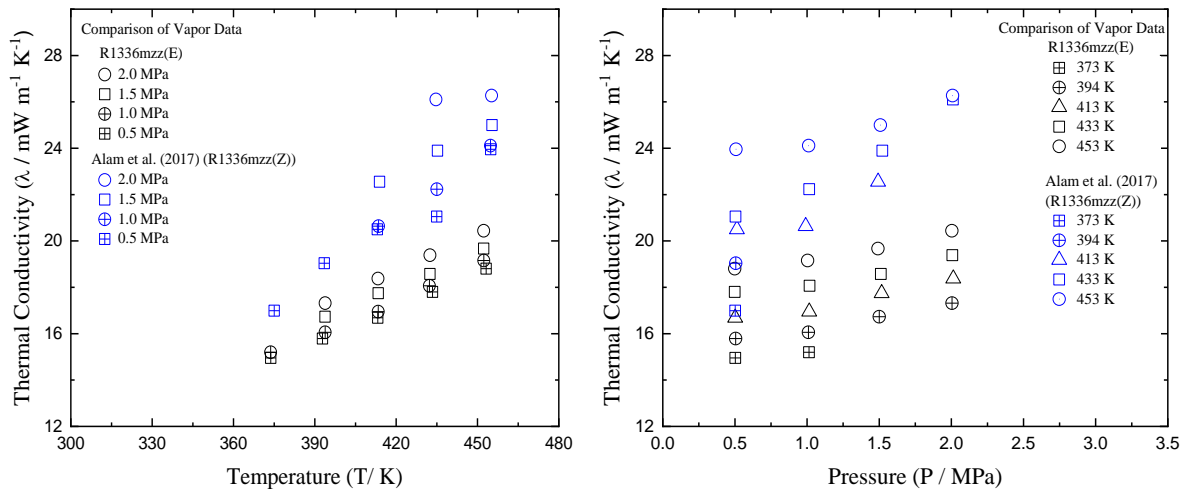


Fig. 4.3.1.9 Comparative vapor thermal conductivity of R1336mzz(E) and R1336mzz(Z) (Alam et al., 2017) concerning the temperature and pressure, respectively

Then from the measurement of R1336mzz(E), the deviations of thermal conductivities are calculated from the predicted values by the ECS model as well as the EoS (Akasaka, 2019a, 2019b). Figs. 4.3.1.10 and 4.3.1.11 show the deviations of the experimentally measured liquid, and vapor, supercritical thermal conductivities from the estimated data by the ECS model. The calculated values from both ECS models are indicated to be similar to this experimental data. In the liquid phase shown in Fig. 4.3.1.10, the measured data agreed and accepted well in the range from 16 % to 21 % deviations. Even though at 393 K, the measurements appear to have a peak of deviation at 22.40 %. While in the vapor and supercritical phases shown in Fig. 4.3.1.11, the deviations range from – 13 to – 26 %, even though the measurements appear to show systematic negative deviation that reaches a peak of 26.47 % at temperature 453 K for vapor, and a peak of 20.55 % at temperature 433 K for supercritical phases, respectively.

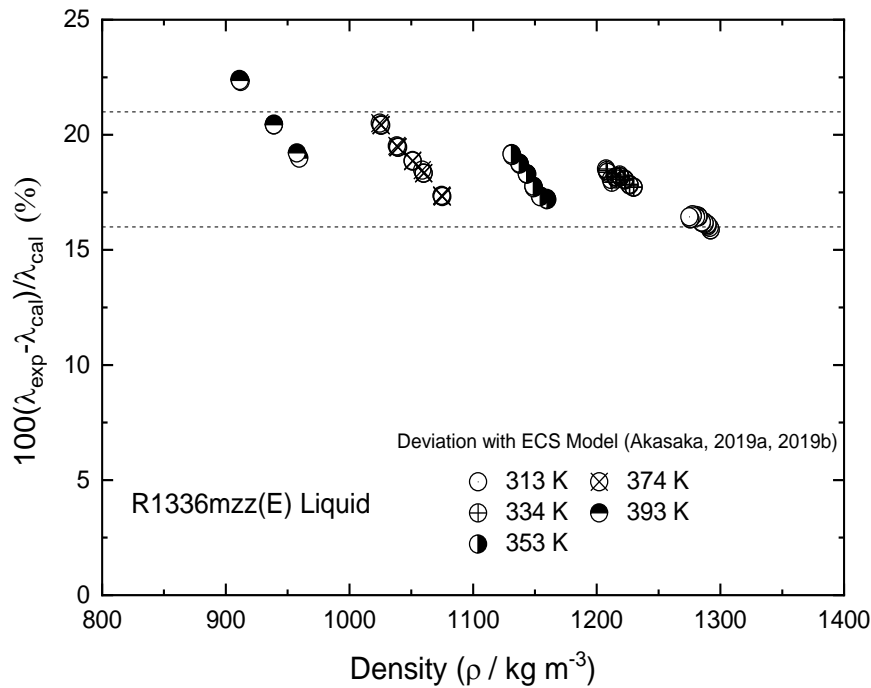


Fig. 4.3.1.10 Comparative study of thermal conductivity data deviations for liquid R1336mzz(E)

The average absolute deviation of the measurement at the liquid phase is found as 17.96 %, while in the vapor and supercritical phases are observed as 21.38 % and 15.14 %, respectively. The viscosity deviations are summarized in Table 4.3.1.5 that indicates the average absolute deviation (AAD %), maximum absolute deviation (MAD %), and average percentage deviation (Bias %), as follows:

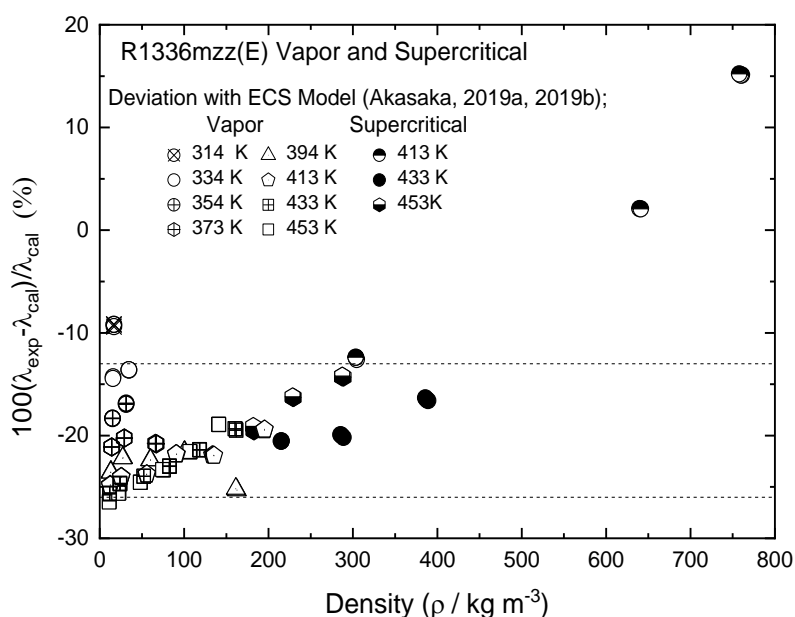


Fig. 4.3.1.11 Comparative study of thermal conductivity data deviations for vapor and supercritical R1336mzz(E)

Table 4.3.1.5 Thermal conductivity data deviations in terms of AAD, MAD, and Bias

Phases	Parameters	ECS Model*
Liquid	AAD (%)	17.96
	MAD (%)	22.40
	Bias (%)	17.96
Vapor	AAD (%)	21.38
	MAD (%)	26.47
	Bias (%)	-21.38
Supercritical	AAD (%)	15.14
	MAD (%)	20.55
	Bias (%)	-11.45

*Calculated with the help of the ECS Model as well as EoS developed by Akasaka (2019a, 2019b)

4.3.1.4 Correlations at saturation state for R1336mzz(E)

The correlations for saturation thermal conductivity of R1336mzz(E) are developed by the extrapolating method using the experimental data up to the saturation conditions at the liquid and vapor phases, respectively. The properties of HFO refrigerant R1336mzz(E) at saturation condition are obtained using the Helmholtz energy equation of state by Akasaka (2019a, 2019b). The thermal conductivity at the saturation condition is obtained by extrapolating the

measured data until a saturation condition. In this context, the extrapolation method to predict the saturated liquid thermal conductivity of R1336mzz(E) by identical temperature and pressure is smoothly comprehensible by Fig. 4.3.1.12. It is identified that the saturated values, only at 386.85 K and 398.55 K, were extrapolated by identical pressure. Similarly, identical temperature and pressure phenomena, the saturated vapor thermal conductivity of R1336mzz(E) were extracted to make the saturation correlation. Then using the linear fitting of the extrapolated thermal conductivity data, the simplified correlation equations both for saturated liquid and vapor data of R1336mzz(E), $\lambda_{sat,L}$ and $\lambda_{sat,V}$ can be developed by Eqs. (4.3.1.1) and (4.3.1.2) as the function saturation temperature.

$$\lambda_{sat,L} = -0.215T_{sat} + 135.72 \quad (4.3.1.1)$$

$$\lambda_{sat,V} = 0.062T_{sat} - 6.99 \quad (4.3.1.2)$$

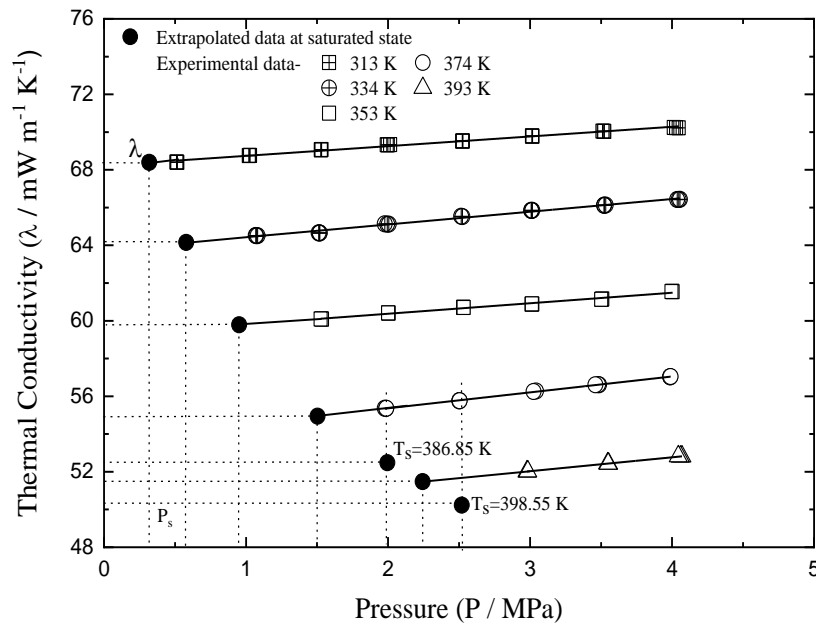


Fig. 4.3.1.12 Extrapolated data of R1336mzz(E) at saturated state in a liquid region

Consequently, Fig. 4.3.1.13 illustrates the variations of the extrapolated data and calculated data by linear fitting of Eqs. (4.3.1.1) and (4.3.1.2) of the liquid and vapor thermal conductivity with the saturation temperature. It is summarized that both saturated liquid and vapor correlations to estimate the thermal conductivity under saturated conditions would appear a good outcome from room to high temperature. Additionally, all the extrapolated values,

calculated values by Eqs. (4.3.1.1) and (4.3.1.2) for the liquid and vapor thermal conductivity of R1336mzz(E) at saturated conditions are also listed in Table 4.3.1.6.

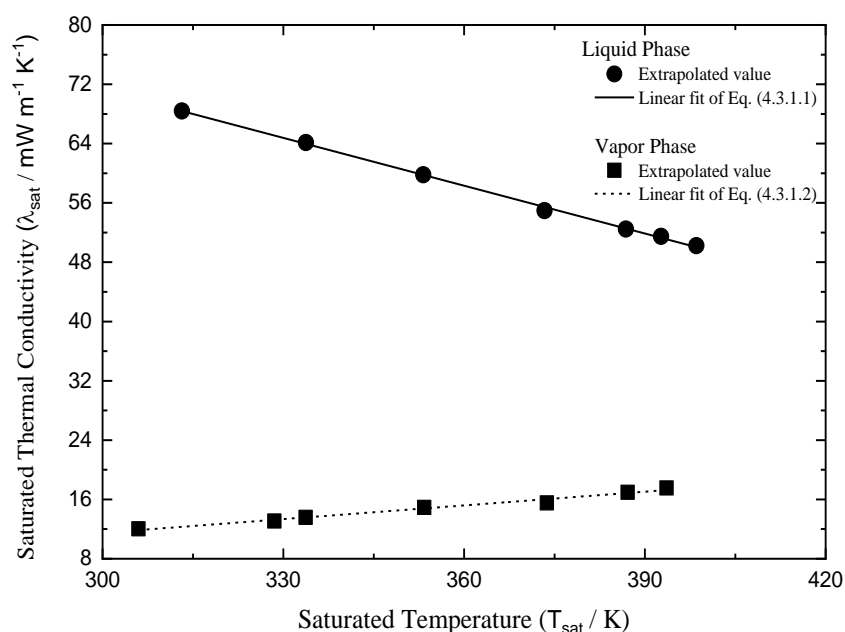


Fig. 4.3.1.13 Saturated thermal conductivity data concerning saturated temperature

Table 4.3.1.6 Saturated thermal conductivity, λ_{sat} (mW m⁻¹ K⁻¹) of R1336mzz(E)

(a) Liquid			
T (K)	P (MPa)	$\lambda_{sat,L}$ (Extrapolated)	$\lambda_{sat,L}$ (Eq. 4.3.1.1)
313.16	0.318	68.39	68.39
333.75	0.580	64.15	63.96
353.23	0.952	59.79	59.78
373.34	1.504	54.95	55.45
386.85	1.995	52.47	52.55
392.70	2.244	51.47	51.29
398.55	2.519	50.23	50.03
(b) Vapor			
T (K)	P (MPa)	$\lambda_{sat,V}$ (Extrapolated)	$\lambda_{sat,V}$ (Eq. 4.3.1.2)
305.95	0.252	12.03	11.98
328.52	0.502	13.09	13.38
333.71	0.579	13.58	13.70
353.39	0.956	14.92	14.92
373.75	1.518	15.53	16.18
387.15	2.007	16.97	17.01
393.61	2.285	17.54	17.41

4.3.1.5 Conclusion

In this work, the thermal conductivity of R1336mzz(E) was measured by applying the technique of transient hot-wire for liquid, vapor, and supercritical regions. In the liquid region, the measurement was conducted at a temperature range from 313 to 393 K over the pressures until 4.0 MPa, and for the vapor region, the measurement was conducted at a temperature range from 313 to 453 K and pressure from 0.25 to 2.50 MPa, respectively. Also, the thermal conductivity of the supercritical region was recorded at a temperature range from 413 to 453 K over the pressure range from 3.0 to 4.0 MPa. The experimentally obtained thermal conductivity of R1336mzz(E) was compared with the measurement of Alam et al. (2017) for R1336mzz(Z) both of liquid and vapor regions, respectively. Therefore, the thermal conductivity data of the supercritical state are somewhat scattered to a great extent than the liquid and vapor states due to the above critical conditions as well as relatively high temperature, pressure, and getting a very smaller portion of an accessible straight line in the slope fitting of the temperature rise vs. logarithmic elapsed time curve. The expanded uncertainties for the thermal conductivity measurements of R1336mzz(E) were reported to 3.06 %, 3.16 %, and 3.23 % at the liquid, vapor, and supercritical regions, respectively. Also, the simplified correlations at saturation state were developed to estimate the thermal conductivity by extrapolating method using the measured data to the saturation condition both for liquid and vapor regions. These saturated conditions data are mostly supportive of the industrial design and simulation in the engineering area.

4.3.2 Thermal conductivity measurement of 3,3,4,4,5,5-HFCPE

4.3.2.1 Overview of 3,3,4,4,5,5-HFCPE

Due to being an expected alternative to the high-temperature heat pumps and organic Rankine cycles, the key targets of this study are to measure the thermal conductivity of 1H, 2H-Hexafluorocyclopentene, shortly 3,3,4,4,5,5-HFCPE, and develop the simplified correlation at saturation conditions in terms of saturated temperature. Special attention is being paid to climate change and the potential effects of low-GWP refrigerants around the world. Human lives are being threatened as a result of the rapid change in the earth's climate, which is a result of global warming. Conventional refrigerants with high GWP values, such as hydrofluorocarbons (HFCs) and hydrochlorofluorocarbons (HCFCs), are the primary contributors to global warming. As a result, the Montreal Protocol and Kyoto Protocol were established to regulate these harmful gases (UNEP, 2014). Therefore, more ecologically friendly alternatives to traditional refrigerants are required for use in common applications like heat pumps and Organic Rankine Cycles (ORCs) (McLinden, 2009; Richter et al., 2011). To meet the challenge, the recently developed refrigerant known as 3,3,4,4,5,5-HFCPE is a promising working fluid with low toxicity and flammability, a zero ODP value, and a lower GWP value. Although the 3,3,4,4,5,5-HFCPE is not a hydro-fluoro-olefin (HFO), it is regarded as a good substitute for HFCs similarly to HFOs due to its above-mentioned friendly properties. The molecular structure and the fundamental characteristics of 3,3,4,4,5,5-HFCPE are given in Fig. 4.3.2.1 and Table 4.3.2.1, respectively. The critical temperature is predicted to be 511.15 K (Lydersen, 1955; Wajima et al., 2017), while the critical pressure is calculated to be 2.923 MPa using the approach of Lydersen (1955). It has zero ODP and a GWP value of 33 (Wajima et al., 2017).

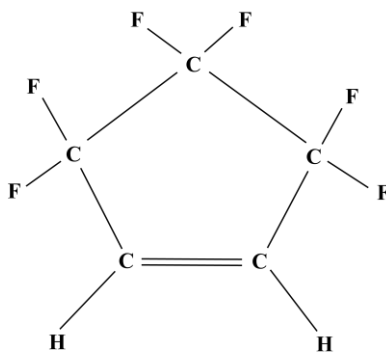


Fig. 4.3.2.1. Molecular structure of 3,3,4,4,5,5-HFCPE

Table 4.3.2.1 Fundamental properties of 3,3,4,4,5,5-HFCPE

Parameters	Value	Reference
Name	1H, 2H-Hexafluorocyclopentene	
Chemical formula	$C_5H_2F_6$	
CASRN	1005-73-8	AIST (2020)
Critical temperature (K)	511.15	Lydersen (1955); Wajima et al. (2017)
Critical pressure (MPa)	2.923	Lydersen (1955)
Molecular weight (g mol ⁻¹)	176.06	AIST (2020)
Flammability (Vol%, 35 °C wet)	4-9	AIST (2020)
Boiling point (K)	341.15	Wajima et al. (2017)
ODP	0	
GWP (100 year)	33	Wajima et al. (2017)

The thermodynamic properties and the transport properties of the working fluids are the most significant tools to design energy systems, practical appliances, and simulations. The transport properties of 3,3,4,4,5,5-HFCPE such as the thermal conductivity and viscosity have become increasingly important in the development of practical applications. In the open literature, there are currently no experimental data regarding the thermodynamic and transport properties of 3,3,4,4,5,5-HFCPE. Our research group had presented some thermal conductivity and kinematic viscosity findings at various conferences (Mondal et al., 2021b; Tuhin et al., 2020). Therefore, in this present study, the thermal conductivities of 3,3,4,4,5,5-HFCPE were measured using the transient hot-wire technique at temperatures from 333 K to 473 K and pressures from 0.5 to 4.0 MPa in the liquid state, wherein for the vapor state temperatures from 393 to 473 K over the pressure up to 1.5 Pa. The simplified correlations expressing the saturation thermal conductivity of 3,3,4,4,5,5-HFCPE were developed by extrapolating the measured data at liquid-vapor saturation conditions in an extrapolation approach. The uncertainties of this measurement are calculated by the GUM method using the law of propagation for uncertainties (Bell, 2001; JCGM 100, 2008; Taylor and Kuyatt, 1994).

4.3.2.2 Measured thermal conductivities of 3,3,4,4,5,5-HFCPE

The thermal conductivity of 3,3,4,4,5,5-HFCPE was measured by utilizing the THW technique with a wide range of temperatures and pressures. Each measurement was conducted repeatedly three times carefully after getting the stable condition of the apparatus. The repeated results did

not exceed $\pm 0.6\%$, where the time interval of two successive measurements was at least 30 minutes. Fig. 4.3.2.2 shows the measurement points of 3,3,4,4,5,5-HFCPE showing the P - T diagram. The critical temperature of 3,3,4,4,5,5-HFCPE is found as 511.15 K (Lydersen, 1955; Wajima et al., 2017) and also the critical pressure is estimated at 2.923 MPa by the method of Lydersen (1955), respectively. The vapor-liquid saturation line was drawn using the Riedel-Plank correlations (Poling et al., 2000; Riedel, 1954; Vetere, 1991). The thermal conductivity of 3,3,4,4,5,5-HFCPE was recorded at a temperature range from 333 to 473 K and pressures up to 4.0 MPa for the liquid phase and from 393 to 473 K up to 1.5 MPa for the vapor phase. The experimental thermal conductivities for the liquid and vapor states are presented in Table 4.3.2.2 and Table 4.3.2.3. The measurement uncertainties of 3,3,4,4,5,5-HFCPE in the liquid and vapor phases are shown below in the Tables.

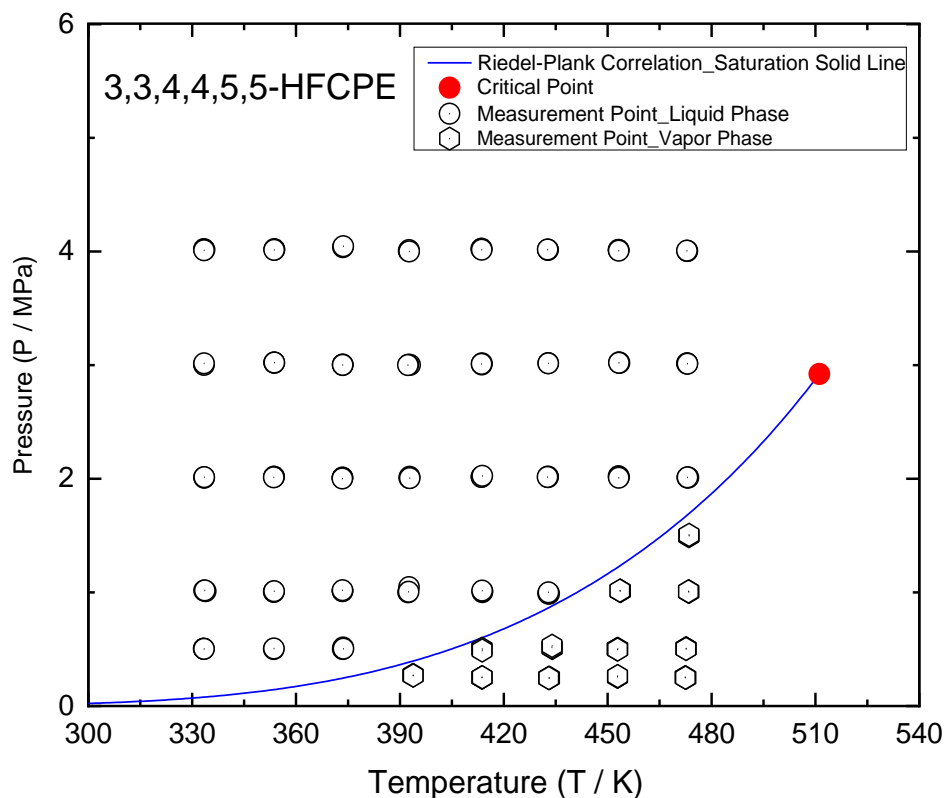


Fig. 4.3.2.2 Experimental points for 3,3,4,4,5,5-HFCPE showing temperature and pressure

Table 4.3.2.2 Experimental thermal conductivities, λ (mW m⁻¹ K⁻¹) of liquid 3,3,4,4,5,5-HFCPE

T (K)	P (MPa)	λ	T (K)	P (MPa)	λ
333.36	4.020	85.04	392.32	3.001	66.51
333.59	4.015	85.05	392.81	2.018	65.28
333.44	4.010	85.06	392.68	2.006	65.27
333.38	3.007	84.28	392.84	2.005	65.27
333.45	3.002	84.28	392.66	1.047	64.17
333.44	3.015	84.28	392.39	1.001	64.16
333.42	2.012	82.83	392.52	1.005	64.17
333.49	2.009	82.83	413.67	4.024	63.31
333.48	2.014	82.82	413.51	4.022	63.32
333.43	1.015	81.32	413.64	4.015	63.32
333.93	1.010	81.32	413.70	3.016	61.93
333.66	1.017	81.31	413.63	3.005	61.93
333.34	0.504	80.36	413.62	3.011	61.93
333.38	0.502	80.36	413.56	2.018	60.63
333.42	0.503	80.36	413.62	2.016	60.64
353.74	4.021	78.56	413.81	2.025	60.64
353.77	4.015	78.56	413.84	1.002	59.54
353.68	4.013	78.56	413.85	1.008	59.54
353.73	3.021	77.17	413.78	1.015	59.54
353.68	3.022	77.16	432.78	4.014	59.36
353.74	3.023	77.16	432.73	4.015	59.36
353.63	2.017	75.78	432.69	4.017	59.36
353.66	2.018	75.78	432.85	3.016	58.17
353.56	2.012	75.78	432.85	3.015	58.19
353.57	1.003	74.55	432.85	3.016	58.19
353.62	1.006	74.56	432.82	2.014	57.28
353.66	1.010	74.55	432.81	2.018	57.28
353.59	0.501	73.55	432.66	2.015	57.29

353.65	0.505	73.56	433.14	0.989	56.34
353.64	0.505	73.55	432.83	0.990	56.34
373.54	4.038	72.53	432.90	0.999	56.33
373.56	4.038	72.53	453.16	4.013	56.01
373.64	4.045	72.53	453.19	4.011	56.01
373.50	3.000	71.34	453.19	4.007	56.01
373.49	3.005	71.33	453.32	3.023	55.07
373.50	3.002	71.34	453.45	3.020	55.07
373.44	2.010	70.00	453.27	3.021	55.07
373.44	2.007	70.00	453.19	2.022	54.02
373.40	2.002	70.01	453.32	2.016	54.02
373.42	1.012	68.80	453.21	2.008	54.02
373.43	1.010	68.81	473.02	4.005	53.09
373.44	1.018	68.80	473.01	4.003	53.09
373.49	0.501	67.64	472.89	4.007	53.09
373.60	0.515	67.65	473.02	3.015	51.91
373.72	0.503	67.65	472.93	3.014	51.91
392.52	4.003	67.65	473.07	3.013	51.91
392.66	4.012	67.64	473.37	2.011	50.98
392.69	4.000	67.64	473.04	2.011	50.99
392.95	3.002	66.51	473.07	2.012	50.99
392.49	3.003	66.50			

Standard uncertainties due to pressure and temperature are $u(P)=0.0017$ MPa and $u(T)=0.0229$ K
Combined standard uncertainty $u_c(\lambda)=1.54$ %; Expanded uncertainty $U_c(\lambda)=3.08$ % with $k=2$ and 95 % confidence level

Table 4.3.2.3 Experimental thermal conductivities, λ (mW m⁻¹ K⁻¹) of vapor 3,3,4,4,5,5-HFCPE

T (K)	P (MPa)	λ	T (K)	P (MPa)	λ
393.78	0.269	15.73	452.72	0.501	20.03
393.81	0.273	15.72	452.96	0.503	20.03
393.84	0.267	15.73	452.87	0.497	20.04
413.75	0.252	17.09	453.70	1.014	20.71
413.66	0.251	17.10	453.67	1.014	20.71
413.78	0.252	17.10	453.56	1.015	20.71
413.66	0.501	17.34	472.62	0.250	21.10
413.77	0.503	17.33	472.39	0.252	21.10
413.77	0.489	17.32	472.45	0.250	21.10
432.95	0.249	18.34	472.67	0.507	21.26
433.22	0.247	18.35	472.69	0.507	21.25
433.03	0.246	18.34	472.67	0.503	21.26
434.01	0.511	18.56	473.44	1.008	21.89
433.91	0.516	18.57	473.45	1.005	21.89
433.97	0.530	18.57	473.37	1.009	21.88
452.88	0.260	19.89	473.43	1.497	23.03
452.83	0.258	19.85	473.53	1.498	23.03
452.87	0.264	19.89	473.50	1.506	23.03

Standard uncertainties due to pressure and temperature are $u(P)=0.0024$ MPa and $u(T)=0.0237$ K
Combined standard uncertainty $u_c(\lambda)=1.76$ %; Expanded uncertainty $U_c(\lambda)=3.52$ % with $k=2$ and 95 % confidence level

Fig. 4.3.2.3 shows the variation of experimental liquid thermal conductivities with temperature. The thermal conductivities of liquid 3,3,4,4,5,5-HFCPE were measured over the pressures at 4.0 MPa and temperatures from 333 to 473 K. Changes in the thermal conductivities are shown in the figure with distinct symbols of temperature, where the recorded thermal conductivity measurements were found in the range of 51.0 to 85.1 mW m⁻¹ K⁻¹. The liquid thermal conductivity data are decreased with rising temperature for all corresponding pressures but increased with increasing the pressure if the temperature remains constant. The greater thermal conductivity data were reported at a lower temperature than that of the higher temperature for the corresponding pressure. The combined standard uncertainty for the liquid phase

measurement was calculated as 1.54 %, where the expanded uncertainty of 3.08 % with $k=2$ and 95 % confidence level.

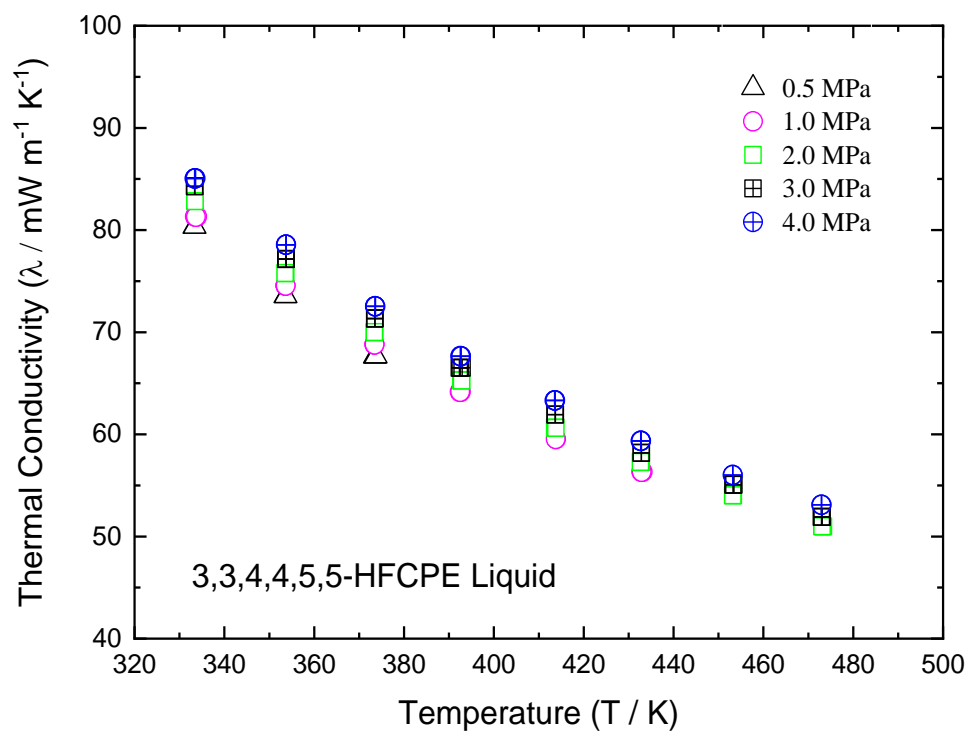


Fig. 4.3.2.3 Variation of measured liquid thermal conductivities of 3,3,4,4,5,5-HFCPE with temperature

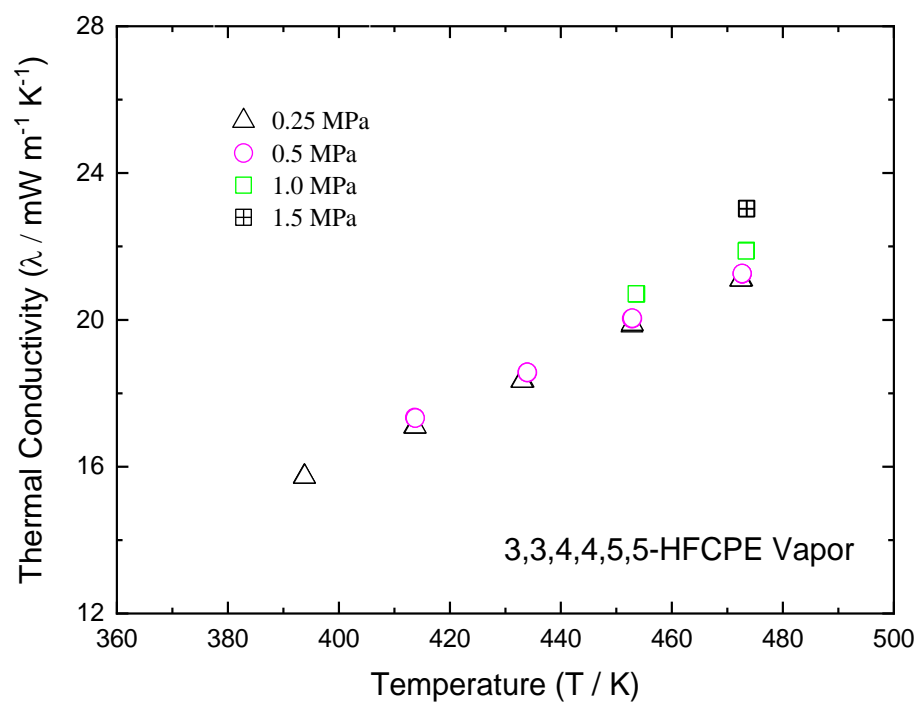
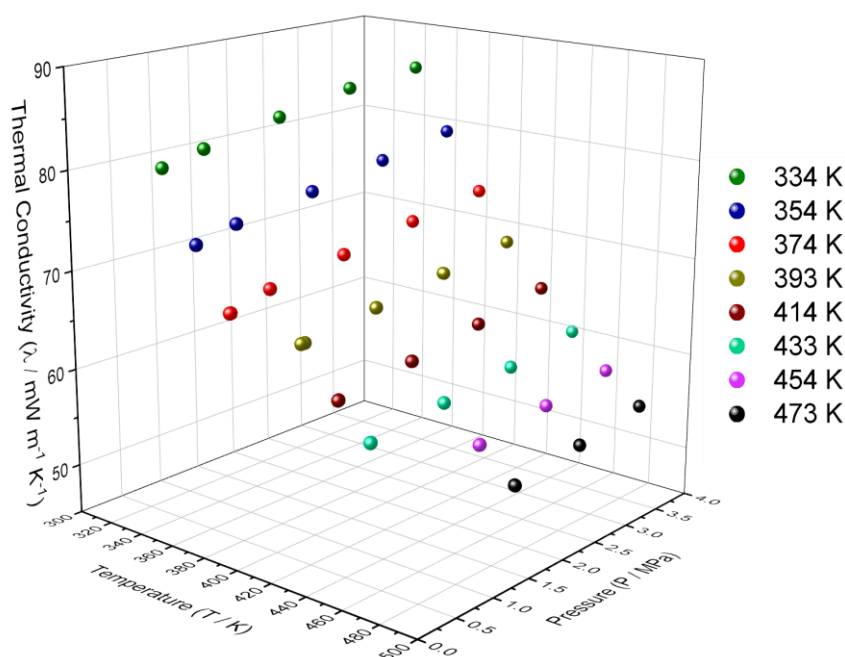


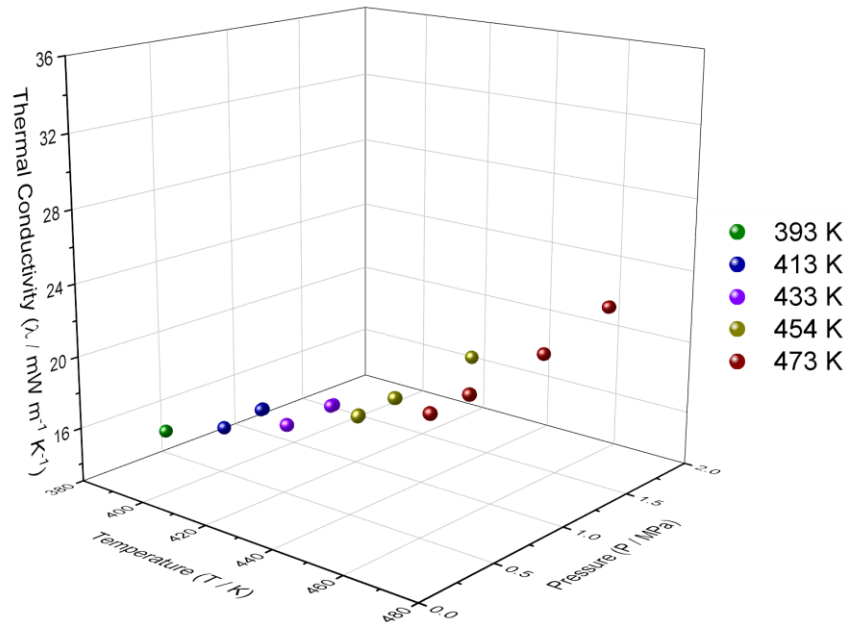
Fig. 4.3.2.4 Variation of measured vapor thermal conductivities of 3,3,4,4,5,5-HFCPE with temperature

Fig. 4.3.2.4 represents the variation of experimental vapor thermal conductivities with temperature. The vapor thermal conductivities of 3,3,4,4,5,5-HFCPE were measured from the temperatures of 393 to 473 K and pressures up to 1.5 MPa. The recorded vapor measurements were found in the range of 15.7 to 23.0 mW m⁻¹ K⁻¹. The vapor thermal conductivities are increased with increasing temperature for all pressures and also increased with increasing the pressure if the temperature remains constant, which is opposite to liquid phase measurements. The combined standard uncertainty for the vapor phase measurement was calculated as 1.76 %, where the expanded uncertainty of 3.52 % with k=2 and 95 % confidence level.

Fig. 4.3.2.5 demonstrates the 3D presentation for all experimental thermal conductivities of 3,3,4,4,5,5-HFCPE with the temperature ranging from 333 to 473 K over the pressure up to 4.0 MPa. This figure indicates the data trend of liquid and vapor 3,3,4,4,5,5-HFCPE that are clearly understood for the readers. Therefore, the vapor thermal conductivities are somewhat scattered a little more than the liquid thermal conductivities due to the smaller part of the straight line found in the unbalanced voltage vs. logarithmic elapse time curve.



(a) Liquid 3,3,4,4,5,5-HFCPE



(b) Vapor 3,3,4,4,5,5-HFCPE

Fig. 4.3.2.5 3D Presentation of the thermal conductivities of 3,3,4,4,5,5-HFCPE with temperature and pressure

Fig. 4.3.2.6 shows the comparison of thermal conductivities of 3,3,4,4,5,5-HFCPE over the known working fluids (cyclopentane, pentane, and cyclohexane). This figure indicates the data trend of 3,3,4,4,5,5-HFCPE for pressures at 4.0 and 1.0 MPa in the liquid and vapor phases. A similar data trend for this working fluid is found both for liquid and vapor phases compared to the known working fluids. The measured data are quite lower than the mentioned three fluids.

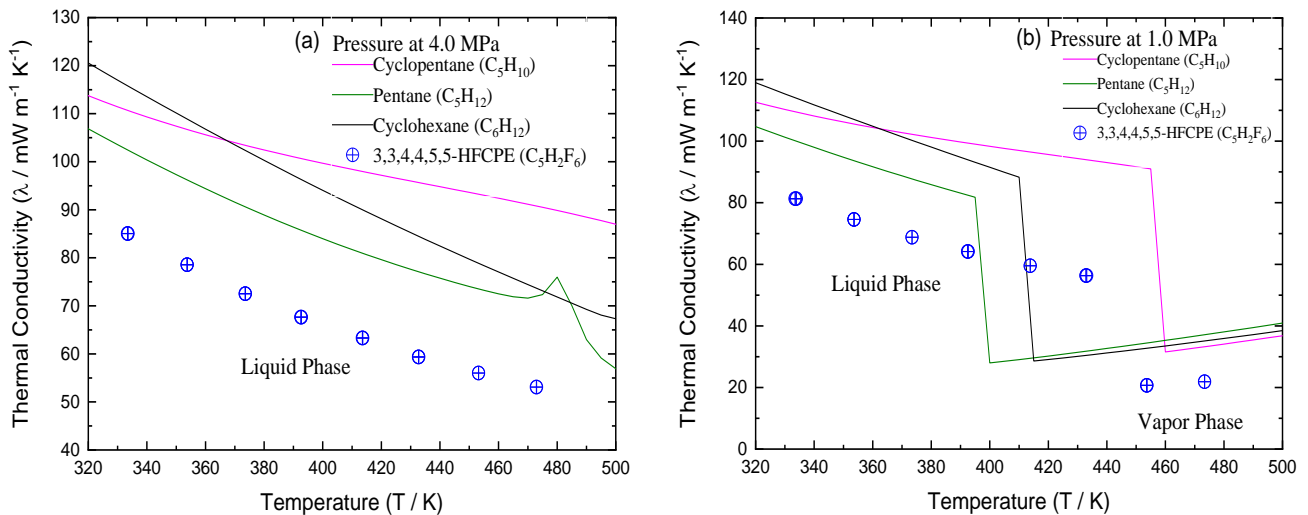


Fig. 4.3.2.6 Comparison of thermal conductivities of 3,3,4,4,5,5-HFCPE for pressures at 4.0 MPa and 1.0 MPa (thermal conductivities of cyclopentane, pentane, and cyclohexane are taken from Huber (2018))

4.3.2.3 Correlations at saturation condition

In an extrapolation approach, simplified correlations were developed in terms of saturation temperature to predict the thermal conductivities at saturation conditions. The saturation properties of 3,3,4,4,5,5-HFCPE were found from the various popular correlations of Riedel-Plank (Poling et al., 2000; Riedel, 1954; Vetere, 1991). The saturated liquid thermal conductivity of 3,3,4,4,5,5-HFCPE was extracted by identical temperature up to saturation conditions that is also understandable by Fig. 4.3.2.7. While in the vapor saturated thermal conductivity of 3,3,4,4,5,5-HFCPE were found both for identical pressure and temperature. Then correlation equations both for liquid and vapor thermal conductivity were derived by the polynomial fitting from the extrapolated data in terms of saturation temperature. The liquid and vapor correlations for 3,3,4,4,5,5-HFCPE to get the saturation thermal conductivities were developed as Eq. (4.3.2.1) and Eq. (4.3.2.2), respectively. Figure 4.3.2.8 shows the extrapolated data as well as polynomial fitting of saturation thermal conductivities for the liquid and vapor phases of 3,3,4,4,5,5-HFCPE. Table 4.3.2.4 summarizes the saturated thermal conductivities both for extrapolated data and calculated data from the correlations at saturation conditions.

$$\lambda_{sat,L} = 8.98 \times 10^{-4} T_{sat}^2 - 9.30 \times 10^{-1} T_{sat} + 289.82 \quad (4.3.2.1)$$

$$\lambda_{sat,V} = 2.64 \times 10^{-4} T_{sat}^2 - 1.35 \times 10^{-1} T_{sat} + 27.75 \quad (4.3.2.2)$$

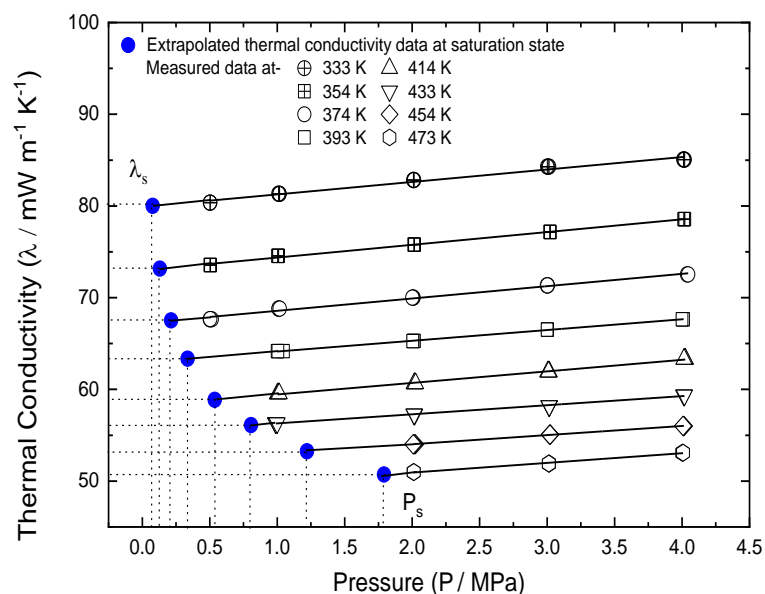


Fig. 4.3.2.7 Extrapolated liquid thermal conductivities at saturation conditions

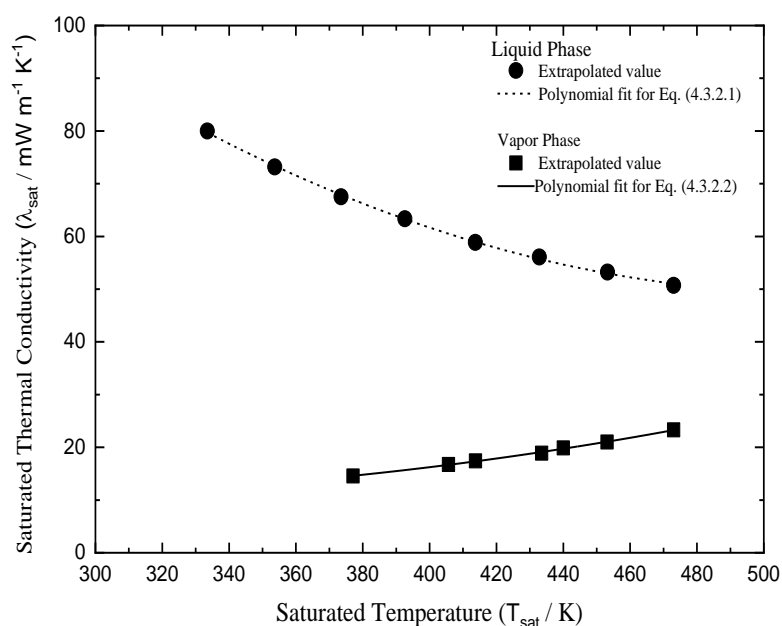


Fig. 4.3.2.8 Variation of saturated thermal conductivities in terms of saturation temperature

Table 4.3.2.4 Saturated thermal conductivities, λ_{sat} (mW m⁻¹ K⁻¹) of 3,3,4,4,5,5-HFCPE

(a) Liquid			
T (K)	P (MPa)	$\lambda_{sat, L}$ (Extrapolated)	$\lambda_{sat, L}$ (Eq. 4.3.2.1)
333.48	0.077	80.01	79.55
353.66	0.131	73.17	73.23
373.51	0.214	67.51	67.74
392.63	0.336	63.35	63.11
413.68	0.537	58.87	58.77
432.83	0.806	56.10	55.52
453.26	1.220	53.25	52.78
473.05	1.792	50.71	50.83
(b) Vapor			
T (K)	P (MPa)	$\lambda_{sat, V}$ (Extrapolated)	$\lambda_{sat, V}$ (Eq. 4.3.2.2)
377.11	0.256	14.57	14.53
405.64	0.506	16.75	16.59
413.73	0.602	17.43	17.26
433.52	0.894	18.88	19.03
440.02	1.011	19.90	19.66
453.12	1.279	20.99	20.99
473.02	1.785	23.31	23.19

4.3.2.4 Conclusion

In this part of the study, the thermal conductivity measurements of 3,3,4,4,5,5-HFCPE had been performed by the transient hot-wire method. The measurements of the thermal conductivities for the 3,3,4,4,5,5-HFCPE were conducted over the pressures up to 4.0MPa at temperatures from 333 to 473 K in the liquid phase, while in the vapor phase at temperatures from 393 to 473 K. The measured liquid and vapor thermal conductivities were found in the range of 51.0 to 85.1 mW m⁻¹ K⁻¹ and 15.7 to 23.0 mW m⁻¹ K⁻¹ for the above pressure and temperature, respectively. The vapor thermal conductivities are somewhat scattered a little more than the liquid thermal conductivities due to the smaller part of the straight line found in the unbalanced voltage vs. logarithmic elapse time curve. The combined standard uncertainties were calculated as 1.54 % and 1.76 % for liquid and vapor phases, respectively, where the expanded uncertainties were found as 3.08 % and 3.52 % with k=2 and a confidence level of 95 % both of liquid and vapor thermal conductivity measurements. The correlations were developed to estimate the saturated liquid and vapor thermal conductivities in terms of saturation temperature using the extrapolation approach from the experimental data up to saturation conditions.

References

- AGC, 2016. AGC Chemicals, AMOLEA® X, Y Series. <https://www.agc-chemicals.com/file.jsp?id=30035>. (in Japanese).
- AIST, 2020. Personal Communication with National Institute of Advanced Industrial Science and Technology (AIST), Japan.
- AIST, 2016. The National Institute of Advanced Industrial Science and Technology, Japan.
- Akasaka, R., 2021. Personal Communication.
- Akasaka, R., 2019a. A Helmholtz Energy Equation of State for R1336mzz(E), in: Proceedings of the 2019 JSRAE Annual Conference. Koto-ku, Tokyo, Japan, p. D121.
- Akasaka, R., 2019b. Personal Communication.
- Akasaka, R., Fukuda, S., Sakoda, N., Higashi, Y., 2020. PvT Property Measurement and

- Development of an Equation of State for New Refrigerant HFO1132 (E), in: Proceedings of the 2020 JSRAE Annual Conference, Paper D144 (1-4), Tsu-City, Japan.
- Akasaka, R., Fukushima, M., Lemmon, E.W., 2016. A Helmholtz Energy Equation of State for Trifluoroethylene (R-1123), in: Proceedings of the 16th International Refrigeration and Air Conditioning Conference. Paper 1698, pp-2297(1-10). <http://docs.lib.purdue.edu/iracc/1698>.
- Alam, M.J., Islam, M.A., Kariya, K., Miyara, A., 2021. Viscosity Measurement of cis-1,3,3,3-tetrafluoropropene (R1234ze(Z)) by Tandem Capillary Tubes Method. *Int. J. Refrig.* (In Press). <https://doi.org/10.1016/j.ijrefrig.2021.04.004>
- Alam, M.J., Islam, M.A., Kariya, K., Miyara, A., 2017. Measurement of thermal conductivity of cis- 1,1,1,4,4,4-hexafluoro-2-butene (R-1336mzz(Z)) by the transient hot-wire method. *Int. J. Refrig.* 84, 220–227. <https://doi.org/10.1016/j.ijrefrig.2017.08.014>
- Alam, M.J., Miyara, A., Kariya, K., Kontomaris, K.K., 2018. Measurement of Viscosity of cis- 1,1,1,4,4,4-Hexafluoro-2-butene (R-1336mzz(Z)) by Tandem Capillary Tubes Method. *J. Chem. Eng. Data* 63, 1706–1712. <https://doi.org/10.1021/acs.jced.8b00036>
- Amakusa, N., Mondal, D., Tuhin, A.R., Kariya, K., Miyara, A., 2021. Viscosity Measurement of R1336mzz(E) by tandem capillary tubes method, in: Proceedings of the HFO2021 2nd IIR Conference on HFOs and Low GWP Blends. pp. 208–212, Japan.
- ASHRAE, 2016. ANSI/ASHRAE Standard 34-2016, in Design and Safety Classification of Refrigerants, Atlanta GA: ASHRAE.
- ASTM, 2004. ASTM E681-04: Standard Test Method for Concentration Limits of Flammability of Chemicals (Vapor and Gases). ASTM International, West Conshohocken, PA. <https://doi.org/10.1520/E0681-04>
- Bell, S., 2001. A Beginner's Guide to Uncertainty of Measurement, Measurement Good Practice Guide No. 11 (Issue 2), Centre for Basic, Thermal and Length Metrology, National Physical Laboratory. Teddington, Middlesex, United Kingdom, TW11 0LW.
- Cheung, H., 1958. Thesis of Thermal Conductivity and Viscosity of Gas Mixture Mixture, Printed for the U.S. Atomic Energy Commission, UCRL-8230.

- Craig, N.C., Entemann, E.A., 1961. Thermodynamics of cis-trans Isomerizations. The 1,2-Difluoroethylenes. J. Am. Chem. Soc. 83, 3047–3050.
<https://doi.org/10.1021/ja01475a019>
- Dang, Y., Kamiaka, T., Dang, C., Hihara, E., 2015a. Liquid viscosity of low-GWP refrigerant mixtures (R32 + R1234yf) and (R125 + R1234yf). J. Chem. Thermodyn. 89, 183–188.
<https://doi.org/10.1016/j.jct.2015.05.009>
- Dang, Y., Kim, H.S., Dang, C., Hihara, E., 2015b. Measurement of vapor viscosity of R1234yf and its binary mixtures with R32, R125. Int. J. Refrig. 58, 131–136.
<https://doi.org/10.1016/j.ijrefrig.2015.06.010>
- Davidson, T.A., 1993. A simple and accurate method for calculating the viscosity of gaseous mixtures, Report of Investigations 9456, USA.
- Domanski, P.A., Brignoli, R., Brown, J.S., Kazakov, A.F., McLinden, M.O., 2017. Low-GWP Refrigerants for Medium and High-Pressure Application 84, 198–209.
<https://doi.org/10.1016/j.ijrefrig.2017.08.019> LOW-GWP
- Grunberg, L., Nissan, A.H., 1949. Mixture Law for Viscosity. J. Biol. Agric. Healthc. 164, 799–800.
- Hashimoto, M., Otsuka, T., Fukushima, M., Okamoto, H., Hayamizu, H., Ueno, K., Akasaka, R., 2019. Development of New Low-GWP Refrigerants–Refrigerant Mixtures Including HFO-1123. Sci. Technol. Built Environ. 25, 776–783.
<https://doi.org/10.1080/23744731.2019.1603779>
- Higashi, Y., 1994. Critical parameters for HFC134a, HFC32 and HFC125. Int. J. Refrig. 17, 524–531. [https://doi.org/10.1016/0140-7007\(94\)90028-0](https://doi.org/10.1016/0140-7007(94)90028-0)
- Higashi, Y., Akasaka, R., 2016. Measurements of Thermodynamic Properties for R1123 and R1123 + R32 Mixture, in: Proceedings of the 16th International Refrigeration and Air Conditioning Conference. Paper 1688, pp-2283(1-10).
<http://docs.lib.purdue.edu/iracc/1688>.
- Higashi, Y., Sakoda, N., Kondou, C., 2020. Determination of Saturated Densities, Critical Temperature and Critical Density for New Refrigerant HFO1132(E), in: Proceedings of

- the 2020 JSRAE Annual Conference, Paper D142 (1-5), Tsu-City, Japan. (in Japanese).
- Hori, Y., Alam, M.J., Kariya, K., Miyara, A., 2018. Measurement of Viscosity of Low GWP refrigerant R32/R1123, in: Proceedings of the 39th Japan Symposium on Thermophysical Properties, Nagoya, Japan.
- Huber, M.L., 2018. Models for viscosity, thermal conductivity, and surface tension of selected pure fluids as implemented in REFPROP v10.0, NISTIR 8209. <https://doi.org/10.6028/NIST.IR.8209>
- Imre, A.R., Ramboz, C., Deiters, U.K., Kraska, T., 2015. Anomalous fluid properties of carbon dioxide in the supercritical region: application to geological CO₂ storage and related hazards. *Environ. Earth Sci.* 73, 4373–4384. <https://doi.org/10.1007/s12665-014-3716-5>
- JCGM 100, 2008. Evaluation of measurement data-Guide to the expression of uncertainty in measurement, GUM 1995 with minor corrections.
- Juhasz, J.R., 2017. Novel Working Fluid, HFO-1336mzz(E), for Use in Waste Heat Recovery Application, in: Proceedings of the 12th IEA Heat Pump Conference. Rotterdam.
- Jung, D.S., Didion, D., 1990. Mixing rule for liquid viscosities of refrigerant mixtures. *Int. J. Refrig.* 13, 243–247. [https://doi.org/10.1016/0140-7007\(90\)90036-V](https://doi.org/10.1016/0140-7007(90)90036-V)
- Kim, M.H., Pettersen, J., Bullard, C.W., 2004. Fundamental process and system design issues in CO₂ vapor compression systems, *Progress in Energy and Combustion Science*. <https://doi.org/10.1016/j.pecs.2003.09.002>
- Kontomaris, K., 2014. HFO-1336mzz-Z: High Temperature Chemical Stability and Use as a Working Fluid in Organic Rankine Cycles, in: Proceedings of 15th International Refrigeration and Air Conditioning Conference. Purdue University, Purdue e-Pubs, pp. 2250 (1–10). <https://doi.org/http://docs.lib.purdue.edu/iracc/1525>
- Lemmon, E.W., Bell, I. H., Huber, M., L., McLinden, M.O., 2018. NIST Standard Reference Database 23: Reference Fluid Thermodynamic Properties-REFPROP (DLL Version 10.0a), NIST, USA. NIST, USA.
- Lemmon, E.W., McLinden, M.O., Wagner, W., 2009. Thermodynamic Properties of Propane. III. A Reference Equation of State for Temperatures from the Melting Line to 650 K and

- Pressures up to 1000 MPa. *J. Chem. Eng. Data* 54, 3141–3180.
<https://doi.org/10.1021/je900217v>
- Lisochkin, Y.A., Poznyak, V.I., 2006. Explosive-hazard estimates for several fluorine-containing monomers and their mixtures, based on the minimum ignition pressure with a fixed igniter energy. *Combust. Explos. Shock Waves* 42, 140–143.
<https://doi.org/10.1007/s10573-006-0031-9>
- Lydersen, A.L., 1955. Estimation of Critical Properties of Organic Compounds. Engineering Experiment Station Report 3, Madison, Wisconsin: University of Wisconsin College Engineering.
- McLinden, M.O., 2009. Thermodynamic Properties of Propane. I. P- ρ -T Behavior from (265 to 500) K with Pressures to 36 MPa. *J. Chem. Eng. Data* 54, 3181–3191.
<https://doi.org/10.1021/je900124n>
- Miyara, A., Alam, M.J., Kariya, K., 2018a. Measurement of viscosity of trans-1-chloro-3,3,3-trifluoropropene (R-1233zd(E)) by tandem capillary tubes method. *Int. J. Refrig.* 92, 86–93. <https://doi.org/10.1016/j.ijrefrig.2018.05.021>
- Miyara, A., Alam, M.J., Kariya, K., 2018b. Measurements of transport properties of low GWP refrigerant HCFO-1224yd(Z) (cis-1-chloro-2,3,3,3-tetrafluoropropene; $\text{CF}_3\text{CF}=\text{CHCl}$), in: Proceedings of the 1st IIR International Conference on the Application of HFO Refrigerants, Birmingham, UK. <https://doi.org/10.18462/iir.hfo.2018.139>
- Miyoshi, K., Mondal, D., Tuhin, A.R., Kariya, K., Miyara, A., 2020. Thermal Conductivity Measurement of HFO Refrigerant R1336mzz(E), in: Proceedings of the 2020 JSRAE Annual Conference, Page-D113 (1-5), Tsu-City, Mie, Japan. (in Japanese).
- Mondal, D., Hori, Y., Kariya, K., Miyara, A., 2019. Measurement of vapor viscosity of R1123/R32 mixture refrigerant by tandem capillary tubes method, in: Proceedings of the 12th Asian Thermophysical Properties Conference (ATPC 2019). Xi'an Jiaotong University, Xi'an, China.
- Mondal, D., Hori, Y., Kariya, K., Miyara, A., Alam, M.J., 2020. Measurement of Viscosity of a Binary Mixture of R1123+R32 Refrigerant by Tandem Capillary Tube Method. *Int. J. Thermophys.* 41, 83 (1–20). <https://doi.org/10.1007/s10765-020-02653-4>

- Mondal, D., Kariya, K., Tuhin, A.R., Miyoshi, K., Miyara, A., 2021a. Thermal Conductivity Measurement and correlation at saturation condition of HFO refrigerant trans-1,1,1,4,4,4-hexafluoro-2-butene (R1336mzz(E)). *Int. J. Refrig.* 129, 109–117. <https://doi.org/10.1016/j.ijrefrig.2021.05.005>
- Mondal, D., Tuhin, A.R., Kariya, K., Miyara, A., 2021b. Measurement of Thermal Conductivity of 3,3,4,4,5,5-HFCPE, in: *Proceedings of the HFO2021 2nd IIR Conference on HFOs and Low GWP Blends*. pp. 200–207, Japan.
- Myhre, G., Shindell, D., Bréon, F.-M., Collins, W., Fuglestad, J., Huang, J., Koch, D., Lamarque, J.-F., Lee, D., Mendoza, B., Nakajima, T., Robock, A., Stephens, G., Takemura, T., Zhang, H., 2013. Anthropogenic and Natural Radiative Forcing, in: *Climate Change 2013: The Physical Science Basis. Contribution of Working Group I to the Fifth Assessment Report of the Intergovernmental Panel on Climate Change*. Cambridge University Press, Cambridge, United Kingdom and New York, NY, USA., pp. 659–740. <https://doi.org/10.1017/CBO9781107415324.018>
- Nakamura, T., Jojima, Y., Iwasaki, S., Kondou, C., Higashi, Y., 2020. Measurements of Triple Point and Surface Tension for a New Refrigerant HFO1132(E), in: *Proceedings of the 2020 JSRAE Annual Conference*, Paper D141 (1-6), Tsu-City, Japan. (in Japanese).
- Otsuka, T., Ueno, K., Okamoto, H., Ippommatsu, M., Dobashi, R., 2018. Analysis of disproportionation process of trifluoroethylene mixtures. *J. Loss Prev. Process Ind.* 54, 179–182. <https://doi.org/10.1016/j.jlp.2018.03.014>
- Perera, U.A., Thu, K., Miyazaki, T., Sakoda, N., Higashi, Y., 2021. Saturation vapour pressure measurements of the new refrigerant HFO1132(E), in: *Proceedings of the 2nd IIR Conference on HFOs and Low GWP Blends*, Japan.
- Perera, U.A., Thu, K., Miyazaki, T., Sakoda, N., Higashi, Y., 2020. Determination of saturation pressure and critical pressure for new refrigerant HFO1132(E), in: *Proceedings of the 2020 JSRAE Annual Conference*, Paper D143 (1-5), Tsu-City, Japan.
- Poling, B.E., Prausnitz, J.M., O’Connell, J.P., 2000. *The Properties of Gases and Liquids*, Fifth. ed. McGraw-Hill.
- Richter, M., McLinden, M.O., Lemmon, E.W., 2011. *Thermodynamic Properties of 2,3,3,3-*

- Tetrafluoroprop-1-ene (R1234yf): Vapor Pressure and P- ρ -T Measurements and an Equation of State. *J. Chem. Eng. Data* 56, 3254–3264. <https://doi.org/10.1021/je200369m>
- Riedel, L., 1954. *Chem. Ing. Tech.* 26, 679.
- Sakoda, N., Higashi, Y., 2021. Thermodynamic properties measurement of HFO1132(E), in: *Proceedings of the HFO2021 2nd IIR Conference on HFOs and Low GWP Blends*, Japan.
- Sakoda, N., Higashi, Y., Akasaka, R., 2021. Measurements of PvT Properties, Vapor Pressures, Saturated Densities, and Critical Parameters for trans-1,1,1,4,4,4-Hexafluoro-2-butene (R1336mzz(E)). *J. Chem. Eng. Data* 6, 734–739. <https://doi.org/10.1021/acs.jced.0c00848>
- Saravi, S.S., Tassou, S.A., 2019. An investigation into sCO₂ compressor performance prediction in the supercritical region for power systems. *Energy Procedia* 161, 403–411. <https://doi.org/10.1016/j.egypro.2019.02.098>
- Sutherland, W., 1895. XXXVII. The viscosity of mixed gases . London, Edinburgh, Dublin *Philos. Mag. J. Sci.* 40, 421–431. <https://doi.org/10.1080/14786449508620789>
- Tanaka, K., Akasaka, R., Sakaue, E., Ishikawa, J., Kontomaris, K.K., 2017a. Measurements of the Critical Parameters for cis-1,1,1,4,4,4-Hexafluoro-2-butene. *J. Chem. Eng. Data* 62, 1135–1138. <https://doi.org/10.1021/acs.jced.6b00990>
- Tanaka, K., Akasaka, R., Sakaue, E., Ishikawa, J., Kontomaris, K.K., 2016. Thermodynamic Properties of cis-1,1,1,4,4,4-Hexafluoro-2-butene (HFO-1336mzz(Z)): Measurements of the P ρ T Property and Determinations of Vapor Pressures, Saturated Liquid and Vapor Densities, and Critical Parameters. *J. Chem. Eng. Data* 61, 2467–2473. <https://doi.org/10.1021/acs.jced.6b00169>
- Tanaka, K., Ishikawa, J., Kontomaris, K.K., 2017b. Thermodynamic properties of HFO-1336mzz(E) (trans-1,1,1,4,4,4-hexafluoro-2-butene) at saturation conditions. *Int. J. Refrig.* 82, 283–287. <https://doi.org/10.1016/j.ijrefrig.2017.06.012>
- Tanaka, K., Ishikawa, J., Kontomaris, K.K., 2017c. P ρ T Property of HFO-1336mzz(E) (trans-1,1,1,4,4,4-Hexafluoro-2-butene). *J. Chem. Eng. Data* 62, 2450–2453. <https://doi.org/10.1021/acs.jced.7b00381>

- Tanaka, T., Okamoto, H., Ueno, K., Irisawa, J., Otsuka, T., Noigami, T., 2014. Development of a new low-GWP refrigerant composed of HFO-1123 (trifluoroethylene), in: Proceedings of the AIChE Annual Meeting, Atlanta.
- Taylor, B.N., Kuyatt, C.E., 1994. Guidelines for Evaluating and Expressing the Uncertainty of NIST Measurement Results, NIST Technical Note 1297, National Institute for Standards and Technology (NIST).
- Tokuhashi, K., Uchimaru, T., Takizawa, K., Kondo, S., 2019. Rate Constants for the Reactions of OH Radicals with the (E)/(Z) Isomers of $\text{CFCl}=\text{CFCl}$ and (E)- $\text{CHF}=\text{CHF}$. *J. Phys. Chem. A* 123, 4834–4843. <https://doi.org/10.1021/acs.jpca.9b02454>
- Tuhin, A.R., Mondal, D., Amakusa, N., Kariya, K., Miyara, A., 2021. Measurement of Transport Properties of R1336mzz(E), in: Proceedings of the Twenty-First Symposium on Thermophysical Properties, Boulder, CO, USA.
- Tuhin, A.R., Mondal, D., Miyoshi, K., Kariya, K., Miyara, A., 2020. Kinematic Viscosity Measurement of 3,3,4,4,5,5 HFCPE, in: Proceedings of the 2020 JSRAE Annual Conference, Paper D112 (1-6), Tsu-City, Japan. Tsu-city, Japan.
- UNEP, 2014. Montreal Protocol on Substances that Deplete the Ozone Layer, 2014 Report of the Refrigeration, Air Conditioning and Heat Pumps Technical Options Committee.
- Vetere, A., 1991. The Riedel Equation. *Ind. Eng. Chem. Res.* 30.
- Viswanath, D.S., Ghosh, T.K., Prasad, D.H.L., Dutt, N.V.K., Rani, K.Y., 2007. Viscosity of Liquids: Theory, Estimation, Experiment, and Data, Springer Editions, Dordrecht, Netherlands.
- Wajima, K., Matsukura, T., Ueda, K., Naoki, K., Suemitsu, R., Akamatsu, Y., Saku, F., Lap, X.L., Tamura, R., Suda, H., Sluice, J., Takizawa, K., Chen, L., Right, C.R., 2017. Heat Source Machine and Operating Method Therefor, Publication of WO2017138614A1, WIPO (PCT). <https://doi.org/patents.google.com/patent/WO2017138614A1/ja>
- Wilke, C.R., 1950. A viscosity equation for gas mixtures. *J. Chem. Phys.* 18, 517–519. <https://doi.org/10.1063/1.1747673>
- Yang, J., Ye, Z., Yu, B., Ouyang, H., Chen, J., 2019. Simultaneous experimental comparison

of low-GWP refrigerants as drop-in replacements to R245fa for Organic Rankine cycle application: R1234ze(Z), R1233zd(E), and R1336mzz(E). *Energy* 173, 721–731. <https://doi.org/10.1016/j.energy.2019.02.054>

Yao, C., Zhao, X., Lv, S., Guo, Z., 2014. Thermal conductivity of ethyl fluoride (HFC161). *Fluid Phase Equilib.* 375, 228–235. <https://doi.org/10.1016/j.fluid.2014.04.038>

Chapter 5

Conclusions and Recommendations

5.1. Conclusions

The viscosity and thermal conductivity are the important transport properties of working fluids that are used as the key tools to design and implement the optimum energy systems, efficient processes, selection of the refrigerant for the practical appliances, and simulations. In this study, the viscosity and thermal conductivity measurements were conducted by the tandem capillary tubes method and the transient hot-wire method, respectively. The viscosities and thermal conductivities of environmentally friendly refrigerants and refrigerant mixtures (e.g., R1336mzz(E), 3,3,4,4,5,5-HFCPE, R1132(E), and a mixture of R1123+R32) were measured effectively in a wide range of temperatures and pressures. In the tandem capillary tubes method, the measurement cell as viscometer was constructed using two capillary tubes that are horizontally installed in series connection to eliminate the end effect of capillary tubes. While in the transient hot wires method, two parallel thin (15 μm diameter) platinum wires are used vertically to construct the measurement cell for eliminating the effects due to axial heat conduction. Based on the experimental study, the key results of the current research are summarized as the followings:

- (1) The reliability test of the apparatus to measure the viscosity and thermal conductivity was done by utilizing the reference fluid of R134a. Obtained values are comparable with standard experimental and correlations values.
- (2) The viscosities of eco-friendly refrigerants R1336mzz(E), 3,3,4,4,5,5-HFCPE, R1132(E), and mixture (R1123+R32) were measured over a wide range of temperature and pressure, where the experimental conditions are listed in Table 5.1.
- (3) The thermal conductivities of eco-friendly refrigerants R1336mzz(E) and 3,3,4,4,5,5-HFCPE were measured over a wide range of temperature and pressure, where the experimental conditions are listed in Table 5.2.

- (4) The uncertainties for all measurements were calculated using the law of propagation by the GUM method. The obtained combined standard uncertainties and expanded uncertainties both for viscosities and thermal conductivities measurement were summarized in Tables 5.3 and 5.4.
- (5) The simplified correlations are developed to predict the viscosities and thermal conductivities by the extrapolation method using the experimental data up to saturation conditions.

Table 5.1 Experimental conditions to measure viscosities of test fluids

Test fluid	Temperature range (K)			Pressure range (MPa)		
	Liquid	Vapor	SpCr*	Liquid	Vapor	SpCr*
R1336mzz(E)	314-394	353-453	413-453	1.00-4.02	0.50-2.02	3.00-4.01
3,3,4,4,5,5-HFCPE	332-494	413-514	-	0.50-4.03	0.50-2.02	-
R1132(E)	302-335	323-345	-	3.00-4.01	2.50-4.00	-
R1123+R32	251-313	323-383	-	2.48-4.06	2.53-4.52	-

*SpCr–Supercritical Phase

Table 5.2 Experimental conditions to measure thermal conductivities of test fluids

Test fluid	Temperature range (K)			Pressure range (MPa)		
	Liquid	Vapor	SpCr*	Liquid	Vapor	SpCr*
R1336mzz(E)	313-393	313-453	413-453	0.51-4.04	0.25-2.52	3.00-4.04
3,3,4,4,5,5-HFCPE	334-473	393-473	-	0.50-4.04	0.25-1.51	-

*SpCr–Supercritical Phase

Table 5.3 Summary of uncertainties for viscosity measurements

Test fluid	Combined Uncertainties (%)			Expanded Uncertainties (%) (k=2 and 95% Confidence Level)		
	Liquid	Vapor	SpCr*	Liquid	Vapor	SpCr*
R1336mzz(E)	1.13	1.15	1.16	2.26	2.30	2.32
3,3,4,4,5,5-HFCPE	1.12	1.47	-	2.24	2.94	-
R1123+R32	1.10	1.30	-	2.21	2.60	-

*SpCr–Supercritical Phase

Table 5.4 Summary of uncertainties for thermal conductivity measurements

Test fluid	Combined Uncertainties (%)			Expanded Uncertainties (%) (k=2 and 95% Confidence Level)		
	Liquid	Vapor	SpCr*	Liquid	Vapor	SpCr*
R1336mzz(E)	1.53	1.58	1.62	3.06	3.16	3.23
3,3,4,4,5,5-HFCPE	1.54	1.76	-	3.08	3.52	-

*SpCr–Supercritical Phase

5.2. Future Recommendations

Some recommendations for future work based on the present research are as the followings

- (1) To measure viscosities and thermal conductivities in a low-temperature zone of working fluids R1336mzz(E), 3,3,4,4,5,5-HFCPE, R1132(E), a mixture of R1123+R32, and others.
- (2) To develop the experimental apparatus to measure the low temperature and high-pressure viscosities and thermal conductivities data for developing the fluid specification correlations.
- (3) To modify the experimental apparatus to measure in a high-temperature and high-pressure range.
- (4) To measure viscosities and thermal conductivities of new pure refrigerants and mixture refrigerants blending in different proportions.
- (5) To develop reliable prediction methods for pure and mixed working fluids.

Appendix

1.0 Measurement of capillary tubes diameter and length:

In this work, the viscosity measurements of working fluids are performed by the method of tandem capillary tubes based on modified Hagen-Poiseuille law. During the measurements, viscosities are greatly influenced by the inner diameter of thin capillary tubes. The fourth power of the diameter or radius of the capillary tubes stimulates the significant effects on the experimental viscosity data. Consequently, it is extremely important to determine the diameter of the capillary tubes with precision. However, the length and the inner diameter of the capillary tube were measured using a reading microscope and the gravimetric method, respectively. In this method, the capillary tube is filled with mercury and the weight of mercury (w) is determined as the following (Kao et al., 1968).

Therefore,

$$w = \rho_{Hg} \pi \int_{L_1}^{L_2} r^2 dl \quad (A1)$$

Therefore, the diameter of capillary tubes can be determined by the gravimetric method as

$$d = 2r = 2 \sqrt{\frac{m_{Hg}}{\pi \rho_{Hg} (L_2 - L_1)_{Hg}}} \quad (A2)$$

where w and ρ_{Hg} are the weight and density of mercury used, $(L_2 - L_1)_{Hg}$ is the length of the mercury column.

Therefore, the mercury is filled to the capillary, and the inner diameter of the capillary is calculated from the length and weight of the mercury column. Also, consider a state in which the temperature of the thin tube is steady with the surroundings. This is to prevent the density of mercury and the length of the mercury column from fluctuating due to the body temperature transmitted when injecting mercury into the capillary tube. The formula for calculating the inner diameter of the thin tube is shown in Eq. (A2).

Fig. A1 shows the measurement of the diameter of the capillary tube from the length and weight of mercury-filled in the capillary by using a microscope and agreed well with the gravimetric method. As shown in the figure, L_3 is the length of the thin capillary tube, and $(L_2 - L_1)_{Hg}$ is the length of the mercury column. Each length was visually measured with an accuracy of 1/100 (mm) using a microscope, and the mass (m_{Hg}) was measured with an accuracy of 1/100 (mg) with a high-precision weighing scale. While Fig. A2 shows the microscopic view of the capillary tubes diameter calculation for the (a) side and (b) face view. The measurement results of the thin capillary tubes used in this experiment are shown in Table A1.

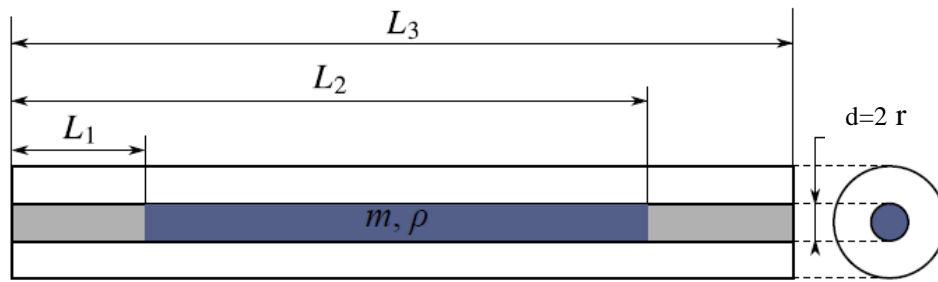


Fig. A1: Measurement of capillary tubes dimensions using gravimetric method

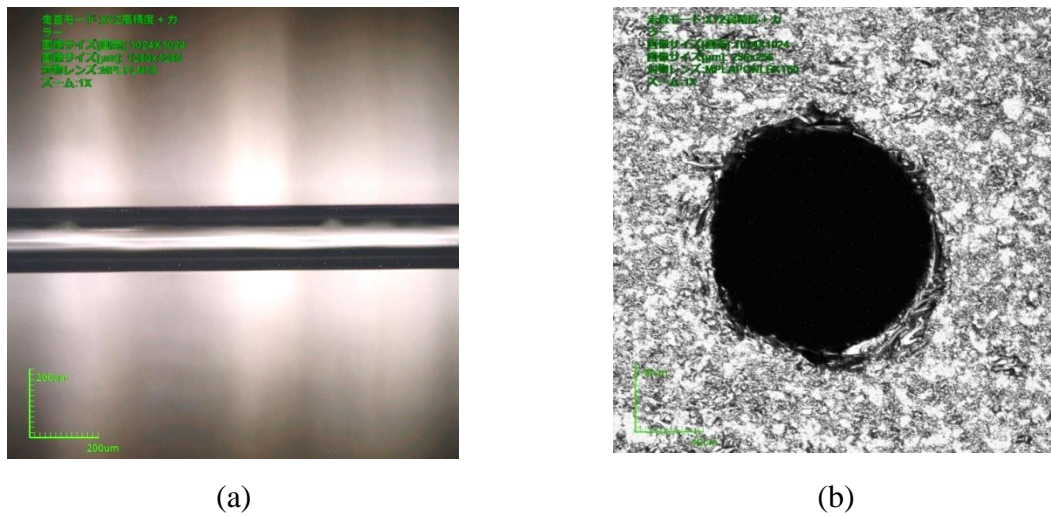


Fig. A2: Measurement of diameter using microscope (a) side (b) face end views of capillary

Table A1: Measurement results of the thin capillary tubes dimensions

Type	Capillary	Length (mm)	Inner diameter (mm)
Electric (<i>heating</i>)	Long	99.85	0.1269
	Short	50.16	0.1268
Oil/nybrine(<i>heating or cooling</i>)	Long	99.98	0.1278
	Short	49.92	0.1279

2.0 Measurement of the length of hot wires:

The lengths of the platinum wires were measured by an absolute digimatic cathetometer with an accuracy of 1/100 (mm). A cathetometer is an instrument for measuring vertical distances in cases where a scale cannot be placed very close to the points whose distance apart is desired. Fig. A3 shows the digimatic cathetometer to measure the length of hot wires and all measurement data to calculate the average lengths are listed in Table A2.

Table A2: Measurement of the length of platinum wires using digimatic cathetometer

Type	Wire	Length of hot wire			
		<i>Run 1</i>	<i>Run 2</i>	<i>Run 3</i>	<i>Average</i>
Electric (heating)	Long	93.45	93.46	93.46	93.46
	Short	44.89	44.90	44.89	44.89
Oil/nybrine(heating or cooling)	Long	50.14	50.15	50.13	50.14
	Short	19.54	19.53	19.54	19.54



Fig. A3: Measurement of the platinum wires length using the digimatic cathetometer

3.0 Uncertainty analysis

Uncertainty analysis was performed to improve the reliability of the measured values in the measurement. The uncertainties of viscosity and thermal conductivity measurements were calculated for the working fluids R1336mzz(E), 3,3,4,4,5,5-HFCPE, R1132(E), and mixture (R1123+R32) using the law of propagation by the GUM method (Bell, 2001; JCGM 100, 2008; Taylor and Kuyatt, 1994). In this method, the errors due to the individual parameter of measurements were considered to measure total combined standard uncertainty as well as expanded uncertainty with $k=2$ and 95 % confidence level. As an example of estimation of uncertainty, the procedure is discussed in the following sections.

3.1 Uncertainty analysis of R1336mzz(E) of viscosity measurement at liquid phase

The apparatus of the tandem capillary tubes method used to measure viscosity is newly developed in this thermal engineering lab. Uncertainty analysis was performed to verify the measurement accuracy and reliability of measured data. The uncertainty analysis process of viscosity for R1336mzz(E) is shown below.

As described in Chapter 3 “Theory and Experimental Apparatus” the viscosity calculation formula in this study is expressed by the formula as below.

$$\eta = \frac{\pi \left(r_l^4 \Delta P_l - r_s^4 \Delta P_s \right)}{8q \left(L_l - L_s \right)} \quad (\text{A3})$$

where, r is the inside tube radius, ΔP_l and ΔP_s are the pressure difference at the inlet and outlet of the long and short capillary tubes, respectively. L_l and L_s are the lengths of long and short capillary tubes, respectively, and q is the flow rate.

a) Uncertainty due to inner diameter of capillary tubes

The diameter of the capillary tube was measured by the gravimetric method. In this method, the capillary is filled with mercury and the weight (w) of mercury is determined as the following equation

$$d = 2r = 2 \sqrt{\frac{m_{Hg}}{\pi \rho_{Hg} (L_2 - L_1)_{Hg}}} \quad (A4)$$

From Eq. (A4),

$$r^4 = (r^2)^2 = \frac{m_{Hg}}{\pi \rho_{Hg} (L_2 - L_1)_{Hg}} \quad (A5)$$

The combined standard uncertainty due to capillary diameter is

$$u(r^4) = 2 u(r^2) \quad (A6)$$

From the above Eq. (A4), it is observed that the uncertainty of diameter measurement depends on errors due to the length and weight measurement of mercury. $(L_2 - L_1)_{Hg}$ is the length of mercury columns. The length and weight of mercury are listed below in Tables A3 and A4, respectively.

Table A3: The length of mercury in the capillary tube

run	Long tube (mm) ($L_2 - L_1$)	Short tube (mm) ($L_2 - L_1$)
1	78.35	24.70
2	78.33	24.68
3	78.36	24.68

Table A4: The weight of mercury in the capillary tubes

run	Long tube (g) m_l	Short tube (g) m_s
1	0.01360	0.00429
2	0.01359	0.00432
3	0.01369	0.00428

The standard uncertainty in the measurement is expressed as, (detailed in Chapter 3, section 3.1.4)

Using the GUM method, type-A evaluation of standard uncertainty;

$$u(x_i)_A = s(\bar{x}_i) = \sqrt{\frac{s^2(x_i)}{n}} \quad (A7)$$

And, type-B evaluation uncertainty for the reading instrument or calibration;

$$u(x_i)_B = \sqrt{\frac{\partial x^2}{12}} \quad (A8)$$

Table A5: Uncertainties records due to diameter of capillary tubes

Sl	$u(x_i)_A$				$u(x_i)_B$	$u(r^4) = 2 u(r^2)$
	$(\partial\eta/\partial L_{HgL})$ $u(L_{HgL})_A$ (%)	$(\partial\eta/\partial L_{HgS})$ $u(L_{HgS})_A$ (%)	$(\partial\eta/\partial m_{HgL})$ $u(m_{HgL})_A$ (%)	$(\partial\eta/\partial m_{HgS})$ $u(m_{HgS})_A$ (%)	$(\partial\eta/\partial d)$ $u(d)_B$ (%)	$(\partial\eta/\partial d) u(d)$ (%)
1.	0.0113	0.0270	0.2334	0.2797	2.89×10^{-6}	0.7309

Therefore, the total standard uncertainty due to diameter is 0.7309 %

b) *Uncertainty due to length measurement of capillary tubes*

Measurement of the length of capillary tubes is carried out three times by microscope and it is considered the average one. The measurement results of the length of the capillary tube are shown below.

Table A6: The lengths of long and short capillary tubes

run	L_l (mm)	L_s (mm)
1	99.86	50.15
2	99.82	50.17
3	99.87	50.17

The uncertainty of the wire length includes the uncertainty of type-A due to the repeatability of measurement and the uncertainty of type-B due to the resolution of the microscope. Type-A and type-B evaluation uncertainties are estimated from Eq. (A7) and Eq. (A8), respectively.

Table A7: Uncertainties records due to the length of capillary tubes

Sl	$u(x_i)_A$		$u(x_i)_B$	$u(x_i)$
	$(\partial\eta/\partial L_l) u(L_l)_A$ (%)	$(\partial\eta/\partial L_s) u(L_s)_A$ (%)	$(\partial\eta/\partial L) u(L)_B$ (%)	$(\partial\eta/\partial L) u(L)$ (%)
1.	0.0153	0.0133	0.0029	0.0205

Therefore, the total standard uncertainty due to length is 0.0205 %

c) *Uncertainty due to differential pressure*

The differential pressure gauge used in this apparatus is PDU-A-50 KP manufactured by Kyowa Denshi. Type-B uncertainty of differential pressure is calculated from the information of the instruction manual, the measurement errors of the apparatus consist of nonlinearity, hysteresis, zero temperature effect, output temperature influence. In addition, type-A uncertainty was estimated from Eq. (A7).

This experiment was carried out by keeping the room temperature in the laboratory at 20°C. the inspection report is detailed below.

Table A8: The inspection report of differential pressure device (at room temperature 20°C)

Parameter	<i>Long tube side</i>	<i>Short tube side</i>
Rated output (RO) [$\mu\text{V}/\text{V}$]	1499	1499
Nonlinearity, N_L [% RO]	0.09	0.07
Hysteresis, H_Y [% RO]	0.03	0.05
Zero temperature effect [% RO / °C]	0.02	0.02
Output temperature effect [% / °C]	0.02	0.02

The rated output described in the inspection report is the output voltage when the applied voltage of 1V is applied. In this experiment, the applied voltage of 8V is always applied to the differential pressure gauge.

Therefore,

$$\text{Rated output (RO)} = 1499 \times 8.0 [\mu\text{V} / \text{V}] \quad (\text{A9})$$

The effects of zero temperature and output temperature are extended as follows.

$$\text{Zero temperature effect, } ZT_e = 0.02 \times 20 = 0.4 [\% \text{ RO}] \quad (\text{A10})$$

$$\text{Output temperature effect, } OT_e = 0.02 \times 20 = 0.4 [\%] \quad (\text{A11})$$

So, the uncertainty due to the pressure difference of long and short tubes are calculated using Eq. (A12)

$$u(x)_B = u(\Delta P)_B = \sqrt{(N_L)^2 + (H_Y)^2 + (ZT_e)^2 + (OT_e)^2} \quad (\text{A12})$$

Table A9: Uncertainties records due to the pressure difference of long and short tubes

Sl	$u(x_i)_A$		$u(x_i)_B$		$u(x_i)$
	$(\partial \eta / \partial \Delta P_l)$ $u(\Delta P_l)_A$ (%)	$(\partial \eta / \partial \Delta P_s)$ $u(\Delta P_s)_A$ (%)	$(\partial \eta / \partial \Delta P_l)$ $u(\Delta P_l)_B$ (%)	$(\partial \eta / \partial \Delta P_s)$ $u(\Delta P_s)_B$ (%)	$(\partial \eta / \partial \Delta P) u(\Delta P)$ (%)
1.	0.0942	0.1951	0.5736	0.5722	0.8387

Therefore, the total standard uncertainty due to length is 0.8387 %

d) Uncertainty due to flow rate

The Coriolis flowmeter used in this experimental apparatus is a mini CORI-FLOW M12 manufactured by Bronkhorst. From the company's calibration certificate, the accuracy of the equipment is indicated as follows.

$$\text{Rated accuracy} = 0.2\%RD + ZS \quad (\text{A13})$$

Here, RD shows the measured value and ZS shows the effect of the zero points. For this device (mini CORI-FLOW M12), refer to the Bronkhorst® Japan Operation Guidebook.

$$\text{Zero Stability} = < 0.02 [g / h] \quad (\text{A14})$$

In this experiment, the maximum measured flow rate for the liquid phase is 37.84 [g/h]. Therefore, the maximum relative standard uncertainty by the flow meter is calculated as follows

$$u(x)_B = \frac{u_q}{q} = \frac{0.2\%RD + ZS}{q} \quad (\text{A15})$$

The above equation is used for estimating type-B uncertainty and Eq. (A3) is used for type-A uncertainty.

Table A10: Uncertainties records due to the flow rate

Sl	$u(x_i)_A$	$u(x_i)_B$	$u(x_i)$
	$(\partial\eta/\partial q) u(q)_A$ (%)	$(\partial\eta/\partial q) u(q)_B$ (%)	$(\partial\eta/\partial q) u(q)$ (%)
1.	0.0366	0.0581	0.0687

Therefore, the total standard uncertainty due to the flow rate is 0.0687 %.

e) Uncertainty due to temperature and pressure

The temperature and pressure uncertainties were calculated from accuracy information from the manufacturer (type-A) and measurements or calibration (type-A or B). The uncertainty due to temperature and pressure are 0.020 K and 0.0037 MPa, respectively.

But the uncertainty due to measurement temperature and pressure were used to calculate the combined uncertainty calculation. Therefore, the uncertainty of temperature and pressure for type-A evaluation is calculated by using Eq. (A7) and found as,

Table A11: Standard uncertainties records due to temperature and pressure

Sl	$u(x_i)_A$	$u(x_i)_A$
	$(\partial\eta/\partial T) u(T) (\%)$	$(\partial\eta/\partial P) u(P) (\%)$
1.	0.0274	0.1857

f) Uncertainty due to the instrument

The uncertainty due to the instruments was calculated from the total standard uncertainty due to capillary tube length and diameter (type-A and type-B), and the standard uncertainty of pressure drop (type-B) from Eq. (A12).

Table A12: Standard uncertainties records due to the instruments

Sl	$u(x_i)_A$		$u(x_i)_B$		$u(x_i)$
	$(\partial\eta/\partial d) u(d) (\%)$	$(\partial\eta/\partial L) u(L) (\%)$	$(\partial\eta/\partial \Delta P_l) u(\Delta P_l)_B (\%)$	$(\partial\eta/\partial \Delta P_s) u(\Delta P_s)_B (\%)$	$(\partial\eta/\partial I) u(I) (\%)$
1.	0.7309	0.0182	0.5736	0.5722	1.0913

Therefore, the total standard uncertainty due to the instruments is 1.09 %.

g) Combined standard uncertainty and Expanded Uncertainty estimation**Table A13:** Components that responsible for the uncertainty calculation of Viscosity measurements

Components that are responsible for the uncertainty	Uncertainty [%]
Diameter of the capillary tube, $\left(\frac{\partial\eta}{\partial d}\right) u(d)$	0.7309
Length of the capillary tube, $\left(\frac{\partial\eta}{\partial L}\right) u(L)$	0.0205
Differential pressure drop, $\left(\frac{\partial\eta}{\partial \Delta P}\right) u(\Delta P)$	0.8387
Flow rate, $\left(\frac{\partial\eta}{\partial q}\right) u(q)$	0.0687
Temperature, $\left(\frac{\partial\eta}{\partial T}\right) u(T)$	0.0274
Pressure, $\left(\frac{\partial\eta}{\partial P}\right) u(P)$	0.1857

Then total combined uncertainty for viscosity measurement was calculated from the below equation as

$$u_c(\eta) = \sqrt{\left(\frac{\partial \eta}{\partial d}\right)^2 u^2(d) + \left(\frac{\partial \eta}{\partial L}\right)^2 u^2(L) + \left(\frac{\partial \eta}{\partial \Delta P}\right)^2 u^2(\Delta P) + \left(\frac{\partial \eta}{\partial q}\right)^2 u^2(q) + \left(\frac{\partial \eta}{\partial T}\right)^2 u^2(T) + \left(\frac{\partial \eta}{\partial P}\right)^2 u^2(P)} \quad (\text{A16})$$

Therefore, the total combined standard uncertainty for R1336mzz(E) viscosity measurement is 0.0113 or 1.13 % for the liquid phase.

The expanded uncertainty was calculated using the following Eq (A17) with $k = 2$ and a 95 % confidence level.

$$U_e(\eta) = k \cdot u_c(\eta) \quad (\text{A17})$$

The expanded uncertainty for viscosity measurement of R1336mzz(E) is 2.26 % for the liquid phase.

3.2 Uncertainty analysis of 3,3,4,4,5,5-HFCPE of thermal conductivity measurement at liquid phase

The apparatus of the transient hot wires method used to measure thermal conductivity is newly manufactured in this thermal engineering lab. Uncertainty analysis was performed to verify the measurement accuracy and reliability of measured data. The uncertainty analysis process of thermal conductivity for 3,3,4,4,5,5-HFCPE at the liquid phase is shown below.

As described in Chapter 3 “Theory and Experimental Apparatus”, the thermal conductivity calculation formula in this study is expressed by the formula below

$$\Delta T(t, r_o) = \frac{Q}{4\pi\lambda} \left(\ln t + \ln \frac{4\alpha}{r_o^2 C} \right) \quad (\text{A18})$$

Where, λ and α are the thermal conductivity and thermal diffusivity, respectively, and Q is the heat flux per unit length with $C = \exp(\gamma)$, $\gamma = 0.5772$ is Euler’s constant.

a) Uncertainty due to length measurement of hot wires

Measurement of the length of hot wires is carried out three times by using an absolute digimatic cathetometer. The measurement results of the length of hot wires are shown below.

Table A14: The lengths of long and short hot wires

run	Long (mm)	Short (mm)
1	93.45	44.89
2	93.46	44.90
3	93.46	44.89

The uncertainty of the wire length includes the uncertainty of type A due to the repeatability of measurement and the uncertainty of type B due to the resolution of a reading device. As mention before, the accuracy of the wire length measuring device is 1/100 (mm). Type-A and type-B evaluation uncertainties are estimated from Eq. (A7) and Eq. (A8), respectively.

Table A15: Uncertainties records due to the length of platinum wires

Sl	$u(x_i)_A$	$u(x_i)_B$	$u(x_i)$
	$[(\partial\lambda/\partial l_L) u(l_L)]_A$ (%)	$[(\partial\lambda/\partial l_S) u(l_S)]_A$ (%)	$[(\partial\lambda/\partial l) u(l)]_B$ (%)
1.	0.0036	0.0111	0.0029
			$(\partial\lambda/\partial l) u(l)$ (%)
			0.0120

Therefore, the total standard uncertainty by measuring the lengths of platinum wires is 0.012 %

b) Uncertainty due to the slope of $d\Delta T/d \ln t$

The uncertainty in the slope of total resistance change as temperature rise vs. logarithm of the elapsed time $d\Delta T/d \ln t$ was estimated by the best linear fitting of the slope. The uncertainty due to the linear fitting of the slope is estimated with the type-A evaluation from Eq. (A7).

Therefore, the standard uncertainty due to the linear fitting of the slope of 3,3,4,4,5,5-HFCPE liquid is 0.001986 or 0.1986 %

c) Uncertainty due to the temperature coefficient of hot wire

From the resistance-temperature relation (Fig. A4) of hot wires calibration, the coefficient of the linear term in the calibration equation should be considered in calculating thermal conductivity. The higher-order terms can be ignored because their contribution to the resistance of the hot wire is very small compared with that of the linear term. The uncertainty of the temperature coefficient of hot wire includes the uncertainty of type-A due to the repeatability of measurements and estimated from the fitting accuracy of the fitted curve using Eq. (A7). Therefore, the standard uncertainty of the temperature coefficient of the hot wires is 0.012345 or 1.2345 %

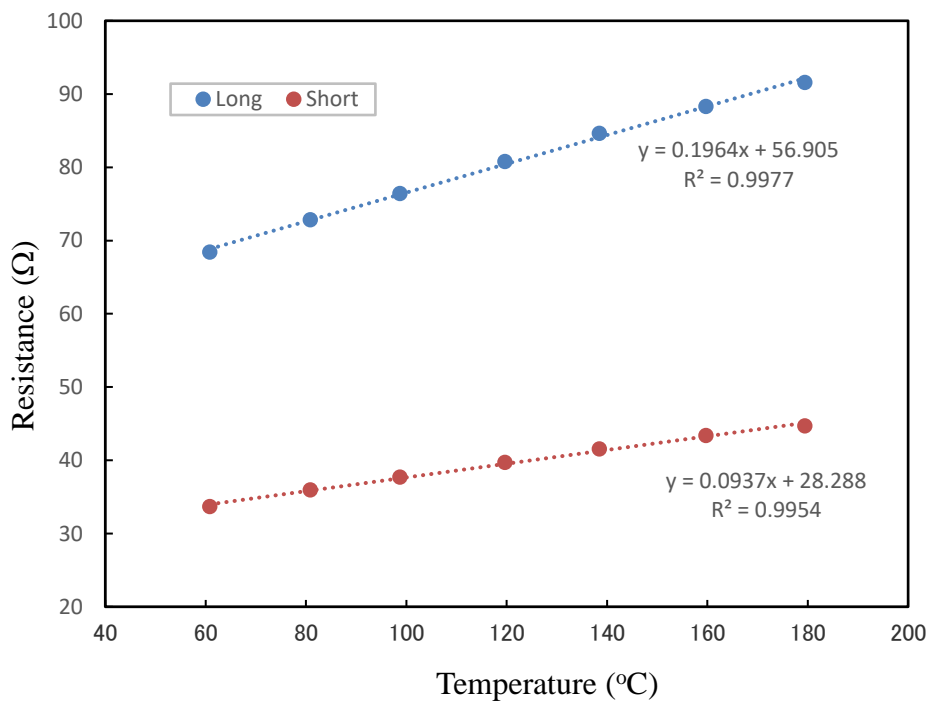


Fig. A4: Resistance vs. temperature curve

d) *Uncertainty due to resistances in the bridge circuit*

Since we used more precision resistors with a very low-temperature coefficient. Therefore, the uncertainty due to resistors is very small compared to the resistance of hot wires. So, the more contribution for standard uncertainty of resistances bridges circuit due to the hot wires. The standard uncertainty due to the resistances was 0.006210 or 0.6210 %

e) *Uncertainty due to heat input to the circuit*

The system power supply was introduced to apply a constant voltage to the bridge circuit. The source voltage was monitored by a precision digital voltmeter and fluctuated with time. Therefore, the standard uncertainty due to heat input was determined as 0.006528 or 0.6528 %.

f) *Uncertainty due to temperature and pressure*

The temperature and pressure uncertainties were calculated from accuracy information from the manufacturer (type-A) and measurements or calibration (type-A or B). The uncertainty due to temperature and pressure are 0.0229 K and 0.0017 MPa, respectively.

But the uncertainty due to measurement temperature was used to calculate the combined uncertainty calculation. Therefore, the uncertainty of temperature for type-A evaluation is calculated by using Eq. (A7) and found as,

Table A16:Standard uncertainties for combined uncertainty calculation due to temperature

Sl	$u(x_i)_A$
	$(\partial\lambda/\partial T) u(T) (\%)$
1.	0.0195

g) *Uncertainty due to the instrument*

The uncertainty due to the instruments include the uncertainties due to platinum wire lengths, resistances in the bridge circuit, and the temperature coefficient of hot platinum wires, respectively. The uncertainty due to the instruments was calculated from the above-mentioned cases. Therefore, the total standard uncertainty due to the instruments is 1.38 %.

h) Combined standard uncertainty and expanded uncertainty estimation

Table A17: Components that responsible for the uncertainty calculation of thermal conductivity measurements

Components that are responsible for the uncertainty	Uncertainty [%]
Length of the platinum wire, $\left(\frac{\partial \lambda}{\partial l}\right)u(l)$	0.0120
The slope of the temperature rise vs. logarithmic elapsed time, $\left(\frac{\partial \lambda}{\partial (d\Delta T/d \ln t)}\right)u(d\Delta T/d \ln t)$	0.1986
Temperature coefficient of platinum hot wire, $\left(\frac{\partial \lambda}{\partial \alpha'}\right)u(\alpha')$	1.2345
Resistance in the bridge circuit, $\left(\frac{\partial \lambda}{\partial R}\right)u(R)$	0.6210
Heat input to the bridge circuit, $\left(\frac{\partial \lambda}{\partial q_h}\right)u(q_h)$	0.6528
Temperature, $\left(\frac{\partial \lambda}{\partial T}\right)u(T)$	0.0195

Then total combined uncertainty for thermal conductivity measurement was calculated from the below equation as

$$u_c(\lambda) = \sqrt{\left(\frac{\partial \lambda}{\partial T}\right)^2 u^2(T) + \left(\frac{\partial \lambda}{\partial (d\Delta T/d \ln t)}\right)^2 u^2(d\Delta T/d \ln t) + \left(\frac{\partial \lambda}{\partial l}\right)^2 u^2(l) + \left(\frac{\partial \lambda}{\partial R}\right)^2 u^2(R) + \left(\frac{\partial \lambda}{\partial \alpha'}\right)^2 u^2(\alpha') + \left(\frac{\partial \lambda}{\partial q_h}\right)^2 u^2(q_h)} \quad (\text{A19})$$

Therefore, the total combined standard uncertainty for thermal conductivity measurement is 0.01541 or 1.54 % for liquid

The expanded uncertainty was calculated using the following Eq (A20) with $k = 2$ and a 95 % confidence level.

$$U_e(\lambda) = k \cdot u_c(\lambda) \quad (\text{A20})$$

The expanded uncertainty for thermal conductivity measurement of 3,3,4,4,5,5-HFCPE is 3.08 % for liquid phase.

4.0 Summary of uncertainties for viscosity and thermal conductivity measurements

The uncertainties of viscosity and thermal conductivity measurements were calculated for the working fluids R1336mzz(E), 3,3,4,4,5,5-HFCPE, R1132(E), and mixture (R1123+R32). The uncertainties are summarized in Table A18 and Table A19 for the viscosity and thermal conductivity measurements, respectively.

Table A18: Summary of uncertainties for viscosity measurements

Test fluid	Combined Uncertainties (%)			Expanded Uncertainties (%) (k=2 and 95% Confidence Level)		
	Liquid	Vapor	SpCr*	Liquid	Vapor	SpCr*
R1336mzz(E)	1.13	1.15	1.16	2.26	2.30	2.32
3,3,4,4,5,5-HFCPE	1.12	1.47	-	2.24	2.94	-
R1123+R32	1.10	1.30	-	2.21	2.60	-

*SpCr–Supercritical Phase

Table A19: Summary of uncertainties for thermal conductivity measurements

Test fluid	Combined Uncertainties (%)			Expanded Uncertainties (%) (k=2 and 95% Confidence Level)		
	Liquid	Vapor	SpCr*	Liquid	Vapor	SpCr*
R1336mzz(E)	1.53	1.58	1.62	3.06	3.16	3.23
3,3,4,4,5,5-HFCPE	1.54	1.76	-	3.08	3.52	-

*SpCr–Supercritical Phase

Reference

Bell, S., 2001. A Beginner's Guide to Uncertainty of Measurement, Measurement Good Practice Guide No. 11 (Issue 2), Centre for Basic, Thermal and Length Metrology, National Physical Laboratory. Teddington, Middlesex, United Kingdom, TW11 0LW.

JCGM 100, 2008. Evaluation of measurement data-Guide to the expression of uncertainty in measurement, GUM 1995 with minor corrections.

Kao, J.T.F., Ruska, W., Kobayashi, R., 1968. Theory and design of an absolute viscometer for low temperature-high pressure applications. Rev. Sci. Instrum. 39, 824–834. <https://doi.org/10.1063/1.1683518>

Taylor, B.N., Kuyatt, C.E., 1994. Guidelines for Evaluating and Expressing the Uncertainty of NIST Measurement Results, NIST Technical Note 1297, National Institute for Standards and Technology (NIST).